DOCTORAL DISSERTATION

Coupling between the DualSPHysics solver and multiphysics libraries: implementation, validation and real engineering applications

Iván Martínez Estévez

2024

International mention

Universidade Vigo

EIDO
Escola Internacional
de Doutoramento

Universidade Vigo
Escola Internacional de Doutoramento

Iván Martínez Estévez

DOCTORAL DISSERTATION

Coupling between the DualSPHysics solver and multiphysics libraries: implementation, validation and real engineering applications

Supervised by:

Dr. Alejandro Jacobo Cabrera Crespo
Dr. José Manuel Domínguez Alonso

Year: 2024

International mention

Campus Universitario de Ourense, Universidade de Vigo
Departamento de Física Aplicada
Environmental Physics Laboratory (EPhysLab), CIM-Uvigo

Iván Martínez Estévez (ivan.martinez.estevez@uvigo.es)

Coupling between the DualSPHysics solver and multiphysics libraries: implementation, validation and real engineering applications

Ourense, January 2024

Universidade Vigo

Escola Internacional de Doutoramento

Dr. Alejandro Jacobo Cabrera Crespo e Dr. José Manuel Domínguez Alonso

FAN CONSTAR que o presente traballo, titulado “Coupling between the DualSPHysics solver and multiphysics libraries: implementation, validation and real engineering applications”, que presenta Iván Martínez Estévez para a obtención do título de Doutor con Mención Internacional, foi elaborado baixo a súa dirección no programa de doutoramento “Auga, sustentabilidade e desenvolvemento” baixo a modalidade de compendio de publicacións.

Ourense, 19 de Xaneiro de 2024.

Os Directores da tese de doutoramento

Dr. Alejandro Jacobo Cabrera Crespo

Dr. José Manuel Domínguez Alonso

Acknowledgments

A todas las personas que me han acompañado y ayudado durante esta etapa.

A mis directores Álex y Jose, por vuestra incansable dedicación y paciencia durante estos años. Agradezco enormemente cada consejo que me ha servido de gran ayuda, tanto en lo personal como en lo profesional. Gracias por depositar tanta confianza en mí y por hacer que este camino haya sido más sencillo.

A Moncho y Maite, por darme la oportunidad de ser parte de vuestro equipo y poder desarrollar mi carrera investigadora. Gracias por acogerme y por vuestros consejos.

A todos mis compañeros del grupo EPhysLab, con los que he compartido increíbles momentos todos estos años y me he sentido como en casa desde el primer día. Especial agradecimiento a Ángel, Xurxo, Orlando, Curro, Diego, Marisela e Irene y a todos con los que he compartido espacio de trabajo durante estos años. Gracias por vuestro apoyo y ayuda.

A todos los colaboradores de esta investigación. Especial agradecimiento a Bonaventura, por tus consejos y toda la ayuda que me has ofrecido durante esta etapa, por ser compañero, amigo y mentor. A Salvatore, compañero y amigo, que me has acompañado en estos años como doctorando y has contribuido enormemente a alcanzar los objetivos. Gracias por vuestra ayuda y contribución a este trabajo.

A mis amigos, por estar siempre a mi lado y compartir tantos momentos juntos. Gracias por ser una fuente constante de apoyo y alegría.

A mi familia, a todos los que habéis estado a mi lado a lo largo de la vida y me habéis transmitido tanto cariño y confianza. Especial mención a mi hermana, a mi abuela y mis padres. No me puedo olvidar de la pequeña de la casa, mi ahijada Carlota, que, sin saberlo, has sido una inyección de alegría y energía desde que has llegado. Gracias por todo, sin vosotros no habría llegado hasta aquí.

A Irene, mi pareja, por estar siempre a mi lado, apoyarme, entenderme y aconsejarme en todas las decisiones importantes, haciendo que todo sea más fácil. Gracias por celebrar mis éxitos como si fueran los tuyos.

Esta tesis de doctorado ha sido financiada por la Xunta de Galicia bajo el "Programa de axudas á etapa predoutoral da Consellería de Cultura, Educación e Universidades da Xunta de Galicia" (ED481A-2021/337) y es parte del proyecto de I+D+i SURVIWEC PID2020-113245RB-I00, financiado por MCIN/AEI/10.13039/501100011033.

Contents

Abstract

Renewables are gaining great importance in recent years, as they represent a clean and limitless option to meet the growing global demand for energy. In fact, the commitment to these energies is an alternative to the electricity produced by polluting energies such as the ones coming from fossil fuels. There are several renewable energy sources, with hydro, wind and solar being the most exploited today. However, the seas and oceans constitute the largest energy storage system in the world, representing enormous energy potential that can be transformed into electricity through different technologies and that would contribute to meeting current energy needs. Thus, wave energy represents one of the most powerful, clean, and constant renewable resources that can be harnessed by means of wave energy converter (WECs) devices. WECs are devices designed to harness wave energy from both coast and offshore. There are many types of WECs, some of the most well-known are: i) point absorber; ii) attenuator; iii) oscillating wave surge converter (OWSC); iv) oscillating water column (OWC); v) rotating mass; and vi) bulge wave, among others. However, wave energy is still in the early stages of development and its energy potential is not fully exploited yet. This is because neither scientists nor engineers have come to an agreement on the type of device that will prevail in the future. Despite the fact that there is no conventional type of WEC, the devices in which the greatest R+D effort has been invested so far are point absorbers. These devices typically consist of a floating buoy that moves up and down with the movement of the waves, and that motion is converted into electricity by a power take-off (PTO) system, which is usually a complex mechanical system.

Probably the biggest challenge for wave energy is to ensure the efficiency and survivability of WECs by making the most of the energy potential of waves. For this reason, there is the need of using tools that facilitate the tasks of design and analysis of the behaviour of WECs. Numerical modelling arises as a good alternative in this field of study, playing a crucial role as a complementary tool to physical experiments. In particular, Computational Fluid Dynamics (CFD) methods are a fundamental tool in many fields of engineering. The models that implement CFD can be divided into mesh-based models and meshless models. Among the mesh-less, it

is worth mentioning the Smoothed Particle Hydrodynamics (SPH) method. SPH is a particle-based method that is able to simulate fluid-structure interactions with high accuracy since the free surface does not require special treatment. In this way, large deformations can be solved avoiding the problems that appear in mesh-based models. However, one of the main limitations of these models is the high computational cost of solving the necessary calculations.

The CFD used in this research is an SPH-based model named DualSPHysics (https://dual.sphysics.org/), which is capable of simulating fluids with free surface and their interaction with fixed and floating structures. This model is ideal for studying the behaviour of WECs under the action of waves even in extreme conditions. Despite the capabilities of DualSPHysics, in many cases it is necessary to use more than one model to solve complex real complex problems. This is because it is not possible to reproduce the different processes or physical mechanisms involved with a single CFD. For example, when modelling the behaviour of a PTO, it is necessary to simulate a complex system using mechanical constraints, such as mechanical brakes, shock-absorbers, and even the presence of components that collide with each other. It should also be considered that some of the devices require of mooring systems that attach them to the seabed to prevent them from drifting due to wave action. Therefore, it is necessary to make use of other tools that allow representing all the components and functionalities of the WECs and their PTO system. This need motivates the main objective of this work, which is to increase the capabilities of the DualSPHysics CFD, providing it with new functionalities that allow to fully simulate any type of WEC. This task is done by coupling DualSPHysics with other models, specifically Project Chrono and MoorDyn+.

The Project Chrono (https://projectchrono.org/) library consists of a multiphysics simulation engine that allows simulating complex mechanisms. Project Chrono is capable of solving a large number of mechanical problems of different complexity, such as rigid and deformable objects, collision with friction between objects by defining material properties, springs, joints, etc. Chrono solves both articulated multi-body systems and collision detection between rigid objects, for which their material properties are defined, using the Discrete Element Method (DEM). Two approaches based on the DEM formulation can be found in Chrono for

resolving frictional contacts between objects. The first approach solves non-smooth contacts (NSC) by introducing complementarity conditions to enforce the non-overlap of the elements that are in contact. The second allows smooth contacts (SMC) to be solved by considering a penalty-based methodology that allows the penetration between elements to experience a partial deformation of the bodies in contact. It is based on an early existing version of this coupling that included a framework in which SPH was used to solve the fluid-rigid object interaction, while the rigid object-object interaction was only simulated using the NSC method. It should be noted that the PTO systems of point absorber devices can be modelled as viscous dampers or friction dampers. The formulation integrated in Chrono only supports the simulation of first ones, therefore, a new development is proposed in this work to also solve friction dampers. Thus, this research presents an extension of the previous work, which includes the NSC approach and integrates the new SMC contact method, as well as a new formulation to simulate PTOs. In addition, the coupling strategy is implemented through a general-purpose communication interface called DSPHChronoLib that deals with two-way coupling provided with an open-source license along with the source code of the software. Moreover, a new formulation for modelling new PTO systems of WECs is implemented in the code. The basis of this two-way coupling is that DualSPHysics solves fluid dynamics and fluid-rigid object interaction using the SPH method. The information of the forces exerted by the fluid on the structures is then transferred to Chrono. Subsequently, Chrono solves the behaviour of rigid objects using DEM and transfers their final positions to DualSPHysics. Finally, DualSPHysics updates the information of the bodies managed by Chrono within the SPH environment. The implementation of this model has to be validated to ensure that the calculations are physically correct. To this end, several reference cases are taken in order to demonstrate that the coupled model is capable of reproducing with sufficient precision the collisions between solids and articulated mechanical systems in simulations where fluid forces are predominant, even when dozens of rigid bodies are involved. Two types of validations are presented, involving fluid-rigid object interaction and collision detection. In both types, accurate results close to the reference data of the experimental tests have been obtained. In addition, mechanical constraints such as linear springs and hinges connected to rigid parts interacting with fluid have been

evaluated to validate the fluid-rigid object interaction and the behaviour of articulated mechanical systems. It should be noted that although simple mechanical systems are reproduced, they can nevertheless be combined with each other to create more sophisticated and complex machines.

Subsequently, a new implementation is considered to increase the capabilities of the coupling between DualSPHysics and Chrono, allowing the simulation of deformable or flexible elements and their interaction with fluid. This feature is essential, for example, to reproduce the parts that are not completely rigid of some WEC devices. The design of WECs with flexible parts is important to increase their survivability, as they can dissipate energy from the strong impacts of waves in the open ocean than completely rigid parts. In this implementation, the Finite Element Analysis (FEA) method included in Chrono has been used to solve flexible elements. The implementation of this functionality in the two-way coupling between DualSPHysics and Chrono allows the simulation of fluid-structure interaction (FSI) combining the SPH-FEA methods in one framework. Specifically, flexible elements are implemented using the Euler-Bernoulli theory for three-dimensional (3-D) beams. This approach is particularly functional and very precise for beam elements subjected to large displacements and deformations. The coupling strategy of this new implementations is similar to the one described above for SPH-DEM. In this case, the structure is discretised into segments, where each segment is an Euler-Bernoulli beam, connected to each other by nodes, where each node is a 3-D finite element. DualSPHysics solves the fluid and the fluid-flexible structure interaction using the SPH method, but in this case, the information of the forces exerted by the fluid on each node of the structure is transferred to Chrono. Subsequently, Chrono solves the behaviour of the flexible objects using FEA and transfers the final position of the nodes to DualSPHysics. Finally, DualSPHysics updates the information of the objects managed by Chrono within the SPH environment, reconstructs the flexible structure in SPH from the calculated deformation and computes the stress on the structure. Reference cases available in the literature are presented to analyse the accuracy of this new implementation. Specifically, four cases are presented to validate the coupled model proposed where the fluid and fluid-structure interaction is resolved with SPH, and the structure deformation is resolved with FEA. Results

obtained show that the numerical model successfully predicts the global dynamics of the system when solving FSI problems, while at the same time, it is very resistant and robust in cases where large deformations take place. Although only two-dimensional (2-D) environments are simulated for this first set of validations, its extension to a 3-D domain is possible and the model can be used for more complex cases, both for structural calculations and to model some flexible parts of WECs.

On the other hand, MoorDyn+ (https://github.com/imestevez/MoorDynPlus) is a model that solves mooring dynamics, which is based on MoorDyn. A coupling between DualSPHysics and MoorDyn had already been implemented, but this mooring library had some implementation problems and did not include all the required functionalities. For this reason, MoorDyn+ has been developed, which is a reimplementation that improves the former code and includes new functionalities such as the ability of simulating multiple floating objects moored to the seabed, moorings between objects or defining breaking tensions in moorings, among others. The moorings are solved with the so-called lumped-mass (LM) method, in which the moorings are discretised as segments connected by nodes. Each segment defines stiffness and damping properties, and the nodes are modelled as point masses. In addition, this model allows simulating the drag and friction of the moorings with the seabed. A two-way coupling is performed between DualSPHysics and MoorDyn+ that allows reproducing moored floating objects, as are the case with several WECs. Despite MoorDyn+ already included enough functionalities to solve most moored devices, it was only capable of reproducing catenary type mooring lines. However, some WECs that are currently under study use tensors or taut-mooring lines. For this reason, it was necessary to include the possibility of simulating these kinds of mooring lines in MoorDyn+ while respecting the formulation. In this way, this new coupling version includes all the features implemented in MoorDyn+ in addition to the new taut-mooring lines.

With all the features integrated into the coupled model, it is intended to demonstrate that the computational code is suitable for simulating complex moving objects and fluid-driven objects to study not only the efficiency, but also the survivability of WECs. The Uppsala WEC (UWEC), which follows a point absorber typology, is considered as a reference case in this research to apply and validate the

code, as well as study its behaviour under extreme wave conditions. Specifically, a 1:20 scale prototype of the UWEC is reproduced, which was experimentally analysed in a wave tank, but maintaining the intrinsic characteristics of the full-scale UWEC. The operating principle of the UWEC combines a floating buoy connected with a mooring to a PTO system that is fixed on a weighted platform and located at seafloor level. The PTO is modelled with a moving piece that travels along a guide (translator). The translator is bounded in its vertical motion by an upper and lower end-stop, which are movable and fixed, respectively. When the translator impacts the upper end-stop system, its vertical motion is modified by the presence of a spring-damper element. The harvesting tool is represented by a friction damper, using the new formulation implemented in this work for this type of system. The movement of the buoy is transmitted through a taut-mooring line, which makes the dynamics of the entire system quite complex and highly dependent on the behaviour of each part. This system requires using the three models described in this paper working together as follows: i) DualSPHysics to model wave generation and interaction with the floating buoy; ii) MoorDyn+ to model the mooring that transmits the movement of the buoy to the PTO; and iii) Chrono to model the PTO involving collision detection, translator, end-stoppers, and spring-damper. Therefore, reproducing all the phenomena involved in the study of the UWEC is a challenge for a single CFD. Hence, the proposed model takes full advantage of the features offered by the coupling of DualSPHysics with the two libraries: Chrono and MoorDyn+. This work proposes, for the first time, the application of an SPH-based model to the UWEC device and the modelling of all its properties. Initially, the generation of extreme waves is simulated with DualSPHysics, and the results are analysed against the data obtained from the experiments. It can be observed that DualSPHysics is capable of generating and propagating extreme waves with great precision, this makes it ideal for studying this type of non-linear phenomena. Two different configurations are then proposed to simulate the PTO, one that mimics the WEC energy harvesting by adding a damping coefficient to the PTO formulation, while the other has no internal damping. The UWEC is simulated under extreme wave conditions and a validation of the temporal evolution of the vertical elevation (heave) and longitudinal displacement (surge) of the buoy is provided, comparing the numerical results with the experimental data. Considering the results obtained

from the simulations, it can be observed that not only the interaction of the waves with the buoy is accurately calculated by DualSPHysics, but also that the effect of the mooring system and the behaviour of the PTO are correct. On the other hand, the forces of the mooring line are also analysed against experimental data, obtaining precise results that capture the pulls exerted by the displacement of the buoy. When analysing this set of results, it can be stated that the use of a damping function helps to reduce the magnitude of the forces suffered by the internal components of the PTO and the mooring line. Finally, a real representation of the sea state is carried out by generating irregular waves with DualSPHysics. Four different configurations of the PTO are defined, and their behaviour is analysed under the effect of the irregular waves. This study serves as a basis for providing solutions that help in the optimisation of the operation of the device in order to improve its survivability. It can be concluded that the UWEC benefits from the use of a higher damping in the PTO. Firstly, the system harvests more energy for smaller wave amplitudes. Secondly, it is observed a reduction in the mobility of the translator and the forces received by the mooring line, thus reducing the detrimental effects on the mechanical structure and foundation of the base, as well as fatigue at the mooring line. Therefore, this research demonstrates that the developed code has the appropriate degree of maturity and completeness to handle highly non-linear simulations and to study the efficiency and survivability of floating devices intended for wave energy conversion.

The formulation and coupling strategy presented represents a great advance for the DualSPHysics model in terms of its general usability and versatility, greatly expanding the relevance of the code. It allows the general characteristics of fluids and complex multiphysics systems to be merged within the same co-operative framework between different computational codes, presenting a much wider range of applicability for a great variety of fields. The tests considered as validation show that the model can be used to reproduce both the most relevant characteristics of real mechanical systems, such as the impacts between objects, and, in general, the dynamics of multi-body systems that can interact with fluids. In addition, the possibility of simulating flexible structures that interact with fluid in this coupling expands the design and modelling capabilities applied to any field, including the

simulation of some flexible WECs (FlexWECs) that are currently under study, semi-submersible floating wind turbines (FWTs) or tension leg platforms (TLPs). All these new capabilities incorporated into the DualSPHysics CFD are achieved thanks to its coupling with Project Chrono. On the other hand, the possibility of integrating the mooring system of the floating devices is essential to fully simulate all the parts that intervene and affect the behaviour of the WECs. Improvements in the code that implements the mooring dynamics solver offer the possibility of reproducing catenary and taut-mooring lines, which favours their applicability to more types of floating devices. Therefore, DualSPHysics is able to simulate moored floating devices using different types of mooring lines, thanks to its coupling with MoorDyn+. Finally, this paper shows the capabilities of a cooperative computation framework involving three different models (DualSPHysics, Chrono and MoorDyn+) to numerically reproduce the response of various concepts and characteristics of WECs. In this way, this computational code becomes a useful tool to address more challenging scenarios than those that could be represented previously.

Resumen

Las energías renovables están cobrando una gran importancia en los últimos años, ya que representan una opción limpia e ilimitada para satisfacer la creciente demanda mundial de energía. De hecho, la apuesta por estas energías es una alternativa a la electricidad producida por energías contaminantes como la procedente de los combustibles fósiles. Existen varias fuentes de energía renovables, siendo la hidráulica, la eólica y la solar las más explotadas en la actualidad. Sin embargo, los mares y los océanos constituyen el mayor sistema de almacenamiento de energía del mundo, suponiendo un enorme potencial energético que puede ser transformado en electricidad a través de diferentes tecnologías y que contribuiría a satisfacer las necesidades energéticas actuales. Así, la energía de las olas o energía undimotriz representa uno de los recursos renovables más potentes, limpios y constantes que puede aprovecharse mediante dispositivos convertidores de energía undimotriz (en inglés *Wave Energy Converter*, WEC). Los WECs son dispositivos destinados a aprovechar la energía de las olas tanto del litoral como de alta mar. Existen muchos tipos de WECs, algunos de los más conocidos son: i) absorbedor puntual (en inglés *point absorber*), ii) atenuador (en inglés *attenuator*), iii) oleada de onda oscilante (en inglés *oscillating wave surge converter*, OWSC), iv) columna de agua oscilante (en inglés *oscillating water column*, OWC), v) masa giratoria (en inglés *rotating mass*) y vi) onda abultada (en inglés *bulge wave*), entre otros. Sin embargo, la energía de las olas se encuentra todavía en las primeras fases de desarrollo y su potencial energético aún no se aprovecha plenamente. Esto se debe a que ni los científicos ni los ingenieros han llegado a un acuerdo sobre el tipo de dispositivo que prevalecerá en el futuro. A pesar de que no existe un tipo convencional de WEC, los dispositivos en los que se ha invertido un mayor esfuerzo de I+D hasta el momento son los absorbedores puntuales. Estos dispositivos consisten normalmente en una boya flotante que sube y baja con el movimiento de las olas y ese movimiento se convierte en electricidad mediante un sistema de toma de fuerza (en inglés *power take-off*, PTO), que por lo general es un sistema mecánico complejo.

Probablemente, el mayor reto de la energía undimotriz sea el de garantizar la eficiencia y la supervivencia de los WECs aprovechando al máximo el potencial energético de las olas. Por ello existe la necesidad de emplear herramientas que faciliten las tareas de diseño y análisis del comportamiento de los WECs. El modelado numérico surge como una buena alternativa en este campo de estudio, jugando un papel crucial como herramienta complementaria a los experimentos físicos. En particular, los métodos de dinámica de fluidos computacional (en inglés *Computational Fluid Dynamics*, CFD) son una herramienta fundamental en muchos campos de la ingeniería. Los modelos que implementan CFD pueden dividirse en modelos basados en una malla y en modelos sin malla. Entre los modelos sin malla, cabe mencionar el método de hidrodinámica de partículas suavizadas (en inglés *Smoothed Particle Hydrodynamics*, SPH). SPH es un método de partículas que puede simular interacciones fluido-estructura con gran precisión, ya que la superficie libre no requiere de un tratamiento especial. De este modo, se pueden resolver grandes deformaciones sin los problemas que aparecen en los modelos de malla. Sin embargo, una de las principales limitaciones de estos modelos es el elevado coste computacional que supone resolver los cálculos necesarios.

El CFD utilizado en esta investigación es un modelo SPH denominado DualSPHysics (https://dual.sphysics.org/), que es capaz de simular fluidos con superficie libre y su interacción con estructuras fijas y flotantes. Este modelo es ideal para estudiar el comportamiento de WECs bajo la acción del oleaje incluso en condiciones extremas. A pesar de las capacidades de DualSPHysics, en muchos casos es necesario el uso de más de un modelo para resolver problemas reales complejos. Esto se debe a que no es posible reproducir con un solo CFD los diferentes procesos o mecanismos físicos involucrados. Por ejemplo, a la hora de modelar el comportamiento de un PTO, es necesario simular un sistema complejo mediante restricciones mecánicas, como pueden ser frenos mecánicos, amortiguadores e incluso la presencia de componentes que colisionan entre sí. También hay que considerar que algunos de los dispositivos requieren sistemas de amarres que los conectan al fondo marino para evitar que se vayan a la deriva debido a la acción del oleaje. Por lo tanto, es necesario hacer uso de otras herramientas que permitan representar todos los componentes y funcionalidades de los WECs y su sistema de

PTO. Esta necesidad motiva el objetivo principal del presente trabajo, el cual es aumentar las capacidades del CFD DualSPHysics, dotándolo de nuevas funcionalidades que permitan simular completamente cualquier tipo de WEC. Esta tarea se realiza mediante el acoplamiento entre DualSPHysics y otros modelos, concretamente con Project Chrono y MoorDyn+.

La librería Project Chrono (https://projectchrono.org/) consiste en un motor de simulación multifísica que permite simular mecanismos complejos. Project Chrono es capaz de resolver gran cantidad de problemas mecánicos de diferente complejidad, tales como objetos rígidos y deformables, colisión con fricción entre objetos definiendo propiedades de los materiales, resortes, articulaciones, etc. Chrono resuelve tanto los sistemas multi cuerpo articulados como la detección de colisiones entre objetos rígidos, para los que se definen sus propiedades de material, usando el método de elementos discretos (en inglés *Discrete Element Method*, DEM). Dentro de Chrono se pueden encontrar dos enfoques basados en la formulación DEM para resolver los contactos por fricción entre objetos. El primero resuelve contactos no suavizados (en inglés *non-smooth contacts*, NSC) introduciendo condiciones de complementariedad para hacer cumplir el no solapamiento de los elementos que están en contacto. El segundo permite resolver contactos suavizados (en inglés *smooth contacts*, SMC) porque incluye una metodología basada en penalizaciones que permite que la penetración entre elementos experimente una deformación parcial de los cuerpos en contacto. Se parte de una primera versión existente de este acoplamiento que incluía un marco en el que se utilizaba SPH para resolver la interacción fluido-objeto rígido, mientras que la interacción objeto-objeto rígido solamente se simulaba usando el método NSC. Cabe señalar que los sistemas de PTO de los dispositivos de tipo absorbedor puntual se pueden modelar como amortiguadores con viscosidad o amortiguadores de fricción. La formulación integrada en Chrono solo soporta la simulación de los primeros, por lo tanto, se propone un nuevo desarrollo para resolver también los amortiguadores de fricción. De este modo, en este trabajo se presenta una extensión del trabajo anterior, que incluye el enfoque NSC y se integra el nuevo método de contacto SMC, así como una nueva formulación para simular PTOs. Además, se implementa la estrategia de acoplamiento mediante una interfaz de comunicación de propósito general

denominada DSPHChronoLib que se ocupa de la transferencia bidireccional de datos (en inglés *two-way coupling*) proporcionada con una licencia de código abierto junto con el código fuente del software. También se incluye en el código una nueva formulación para modelar el PTO de los WECs. La base de este *two-way coupling* es que DualSPHysics resuelve la dinámica del fluido y la interacción fluido-objeto rígido usando el método SPH. A continuación, se transfiere la información de las fuerzas ejercidas por el fluido sobre las estructuras a Chrono. Posteriormente, Chrono resuelve el comportamiento de los objetos rígidos usando DEM y transfiere la posición final a DualSPHysics. Finalmente, DualSPHysics actualiza la información de los objetos gestionados por Chrono dentro del entorno SPH. La implementación de este modelo necesita ser validada para asegurarse de que los cálculos son correctos desde un punto de vista físico. Para ello, se toman varios casos de referencia con el fin de que el modelo acoplado demuestre ser capaz de reproducir con suficiente precisión las colisiones entre sólidos y sistemas mecánicos articulados en simulaciones donde predominan las fuerzas de los fluidos, incluso cuando están implicados decenas de cuerpos rígidos. Se presentan dos tipos de validaciones en las que intervienen la interacción de fluido-objeto rígido y la detección de colisiones. En ellas se obtienen unos resultados precisos cercanos a los datos tomados como referencia de ensayos experimentales. Además, se han evaluado restricciones mecánicas como muelles lineales y bisagras conectadas a partes rígidas que interactúan con fluido para validar la interacción fluido-objeto rígido y el comportamiento de los sistemas mecánicos articulados. Hay que tener en cuenta que, aunque se reproducen sistemas mecánicos sencillos, sin embargo, estos pueden combinarse entre sí para crear máquinas más sofisticadas y complejas. Posteriormente se realiza una nueva implementación para aumentar las capacidades del acoplamiento entre DualSPHysics y Chrono permitiendo la simulación de elementos deformables o flexibles y su interacción con fluido. Esta característica es fundamental, por ejemplo, para reproducir las partes que no son completamente rígidas de algunos dispositivos WECs. El diseño de los WEC con partes flexibles es importante para aumentar su capacidad de supervivencia, ya que pueden disipar más energía de los fuertes impactos de las olas en mar abierto que partes completamente rígidas. En esta implementación se ha usado el método de Análisis de Elementos Finitos (en inglés *Finite Element Analysis*, FEA) integrado en

Chrono para resolver elementos flexibles. La implementación de esta funcionalidad en el *two-way coupling* entre DualSPHysics y Chrono permite la simulación de la interacción de fluido-estructura (en inglés *fluid-structure interaction*, FSI) combinando los métodos SPH-FEA en un *software*. Concretamente, se implementan estructuras flexibles que se resuelven con la teoría de Euler-Bernoulli para vigas tridimensionales (3D). Este enfoque es particularmente funcional y muy preciso para elementos de viga sometidos a grandes desplazamientos y deformaciones. La estrategia de acoplamiento de esta nueva implementación es similar a la anteriormente descrita para SPH-DEM. En este caso la estructura se discretiza en segmentos, donde cada segmento es una viga Euler-Bernoulli, conectados entre sí mediante nodos, donde cada nodo es un elemento finito en 3D. DualSPHysics resuelve el fluido y la interacción entre el fluido-objeto flexible usando el método SPH, pero en este caso, se transfiere la información de las fuerzas ejercidas por el fluido sobre cada uno de los nodos de la estructura a Chrono. Posteriormente, Chrono resuelve el comportamiento de los objetos flexibles mediante FEA y transfiere la posición final de los nodos a DualSPHysics. Finalmente, DualSPHysics actualiza la información de los objetos gestionados por Chrono dentro del entorno SPH, reconstruye la estructura flexible en SPH a partir de la deformación calculada y calcula la tensión que sufre la estructura. Se plantean casos de referencia disponibles en la literatura útiles para analizar la precisión de esta nueva implementación. Concretamente, se presentan cuatro casos para validar el modelo acoplado propuesto donde el fluido y la interacción fluido-estructura se resuelve con SPH y la deformación de la estructura se resuelve con FEA. Los resultados obtenidos muestran que el modelo numérico predice con éxito la dinámica global del sistema a la hora de resolver problemas de FSI, al mismo tiempo que se muestra muy resistente y robusto en casos donde se producen grandes deformaciones. A pesar de que para este primer conjunto de validaciones se simulan únicamente entornos bidimensionales (2D), su extensión a un dominio 3D es posible y el modelo puede ser utilizado para casos más complejos, tanto para cálculos estructurales, como para modelar algunas partes de WECs que sean flexibles.

Por otro lado, MoorDyn+ (https://github.com/imestevez/MoorDynPlus) es un modelo que resuelve dinámica de amarres y que está basado en MoorDyn. Ya existía

una implementación del acoplamiento entre DualSPHysics y MoorDyn, pero esta librería de amarres presentaba algunos problemas de implementación y no incluía todas las funcionalidades que se requerían. Por esta razón, se desarrolla MoorDyn+ que es una reimplementación que mejora el código antiguo e incluye nuevas funcionalidades como la capacidad de simular múltiples objetos flotantes amarrados al fondo marino, amares entre objetos o definir tensiones de rotura de los amarres, entre otras. El método utilizado para resolver los amarres es el denominado *lumped-mass* (LM) en el que los amarres se discretizan como segmentos conectados por nodos. Cada segmento tiene propiedades de rigidez y amortiguación y los nodos son masas puntuales. Además, permite simular el arrastre y fricción de los amarres con el fondo marino. Se realiza un *two-way coupling* entre DualSPHysics y MoorDyn+ que permite reproducir objetos flotantes amarrados, como es el caso de algunos WECs. A pesar de que MoorDyn+ ya incluía las funcionalidades suficientes para resolver la gran mayoría de dispositivos amarrados, solamente era capaz de reproducir líneas de amarre de tipo catenaria. Sin embargo, algunos WECs que están actualmente bajo estudio utilizan sistemas de amarre con líneas con pretensión o tensores (en inglés *taut-mooring lines*). Por esta razón, fue necesario incluir la posibilidad de simular estos tipos de líneas de amarre en MoorDyn+ respetando la formulación. De esta forma, esta nueva versión de acoplamiento incluye todas las características implementadas en MoorDyn+ además de los nuevos tensores.

Con todas las características integradas en el modelo acoplado, se pretende demostrar que el código computacional es adecuado para simular objetos complejos en movimiento y objetos impulsados por fluidos para estudiar no sólo la eficiencia, sino también la capacidad de supervivencia de los WECs. Se considera el WEC de Uppsala (UWEC), de tipo absorbedor puntual, como caso de referencia en esta investigación para aplicar y validar el código, analizando comportamiento bajo condiciones extremas de oleaje. Específicamente, se reproduce un prototipo a escala 1:20 del UWEC que fue analizado experimentalmente en un tanque de olas, pero que mantiene las características intrínsecas del UWEC de escala real. El principio de funcionamiento del UWEC combina una boya flotante conectada con un amarre a un sistema de PTO que está fijado sobre una plataforma lastrada y situada a nivel del

fondo marino. El PTO se modela con una pieza móvil que se desplaza a lo largo de una guía (*translator*). El *translator* está limitado en su movimiento vertical por un freno o tope superior e inferior (*end-stoppers*), que son móviles y fijos, respectivamente. Cuando el *translator* impacta en el sistema de tope superior, su movimiento vertical se ve modificado por la presencia de un resorte. La herramienta de recolección está representada por un amortiguador de fricción, utilizando la nueva formulación implementada en este trabajo para este tipo de sistemas. El movimiento de la boya se transmite a través de una línea de amarre con pretensión, lo que hace que la dinámica de todo el sistema sea bastante compleja y dependa en gran medida del comportamiento de cada una de las partes. Este sistema requiere usar los tres modelos descritos en este trabajo funcionando conjuntamente de la siguiente forma: i) DualSPHysics para modelar la generación del oleaje y su interacción con la boya flotante; ii) MoorDyn+ para modelar el amarre que transmite el movimiento de la boya al PTO; y iii) Chrono para modelar el PTO en el que intervienen detección de colisiones, guías de desplazamiento, amortiguadores y resortes. Por lo tanto, reproducir todos los fenómenos que intervienen a la hora de estudiar el UWEC es un reto para un único CFD. En consecuencia, el modelo propuesto aprovecha plenamente las características que ofrece el acoplamiento de DualSPHysics con las dos librerías: Chrono y MoorDyn+. Este trabajo propone, por primera vez, la aplicación de un modelo basado en SPH para el dispositivo UWEC y la modelización de todas sus propiedades. Inicialmente se simula la generación de oleaje extremo con DualSPHysics y se analizan los resultados frente a los datos obtenidos experimentalmente. Se puede observar que DualSPHysics es capaz de generar y propagar oleaje extremo con gran precisión, esto lo hace ideal para estudiar este tipo de fenómenos no lineales. Acto seguido se proponen dos configuraciones diferentes para simular el PTO, una que imita la recolección de energía del WEC agregando un coeficiente de amortiguación a la formulación del PTO, mientras la otra no tiene amortiguación interna. Se simula el UWEC bajo las condiciones de oleaje extremo y se proporciona una validación de la evolución temporal de los movimientos de elevación vertical (*heave*) y desplazamiento longitudinal (*surge*) de la boya, comparando los resultados numéricos con los datos experimentales. Teniendo en cuenta los resultados obtenidos, se puede observar que no solo la interacción del oleaje con la boya es calculada con precisión por

DualSPHysics, sino que también el efecto del sistema de amarre y el comportamiento del PTO son correctos. Por otro lado, también se analizan las fuerzas de la línea de amarre frente a los datos experimentales, obteniendo unos resultados precisos que capturan los tirones ejercidos por el desplazamiento de la boya. Mediante el análisis de este conjunto de resultados se puede afirmar que el uso de una función de amortiguación ayuda a reducir la magnitud de las fuerzas que sufren los componentes internos de la toma de fuerza y la línea de amarre. Finalmente, se lleva a cabo una representación real del estado del mar mediante la generación de oleaje irregular con DualSPHysics. Se definen cuatro configuraciones distintas del PTO y se analiza su comportamiento bajo el efecto del oleaje irregular. Este estudio sirve como base para proporcionar soluciones que ayuden en la optimización del funcionamiento del dispositivo con el fin de aumentar su capacidad de supervivencia. Se puede concluir que el UWEC se beneficia del uso de una amortiguación mayor en el PTO. En primer lugar, el sistema recolecta más energía para amplitudes de olas más pequeñas. En segundo lugar, observa una reducción de la movilidad del *translator* y de las fuerzas que recibe la línea de amarre, reduciendo así los efectos perjudiciales en la estructura mecánica y en los cimientos de la base, así como la fatiga en la línea de amarre. Por lo tanto, en esta investigación se demuestra que el código desarrollado tiene el grado de madurez y completitud adecuado para manejar simulaciones altamente no lineales y para estudiar la eficiencia y capacidad de supervivencia de dispositivos flotantes destinados a la conversión de energía undimotriz.

La formulación y estrategia de acoplamiento presentada, supone un gran avance para el modelo DualSPHysics en cuanto su usabilidad general y versatilidad, ampliando en gran medida la relevancia del código. Permite fusionar las características generales de fluidos y sistemas multi físicos complejos dentro del mismo marco colaborativo entre distintos códigos computacionales, presentando un rango mucho más amplio de aplicabilidad para una gran variedad de campos. Las pruebas consideradas como validación muestran que el modelo puede utilizarse para reproducir tanto las características más relevantes de los sistemas mecánicos reales, como los impactos entre objetos, y, en general, la dinámica de sistemas multi cuerpo que pueden interactuar con fluidos. Además, la posibilidad de simular

estructuras flexibles que interactúan con fluido en este acoplamiento, amplia las capacidades de diseño y modelado aplicado a cualquier ámbito, incluso para reproducir algunos WECs flexibles (en inglés *Flexible Wave Energy Converter*, FlexWEC) que están actualmente bajo estudio, aerogeneradores flotantes semi sumergibles (en inglés *Floating Wind Turbine,* FWT) o plataformas de cables en tensión (en inglés *Tension Leg Platforms,* TLP). Todas estas nuevas capacidades incorporadas al CFD DualSPHysics, se consiguen gracias a su acoplamiento con Project Chrono. Por otro lado, la posibilidad de integrar el sistema de amarre de los dispositivos flotantes es fundamental para simular de forma completa todas las partes que intervienen y afectan al comportamiento de los WECs. Las mejoras en el código que resuelve la dinámica de amarres ofrecen la posibilidad de reproducir amarres de tipo catenaria y tensores, lo que favorece su aplicabilidad a más tipos de dispositivos flotantes. Por lo tanto, DualSPHysics es capaz de simular dispositivos flotantes amarrados mediante diversos sistemas, gracias a su acoplamiento con MoorDyn+. Finalmente, este trabajo muestra las capacidades de un marco de cálculo cooperativo que involucra tres modelos diferentes (DualSPHysics, Chrono y MoorDyn+) para reproducir numéricamente la respuesta de diversos conceptos y características de los WECs. De este modo, este código computacional se convierte en una herramienta útil para abordar escenarios más desafiantes que los que se podían representar anteriormente.

List of Figures

List of Tables

List of Acronymous

AWAS: *Active Wave Absorption System*

CFD: *Computational Fluid Dynamics*

CPU: *Central Processing Unit*

CR: *Co-rotational*

CUDA: *Compute Unified Device Architecture*

DAE: *Differential Algebraic Equations*

DBC: *Dynamic Boundary Conditions*

DEM: *Discrete Element Method*

DOF: *Degrees of Freedom*

DVI: *Differential Variational Inequality*

FE: *Finite Element*

FEA: *Finite Element Analysis*

FEM: *Finite Element Method*

FlexWEC: *Flexible Wave Energy Converter*

FOSWEC: *Floating Oscillating Wave Energy Converter*

FWT: *Floating wind turbine*

FSI: *Fluid-structure interaction*

GPU: *Graphics Processing Units*

HPC: *High Performance Computing*

JCR: *Journal Citation Reports*

LGPL: *Lesser General Public License*

LM: *Lumped-mass*

mDBC: *Modified Dynamic Boundary Conditions*

MPI: *Message Passing Interface*

N-S: *Navier-Stokes*

NSC: *Non-smooth contacts*

OWC: *Oscillating water column*

OWSC: *Oscillating wave surge converter*

PTO: *Power take-off*

RAM: *Random Access Memory*

RMSE: *Root mean square error*

SMC: *Smooth contacts*

SPH: *Smoothed Particle Hydrodynamics*

SPS: *Sub-particle scale model*

TLP: *Tension leg platforms*

TSDA: *Translational spring-damper-actuator*

UWEC: *Uppsala WEC*

WEC: *Wave Energy Converter*

CHAPTER 1

Introduction

The first chapter contains an overview of this doctoral thesis. Specifically, motivation and literature review on the main related topics are addressed, as well as the structure of this dissertation.

1.1 Motivation

Renewable energies are gaining significance in recent years as they represent a clean and unlimited option to support the global growing demand for energy. In fact, the promotion of these energies is an alternative to the electricity produced by unsustainable and contaminating energies such as the ones coming from the combustion of fossil fuels. However, the growth in energy demand requires fossil fuels to remain the main contributors to producing all the energy needed for the planet (Olabi and Abdelkareem, 2022). It is worth mentioning that the dependence on fossil fuels has not only led to the depletion of finite resources, but has also contributed significantly to environmental degradation, air pollution, especially considering the emission of greenhouse gases and its impact on climate change. In response to these challenges, the world is turning to renewable energies, developing a diverse suite of technologies that harness natural resources to provide a clean, sustainable, and endless source of energy. Likewise, renewable energy sources are crucial to achieve climate goals through international and national agreements and commitments in the fight against climate change to reduce the carbon footprint of the countries (Gul and Chaudhry, 2022). Therefore, renewable energies play an important role in mitigating the climate change (Owusu and Asumadu-Sarkodie, 2016). In fact, it may be possible that fossil could be replaced by renewable energy in the future (Holechek et al., 2022). However, in 2022, the energy produced from fossil fuels still satisfies the 81.79% of the global energy demand, whereas the consume of renewable energy is around the 14.21%, growing by 0.76% compared to 2021 (Energy Institute, 2023).

Renewable energies can be classified into different groups depending on the source, where hydroelectric, wind and solar energy are currently the most exploited. Nevertheless, seas and oceans constitute the largest energy storage system in the world, representing an enormous energy potential that can be transformed into electricity through different technologies and would contribute to meeting the current energy needs to satisfy the global demand. In this way, marine renewable energies comprise a wide range of resources, including tidal, marine currents and wave energy, providing sustainable solutions that exploit the enormous potential of the oceans. Wave energy is particularly promising because it is consistent and abundant in coastal areas, in fact, it represents one of the most powerful, cleanest, and constant renewable resources. The wave power at a given site may be available up to 90% of the time, while solar and wind availability tend to be around the 20–30% (Drew et al., 2009). Wave energy converters (WECs) are devices intended to harness energy from coastal waves and deeper offshore waters and convert it into electricity by means of a power take-off (PTO) system (Ahamed et al., 2020). There are many types of WECs that can be grouped into different categories depending on the operation of their PTO, where some of the most common ones are: i) point absorber, ii) attenuator, iii) oscillating wave surge converter (OWSC), iv) oscillating water column (OWC), v) rotating mass and vi) bulge wave, among others. Nevertheless, wave energy is still in the early stages of development and its energy potential is not yet fully exploited because neither scientists nor engineers have reached an agreement on the type of WEC that will prevail in the future (Kamranzad and Hadadpour, 2020). Despite that there is not a main type of WEC, it can be assumed that the most commonly used are the point absorbers as they are the type of devices in which the greatest R&D effort has been invested up to the present (López et al., 2013; Binh et al., 2016; Commission et al., 2020) and it is considered the most cost-effective technology for wave energy extraction (Li and Yu, 2012). These devices normally consist of a floating buoy that moves up and down with the movement of the waves and that motion is converted into electricity through the PTO. PTOs are generally complex mechanical systems based on different principles, where the most common are hydraulic PTOs, linear generators, air turbines and low-pressure water turbines (Pecher and Kofoed, 2017). However, it should be noted that it is very difficult to decide on a single WEC device capable of harnessing

the potential energy on any coast or ocean in the world. The design of effective WECs involves challenges related to dynamic wave interactions, material selection, and energy conversion efficiency. Furthermore, the optimisation of the WEC performance requires in-depth knowledge and research on the complex fluid-structure interactions occurring in the marine environment (Trueworthy and DuPont, 2020; Golbaz et al., 2022) and moreover, the placement of WECs in an array also affects the power absorption due to hydrodynamic interactions (Falnes, 2002; deCastro et al., 2024; Shadmani et al., 2024).

Numerical modelling plays a crucial role as a complementary tool to physical experiments. Computational Fluid Dynamics (CFD) methods are fundamental tools in many fields of engineering such as coastal and ocean engineering. It allows to perform numerical studies without the need of building prototypes or real scale devices, allowing the reduction of economic costs and time when multiple configurations should be evaluated. Numerical models cannot replace physical experiments, but they can significantly reduce their number and, at the same time, can provide information that is difficult or impossible to measure in physical tests. In this case, numerical modelling is able to give support during the design stage of WECs (Folley, 2016). CFD methods can be mainly divided into mesh-based and meshless methods. Among the meshless models, different approaches have been developed, but it is worth mentioning the Smoothed Particle Hydrodynamics (SPH) method, which has been growing in maturity and robustness in recent years (Violeau and Rogers, 2016). SPH is a Lagrangian particle-based method where the fluid dynamics equations are solved in computational nodes denoted as particles that can move freely through the domain. This characteristic allows the SPH method to simulate fluid-solid interactions with high accuracy, since the free surface does not require a special treatment and high deformations can be solved without the problematic that supposes in mesh-based methods. The properties of the SPH method make it suitable to be applied for coastal engineering applications (Gotoh and Khayyer, 2018) and specifically, for reproducing WECs due to the fact that this method can fully capture non-linearities (Penalba et al., 2017a). However, one of the main limitations of these models is its high computational cost.

The DualSPHysics (Domínguez et al., 2022) software is a Lagrangian open-source CFD solver based on the SPH method. This code has been developed to simulate free-surface flows and the interaction between fluid and fixed and floating structures. DualSPHysics is an evolution of the FOTRAN-based open-source code SPHysics (Gomez-Gesteira et al., 2012a, 2012b), from which it inherits the core formulation. In addition, it is a highly parallelised hybrid code (Crespo et al., 2015), being able to run on both shared memory Central Processing Unit (CPU) systems (e.g., multi-core CPUs) using OpenMP, or on Graphics Processing Units (GPUs) using the Compute Unified Device Architecture (CUDA) parallel computing framework for Nvidia GPUs (Domínguez et al., 2013a, 2013b). DualSPHysics is a reference solver for coastal engineering applications and has been successfully applied to several research investigations (González-Cao et al., 2019; Altomare et al., 2022; Suzuki et al., 2022; Altomare et al., 2023; Capasso et al., 2023b; Tagliafierro et al., 2023a). Despite the capabilities of DualSPHysics, in many cases, the use of a single model is not sufficient to simulate complex real problems since there are various processes or physical phenomena that cannot be solved by a single CFD. For example, PTO modelling requires the simulation of complex systems with mechanical constraints, such as hydraulic brakes, shock absorbers, or even the presence of components that collide with each other (Dang et al., 2019; Liu et al., 2017). It should also be considered that some of the devices include mooring systems that connect them to the seabed to prevent them from drifting away under the action of the waves. Therefore, it is necessary to make use of other tools that can represent all the components and functionalities of the WECs and their PTO.

The development of coupled frameworks, where different methods are involved, has been considered essential to support scientific research to reproduce the wide variety of physical systems currently in use or under development. Thus, CFD-based codes benefit from coupling with other methods or solvers to expand their capabilities, being able to simulate phenomena that a single CFD is not capable of solving on its own. Sometimes, the coupling development integrates two different formulations based on the same method, as found in the literature, where two different SPH-based formulations were coupled to solve new problems such as the study of fluid flows interacting with laminated composite elastic structures (Khayyer et al., 2021). However, the coupling of SPH with other methods has been

subject of significant research and development to address more complex physical phenomena. Several studies demonstrated the flexibility of an SPH code coupled with different models, for example, to apply an open boundary formulation to accurately generate, propagate and absorb waves (Verbrugghe et al., 2019), to simulate wave propagation and high-dynamic impact of a wave train on a complex-shaped floating body (Oger et al., 2014), or even to address multiphysics simulations, in which collision detection takes place (Canelas et al., 2016). Additionally, fluid-structure interactions (FSI) with large deformations has been investigated using other approaches coupled with SPH (De Vuyst et al., 2005; Myers et al., 2023).

The Discrete Element Method (DEM) is a numerical technique applied to describe the dynamics of large material point systems possessing a specified geometry (Cundall and Strack, 1979) and the computational modelling of multi-body contacts (Bićanić, 2007). This method is appropriate and accurate for solving scenarios that comprise a large number of elements subject to collisions, such as the interaction of granular materials (Jing and Stephansson, 2007; Hu et al., 2021). Latest advances conducted to the development of new algorithms to solve the rigid bodies with arbitrary shapes and frictional contacts (Tasora and Anitescu, 2010). DEM is a meshless method, so it can be easily coupled with particle-based methods like SPH. Regarding the coupling SPH-DEM, several works analysed the behaviour of granular flow systems interacting with fluid (Jo et al., 2022; Zou et al., 2022), where the solid-solid interaction is solved with DEM and the fluid-solid interaction with SPH. Moreover, the SPH-DEM was also successfully applied to study debris flow (Canelas et al., 2016) the interaction of polyhedral granular materials with fluid (Sun et al., 2023), landslide tsunamis (Xu and Dong, 2021), slurry transport and mixing (He et al., 2018), and the modelling of cable-controlled remotely operated vehicles (Su et al., 2024). An SPH-DEM code, which incorporates energy-tracking impulse method for multiple-body contacts, was proposed to solve fluid–rigid-body interactions for violent free-surface flow problems (Asai et al., 2021). Other studies conducted the use of an SPH-DEM to reproduce flexible structures including FSI (Wu et al., 2016; Nasar et al., 2019; Capasso et al., 2022).

Despite FSI problems are able to be analysed using DEM-based models, traditionally, they were addressed through mesh-based methods, often using the Finite Element Methods (FEM) to solve both the fluid and the structure independently (Benson, 1992). Issues related to the treatment of the mesh when tracking the motion of the solid objects, makes that meshless approaches are more convenient to solve the fluid while keeping mesh-based techniques, such as FEM, to solve the structures. Then, the SPH Lagrangian particle method is particularly suitable for investigating FSI problems due to its meshless nature (Khayyer et al., 2022a). In fact, several fully Lagrangian approaches were proposed to solve both the fluid and structure with SPH-based methods (Antoci et al., 2007; Khayyer et al., 2018; Sun et al., 2021; Morikawa and Asai, 2021; O'Connor et al., 2022; Meng et al., 2022; Ren et al., 2023; Khayyer et al., 2024). However, as available in the literature, it should be noted that SPH-FEM coupling is a recent hybrid approach that exploits the strengths of both models on dealing with FSI problems (Li et al., 2015). Considering this, an efficient SPH-FEM coupling to study violent FSI was proposed (Fourey et al., 2017) and subsequently, applied to 3-D tire hydroplaning simulations on rough ground (Yang et al., 2022). Additionally, a multi-resolution technology for discretising both the fluid and the structure through an SPH-FEM code was also investigated (Chen et al., 2022).

Project Chrono (Tasora et al., 2016) is an open-source multiphysics engine that can be integrated as a third-party application coupled with other models. Among all its available features, this simulation engine can solve multi-body collisions with frictional contacts in very large multi-body systems with mechanical constraints using DEM-based algorithms. Furthermore, this engine is also capable of simulating flexible structures but using a FEM-based formulation. Some features of this library have been validated in several works (Anitescu and Tasora, 2010; Pazouki et al., 2017; Tasora and Masarati, 2015). A first coupling between DualSPHysics and Chrono was presented (Canelas et al., 2018), describing a SPH-Differential Variational Inequality (DVI) framework that allows simulating non-smooth contacts (NSC) using a DEM approach with complementarities, which enforce the non-penetration of the rigid bodies when colliding. The use of this approach was presented in several works (Brito et al., 2020; Ropero-Giralda et al., 2020; Quartier et al., 2021a). Subsequently, another coupling between a different SPH-based code

and Chrono has been described (Wei et al., 2019). However, the present work proposes an extension of the previous coupling, keeping all the features available before, but including a new method to solve smooth contacts (SMC) based on DEM with penalties and solved with Differential Algebraic Equations (DAE). This new method allows the penetration between elements to experience a partial deformation of the bodies when solving their contact. On the other hand, Chrono implements a non-linear Finite Element Analysis (FEA) method that can deal with flexible structures, which is based on FEM (Tasora et al., 2016). This method is suitable for simulating FSI problems when integrates that functionality in the coupling with DualSPHysics. Therefore, in addition, a two-way coupling SPH-FEA is proposed to solve FSI, where the SPH-based model solves the fluid, whereas the FEA solves the structural dynamics. For this implementation, the structural element is solved as a linear elastic beam using the Euler–Bernoulli beam theory (Bauchau and Craig, 2009). Then, this novel implementation aims to integrate in the same co-operative framework (DualSPHysics-Chrono) two different coupled models: i) SPH-DEM to reproduce very large multibody systems that comprise mechanical constrains, collision detection of rigid bodies and its interaction with fluid; and ii) SPH-FEA for solving FSI problems where the flexible structure is solved using the Euler-Bernoulli beam theory.

Regarding the complexity of WECs and is components, it is worth noting that mooring systems play an important role in their behaviour, as pointed out by several studies (Johanning et al., 2006; Davidson and Ringwood, 2017). There are many mooring solvers, such as Moody (Ferri and Palm, 2015), MoorDyn (Hall, 2015) or OrcaFlex (Randolph and Quiggin, 2010). A first approach based on a quasi-static mooring solver was developed in DualSPHysics (Barreiro et al., 2016), and later, DualSPHysics has been coupled with MoorDyn (Domínguez et al., 2019). However, a reimplementation of the mooring solver was proposed, giving rise to the new MoorDyn+ (Martínez-Estévez, 2022), which was also coupled to DualSPHysics. MoorDyn+ is an open-source mooring dynamic library based on a lumped-mass (LM) numerical approach. This code solves the behaviour of catenary moorings, computes tensions in the mooring lines, sea bottom friction, axial stiffness, and hydrodynamic drag and added mass. Additionally, this novel implementation includes mandatory functionalities such as a robust control of errors, the possibility

of defining break tensions to the mooring lines, multiple fluid-driven objects can be moored in the same simulation and mooring lines can attach not only bodies to the seabed but also interconnect different bodies. The two-way coupling DualSPHysics-MoorDyn+ has been successfully applied and validated for studying moored floating devices (Capasso et al., 2023a; Pribadi et al., 2023). However, it is necessary to develop another new feature in MoorDyn+ to be able to reproduce the pre-tensioned mooring lines, commonly referred to as taut mooring lines, tensors or anchor legs, that some WECs may have in their configuration (Davidson and Ringwood, 2017).

Therefore, in this work, an extension of the capabilities of DualSPHysics is presented through two-way coupling techniques with multiphysics libraries. The governing equations to solve fluids are handled by the SPH model. The DEM framework solves the collisions with frictional contacts (NSC or SMC) in very large multibody systems comprising mechanical constraints, whereas the FEA methodology solves the flexible structures, and a LM approach simulates the mooring dynamics. The coupling strategy represents a major advance for the DualSPHysics model in terms of its general usability and versatility, greatly expanding the relevance of the code. There are several advantages when using coupling techniques in comparison with other methods. Firstly, the accuracy and robustness of the three solvers employed in a co-operative framework is preserved. Moreover, this methodology allows the possibility of using distinct spatial resolutions for each model, providing a key distinctive feature: *uncoupled resolutions*. The basis of this concept is that even though both models are synchronised and communicate to each other during the simulation, they solve their own systems separately in different environments and the resolutions employed are independent. Thanks to the strategy, new features implemented in the multiphysics libraries can be exploited within the coupled code and so, extending its capabilities without requiring large developments or major changes in the code. In conclusion, this work shows the capabilities of a co-operative computation framework that involves three different open-source codes (DualSPHysics-Chrono-MoorDyn+) to numerically reproduce the response of various concepts and characteristics of WECs, thus allowing to address more challenging scenarios than those that could previously be represented by one or several separate models. Finally, this work

proposes, for the first time, the application of this coupled model to study the Uppsala WEC (UWEC) device. This coupled code overcomes the challenges of studying these types of devices by simulating this taut-moored point-absorber WEC that includes a linear PTO system under extreme wave conditions.

1.2 Thesis layout

The most relevant work related to this doctoral thesis has been already published in international peer-reviewed scientific journals. Therefore, this thesis is presented as a compendium of three scientific articles with the following structure:

Chapter 1: Includes the state-of-art of the topics related to the thesis, the motivation and the structure of the manuscript.

Chapter 2: Provides the objectives initially defined to conduct the research about numerical modelling of WECs.

Chapter 3: Describes the numerical models and their main formulation, as well as the coupling strategy used and the new implementations that give rise to the novel computational code presented.

Chapter 4: Contains the set of scientific articles that make up the thesis by compendium.

Chapter 5: Offers a discussion of the most relevant results obtained during this doctoral thesis.

Chapter 6: Draws the general conclusions of this thesis as well as the future work.

CHAPTER 2

Objectives

This chapter presents the main objective and sub-objectives of the doctoral thesis. The main objective of this work is to develop a numerical tool to be used by the scientific and industrial community to promote new technologies to harness wave energy and support the design stage of WECs. This goal is divided into the following two specific sub-objectives:

i) Extend the capabilities of the DualSPHysics code. This goal aims to improve the DualSPHysics solver with new features to simulate more complex scenarios and problems present in the wide variety of WECs currently under development. Specifically, the functionalities of the existing couplings between DualSPHysics with Chrono and DualSPHysics with MoorDyn+ should be extended. Additionally, some developments are required to address the most common types of PTO systems depending on the type of WEC. In the case of point absorber devices, viscous dampers and friction dampers are required. Moreover, a new contact method that allows some penetration between rigid bodies when interact, denoted as smooth contacts (SMC), should be integrated to solve the collisions of some parts of the PTO of WECs. Furthermore, some WECs include flexible and deformable solid parts, so it is necessary to incorporate the possibility of simulating flexible objects and its interaction with fluid. On the other hand, there are different types of mooring lines used to connect floating devices to the seabed, mainly catenary and taut-mooring lines. However, only catenary lines were allowed before, so the implementation of taut-mooring lines should be also considered. New developments implemented in the DualSPHysics code will be optimised using High Performance Computing (HPC) techniques to speed up the computational code, ensuring that the simulations can be performed at reasonable execution times.

ii) Application in the design of WECs. Previous sub-objective will allow addressing more complex and diverse problems in the study of WECs, with the required level of detail and at reasonable execution times. Therefore, this objective

will allow the practical demonstration of the capabilities of the resulting computational solver by applying it for the following cases: i) study the efficiency of floating devices to generate energy from waves and ii) assessing the survivability of floating devices subjected to extreme waves. Specifically, this work will focus on the Uppsala WEC (UWEC), which is a complex taut-moored point-absorber WEC that includes a linear PTO system.

CHAPTER 3

Methodology

This chapter describes the basis and core formulation implemented in the numerical models used in this research: i) DualSPHysics; ii) Project Chrono; and iii) MoorDyn+. Furthermore, this chapter presents the coupling of the codes in a co-operative framework, showing the communication flow to solve an integration time step.

3.1 DualSPHysics

DualSPHysics is an open-source CFD-based code that implements the Lagrangian SPH method. This code is provided within a complete software package with pre- and post-processing tools (García-Feal et al., 2022), which accounts for more than 130 thousand downloads since 2011. This code was originally developed to simulate free-surface flows and their interaction with fixed and floating structures. The following subsections present the main formulation implemented in DualSPHysics (Domínguez et al., 2022), so that, the governing equations to solve the system, the novel approach for the boundary conditions and the management of fluid-driven objects.

3.1.1 Smoothed Particle Hydrodynamics principle

SPH is a Lagrangian meshless method in which a continuum is discretised into a set of particles, where the equations of fluid dynamics are solved. The physical quantities of each particle are calculated from an interpolation of the quantities of their neighbouring particles. The neighbour contribution is obtained by a weighted function (W), also known as kernel, whose area of influence is determined by the smoothing length (h), generally $2h$, as represented in Figure 1.

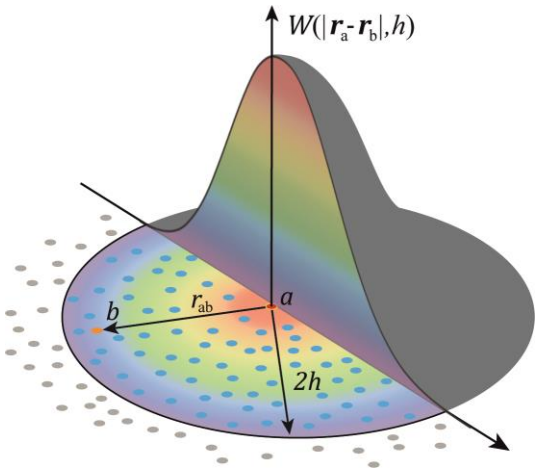

Figure 1. Representation of smoothing kernel function.

The SPH basis for any function F is represented, in discrete form, by the interpolation of the contribution of all particles belonging to the compact support of the kernel function, following:

$$F(\boldsymbol{r}_a) \approx \sum_b F(\boldsymbol{r}_b)\frac{m_b}{\rho_b}W(\boldsymbol{r}_a - \boldsymbol{r}_b, h) \tag{1}$$

where the subscripts a and b refer to the target particle and the neighbouring particle, respectively, $\boldsymbol{r}$ is the position of the particle where the function is computed, m is the mass, ρ is the density, $W(\boldsymbol{r}, h)$ is the weighting function. In this work, the Quintic Wendland kernel (Wendland, 1995) is used.

3.1.2 Governing equations

The motion of the particles in a fluid dynamics system is governed with the discrete form of the Navier-Stokes (N-S) equations, where the momentum and continuity equation can be written in Lagrangian form as:

$$\frac{d\boldsymbol{v}_a}{dt} = -\sum_b m_b\left(\frac{p_b + p_a}{\rho_b\rho_a}\right)\boldsymbol{\nabla}_a W_{ab} + \boldsymbol{g} + \boldsymbol{\Gamma}_a, \tag{2}$$

$$\frac{d\rho_a}{dt} = \sum_b m_b \boldsymbol{v}_{ab}\cdot\boldsymbol{\nabla}_a W_{ab} + D \tag{3}$$

where t is the time of the simulation, $\boldsymbol{v}$ is the velocity, p is the pressure, W_{ab} is the kernel function, $\boldsymbol{g}$ is the gravity acceleration and $\boldsymbol{\Gamma}_a$ is the viscosity term (see Section 4.1). The DualSPHysics code has two different viscosity treatments (Domínguez et al., 2022), whose formulation can be added to the momentum equation: i) laminar viscosity with a sub-particle scale model (SPS); and ii) artificial viscosity. In addition, a density diffusion (D) term is included to reduce fluctuations in the density field (Fourtakas et al., 2019).

DualSPHysics implements a weakly compressible SPH formulation to solve the fluid. Thus, an equation of state is used to obtain the fluid pressure (p) from the particle density.

$$p = \frac{c_s^2 \rho_0}{\gamma}\left[\left(\frac{\rho}{\rho_0}\right)^{\gamma} - 1\right] \tag{4}$$

being $c_s = \sqrt{\partial p/\partial \rho}$ the numerical speed of sound, γ=7 the polytropic constant and ρ_0 the reference density of the fluid.

3.1.3 Boundary conditions

DualSPHysics implements the modified Dynamic Boundary Conditions (mDBC) method (English et al., 2022), which is a modification of the original DBC (Crespo et al., 2007). Hence, the arrangement of the boundary particles within the mDBC approach follows the DBC principle. However, a boundary interface is defined some distance from the innermost layer of boundary particles, usually at $dp/2$ for simple shapes, being dp the initial inter-particle distance in SPH. Figure 2 shows an example of the mDBC approach, in which the boundary interface is represented with a purple line. Normal vectors (arrows) are defined then from the boundary particles to the boundary interface, pointing in the direction of the fluid domain. A ghost node (cross) is created in the fluid domain, which is projected according to its normal vector, for each boundary particle (the so-called target boundary particle), following (Marrone et al., 2011). For flat boundaries, the ghost node is mirrored across the boundary interface. In the case of boundary particles located in a corner, the ghost node is mirrored through of that corner into the fluid domain.

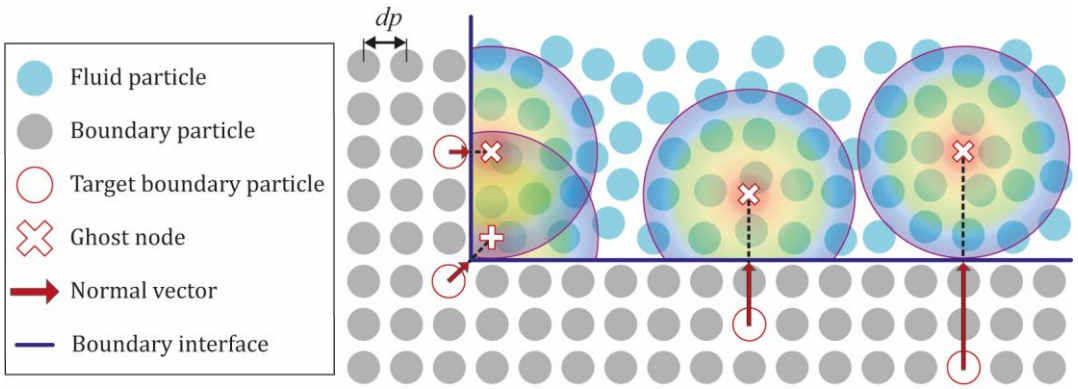

Figure 2. Projection of ghost nodes when the mDBC method is applied.

In this novel approach, each boundary particle receives the fluid properties computed by a corrected SPH approximation at its ghost node, where the density field is evaluated following a first-order consistent SPH interpolation (Liu and Liu, 2006).

3.1.4 Fluid-driven objects

In DualSPHysics, a fluid-driven object is treated as a rigid body and its motion is calculated according to its interaction with the fluid. Then, the basic equations of rigid body dynamics are implemented in DualSPHysics to solve the motion of fluid-driven objects. Considering that a rigid body is composed of as set of boundary particles, the mDBC approach is applied to compute the fluid-solid interaction. Thus, each boundary particle k belonging to the rigid body, experiences a force per unit mass ($\boldsymbol{f}_k$) computed as:

$$\boldsymbol{f}_k = \sum_b \frac{d\boldsymbol{v}_{kb}}{dt} + \boldsymbol{g} \tag{5}$$

being $d\boldsymbol{v}_{kb}/dt$ the acceleration exerted by the fluid particle b on the boundary particle k. When the net force on the boundary particles is computed, the basic equations of motions can be applied:

$$M\frac{d\boldsymbol{V}}{dt} = \sum_k m_k \boldsymbol{f}_k, \tag{6}$$

$$\boldsymbol{I}\frac{d\boldsymbol{\Omega}}{dt} = \sum_k m_k(\boldsymbol{r}_k - \boldsymbol{R}_0) \times \boldsymbol{f}_k \tag{7}$$

where M is the total mass of the rigid body, $\boldsymbol{I}$ is the moment of inertia matrix, $\boldsymbol{V}$ is the velocity, $\boldsymbol{\Omega}$ is the rotational velocity, $\boldsymbol{r}_k$ is the position of the particle k and $\boldsymbol{R}_0$ the position of the centre of mass. Equations (6) and (7) are integrated in time to predict the values of $\boldsymbol{V}$ and $\boldsymbol{\Omega}$ to be used at the beginning of the next time step. Each boundary particle that belongs to the rigid body will have the following velocity:

$$\boldsymbol{v}_k = \boldsymbol{V} + \boldsymbol{\Omega} \times (\boldsymbol{r}_k - \boldsymbol{R}_0). \tag{8}$$

3.2 Project Chrono

Project Chrono (Tasora et al., 2016) is a multiphysics library that deals with the dynamics of the rigid bodies within a Discrete Element Method (DEM) framework, while it solves the flexible bodies within a Finite Element Analysis (FEA) formulation. Both features can be solved using the core module of Project Chrono denoted as Chrono (*Chrono::Engine*). Next subsections present the governing equations to solve the dynamics of the system, the collision detection algorithms, the multi-body dynamics, and the structural dynamics available in this coupling.

3.2.1 Rigid body dynamics

There are two formulations available to solve the rigid body dynamics with frictional contacts, which are integrated in this work. The first one is known as DEM-P or smooth contacts (SMC), which is solved with Differential Algebraic Equations (DAE), includes a penalty-based (DEM-P) methodology that allows the penetration between elements to experience a partial deformation of the bodies in contact. The second, called DEM-C or non-smooth contacts (NSC), which is solved with a Differential Variational Inequality (DVI) formulation introduces complementarity conditions to enforce the non-penetration of the elements that are in contact. For both SMC and NSC methods, the collision detection is simulated using state-of-the-art collision detection algorithms that compute frictional contact forces. This feature allows the definition of collision shapes by using meshes or external geometries, where material properties can be defined (such as Young's modulus, Poisson's ratio, and restitution and friction coefficients).

The dynamics of multi-body systems composed by rigid bodies is solved with a system of index-3 DAEs (Tasora et al., 2016).

$$\frac{d\boldsymbol{q}}{dt} = \boldsymbol{L}(\boldsymbol{q})\boldsymbol{v}, \tag{9}$$

$$\boldsymbol{M}\frac{d\boldsymbol{v}}{dt} = \boldsymbol{f}_t(t, \boldsymbol{q}, \boldsymbol{v}), \tag{10}$$

$$\boldsymbol{f}_t(t, \boldsymbol{q}, \boldsymbol{v}) = \boldsymbol{f}_e - \boldsymbol{f}_c, \tag{11}$$

being $\boldsymbol{f}_e = \boldsymbol{f}_e(t, \boldsymbol{q}, \boldsymbol{v})$ and $\boldsymbol{f}_c = \boldsymbol{f}_c(\boldsymbol{q}, t)$.

The term $\boldsymbol{L}(\boldsymbol{q})$ indicates a linear transformation of the generalised positions ($\boldsymbol{q}$), $\boldsymbol{v}$ are the velocities, $\boldsymbol{M}$ is the matrix of mass and $\boldsymbol{f}_t$ is the total force, which is calculated according the external and constraint forces, $\boldsymbol{f}_e$ and $\boldsymbol{f}_c$, respectively.

The SMC approach deals with contacts where penetrations between bodies are allowed (so they can "overlap") to experience local deformation. When an overlap occurs, a corrective force is added at the contact point by means of a normal and a tangential contact force, which are calculated according (Machado et al., 2012). Details of this implementation can be found in (Section 4.1). On the other hand, the NSC method considers the elements as rigid bodies by applying non-penetration constraints, which can be solved as complementarity conditions with a Coulomb friction model. The continuous model is represented with a DVI formulation (Anitescu and Tasora, 2010) by rewriting the Eq. (10) and adding a set of generalised forces using projectors to ensure the non-penetration (see Section 4.1). Figure 3 shows a representation of the domain in SPH (left) and the two methods to solve the collision detection between two bodies in Chrono (right). For the SMC approach, an internal layer (the so-called margin) is used to impose the maximum allowed overlap for colliding bodies. Conversely, for NSC, the contact is solved on the surface of the shape since this method enforces the non-penetration.

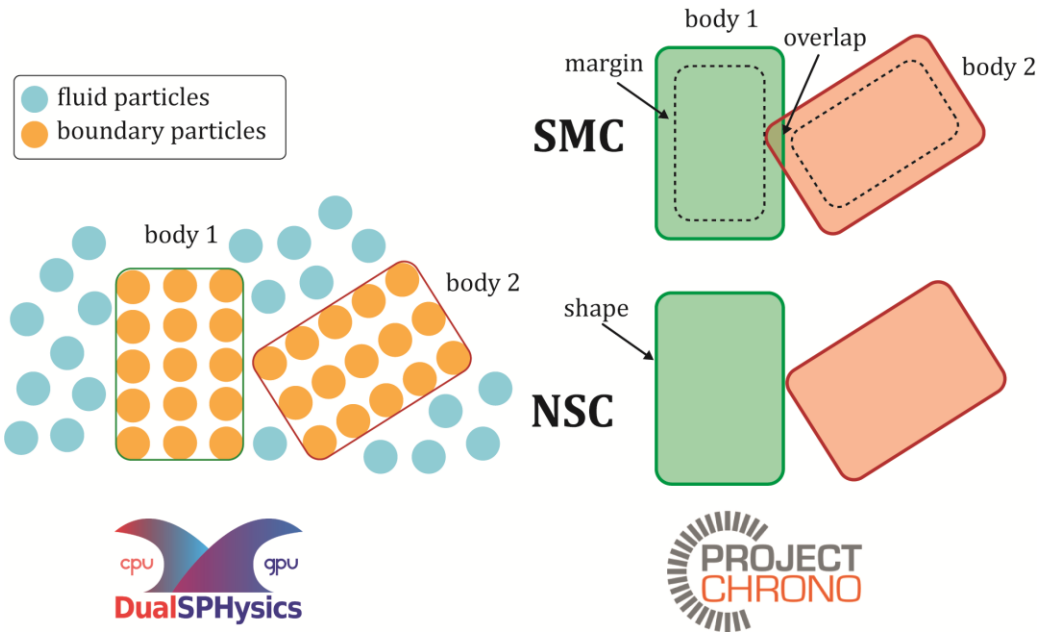

Figure 3. Particle discretisation of the domain in SPH (left) and representation of the SMC and NSC approaches to solve the collisions using DEM (right).

3.2.2 Multi-body dynamics

This multiphysics library deals with articulated multi-body systems, where mechanical constraints can be applied to the rigid bodies. The constraints change the behaviour of the bodies by adding an additional force ($\boldsymbol{f}_c$) to the total force of the rigid bodies ($\boldsymbol{f}_t$) in Eq. (11). Considering a mechanical constraint as a spring-damper connecting that vary the bilateral constraint exerted on two connected bodies, the direction in which the force is applied along the spring-damper ($\hat{\boldsymbol{t}}_{sd}$) can be evaluated as:

$$\hat{\boldsymbol{t}}_{sd} = \frac{\boldsymbol{r}_j - \boldsymbol{r}_i}{|\boldsymbol{r}_j - \boldsymbol{r}_i|} \tag{12}$$

where $\boldsymbol{r}_i$ and $\boldsymbol{r}_j$ are the position of the joint points i and j, respectively.

There are two formulations implemented in this work to describe spring-dampers that make it possible to simulate some PTO systems of point absorber devices, such as: i) viscous dampers; and ii) friction dampers. The first one is reproduced as a translational spring-damper actuator (TSDA) that allows the modelling of PTO viscous dampers, whose constraining force can be given as:

$$\boldsymbol{f}_c = k_c \boldsymbol{r}_{ij} \cdot \hat{\boldsymbol{t}}_{sd} + c_c \boldsymbol{v}_{ij} \cdot \hat{\boldsymbol{t}}_{sd} \tag{13}$$

where $\boldsymbol{r}_{ij}$ and $\boldsymbol{v}_{ij}$ are the relative position and velocity between points i and j, respectively. In addition, k_c and c_c are the stiffness and damping coefficients.

The second one is a Coulomb damper that allows the modelling of friction dampers. This formulation is a new implementation presented in Section 4.1, which is not available in the official Project Chrono package. The constraining force for this element can be written as:

$$\boldsymbol{f}_c = -sign(\boldsymbol{v}_{ij} \cdot \hat{\boldsymbol{t}}_{sd}) F_\mu \tag{14}$$

where F_μ is the friction Coulomb force.

3.2.3 Structural dynamics

Project Chrono also supports the non-linear Finite Element Analysis (FEA) modelling to solve flexible multi-body systems (Tasora et al., 2016). In this work, a non-linear FEA via co-rotational (CR) formulation is implemented to solve the flexible structures that can experience large deformations, such as the classical 3-D Euler-Bernoulli beams (Rankin and Nour-Omid, 1988). Thus, the classical Euler-Bernoulli beam theory is used to provide a simplified framework for reproducing the response of structural elements. Figure 4 shows a schematic of a Euler–Bernoulli beam, in this case, represented in 2-D. A full description of this feature is available in Section 4.2.

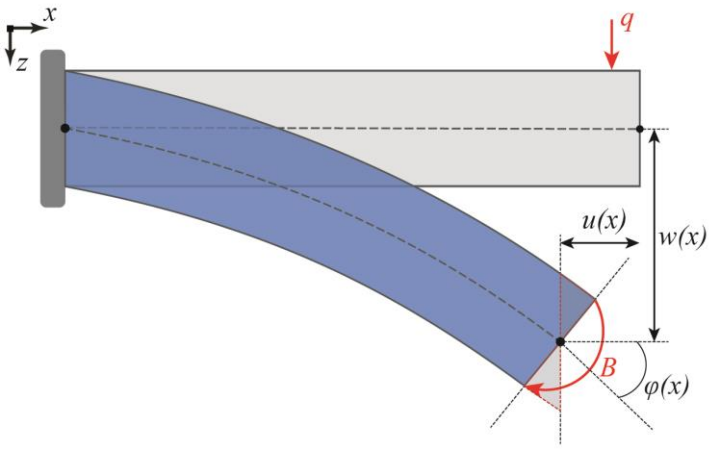

Figure 4. Schematic of the Euler–Bernoulli beam theory in 2-D.

The main kinematic formulation about the Euler-Bernoulli beams can be written as:

$$w = w(x), \tag{15}$$

$$\varphi(x) = -\frac{dw(x)}{dx} \tag{16}$$

where x is the position along the axis direction of the beam, w is the displacement orthogonal to the axis or axial displacement, and φ is the curvature with respect to the axial direction of the beam.

Assuming that the structure is modelled as a co-rotated Euler-Bernoulli beam, when the deflection φ along the axis is known, the bending moment function (B) can be evaluated as:

$$B(x) = EI\left(\frac{d\varphi(x)}{dx}\right) \tag{17}$$

where E is the Young's Modulus and I is the second moment of the inertia of the cross-section, being EI the flexural rigidity.

The computation of the normal stress along the cross section (σ_{xx}) induced by the bending moment (B) is implemented using the Navier's hypothesis (Gere and Goodno, 2012) as:

$$\sigma_{xx} = -\frac{B(x)}{I} y \tag{18}$$

where y is the distance between the point of interest (particle of the beam) and the beam axis along the height of the cross section. More details can be found in Section 4.2.

3.3 MoorDyn+

MoorDyn+ (Martínez-Estévez, 2022) is a dynamic mooring library that discretises the mooring lines using a lumped-mass (LM) formulation for modelling axial elasticity, hydrodynamics, and bottom contact following the MoorDyn library (Hall and Goupee, 2015). MoorDyn+ allows solving catenary and taut-mooring lines, a robust error control has been developed and several problems of the original MoorDyn code have been fixed. It allows the inclusion of more than one moored floating objects and the use of different water depths in the same simulation. Moreover, mooring lines can interconnect floating objects and breaking tensions can be defined for the mooring lines. Next subsections describe the main formulation of the LM-based approach, the force management of the mooring solver and the mooring line dynamic system to compute the motion of the lines.

3.3.1 Lumped-mass formulation

The unstretched length (L_0) of a mooring line is divided into N segments of equal length, connected by $N + 1$ nodes. Each node (i, $i \in [1, N + 1]$) is a point mass with weight and buoyancy, whereas each segment is modelled as a linear spring-damper to provide elasticity in the axial direction. Considering $\boldsymbol{r}_i$ and $\boldsymbol{r}_{i+1}$ the position of adjacent nodes, the strain (e) in the segment connecting the two nodes ($i + 1/2$) is calculated as:

$$e_{i+1/2} = \left(\frac{\|\boldsymbol{r}_{i+1} + \boldsymbol{r}_i\|}{l} - 1 \right) \tag{19}$$

being $l = L_0/N$ the unstretched length of each segment.

The position of each node is constructed by considering the internal forces coming from the two connected segments. The tangential direction is then defined as:

$$\hat{\boldsymbol{t}}_i = \left(\frac{\boldsymbol{r}_{i+1} - \boldsymbol{r}_{i-1}}{|\boldsymbol{r}_{i+1} - \boldsymbol{r}_{i-1}|}\right) \tag{20}$$

where $\boldsymbol{r}_{i+1}$ and $\boldsymbol{r}_{i-1}$ identify the position of the following and previous nodes in the line, respectively.

3.3.2 Force management

The tension forces acting within each segment due to material stiffness (T) and internal damping (C) are then calculated as:

$$T_{i+1/2} = EAe_{i+1/2}, \tag{21}$$

$$C_{i+1/2} = C_{int}A\dot{e}_{i+1/2} \tag{22}$$

being $\dot{e} = \partial e/\partial t$, $A = \pi/4d_m^2$ is the area, while d_m is the diameter of the mooring line. The term E is the elasticity or Young's modulus and C_{int} is the internal damping coefficient. Then, from the Morison equation (Morison et al., 1950), the drag force in the transverse ($\boldsymbol{D}_{trans}$) and tangential ($\boldsymbol{D}_t$) directions are applied to each node (see Section 4.3).

3.3.3 Mass and integration

The added mass force at each node, considering the tangential and the transverse contributions, can be expressed as:

$$\boldsymbol{m}_{a,i} = Al\rho[C_{an}(\boldsymbol{I_m} - \hat{\boldsymbol{t}}_i\hat{\boldsymbol{t}}_i^T) + C_{at}\hat{\boldsymbol{t}}_i\hat{\boldsymbol{t}}_i^T] \tag{23}$$

where ρ is the density of the fluid, $\boldsymbol{I_m}$ is the identity matrix, and C_{an} and C_{at} are transverse and tangential added mass coefficients, respectively.

The total equation of motion is described by a second-order system of equations that accounts for the mooring line dynamics considering the node mass matrix ($\boldsymbol{m}_i$), the seabed contact force ($\boldsymbol{S}_i$) and submerged weight ($\boldsymbol{W}_i$) (Hall and Goupee, 2015), which can be written as:

$$\begin{aligned}(\boldsymbol{m}_i + \boldsymbol{m}_{a,i})\ddot{\boldsymbol{r}}_i = \boldsymbol{T}_{i+1/2} - \boldsymbol{T}_{i-1/2} + \boldsymbol{C}_{i+1/2} - \boldsymbol{C}_{i-1/2} \\ + \boldsymbol{W}_i + \boldsymbol{S}_i + \boldsymbol{D}_{t,i} + \boldsymbol{D}_{trans,i}\end{aligned} \tag{24}$$

being $\boldsymbol{m}_i = Al\rho_m \boldsymbol{I_m}$ and $\ddot{\boldsymbol{r}}_i = \partial^2 \boldsymbol{r}_i / \partial t^2$, where ρ_m is the density of the mooring. Details of the formulation integrated in MoorDyn+ can be found in Section 4.3.

3.4 Coupling techniques

This section describes the two-way coupling procedures presented in this thesis. Figure 5 depicts a scheme of the architecture of the coupled model involving the three solvers (DualSPHysics, Project Chrono, and MoorDyn+). This framework follows a *master-slave* software architecture that makes it a modular and specialised coupled framework. Each solver can be interpreted then as a module in charge of specific tasks, where DualSPHysics is the *master* acting as the central control unit, whereas the coupled libraries are the *slaves*. DualSPHysics controls the communication process making calls to the other solvers, distributes information from the fluid and gathers the results from the *slaves* to maintain the SPH environment updated and synchronised. Therefore, this strategy ensures a centralised control, making it easier to manage and coordinate the overall system. The internal time step of the SPH integrator (Δt_{SPH}) imposes the advance in time of the entire system. Likewise, each *slave* solves their specific tasks within their integrators with their own time steps, but for each DualSPHysics call, they solve the time interval set by Δt_{SPH}. This guarantees that the system is stable and synchronised during the simulation. Furthermore, this modular architecture ensures that the system is scalable and maintainable. Additional *slave* components can be integrated seamlessly, and changes to any module can be introduced without affecting the core code. Assuming that modules are designed for specific tasks or functions, if they are accurate as stand-alone components, their accuracy is preserved when they are coupled together by this methodology. For this implementation, all the solvers share the computational resources since they are executed on the same processor and share the Random Access Memory (RAM). However, this strategy can be extended to distributed systems in order to simulate very large-scale systems using Message Passing Interface (MPI), where each solver

can be executed in different nodes or workstations. In this way, each solver can fully exploit the computational resources of its node.

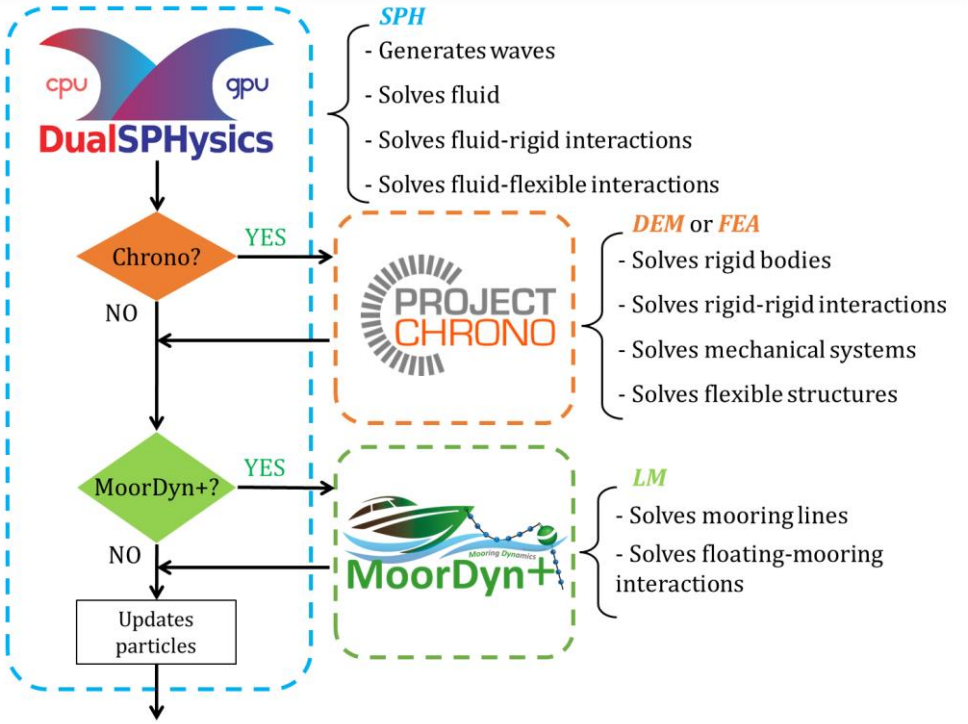

Figure 5. Scheme of the co-operative framework involving the three numerical models.

The coupling procedures are presented in the following subsections, describing the main tasks involved. It should be noted that for each coupling, DualSPHysics compute the SPH particle interaction by solving the equations (2) and (3). Specifically, from the fluid-floating body interaction, the linear ($d\boldsymbol{V}/dt$) and angular ($d\boldsymbol{\Omega}/dt$) accelerations exerted from the fluid on the bodies are obtained and transferred to the other models.

3.4.1 SPH-DEM coupling

The SPH-DEM coupling integrates the SPH-based code DualSPHysics with the DEM approach implemented in Chrono to solve fluid-solid-solid interactions. DualSPHysics controls the flow and exchanges data with Chrono via a general-purpose communication interface called DSPHChronoLib. Figure 6 shows a scheme of the coupling procedure. The use of DSPHChronoLib introduces an additional layer

of abstraction to this coupled model, resulting in a *low-coupling* concept that ensures that changes made in Chrono side will not affect the operation of DualSPHysics (and vice versa). In this way, new Chrono features can be added to the coupling without any loss of accuracy of the functionalities that have already been implemented. The description of DSPHChronoLib and this coupling are available in Section 4.1.

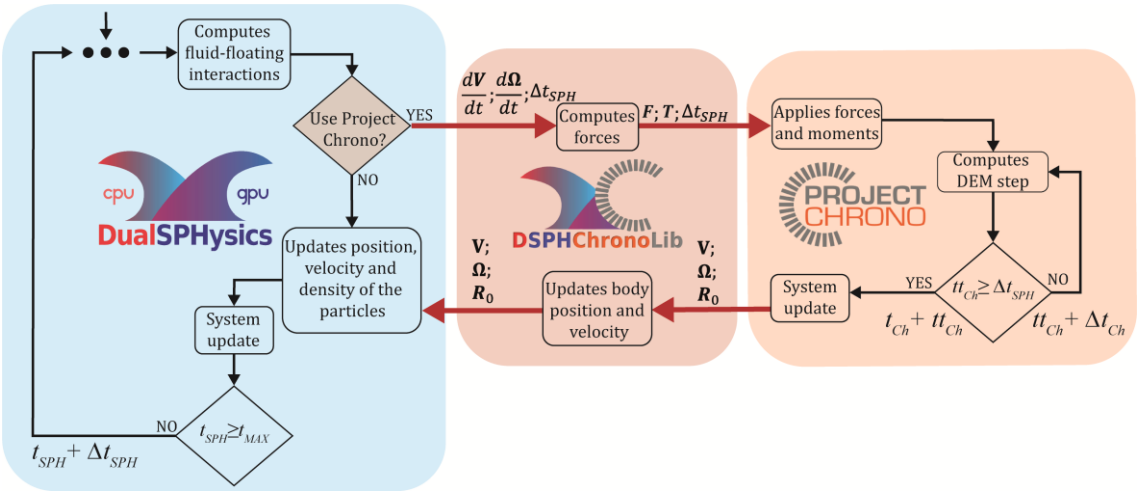

Figure 6. Flowchart of the two-way SPH-DEM coupling procedure.

In this implementation, a DualSPHysics time step can be split into three parts: i) computing the forces on the rigid bodies; ii) solving the dynamics of the rigid bodies; and iii) updating the particle properties. The three steps are explained in detail below:

i) Linear and angular accelerations and the internal SPH time step (Δt_{SPH}) are transferred to the DSPHChronoLib. Then, linear forces ($\boldsymbol{F}$) and moments ($\boldsymbol{T}$) are calculated in DSPHChronoLib by solving equations (6) and (7), respectively. Finally, DSPHChronoLib transfers $\boldsymbol{F}$, $\boldsymbol{T}$ and Δt_{SPH} to Chrono.

ii) Chrono applies $\boldsymbol{F}$ and $\boldsymbol{T}$ as external forces ($\boldsymbol{f}_e$) to the rigid bodies together with the constraint forces ($\boldsymbol{f}_c$) if mechanical constraints are defined. Then, the total force is computed for each rigid object according to Eq. (11) and the state of the rigid body system is solved in time until the loop exit condition is satisfied ($tt_{Ch} \geq \Delta t_{SPH}$). Chrono updates the system

configuration to be transferred to DSPHChronoLib, so that the linear ($\boldsymbol{V}$) and angular ($\boldsymbol{\Omega}$) velocities, and the centre of mass position ($\boldsymbol{R}_0$) of each rigid body are returned to DualSPHysics.

iii) DualSPHysics updates the properties of particles in the entire SPH domain. The velocity $\boldsymbol{v}$ of the rigid body particles is updated by solving Eq. (8). At this point, the system is updated, synchronised in time for both models ($t_{SPH} = t_{Ch}$), and ready to solve the next time step, if any.

3.4.2 SPH-FEA coupling

The behaviour of the deformable object is simulated using the FEA structural solver integrated in Chrono. The entire domain is described using subsets of particles within the SPH solver, including the flexible structure as a set of boundary particles. On the other hand, within the FEA solver, the structure is built with a set of N segments connecting $N + 1$ nodes, denoted as n_i, where $i \in [0, N]$, as depicted in Figure 7. The segments are modelled using beam elements solved by the Euler-Bernoulli formulation, whereas the beam nodes are 3-D finite element nodes with 6 degrees of freedom (DOFs).

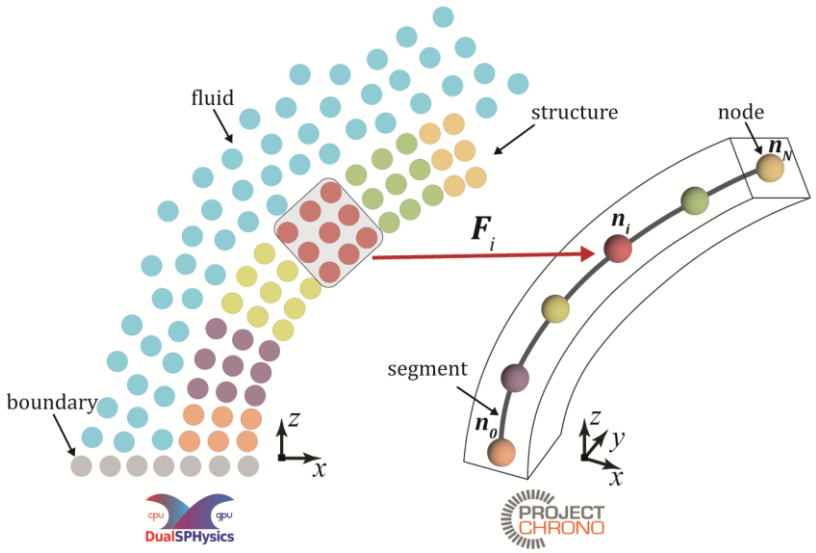

Figure 7. Discretisation of the structure in the SPH (left) and FEA (right).

DualSPHysics and Chrono exchange data via DSPHChronoLib to simulate the fluid-elastic structure interactions (FSI) in a two-way process. Figure 8 shows a schematic of the coupling procedure.

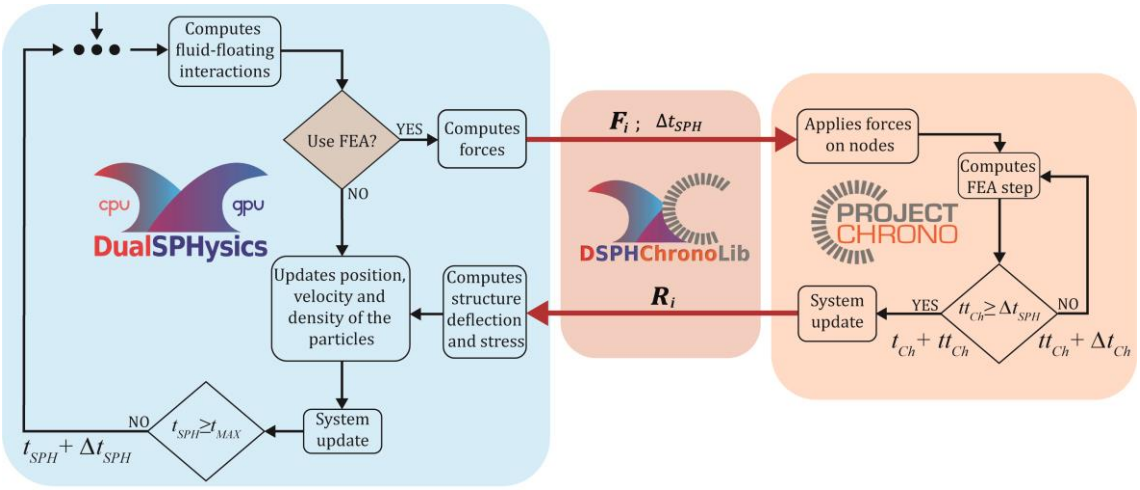

Figure 8. Flowchart of the two-way SPH-FEA coupling procedure.

The process of simulating an SPH time step (Δt_{SPH}) can be split into three steps: i) computing the linear forces on the structure; ii) solving the motion of the structure; and iii) updating the properties of the structure particles. The description of this coupling is available in Section 4.2.

i) The SPH model calculates the linear forces ($\boldsymbol{F}_i$) on the flexible structure by solving Eq. (5).

ii) DualSPHysics transfers $\boldsymbol{F}_i$ to Chrono via DSPHChronoLib. The FEA structural solver applies $\boldsymbol{F}_i$ on its respective node n_i and computes the motion of the structure. This process continues until the loop exit condition is satisfied ($tt_{Ch} \geq \Delta t_{SPH}$) and Chrono updates the system.

iii) Chrono transfers back the node positions ($\boldsymbol{R}_i$) to DualSPHysics through DSPHChronoLib. Then, DualSPHysics computes the deformation and the stress, by solving Eq. (18), of the shape in SPH and updates properties of the particles. At this point, the system is updated, synchronised in time for both models ($t_{SPH} = t_{Ch}$), and ready to solve the next time step, if any.

3.4.3 SPH-LM coupling

The coupling with the LM-based MoorDyn+ follows an approach where the fairlead kinematics are transferred to MoorDyn+. The dynamics of the mooring system are then calculated to give the forces exerted by the moorings on the fluid driven objects. This coupling procedure is based on the previously existing implementation (Domínguez et al., 2019). Figure 9 shows a scheme of the coupling procedure.

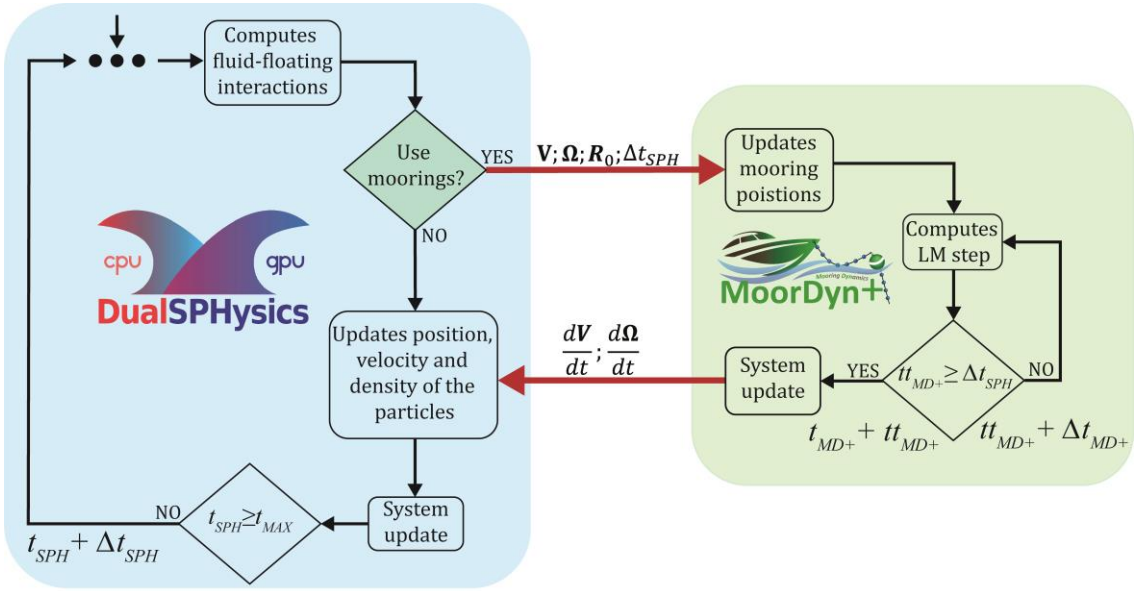

Figure 9. Flowchart of the two-way SPH-LM coupling procedure.

The process of simulating an SPH time step (Δt_{SPH}) can be split into three steps: i) computing the floating linear and angular velocities; ii) computing forces exerted by the moorings; and iii) updating the properties of the floating particles. A more detailed description of this coupling is available in Section 4.3.

i) Motions and rotations obtained in DualSPHysics and the SPH time step ($\boldsymbol{V}$, $\boldsymbol{\Omega}$, $\boldsymbol{R}_0$, Δt_{SPH}) are transferred to MoorDyn+. The mooring solver uses these quantities as an input to compute the kinematics of the mooring line fairlead.

ii) MoorDyn+ solves the mooring line behaviour until the loop exit condition is satisfied ($tt_{MD+} \geq \Delta t_{SPH}$). After that, MoorDyn+ updates the position of

the mooring line segments and computes the forces at the fairlead connections by Eq. (24). Then, accelerations of the fairleads ($d\mathbf{V}/dt$, $d\mathbf{\Omega}/dt$) are transferred back to DualSPHysics.

iii) The forces exerted by the mooring lines are added in DualSPHysics to obtain the final resulting force acting on the fluid-driven objects, which is used to calculate the final motions and rotations of the floating object. At this point, the system is updated, synchronised in time for both models ($t_{SPH} = t_{MD+}$), and ready to solve the next time step, if any.

CHAPTER 4

Set of Publications

This chapter includes the three open-access articles that compose this doctoral dissertation by compendium of scientific publications. The information of the journals obtained from the 2022 Journal Citation Reports (JCR) is also included.

4.1 Coupling of an SPH-based solver with a multiphysics library

The first article is entitled "**Coupling of an SPH-based solver with a multiphysics library**" by **Martínez-Estévez, I.**, Domínguez, J. M., Tagliafierro, B., Canelas, R. B., García-Feal, O., Crespo, A. J. C., & Gómez-Gesteira, M. Published in the journal *Computer Physics Communications* in 2022.

Table 1. Information of the journal Computer Physics Communications from 2022 JCR.

	Journal information
Journal	*Computer Physics Communications*
Online ISSN	*1879-2944*
Country	*Netherlands*
Editorial	*Elsevier*
Impact factor	*6,2*
Quartile	*Q1 (Computer Science, Interdisciplinary Applications)*

Computer Physics Communications 283 (2023) 108581

Contents lists available at ScienceDirect

Computer Physics Communications

journal homepage: www.elsevier.com/locate/cpc

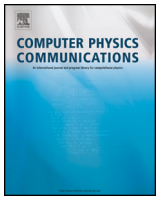

Coupling of an SPH-based solver with a multiphysics library ☆,☆☆

I. Martínez-Estévez [a,*], J.M. Domínguez [a], B. Tagliafierro [b], R.B. Canelas [c], O. García-Feal [a], A.J.C. Crespo [a], M. Gómez-Gesteira [a]

[a] Environmental Physics Laboratory, CIM-UVIGO, Universidade de Vigo, Spain
[b] Department of Civil Engineering, University of Salerno, Italy
[c] Bentley Systems, Lisbon, Portugal

ARTICLE INFO

Article history:
Received 3 June 2022
Received in revised form 20 October 2022
Accepted 25 October 2022
Available online 28 October 2022

Keywords:
SPH
DEM
DualSPHysics
Project Chrono
Multiphysics coupling

ABSTRACT

A two-way coupling between the Smoothed Particle Hydrodynamics-based (SPH) code with a multiphysics library to solve complex fluid-solid interaction problems is proposed. This work provides full access to the package for the use of this coupling by releasing the source code, completed with guidelines for its compilation and utilization, and self-contained template setups for practical uses of the novel implemented features, is provided here. The presented coupling expands the applicability of two different solvers allowing to simulate fluids, multibody systems, collisions with frictional contacts using either non-smooth contact (NSC) or smooth contact (SMC) methods, all integrated under the same framework. The fluid solver is the open-source code DualSPHysics, highly optimised for simulating free-surface phenomena and structure interactions, uniquely positioned as a general-purpose Computational Fluid Dynamics (CFD) software with a GPU-accelerated solver. Mechanical systems that comprise collision detection and/or multibody dynamics are solved by the multiphysics library Project Chrono, which uses a Discrete Element Method (DEM). Therefore, this SPH-DEM coupling approach can manage interactions between fluid and complex multibody systems with relative constraints, springs, or mechanical joints.

Program summary

Program title: DualSPHysics-Chrono
CPC Library link to program files: https://doi.org/10.17632/g2cc37dw4f.1
Licensing provisions: DualSPHysics and DSPHChronoLib under GNU Lesser General Public License (LGPL); Project Chrono under BSD-3-Clause License.
Programming language: C++ and CUDA
Nature of problem: The simulation of turbulent free-surface flows in interaction with complex fixed or floating structures is essential to address typical marine and coastal engineering problems. The Smoothed Particle Hydrodynamics (SPH) method is particularly suitable for solving this type of nonlinear problems. However, this type of application usually requires mechanical restrictions between the different structural elements (spherical joints, hinges, or springs), as well as the correct simulation of collisions between solid objects. In these cases, it is necessary to combine the SPH method with other numerical methods that allow performing these multiphysics simulations.
Solution method: DualSPHysics-Chrono is a two-way coupling between an SPH solver and a multiphysics library that combines fluid simulation using a Lagrangian approximation and interactions between solids using Discrete Element Method (DEM). DualSPHysics solver is a GPU-optimized implementation of the SPH method that allows efficient simulation of fluid-structure interaction problems. Whereas Project Chrono is a DEM implementation for simulating multibody dynamics that includes collision detection and numerous mechanical constraints to solve complex mechanisms. The coupling of DualSPHysics and Project Chrono combines the capabilities of both models under a free software framework.

☆ The review of this paper was arranged by Prof. N.S. Scott.

☆☆ This paper and its associated computer program are available via the Computer Physics Communications homepage on ScienceDirect (http://www.sciencedirect.com/science/journal/00104655).

* Corresponding author.
E-mail address: ivan.martinez.estevez@uvigo.es (I. Martínez-Estévez).

https://doi.org/10.1016/j.cpc.2022.108581

Additional comments including restrictions and unusual features: The SPH solver includes a version implemented with CUDA (Compute Unified Device Architecture) to exploit the parallelism of NVIDIA graphics processing units (GPUs).

1. Introduction

In recent years, meshless models have gained great popularity, among other reasons, because they can solve problems where traditional mesh-based models present limitations. Those limitations are related to the fact that large deformations of the mesh can lead to inconsistencies and require expensive ad-hoc procedures to keep the accuracy during the simulation. In cases where numerous fluid-driven objects are considered and may collide with each other under the action of fluids, the domain can be highly distorted, so meshless methods present themselves as a natural of dealing with this class of phenomena. The Smoothed Particle Hydrodynamics (SPH) method has been highlighted among the meshless methods due its growth in maturity for solving engineering problems [1–5]. SPH is a particle method where calculations are carried out at computational nodes (particles) that can move without fixed connectivity across the spatial domain. The method supports the simulation of violent free-surface flows and fluid-rigid body interactions because the free surface does not require a special treatment and high deformations of that can be efficiently solved without mesh distortion. However, as suggested and supported by the SPH rEsearch and engineeRing International Community (SPHERIC) [6], a great deal of research has been carried out to enhance the scheme stability: pressure field consistence [7,8], high-order schemes [9,10], spatial particle anisotropy [11] and performance [12,13]. Worth mentioning that the SPH method can be applied for solving multi-phase flows, such as two-phase liquid [14], two-phase air-water [15], or two-phase liquid-sediments [16].

The open-source DualSPHysics [17] code is a Computational Fluid Dynamics (CFD) solver based on the SPH method. This code can be freely downloaded from the website http://www.dual.sphysics.org, where a full software package is available with pre- and post-processing tools [18], having exceeded 100 thousand downloads since 2011. It was developed to simulate free-surface flows and their interaction with fixed and floating structures. It inherits the core formulation from the open-source FORTRAN-based code SPHysics [19,20], which was taken to a first C++ version to having optimization of the parallel structure mostly for the neighbour search list interaction reconstruction [21], and then implemented in CUDA parallel computing platform to keep up with the increasing demand for hardware resources [22]. In fact, DualSPHysics is a highly parallelised implementation of the SPH method and has since kept its capabilities of being accelerated for shared memory central processing unit (CPU) systems (e.g., multi-core CPUs) and graphics processing units (GPUs) [23,24]. It is a reference for coastal engineering applications and has been applied successfully to several research investigations [25–28], and some of its latest developments can be found in [29].

The discrete element method (DEM) [30] was first intended as a method to solve the dynamics of large systems of material points that possess a specified geometry, meaning that each discrete element is fully described by its position and rotation vectors. Furthermore, due to its development towards simulating particulate system flows that may comprise millions of instances, tracking the interactions among discrete elements is of critical relevance; various contact laws and techniques (e.g., the penalty based introduced by Cundall and Strack [30]) are utilised to enforce such behaviour in accordance with the most accurate physical representation of the phenomenon being modelled [31]. The use of these techniques represents a reference for its precision and accuracy in simulating granular flows [32]. This last field of applications has led researchers to develop very fast algorithms for primitive shapes, the most common of which being the sphere [33].

Practical interest in using computational models to support scientific research has led to the development of many coupled frameworks, within which a variety of physical systems can be simulated. CFD-based solvers benefit from coupling and co-simulation techniques that extend their applicability beyond the simple fluid simulations; more broadly, recent proposed implementations [34–37] show the viability of particle-based CFD solvers in dealing with highly nonlinear phenomena that would otherwise stress the inherent limitations of mesh-based approaches. For some of the mentioned applications, coupling with mesh-based methods is still recognised as state-of-the-art in current research as complex re-meshing techniques are required to ensure mesh consistency [38], and other issues in the treatment of the nonlinear advection term or mass conservation [39,40]. Furthermore, the high computational cost keeps this type of solvers at a development stage. Anyhow, some applications of mesh-based approaches (Eulerian) coupled to Lagrangian DEM approaches can be found in the literature [41].

Meshless methods, when employed for simulating fluid phases, can improve the overall model accuracy, reliability and versatility [42], for instance, the SPH and DEM methods are homogenously Lagrangian and able to deal with large displacements from the initial configuration. A first class of SPH-DEM couplings comprises models that are purposed to investigate the behaviour of granular systems in which the interaction with fluid phases (generally liquids) is relevant [37,43,44]. More specifically, a coupling of a DEM with an SPH model is proposed in Canelas et al. [45], where a two-way Distributed Contact DEM (DCDEM) formulation is coupled to a Weakly Compressible SPH (WCSPH) solver, and then successfully applied to a complex debris flow case that has never been addressed by traditional mesh-based approaches [46]. Similarly, a WCSPH-DEM is presented in He et al. [47]. A stabilised Incompressible SPH (ISPH) coupled to a DEM with a penalty approach to solve the solid-solid interactions is proposed in Asai et al. [48]. A new SPH-DEM coupling for solving the dynamic of granular systems discretised with the SPH method and using the DEM approach to describe a relatively small rigid system interacting with an SPH fluid phase was introduced in Hu et al. [32]. Other researchers have focused on similar coupling techniques, but including particular mechanical relationships dictating the motion of the rigid DEM instances such that they mimic flexible elements [49,50]. In Capasso et al. [51], a system of DEM elements, which have rotational spring connections among them, is validated to solve the dynamics of flexible beam elements interacting with fluids, suggesting a high precision and resilience of the Lagrangian framework to incorporate new methodologies.

The authors present a new structured version of the DualSPHysics code coupled to the multiphysics library Project Chrono [52] using a co-simulating environment, and thus improving the applicability of the proposed SPH framework to industrial practice to a much greater extend. Project Chrono is a multiphysics simulation engine that can be compiled as a library to be coupled with third-party applications. This multiphysics library can deal with collision detection between rigid bodies and with multibody dynamics where mechanical constraints can be applied to the bodies.

A coupling between an SPH solver and the Project Chrono library was applied to model wave energy converters in Wei et al. [53]. In addition, a first coupling between DualSPHysics and Project Chrono was presented in Canelas et al. [54], where a SPH-Differential Variational Inequality (DVI) framework that allows simulating non-smooth contacts (NSC) is described. The here presented coupling is an extension of the previous work, which includes the features reported in [54] and, in addition, a method integrated in Project Chrono to solve smooth contacts (SMC) that allows the penetration between elements to experience a partial deformation of the bodies in contact. Moreover, this work describes the coupling strategy using a communication interface that deals with the two-way data transfer provided with an open-source license along with this program paper. Therefore, in this work, an implementation of the two-way coupling is presented; the governing equations to solve fluids are handled by the SPH model, whereas the DEM framework solves the rigid-rigid body interactions with frictional contacts (NSC or SMC) in very large multibody systems and comprising mechanical constraints. Within the field of renewable energy, the coupling with DEM allows the modelling of mechanical energy absorption systems and several successful applications have been recently presented [55–57], making it clear that Particle-based schemes can be of great use for industrial applications. Some examples of the relevance of multiphysics frameworks are given in Tagliafierro et al. [58,59], in which the coupling of an SPH fluid solver, a third library for the management of mooring lines [60], and the Project Chrono library, allowed to perform the validation of marine renewable energy devices.

The contents of this paper are organised as follows: Section 2 shows the main formulation implemented in the SPH solver, mainly addressing Newtonian fluid simulations; Section 3 presents the features of the multiphysics library and the capabilities implemented in this coupling; Section 4 describes the coupling procedure between both models with particular reference to the time integration procedure and geometrical connection between the two Lagrangian models. Section 5 presents the software package, including information on the compilation procedures for both CPU and GPU versions; following, Section 6 provides four benchmark cases for evaluating the accuracy of the proposed framework contrasting against experimental data, and Section 7 reports on the performance of the coupling strategy for fluid-structure interaction when the multibody dynamics is solved. Section 8 draws the conclusions of this work and remarks possible future work that can stem from the proposed coupling technique.

2. Smoothed particle hydrodynamics model

This section introduces the main formulation implemented in the DualSPHysics solver [17] based on the SPH method, the novel approach for the boundary conditions, and the equations of body dynamics to solve the fluid-driven objects that interact with the fluid domain.

2.1. SPH basis

The SPH Lagrangian meshless method discretises a continuum using a set of computational nodes or *particles*. The motion of the particles is obtained according to the physical properties of a set of neighbour particles, where the contribution of their neighbours is determined by a weighting function or kernel (W) with an area of influence defined by the smoothing length (h). Therefore, the SPH principle is represented by the integral approximation of any function $F(\boldsymbol{r})$ as:

$$F(\boldsymbol{r}) = \int F(\boldsymbol{r}') W(\boldsymbol{r} - \boldsymbol{r}', h)\, d\boldsymbol{r}' \tag{1}$$

where $\boldsymbol{r}$ is the position of the point to compute the function, $\boldsymbol{r}'$ is a temporally position variable. In discrete form, the function F is approximated by interpolating the contributions of the particles within the compact support of the kernel function by following:

$$F(\boldsymbol{r}_a) \approx \sum_b F(\boldsymbol{r}_b) W(\boldsymbol{r}_a - \boldsymbol{r}_b, h) \frac{m_b}{\rho_b} \tag{2}$$

where a is the target particle, b is a neighbouring particle, m is the mass, ρ is the density. The weighting function $W(\boldsymbol{r}, h)$ used in this work is the Quintic Wendland kernel [61] defined by:

$$W(q) = \alpha_{\mathrm{D}} \left(1 - \frac{q}{2}\right)^4 (2q+1), 0 \le q \le 2 \tag{3}$$

where $q = r/h$ is the non-dimensional distance between particles, being α_D and $21/16\pi \mathrm{h}^3$ in 3-D, and r is the distance between particles a and b.

2.2. Governing equations

The discrete form of the Navier-Stokes (N-S) equations is used to govern the motion of the particles in a fluid dynamics system. The momentum equation in Lagrangian form can be written as:

$$\frac{d\boldsymbol{v}_a}{dt} = -\sum_b m_b \left(\frac{p_b + p_a}{\rho_b \rho_a}\right) \nabla_a W_{ab} + \boldsymbol{g} + \boldsymbol{\Gamma}_a \tag{4}$$

where t is the simulation time, $\boldsymbol{v}$ is the velocity, p is the pressure, $\boldsymbol{g}$ is the gravity acceleration, W_{ab} is the kernel function and $\boldsymbol{\Gamma}_a$ is the viscosity term.

DualSPHysics implements two different viscosity treatments that can be included to the momentum equation: i) laminar viscosity with a sub-particle scale model (SPS) (Eq. (5)); and ii) artificial viscosity (Eq. (6)).

$$\boldsymbol{\Gamma}_a = \sum_b m_b \frac{4\upsilon_0 \boldsymbol{r}_{ab} \cdot \nabla_a W_{ab}}{(\rho_a + \rho_b)\left(r_{ab}^2 + 0.01h^2\right)} \boldsymbol{v}_{ab} + \sum_b m_b \left(\frac{\tau_a^{ij} + \tau_b^{ij}}{\rho_b \rho_a}\right) \nabla^i W_{ab}, \tag{5}$$

$$\boldsymbol{\Gamma}_a = -\sum_b m_b \Pi_{ab} \nabla_a W_{ab}, \tag{6}$$

$$\text{being } \Pi_{\mathrm{ab}} = \begin{cases} \left(\frac{-\alpha \overline{c_{sab}}}{\overline{\rho_{ab}}}\right)\left(\frac{h \boldsymbol{v}_{ab} \cdot \boldsymbol{r}_{ab}}{r_{ab}^2 + 0.01h^2}\right) & \boldsymbol{v}_{ab} \cdot \boldsymbol{r}_{ab} < 0 \\ 0 & \boldsymbol{v}_{ab} \cdot \boldsymbol{r}_{ab} > 0 \end{cases}.$$

In Eq. (5), the laminar viscosity (first term) is approximated by Lo and Shao [62] and the SPS model (second term) is described by Dalrymple and Rogers [63] in which a Favre averaging in a weakly compressible approach is used, where υ_0 denotes the kinematic viscosity of the fluid and τ is the SPS stress tensor in Einstein notation in coordinate directions i and j according to:

$$\tau^{\mathrm{ij}} = \overline{\mathrm{v^i v^j}} - \overline{v^i}\,\overline{v^j} \tag{7}$$

modelled by an eddy viscosity closure as:

$$\frac{\tau^{ij}}{\rho} = 2\nu_{SPS}\left(S^{ij} - \frac{1}{3}S^{ii}\delta^{ij}\right) - \frac{2}{3}C_L\Delta^2\delta^{ij}\left|S^{ij}\right|^2 \tag{8}$$

being $\nu_{SPS} = [C_S\Delta]^2\left|S^{ij}\right|^2$ the turbulent eddy viscosity, C_S=0.12 is the Smagorinsky's constant, C_L=0.0066, Δ is the initial particle spacing and $|S^{ij}|$=1/2($2S^{ij}S^{ij}$)$^{1/2}$, being S^{ij} an element of the SPS strain tensor. Details of the implementation of this dissipation term in DualSPHysics are given in Domínguez et al. [17]. On the other

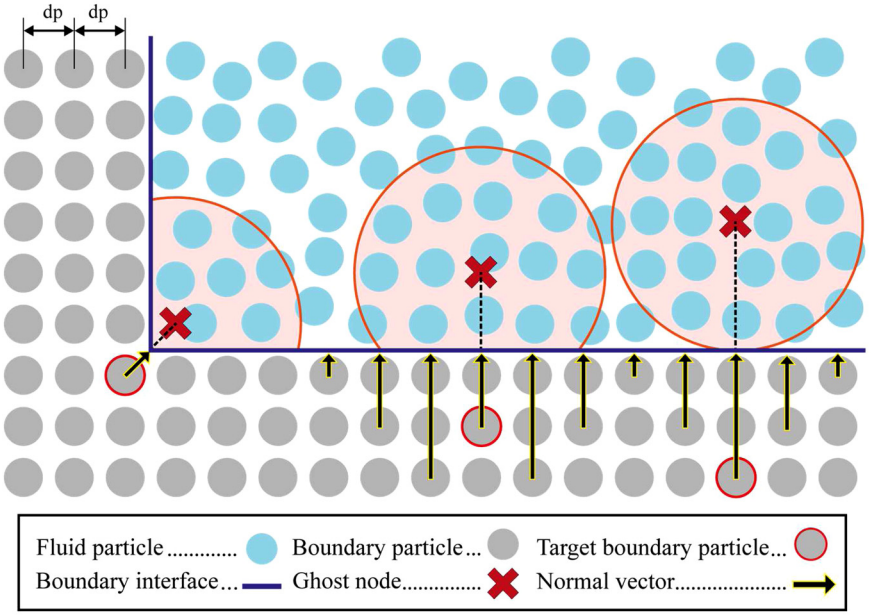

Fig. 1. Projection of ghost nodes when the mDBC method is applied. (For interpretation of the colours in the figure(s), the reader is referred to the web version of this article.)

hand, Eq. (6) defines the artificial viscosity treatment based on the work proposed by Monaghan [64], where Π_{ab} is the artificial viscosity term, α is the artificial viscosity coefficient to introduce the proper dissipation, and $\overline{c_{sab}}$ and $\overline{\rho_{ab}}$ are the mean of the speed of sound (c_s) and density of particles a and b, respectively.

Furthermore, the continuity equation can be written, in Lagrangian form, as:

$$\frac{d\rho_a}{dt} = \sum_b m_b \boldsymbol{v}_{ab} \cdot \nabla_a W_{ab} + D, \tag{9}$$

being $D = 2\delta h c_s \sum_b \left(\rho_{ba}^T - \rho_{ab}^H\right) \frac{\boldsymbol{r}_{ab} \cdot \nabla_a W_{ab}}{r_{ab}^2} \frac{m_b}{\rho_b}$,

where a density diffusion (D) term is included following the formulation presented in Fourtakas et al. [65], being δ the coefficient that controls this diffusion term (set to 0.1 for the applications in this work) and subscripts T and H represent the total and hydrostatic component of the density for a weakly compressible fluid. Then, the hydrostatic pressure difference of particles a and b is computed as:

$$p_{ab}^H = \rho_0 g z_{ab} \tag{10}$$

where z_{ab} is the vertical distance between particles a and b.

The weakly compressible SPH formulation is used to solve the fluid in DualSPHysics. Thus, an equation of state is used to obtain the fluid pressure (p) from the particle density.

$$p = \frac{c_s^2 \rho_0}{\gamma} \left[\left(\frac{\rho}{\rho_0} \right)^\gamma - 1 \right] \tag{11}$$

where ρ_0 is the reference density of the fluid and γ=7 is the politropic constant.

The properties of each particle (position, velocity, density and pressure) are integrated in time using a Symplectic algorithm [66], whose implementation in DualSPHysics is presented in [17]. A variable time step (Δt_{SPH}) is used in DualSPHysics based on the CFL (Courant-Friedrichs-Lewy) condition, the force terms and the viscous diffusion term following [67].

2.3. Boundary conditions

Dynamic Boundary Condition (DBC) is the default method implemented in DualSPHysics, proposed by Crespo et al. [68]. In case of a fluid particle approaching a boundary particle k, the density of the particle k increases and therefore, the pressure too. This modification in the pressure field in the momentum equation (4), involves that a repulsive force is exerted on the fluid particle. Although this method has been applied successfully to solve coastal engineering problems [69,70], it leads to several disadvantages such as the appearance of unphysically large boundary layer (or gaps) when the not-wet boundary particles will interact with fluid. Therefore, a novel modification of DBC (the so-called mDBC) proposed by English et al. [71], improves the original DBC when fluid-boundary particle interactions are evaluated.

The boundary particle arrangement within the mDBC implementation is followed in the same way as the original DBC, where all particles are initially created at a distance dp (typically of the order of h). However, a boundary interface is located at a certain distance away from the innermost boundary particle layer, generally at a $dp/2$ for simple geometries. Fig. 1 shows an example of this new approach, where the boundary interface is defined with a purple line. A ghost node (red cross) is created in the fluid domain for each boundary particle (the so-called target boundary particle in Fig. 1), following the procedure proposed by Marrone et al. [72]. Normal vectors (arrows) are defined from the boundary particles to the boundary interface, pointing in the fluid domain direction. Then, the ghost node is projected according to its normal vector. When flat boundaries are modelled, the ghost node is mirrored across the boundary interface. In the particular case of boundary particles placed in a corner, the ghost node is mirrored through of this corner into the fluid domain. More details can be found in [71].

2.4. Fluid-driven objects

In DualSPHysics, the basic equations of rigid body dynamics are implemented in order to simulate the motion of fluid-driven objects. The motion of a fluid-driven object, which is treated as a rigid body, is derived by considering its interaction with fluid. The net force is computed on each boundary particle of the rigid body

according to the sum of the contributions of all surrounding fluid particles. Therefore, each boundary particle k experiences a force per unit mass given by:

$$\boldsymbol{f}_k = \sum_a \boldsymbol{f}_{ka} \tag{12}$$

where $\boldsymbol{f}_{ka}$ is the force per unit mass exerted by the fluid particle a on the boundary particle k. This approach is able to preserve the exchange of longitudinal and tangential fluid forces at the fluid-boundary interfaces, when the fluid force field can include them. Once the net force on the boundary particles is computed, the basic equations of motions can be applied:

$$M\frac{d\boldsymbol{V}}{dt} = \sum_k m_k \boldsymbol{f}_k, \tag{13}$$

$$\boldsymbol{I}\frac{d\boldsymbol{\Omega}}{dt} = \sum_k m_k \left(\boldsymbol{r}_k - \boldsymbol{R}_0\right) \times \boldsymbol{f}_k \tag{14}$$

where M is the mass of the rigid body, $\boldsymbol{I}$ is the moment of inertia, $\boldsymbol{V}$ is the velocity, $\boldsymbol{\Omega}$ is the rotational velocity, $\boldsymbol{r}_k$ is the position of the particle k and $\boldsymbol{R}_0$ the position of the centre of mass. Equations (13) and (14) are integrated in time to predict the values of $\boldsymbol{V}$ and $\boldsymbol{\Omega}$ to be used at the beginning of the next time step. Each boundary particle that belongs to the rigid body will have a velocity $\boldsymbol{v}_k$ given by:

$$\boldsymbol{v}_k = \boldsymbol{V} + \boldsymbol{\Omega} \times \left(\boldsymbol{r}_k - \boldsymbol{R}_0\right) \tag{15}$$

This technique has been proven to ensure conservation of linear and angular momentum in Monaghan et al. [73].

3. Multiphysics library

Project Chrono [52] deals with the dynamics of the rigid bodies within a DEM framework. Therefore, the bodies are considered as DEM elements when are solved by this library. The two approaches described behind the DEM formulation to solve the frictional contacts, are presented in this work. The first one is known as DEM-P (or soft-body) because it includes a penalty-based methodology that allows the penetration between elements to experience a partial deformation of the bodies in contact. This approach is solved with Differential Algebraic Equations (DAE). The second one, which can be called DEM-C, introduces complementarity conditions to enforce the non-penetration of the elements that are in contact. Project Chrono implements a Differential Variational Inequality (DVI) formulation to deal with this kind of problems. Therefore, mutual contact between rigid bodies and the consequent friction can be evaluated via a penalty approach or within a DVI formulation.

The collision detection between rigid objects is solved using state-of-the-art collision detection algorithms, which compute frictional contact forces. This feature allows defining collision shapes by using meshes or external geometries, where material properties can be defined. Project Chrono implements two approaches to solve the collision detection based on the methods explained before: i) smooth contacts (SMC) solved by DEM-P; and ii) non-smooth contacts (NSC) solved by DEM-C. The new notation for naming the contact methods is related to the way they are called in the source code of the *Chrono::Engine* module.

The next subsections present the governing equations to solve the dynamics of the system, the collision detection algorithms, and the multibody dynamics available in this coupling.

3.1. Rigid body dynamics

The dynamics of multibody systems composed by rigid bodies is solved with a system of index-3 DAEs [52].

$$\frac{d\boldsymbol{q}}{dt} = \boldsymbol{L}\left(\boldsymbol{q}\right)\boldsymbol{v}, \tag{16}$$

$$\boldsymbol{M}\frac{d\boldsymbol{v}}{dt} = \boldsymbol{f}_t\left(t, \boldsymbol{q}, \boldsymbol{v}\right), \tag{17}$$

$$\boldsymbol{f}_t\left(t, \boldsymbol{q}, \boldsymbol{v}\right) = \boldsymbol{f}_e - \boldsymbol{f}_c, \tag{18}$$

being $\boldsymbol{f}_e = \boldsymbol{f}_e\left(t, \boldsymbol{q}, \boldsymbol{v}\right)$ and $\boldsymbol{f}_c = \boldsymbol{f}_c(\boldsymbol{q}, t)$.

Equation (16) relates the time derivative of the generalized positions ($\boldsymbol{q}$) and velocities ($\boldsymbol{v}$) by using a linear transformation $\boldsymbol{L}(\boldsymbol{q})$. In the force balance equation (17), the total force ($\boldsymbol{f}_t$) ties the external and constraint forces, $\boldsymbol{f}_e$ and $\boldsymbol{f}_c$, respectively and the matrix of mass ($\boldsymbol{M}$) is considered. The constraint forces are related to multibody systems with articulations or mechanical constraints, which restrict the motion of the rigid objects.

The DEM-P or soft-body approach deals with contacts where penetrations between bodies are allowed (so they can "overlap") or experience local deformation. When an overlapping takes place, a corrective force is added on the contact point. Thus, once the overlap distance δ_n is detected, the contact normal and tangential forces, $\boldsymbol{F}_n$ and $\boldsymbol{F}_t$ respectively, are computed following the hertzian contact theory [74]:

$$\boldsymbol{F}_n = \sqrt{\overline{R}\delta_n}\left(k_n\boldsymbol{u}_n - c_n\overline{m}\boldsymbol{v}_n\right), \tag{19}$$

$$\boldsymbol{F}_t = \sqrt{\overline{R}\delta_n}\left(-k_t\boldsymbol{u}_t - c_t\overline{m}\boldsymbol{v}_t\right) \tag{20}$$

where $\overline{R}$ is the effective radius of curvature and $\overline{m}$ is the effective mass. The quantities of the normal and tangential stiffness and damping coefficients (k_n, k_t, c_n and c_t, respectively) are defined internally starting from the parameters given by the user such as the modulus of elasticity (E), Poisson's ratio (v_c) and the coefficient of restitution (e). In normal contact direction, the local body deformation is defined as the penetration of the two bodies by $\boldsymbol{u}_n = \delta_n\,\boldsymbol{n}_n$, where $\boldsymbol{n}_n$ is the contact-normal unit vector. In the contact tangential direction, the deformation is defined by following the total tangential displacement of the initial contact points on the two bodies for each time step, $\boldsymbol{u}_t = \boldsymbol{v}_t\,\Delta_t$. To enforce the Coulomb friction laws when $|\boldsymbol{F}_t| > \mu|\boldsymbol{F}_n|$, the maximum allowable $\boldsymbol{F}_t$ is defined according $|\boldsymbol{F}_t| = \mu|\boldsymbol{F}_n|$, where μ is the Coulomb friction coefficient. Details of this implementation are provided in Fleischmann et al. [75].

On the other hand, the DEM-C method considers the elements as rigid bodies by applying non-penetration constraints, which can be written as complementarity conditions with a Coulomb friction model. The continuous model is represented by a DVI based on the formulation presented in Anitescu and Tasora [76]. Then, Eq. (17) can be written as:

$$\boldsymbol{M}\frac{d\boldsymbol{v}}{dt} = \boldsymbol{f}_t(t, \boldsymbol{q}, \boldsymbol{v}) + \sum_{i\in P}\left(\hat{\gamma}_n^i\boldsymbol{D}_n^i + \hat{\gamma}_u^i\boldsymbol{D}_u^i + \hat{\gamma}_w^i\boldsymbol{D}_w^i\right), \tag{21}$$

$$i \in P \left\{ \begin{array}{c} \hat{\gamma}_n^i \geq 0 \perp \Phi^i\left(\boldsymbol{q}\right) \geq 0 \\ (\hat{\gamma}_u^i, \hat{\gamma}_w^i) = argmin(\hat{\gamma}_u^i\boldsymbol{D}_u^i + \hat{\gamma}_v^i\boldsymbol{D}_w^i)^T\boldsymbol{v} \\ \sqrt{(\hat{\gamma}_u^i)^2 + (\hat{\gamma}_w^i)^2} \end{array} \right., \tag{22}$$

being $\mu\hat{\gamma}_n \geq \sqrt{\hat{\gamma}_u^2 + \hat{\gamma}_w^2}$,

$$\boldsymbol{F}_n = \hat{\gamma}_n\boldsymbol{D}_n,\ \boldsymbol{F}_t = \hat{\gamma}_u\boldsymbol{D}_u + \hat{\gamma}_w\boldsymbol{D}_w \tag{23}$$

The frictional contact force associated with the i-th contact over the total number of contacts (P) leads to a set of generalised forces

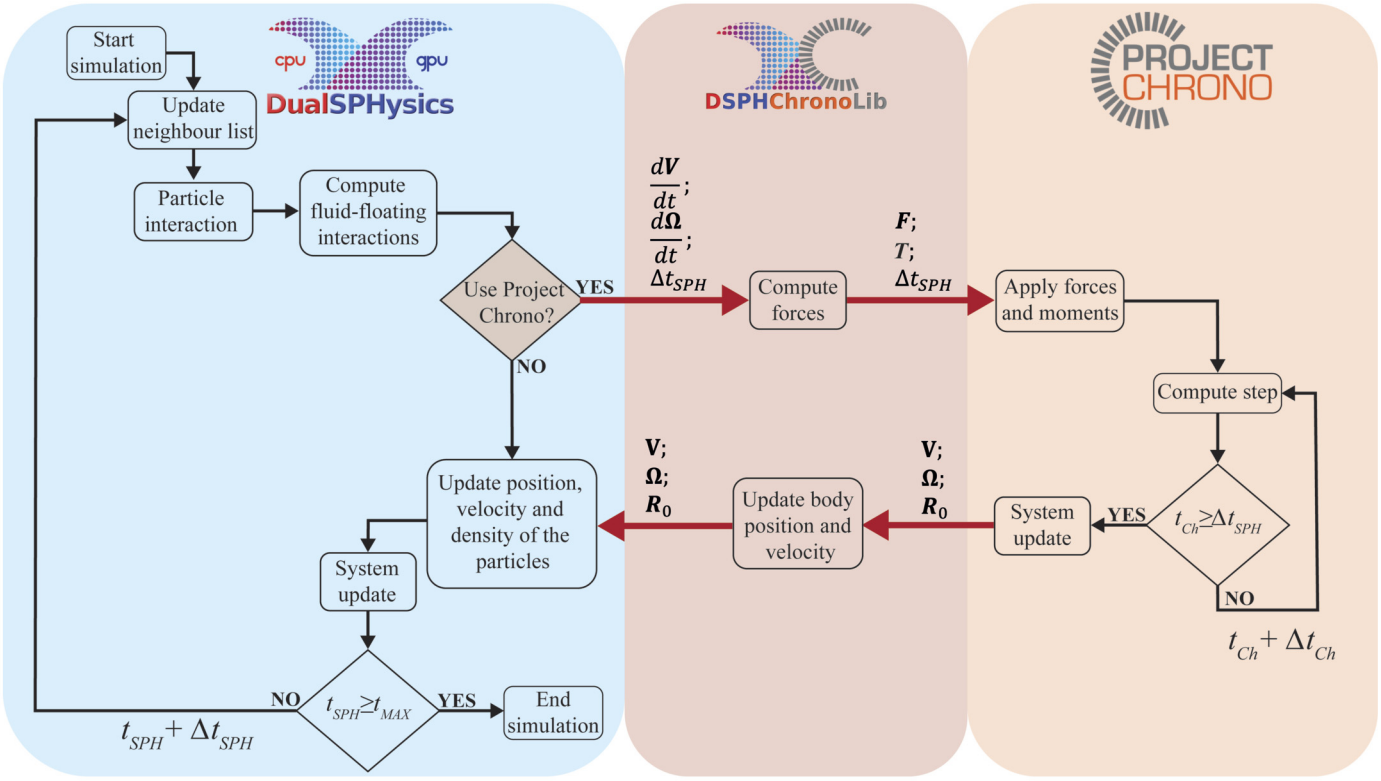

Fig. 2. Flowchart of the DualSPHysics-Chrono coupling.

using projectors ($\boldsymbol{D}_n^i$, $\boldsymbol{D}_u^i$, $\boldsymbol{D}_v^i$) [76]. When two bodies are in contact, a friction force is now assumed. Therefore, a function $\Phi(\boldsymbol{q})$ (the so-called gap function) is used to ensure the non-penetration constraint that satisfies: i) $\Phi(\boldsymbol{q}) > 0$, bodies are separated; ii) $\Phi(\boldsymbol{q}) = 0$, bodies are in contact; and iii) $\Phi(\boldsymbol{q}) < 0$, bodies are interpenetrating. For this reason, in the DEM-C method, the gap function becomes $\Phi(\boldsymbol{q}) \geq 0$ to enforce the non-penetration. The contact normal ($\boldsymbol{F}_n$) and tangential ($\boldsymbol{F}_t$) forces are calculated according to the force multipliers $\hat{\gamma}_n \geq 0$, $\hat{\gamma}_u$ and $\hat{\gamma}_w$, where the subscript n refers to the normal component and u, w refer to the two independent tangential directions during the collision. A complete explanation of this method using the DVI formulation can be found in [76] and a comparison between the two DEM approaches is presented in Pazouki et al. [77].

3.2. Multibody dynamics

This Project Chrono library deals with articulated multibody systems, where mechanical constraints can be applied to the rigid bodies. The constraints change the behaviour of the bodies by adding an extra force ($\boldsymbol{f}_c$) to the total force of the rigid bodies ($\boldsymbol{f}_t$) in Eq. (18). The set of mechanical constraints can be split into: springs or damper actuators; and mechanical joints based on a "lock formulation".

There are two formulations to describe linear springs that change the bilateral constraint exerted on the bodies. The first one is a translational spring-damper-actuator (TSDA) whose formulation is shown in (24). The second one represents a coulomb damper which works following (25). The latter one is a new implementation added in this work, which is not provided in the official package of Project Chrono. The magnitude of the force for the two elements can be give as follows:

$$f_c = k_c\,(d - l) + c_c\,v_z, \tag{24}$$

$$f_c = -sign\,(v_z)\,F_b \tag{25}$$

where d is the distance between the two origins of bodies, l is equilibrium length of the spring, v_z is the velocity that the spring experiences, F_b is the Coulomb force, k_c is the stiffness and c_c is the damping coefficients.

Mechanical joints are based on the same concept of "lock formulation", which is characterized to lock/unlock different components of the 6 degrees of freedom (DOFs) allowed in three dimensions. The kind of constraint is defined by using the vector $\boldsymbol{j}$ as:

$$\boldsymbol{j} = \{\boldsymbol{q}_c, \boldsymbol{e}_c\} \tag{26}$$

where $\boldsymbol{q}_c$ is a vector that refers to the translation in 3-D constraints and $\boldsymbol{e}_c$ indicates the rotation ones expressed in quaternions. The elements of $\boldsymbol{q}_c$ and $\boldsymbol{e}_c$ are defined by 1 or 0, which means the object attached with this mechanical constraint is locked and unlocked, respectively, in the desired direction. The mechanical joints under this formulation compute constraints following:

$$\boldsymbol{f}_c = k_r\boldsymbol{\theta} + c_r\dot{\boldsymbol{\theta}} \tag{27}$$

where $\boldsymbol{\theta}$ is the relative angle of rotation, $\dot{\boldsymbol{\theta}}$ is the angular velocity, k_r and c_r are the rotational stiffness and damping coefficients, respectively. The available mechanical joints in our coupling are:

i) Hinges or revolute joints which allow rotation along a vector. The translation is restricted for the 3-DOF and the rotation is allowed along one axis by considering $\boldsymbol{q}_c = \{1, 1, 1\}$ and $\boldsymbol{e}_c = \{0, 1, 1, 0\}$.
ii) Spherical joints allow free rotation at a point. The translation is restricted for the 3-DOF as the previous one by using $\boldsymbol{q}_c = \{1, 1, 1\}$ and $\boldsymbol{e}_c = \{0, 0, 0, 0\}$.
iii) Point-line joints solve a body sliding along a vector. The rotation totally unlocked following $\boldsymbol{e}_c = \{0, 0, 0, 0\}$ and the translation is free along an axis and by considering $\boldsymbol{q}_c = \{0, 1, 1\}$, $\boldsymbol{q}_c = \{1, 0, 1\}$ or $\boldsymbol{q}_c = \{1, 1, 0\}$.

Table 1
List of source files of DualSPHysics related to the coupling with Project Chrono.

Source files	Description
DSPHChronoLib.h	Declares the interface between DualSPHysics-Project Chrono.
DualSphDef.h	Declares definitions and specific types for DualSPHysics program.
main.cpp	Main file of the project that executes the code on CPU or GPU.
JChronoData.h	Declares the data read from the XML input file to configure the elements handled by Project Chrono.
JChronoObjects (.h .cpp)	Declares/implements the class that defines all the attributes and functions to manage the rigid objects to be handled by Project Chrono.
JSph (.h .cpp)	Declares/implements the class that defines all the attributes and functions that CPU and GPU simulations share.
JSphCpu (.h .cpp)	Declares/implements the class that defines the attributes and functions used only in CPU simulations.
JSphCpuSingle (.h .cpp)	Declares/implements the class that defines the attributes and functions used only in Single-CPU.
JSphGpu (.h .cpp)	Declares/implements the class that defines the attributes and functions used only in GPU simulations.
JSphGpu_ker (.h.cu)	Declares/implements functions and CUDA kernels for the particle interaction and system update.
JSphGpuSingle_ker (.h .cu)	Declares/implements functions and CUDA kernels used only in Single-GPU.
JSphGpuSingle (.h .cpp)	Declares/implements the class that defines the attributes and functions used only in Single-GPU.

4. Coupling procedure

The implementation presented in this work is based on a two-way coupling procedure. DualSPHysics controls the flow events with calls to Project Chrono via a communication interface called DSPHChronoLib that handles the data exchange between both models. A schematic of the coupling procedure is shown in Fig. 2, in which the main steps that achieve the two-way communication during a single integration time step are depicted.

Ideally, a time step can be split into three parts, following a temporal ordering: i) compute forces on the rigid bodies; ii) solve the dynamics of the rigid bodies; and iii) update the particle properties. In the following, the three steps are explained in detail:

i) DualSPHysics computes the particle interaction by solving the SPH governing equations (4) and (9) considering the fluid-rigid object interaction and linear ($d\boldsymbol{V}/dt$) and angular ($d\boldsymbol{\Omega}/dt$) accelerations of the rigid bodies are obtained. Then, velocities and the internal SPH time step (Δt_{SPH}) are transferred to the DSPHChronoLib, and linear forces ($\boldsymbol{F}$) and moment or torsional momenta ($\boldsymbol{T}$) are computed by solving equations (13) and (14), respectively. Finally, DSPHChronoLib transfers $\boldsymbol{F}$, $\boldsymbol{T}$, and Δt_{SPH} to Project Chrono.

ii) Project Chrono applies $\boldsymbol{F}$ and $\boldsymbol{T}$ as external forces ($\boldsymbol{f}_e$) to the rigid bodies. When rigid body systems comprise mechanical constraints (internal and/or external), the constraint forces ($\boldsymbol{f}_c$) defined by the multibody dynamics model are also applied. Note that this latter computation takes place internally in Project Chrono. Then, the total force is computed for each rigid object according to Eq. (18). The state of the rigid body system is marched in time by solving equations (16) and (21), which usually takes several internal integration time steps (Δt_{Ch}), and as such the procedure goes on until the loop exit condition is satisfied, that is $t_{Ch} \geq \Delta t_{SPH}$. In each Project Chrono sub-step, directly stemming from the way they are defined, the constraint and contact forces are continuously updated, whereas the fluid forces are linearly interacting. At this stage, Project Chrono updates the system configuration to be sent to DSPHChronoLib, so that the linear ($\boldsymbol{V}$) and angular ($\boldsymbol{\Omega}$) velocities, and the position of the centre of mass ($\boldsymbol{R}_0$) of each rigid body are transferred back to DualSPHysics.

iii) DualSPHysics updates the position ($\boldsymbol{r}$), velocity ($\boldsymbol{v}$), density (ρ) and pressure (p) of all particles in the entire SPH domain. The velocity $\boldsymbol{v}$ of the boundary particles that belong to rigid bodies that are handled by Project Chrono is updated by solving (15) and therefore, linear and angular momentum are preserved. At this point, the system is ready to be updated and to solve the next time step, if any.

5. Program documentation

This section includes technical information on the DualSPHysics-Chrono program based on DualSPHysics v5.0 package coupled to Project Chrono v4.0.0, and the communication interface DSPHChronoLib; the source code, the compilation process, the format files involved during the preparation for the simulations, and the procedure to run the code are presented. DualSPHysics and the Project Chrono are published as open-source code, under GNU Lesser General Public License (LGPL) and BSD-3 license, respectively.

5.1. Source files

The software tools included in this work are composed of a set of C++ and CUDA files. In this section, the most relevant source files that allow the coupling between DualSPHysics and Project Chrono via the DSPHChronoLib are shown alongside a brief description. Table 1 lists a group of source files belonging to DualSPHysics, where the *DSPHChronoLib* and *JChronoData* are header files (*.h*), which declare the functions and classes implemented in the DSPHChronoLib code to exchange data. The files *JChronoObjects* include a class that declares and implements functions that are used to handle the communication between DualSPHysics and DSPHChronoLib. Therefore, the DualSPHysics code makes calls to DSPHChronoLib through the functions implemented in *JChronoObjects*. The files *JSphCpuSingle* and *JSphGpuSingle* implement the Symplectic integrator that is used to solve SPH time steps (Δt_{SPH}) for both CPU and GPU execution modes, respectively.

For the sake of conciseness, in the following description only the CPU implementation is given; nevertheless, similar descriptions and structures apply for the GPU implementation. The class *JSphCpuSingle* implements the function *JSphCpuSingle::ComputeStep_Sym* that performs the particle interaction computation and updates the particles magnitude using the Symplectic integrator. In this part, the function *JSphCpuSingle::RunFloating* is called to obtain the accelerations of the rigid bodies to be solved by Project Chrono. Fig. 3 shows a schematic of the flow events when the Symplectic algorithm is used, reporting the functions and files involved in this process; note that the Symplectic algorithm resolves each Δt_{SPH} in two sub-steps (Predictor and Corrector). Details of the implementation of this integrator scheme can be found in [17].

Table 2 describes the source files used to generate the DSPHChronoLib library. The *DSPHChronoLib* files contain the base class that defines the basic functions that connects DualSPHysics and Project Chrono. Likewise, the *DSPHChronoLibSC* file includes an implementation of the sub-class based on a hierarchical inheritance where the *DSPHChronoLib* works as a parent class. This sub-class establishes the needed communication exchange for the two-way

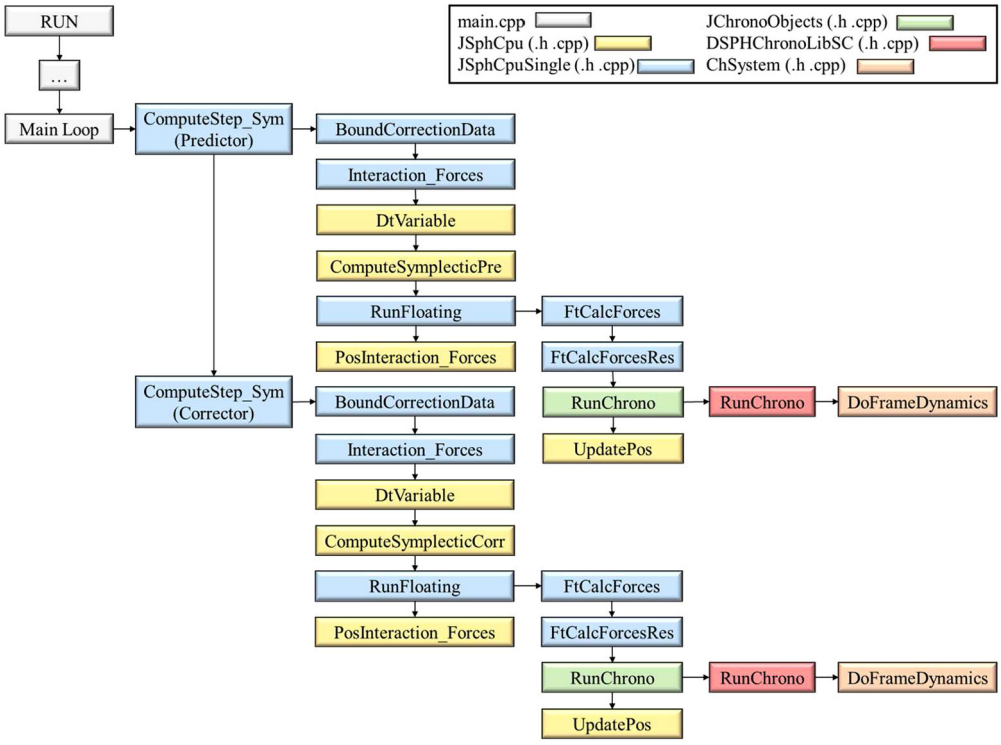

Fig. 3. Schematic of the flow events in DualSPHysics coupled with Project Chrono using the Symplectic integrator.

Table 2
List of source files of DSPHChronoLib.

Source files	Description
DSPHChronoLib (.h .cpp)	Declares/Implements the interface between DualSPHysics-Project Chrono.
DSPHChronoLibSC.cpp	Implements the functions to execute Project Chrono in single-core mode.
FunDSPHChrono (.h .cpp)	Declares/implements basic/specific functions for the coupling.
JChronoData (.h .cpp)	Declares/implements the data read from the XML input file to configure the elements handled by Project Chrono.

coupling between DualSPHysics and Project Chrono for CPU single-core simulations. In addition, the *JChronoData* files define and implement several classes that represent the allowed types of objects to be simulated by Project Chrono (e.g., rigid floating objects, mechanical constraints, etc.), where each object contains the variables that are transferred between DualSPHysics and Project Chrono during the simulation.

The source files of Project Chrono library directly used in this coupling are included in the Table 3. The *ChBody* and *ChBodyEasy* files contain the classes and functions used to define the geometry of the rigid bodies. The *ChLinkSpring* is a kind of mechanical constraint that allows simulating a TSDA by solving (24). On the other hand, the *LinkCoulombDamping* is a novel implementation based on the TSDA algorithm, which is included in this work and solves (25). The *ChLinkLock* files implement a set of mechanical joints based on a "lock formulation", including the classes *ChLinkLockRevolute*, *ChLinkLockSpherical*, and *ChLinkLockPointLine* corresponding to the hinge, spherical joint, and point-line joint, respectively, (presented in Section 3.2). The DEM-C and DEM-P are approaches to solve the collision detection, both available in this work, and are implemented through the classes *ChSystemNSC* (non-smooth contacts) and *ChSystemSMC* (smooth contacts), respectively. The material properties for the rigid bodies are defined by the classes *ChMaterialSurfaceNSC* and *ChMaterialSurfaceSMC*. The latter allows to include the elastic parameters such as the modulus of elasticity (E) and the Poisson's ratio (v_c) to experience local deformation when the bodies collide.

5.2. Compilation

A compilation process is needed in order to generate the DualSPHysics executables and the dynamic libraries of DSPHChronoLib and Project Chrono. The DualSPHysics code can be compiled to be executed either on CPUs or on GPUs. To run DualSPHysics on x64 architectures, the GNU G++ compiler for Linux-based operative systems is used. On the other hand, to run DualSPHysics on a GPU-accelerated system, a NVIDIA graphics card compatible with the GPU programming language CUDA is needed. The CUDA toolkit (https://developer.nvidia.com/cuda-downloads), which includes the NVCC compiler, must be installed on the computer. The GPU codes are compiled for compute capabilities *sm*30, *sm*35, *sm*50, *sm*52, *sm*61, *sm*70 with CUDA v9.2 (by default). Irrespective of the previous compilation choice, DSPHChronoLib and Project Chrono libraries are compiled only for CPU, with the same C++ compiler used for DualSPHysics.

DualSPHysics-Chrono package contains several folders:

- *bin*/*linux*: Executables of DualSPHysics, pre- and post-processing tools, and dynamic libraries.
- *lib*/*linux_gcc:* Precompiled libraries for x64 platforms on Linux.
- *src*/*source*: All source files and *Makefiles* to compile DualSPHysics.
- *src_extra:* The resources of DSPHChronoLib.

Table 3
List of source files of Project Chrono.

Source files	Description
ChBody (.h .cpp)	Declares/implements functions for rigid bodies that can move in 3-D space.
ChBodyEasy (.h .cpp)	Declares/implements functions for quick creation of rigid bodies with a triangle mesh shape.
ChCollisionModel (.h .cpp)	Declares/implements the geometric model for collision detection.
ChFrame (.h .cpp)	Declares/implements functions for coordinating systems in 3-D space.
ChLinkBase (.h .cpp)	Declares/implements basic functions for all types of constraints that act like mechanical joints in 3-D space.
ChLinkCoulombDamping (.h .cpp)	Declares/implements the class that defines the attributes and functions for the Coulomb damper actuator.
ChLinkForce (.h .cpp)	Declares/implements the class that defines the attributes and functions to apply forces on mechanical joints.
ChLinkLock (.h .cpp)	Declares/implements the base classes for joints implemented using the "lock formulation".
ChLinkSpring (.h .cpp)	Declares/implements the class that defines the attributes and functions for translational spring-damper-actuator (TSDA).
ChMaterialSurface (.h .cpp)	Declares/implements the base class for specifying material properties for contact force generation.
ChMaterialSurfaceNSC (.h .cpp)	Declares/implements the class that defines the attributes and functions material data for non-smooth (complementarity) contact method.
ChMaterialSurfaceSMC (.h .cpp)	Declares/implements the class that defines the attributes and functions material data for smooth (penalty-based) contact method.
ChSystemNSC (.h .cpp)	Declares/implements the class for a physical system to use a non-smooth (complementarity) contact method.
ChSystemSMC (.h .cpp)	Declares/implements the class for a physical system to use a smooth (penalty-based) contact method.

The package bundled to this manuscript contains precompiled executables of DualSPHysics and dynamic libraries of DSPHChrono-Lib and Project Chrono (files *libdsphchrono.so* and *libChronoEngine.so*, respectively), so that the released version can be readily used on most hardware, and thus avoiding the compilation altogether if no changes are included in the source code. Otherwise, if the compilation of the dynamic libraries is required, an extended documentation is available in the *Guide_DualSPHysics-Chrono.pdf* file provided in this package. To compile DualSPHysics with Project Chrono, the files *libChronoEngine.so* and *libdsphchrono.so* should be located in *DualSPHysics-Chrono*/*bin*/*linux* and in *DualSPHysics-Chrono*/*src*/*lib*/*linux_gcc*. In addition, the source file *DualSphDef.h* (in *DualSPHysics-Chrono*/*src*/*source*), which contains the macros definition to allow this coupling, should include the line `#define DISABLE_CHRONO` commented out. The GNU G++ compiler version 7.3.1, or greater, should be used to compile the code. Finally, the *make* tool must be installed on the computer to compile the code through the *Makefiles* already provided in the folder *DualSPHysics-Chrono*/*src*/*source*. When it is required to compile the GPU version, the variable `DIRTOOLKIT` (in *Makefile*) must be modified to define the CUDA path. Then, to compile the source code, the following lines must be executed, where the flag **`-f`** is used to specify the name of the target file:

i) `$ make -f Makefile_cpu`. This command will compile the code for CPU and create the executable *DualSPHysics5.0 CPU_linux64* in the folder *DualSPHysics-Chrono*/*bin*/*linux*.
ii) `$ make -f Makefile`. This command will compile the code for CPU&GPU and create the executable *DualSPHysics5.0_ linux64* in the folder *DualSPHysics-Chrono*/*bin*/*linux*.

DualSPHysics is parallelised to run on multi-CPU devices by using the OpenMP technology. To exclude the use of OpenMP the flags `-fopenmp` and `-lgomp` should be removed from the *Makefiles* and the line `#define OMP_USE` in the source file *OmpDefs.h* should be commented out.

5.3. Format of the files

Several format files are used for input definition and output data during the different parts of the execution flow of the DualSPHysics code. The input configuration file is formatted with the marking meta-language XML (eXtensible Markup Language, *.xml*). This format is based on labels (or tags), which allows users to easily organise and tag documents.

In DualSPHysics, the binary format BINX4 (*.bi4*) is used for input/output data. This format allows managing the information of a very large number of particles avoiding the computational cost related to generate/process plain text formats (ASCII). This format also allows storing data in single and double precision of real numbers without loss of information, e.g., the position of the particles. The DualSPHysics code loads the initial state of the particles from a binary file (*Case.bi4*) generated by the pre-processing tool (GenCase) provided in the DualSPHysics package. On the other hand, DualSPHysics stores the output data including the particle magnitudes during the simulations in binary files (*.bi4*).

Another format file used in DualSPHysics is the VTK (The Visualisation Toolkit, *.vtk*). This format is mainly used for the visualisation of the progress and results of the simulation. However, VTK files can also be used as input files during the pre-processing stage to generate the initial SPH domain. In addition, other formats can be used as input data like the STL (STereoLithography, *.stl*) or the OBJ (*.obj*), which allow defining 3-D geometries.

The CSV (Comma-separated values, *.csv*) data format can be used in DualSPHysics for input/output data. It is compatible with any data analysis tool and allows saving information by following a structured organisation based on rows and columns. Despite the main use of this kind of files is for saving data, DualSPHysics can read information from CSVs to impose predefined magnitudes on the elements during the simulation (e.g.: external forces or velocities, predefined motion for objects, etc.).

5.4. Running the code

Two input files are needed to run the DualSPHysics code. One of them is an XML file (*Case.xml*) that defines all parameters and elements to configure the system and the execution of the code. The latter is a binary file (*Case.bi4*), which contains the information of the particles at the initial state. Both input files are generated by the pre-processing tool GenCase, which is developed by the DualSPHysics team and provided precompiled in the package. The benchmarks presented in this manuscript are provided in the folder *DualSPHysics-Chrono*/*examples*/*chrono* and can be used to run the code coupled with Project Chrono, where for each benchmark-case, two scripts are included to run the code on Linux: *xCaseName_linux64_CPU.sh* for CPU and *xCaseName_linux64_GPU.sh* for GPU.

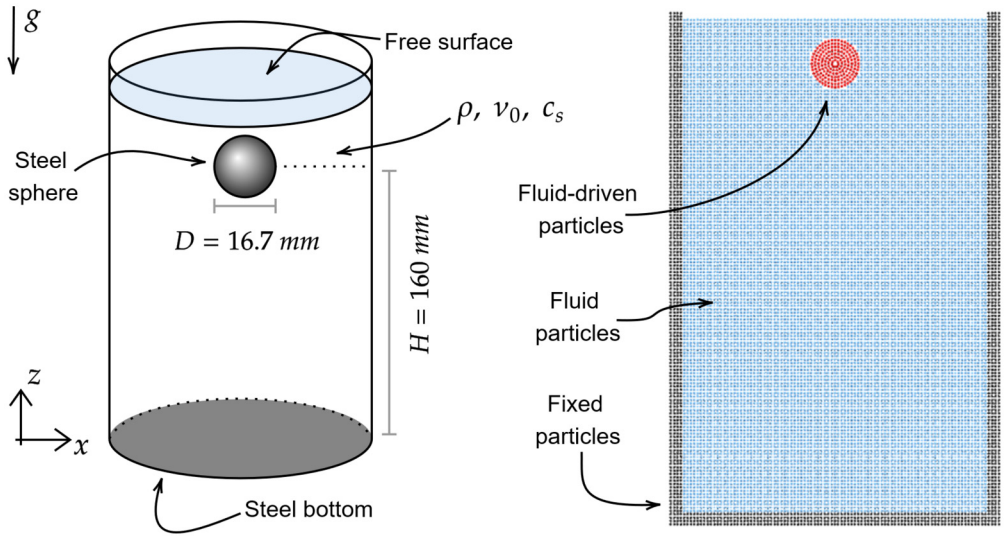

Fig. 4. Schematic of particle settling initial setup (left) and the SPH particle discretisation corresponding to $dp = D/10$ (right) across the vertical direction.

For example, to launch the benchmark *01_BallDrop* on Linux for CPU, the following steps can be considered:

```
$ cd DualSPHysics-Chrono/examples/chrono/01_
BallDrop

$ ./xFluidSteel16_3D_10_linux64_CPU.sh
```

Once launched, this script will call the pre-processing tool to create the initial setup (GenCase). After that, the DualSPHysics code is called to carry out the simulation (processing). Finally, the post-processing tools are executed to generate output data in order to analyse the simulation (e.g., VTK files for visualisation, CSV files to analyse the trajectory of the floating bodies, etc.).

6. Validation

Reference case benchmarks are here used to assess the accuracy of this coupling in simulating the mechanical behaviour of specific physical systems that, however, can be compounded to make more sophisticated and complex machines. The simulation setups and their data discussions presented in this section all refer to 3-D environments, in which the fluid is simulated considering a ratio between the smoothing length (h) and the initial inter-particle distance (dp) of h/dp=2.0 and using the laminar viscosity and SPS turbulence model, including Eq. (5) to the momentum equation (4).

6.1. Collision detection with SMC algorithm

The experimental setup proposed in Hagemeier et al. [78] has been designed to study the behaviour of particular systems when sedimentation processes evolve into multiphase flows (*particle settlings*). The controlled environment is set to create favourable conditions for investigating the particulate's gravity-driven sedimentation processes into multiphase flows, allowing tracking the position of the system evolution in time. The experimental setup that is used for this validation comprises a steel sphere (of diameter D=16.7 mm), initially completely submerged in liquid and kept still by a vacuum tweezer; a sudden release of air pressure in this device activates the motion of the sphere, corresponding to *time*=0 s. According to the information provided in the reference paper, the liquid, which is a mixture of water and glycerine, can be characterised using: density ρ=1141 kg/m^3, kinematic viscosity υ_0=8·10^{-6} m^2/s (measured at room temperature); the speed of sound is numerically lowered to c_s=150 m/s. The test took place in a cylindrical container of radius 110 mm. The centre of gravity (CoG) of the sphere is initially located at H=160 mm above the tank bottom (Fig. 4) and the sphere mass corresponds to m =18.85 g (ρ= 7729 kg/m^3). To guarantee an adequate control over the phenomenon under study, the bottom surface of the tank is made of a thick stainless-steel plate to achieve negligible deformation at the instant of impact.

The numerical model follows from the geometrical description hence creating the experimental setup at the same scale in 3-D, which is desirable to avoid scale effects on the dynamics of the system due to the chosen scaling algorithm. The motion of the sphere in fluid is solved by the pure SPH solver, which considers the mDBC technique to discretize the sphere volume, the lateral walls of the tank, and its bottom surface. To provide more accuracy to the numerical solution, a more realistic algorithm for solving the sphere-to-bottom interaction is used: the DEM-P method introduced from the coupling. The outer surfaces of these two solid geometries possess specific properties that correspond to the actual material being modelled, that is, stainless steel, which can be characterised by Young's modulus E=210 GPa, Poisson's ratio ν_c=0.33, and restitution coefficient e=0.80, using sensible values retrieved from literature regarding similar situations. Fig. 5 shows four 3-D visualizations of the simulation with $dp=D/10$ starting from the initial configuration (*time*=0.00 s) to the first impact. The first row proposes particle colouring that highlights the magnitude of the velocity field, which allows to notice the wake formation, whereas the second, highlights the total value of the fluid pressure, showing that the ball is moving through hydrostatic still water.

Fig. 6 shows the vertical component of the sphere CoG, compared to the 95-percent-confidence interval that is built from three experimental repetitions. The lines representative of the response of the numerical model correspond to three different dp, taken as inversely proportional to the sphere diameter D, in this case $dp=D/10$, $D/15$ and $D/20$. The red curve ($dp=D/10$), which represents data for the coarsest resolution, shows a small deviation from the experimental range, despite having a quite consistent experimental response. This suggests that the SPH fluid resolution is not enough to solve the solid-fluid interaction with sufficient accuracy, thus introducing more dissipation than in reality. This cascades into the inaccuracy of the first bounce, due to the sphere lower kinetic energy, which resolves into underestimating the first peak of the trajectory (*time* ≈ 0.30 s). As the resolution increases ($dp=D/15$ and $D/20$), the two curves adhere better to the experimental re-

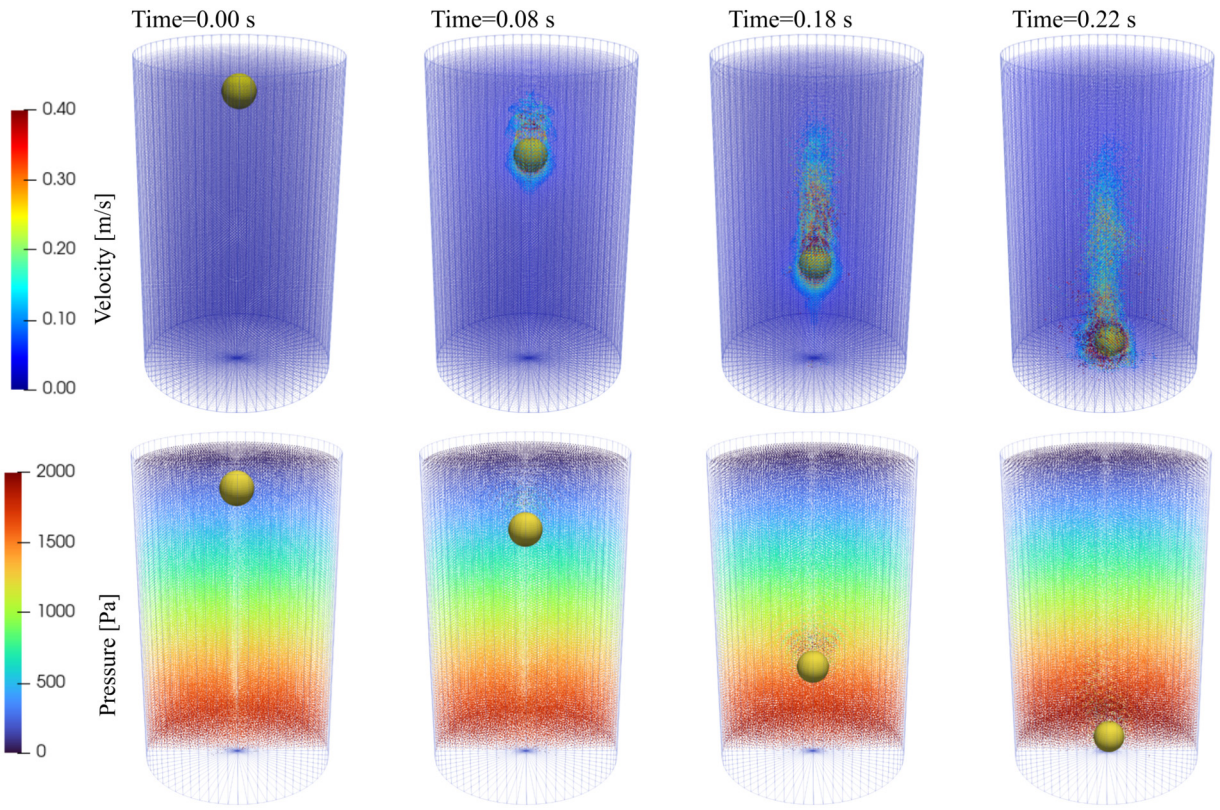

Fig. 5. 3-D visualizations of the falling ball in water covering the first impact for the case with $dp=D/10$. The particle colouring highlights the fluid velocity magnitude on the top row and the pressure field on the bottom row.

Table 4
RMSE and first two bouncing periods comparison.

Case	RMSE	T_1 [s]	T_2 [s]
Mean Exp.	0.0023	0.214	0.168
D/10	0.0085	0.218	0.189
D/15	0.0029	0.209	0.194
D/20	0.0017	0.206	0.192

sponse since the numerical response is in strict agreement with the reference interval. Consequently, the trajectory after the first and second bounce is well captured, thus demonstrating that for this resolution not only is the system able to resolve the fluid-solid interaction, but also the collision between the two instances. By delivering good prediction, the chosen restitution coefficient has proven to be practically right, although it cannot be verified with respect to the experimental reference. A more thorough comparison of the model performance is provided alongside Table 4. The root mean square error (RMSE) estimator is used here to provide a quantitative measure of the accuracy of the produced results. The first row of Table 4 reports the mean RMSE for the three experimental repetitions restricted to the first two ball bounces, and the elapsed time from ball release to first bounce (T_1) and from first to second bounce (T_2). By comparing this information with the same data retrieved from the numerical simulations, a converging pattern is forming when increasing the resolution, although some precision is lost when accounting for the estimation of the second bounce.

6.2. Collision detection with NSC contacts among multiple bodies

To further validate the proposed contact detection implementation, and the capability of the proposed coupling to fluid-rigid body interaction with large systems using the DEM-C approach. It should be noted that this benchmark was also reproduced and presented in Ng et al. [79], where an SPH–VCPM–DEM method was used. The setup comprising several cylinders (diameter D =1.0 cm, length of L =9.9 cm, and density ρ=2700 kg/m^3), piled up as to create an unstable column of material that eventually breaks due to the gravitational pull. The outer surface of each solid cylinder is characterized as to reproduce the aluminium contact properties, i.e., Young's modulus E=69 GPa, Poisson's ratio ν_c=0.33, and restitution coefficient e=0.75, Coulomb friction coefficient μ=0.45

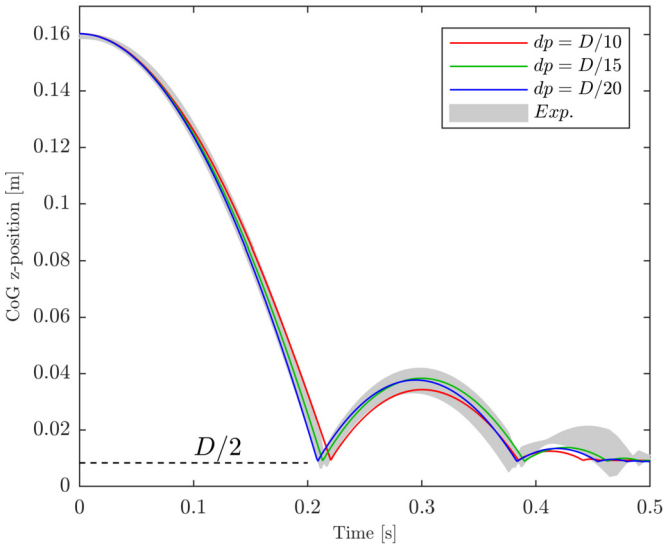

Fig. 6. Comparison of the experimental [78] and numerical vertical position of the steel ball with respect to different resolutions.

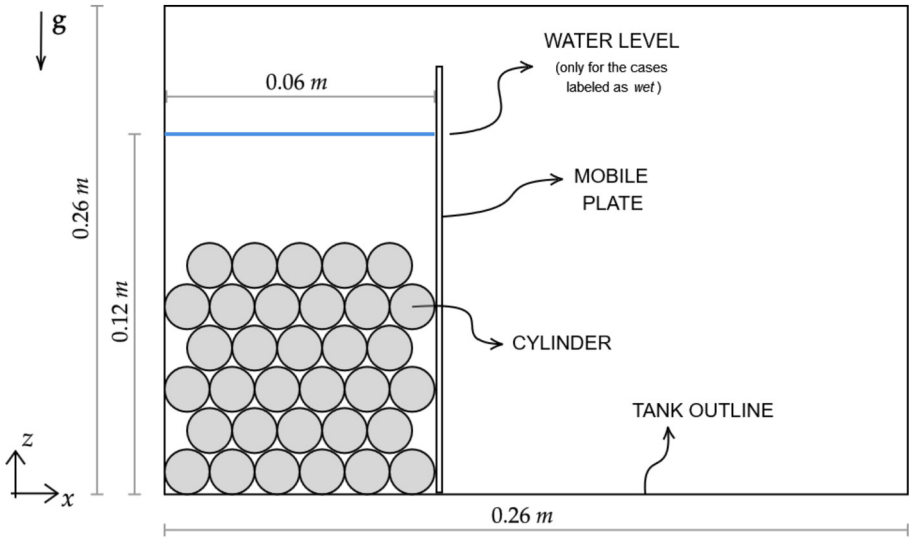

Fig. 7. Schematic diagram of the problem involving the collapse of a pile of 6-layer of cylinders.

[45,79]. The cylinders are arranged into layers to form a hexagonal lattice by alternatively staggering rows of five and six cylinders until the wanted height of the pile is reached. Note that not only does this provide the highest possible packing ratio, but also a numerical statically-unstable initial condition, thereby provoking the self-activation of the column collapse by design. The rows are laid into a tank that is 0.26 m long, 0.10 m wide, and 0.26 m height, made of acrylic resin (E=3.00 GPa, ν_c=0.30, e=0.75), in close adjacency to one of the vertical walls, and kept at rest thanks to the use of a mobile gate that triggers the rows collapse at time zero. It is worth noting that the small clearance between the length of the cylinders and the width of the tank provides the system with the right restraints to configure a pseudo bi-dimensional response. This means that the dynamics of the collapsing column of cylinders is well reproduced even if one of the dimensions, i.e., the y-direction, the experiment took place in is disregarded. This is twofold convenient since it allows to both enhance test reproducibility and reduce the computational runtime. However, the validations presented in this section are performed in 3D.

The case corresponds to the experimental test performed in Zhang et al. [80] and to which this analysis refers to establish the accuracy of the proposed coupling. The first validation provided here deals with a pile of cylinders that comprises six staggered rows, totalling 33 rigid bodies managed by Project Chrono. In this test, the evolution of the system purely depends on the accuracy provided by the multiphysics library due to the absence of water, and as such often referred as *dry*, indicating that although in principle the physical test was performed in presence of air, the fluid phase hardly affects the dynamics of the collapsing pile. Regardless, since the instance geometries live within the SPH environment, an initial interparticle distance must be assigned, and here it is set to dp=D/15 (0.000$\overline{6}$ m). The initial setup includes the cylinder shapes and the tank, the collision properties of which were given in the previous paragraph. It is important to mention that as a matter of fact, colliding shapes should be initialized such that no collision is detected to avoid numerical inconsistency. The mentioned condition is satisfied by generating the cylinder shapes with a clearance of 0.5 dp in all direction, which is shown in the first row of Fig. 7 (lateral view). Then, to achieve a state that closely comply with the physical setup, the numerical model is let run for 0.30 seconds prior to removing the gate (imposed velocity of 2.0 m/s along z) and thus activating the collapse mechanism.

Fig. 8 and Fig. 9 display the results of the simulation. Fig. 8 (second to fifth row) proposes a visual comparison between the experimental pictures (first column) and the visualizations of the numerical model (second column), conveniently shifted in time as to account for the prior 0.30 seconds of simulation. Different colouring of the circles helps the reader track the motion of the cylinders in time: this visualization substantiated into good agreement of the overall outline of the collapsed pile, even capturing the motion of isolated cylinders. Furthermore, Fig. 9, which tracks the position of the overall centre of mass of the system in time (right-hand side: x-position; left-hand side: y-position), provides a quantitative estimation of the accuracy of the model outcome in contrast with the experimental reference and the numerical solution in [80]. Each chart confirms detailed precision delivered by the solver, which behaves reasonably well, with small inconsistencies within a $\pm$2% range that, however, configure perfectly acceptable discrepancy considering the chaotic nature of the phenomenon. This is further backed up by the numerical results reported for the sake of comparison, which show similar trends for the overall position of the centre of mass of the system.

A final validation to the capabilities of the numerical modelling to deal with multibody contacts while interacting with fluid (*wet*) is provided in the following, starting from the setup proposed in Fig. 7, for which the reported water level line is relevant. The fluid phase (ρ=1000 kg/m^3, kinematic viscosity υ_0=10^{-5} m^2/s, speed of sound c_s=150 m/s) fills the gaps in between the cylinders up to a level that sets 0.12 m above the tank bottom, and the same plate that confines the cylinders holds the water column till its vertical activation. Note that the following simulations are performed in 3D, building the same geometrical features of the experimental layout. The motion constraints produced by the interaction of the tank lateral walls and the lateral surfaces of the cylinders are modelled herein by motion restrictions directly applied to each rigid bodies.

Fig. 10 reports the model results, providing a visual comparison of the overall system evolution in time. Again, the test begins with the plate sliding upwards with imposed velocity of 2.0 m/s along z, as specified in the reference paper. Then, a slight shift in time is applied to re-establish consistency between the numerical and experimental datasets; the time of the first snapshot (*Time*=0.10 s) is set by considering a similar profile developed by the water column: the required shift equals 0.030 s, and it is thereby applied. The second and the third snapshots, respectively at *Time*=0.30 s and *Time*=0.50 s, reveal that the rigid bodies dynamics is well captured. Red shapes are over imposed to the main clusters that develop during the mixing flow process to make this clearer. Ad-

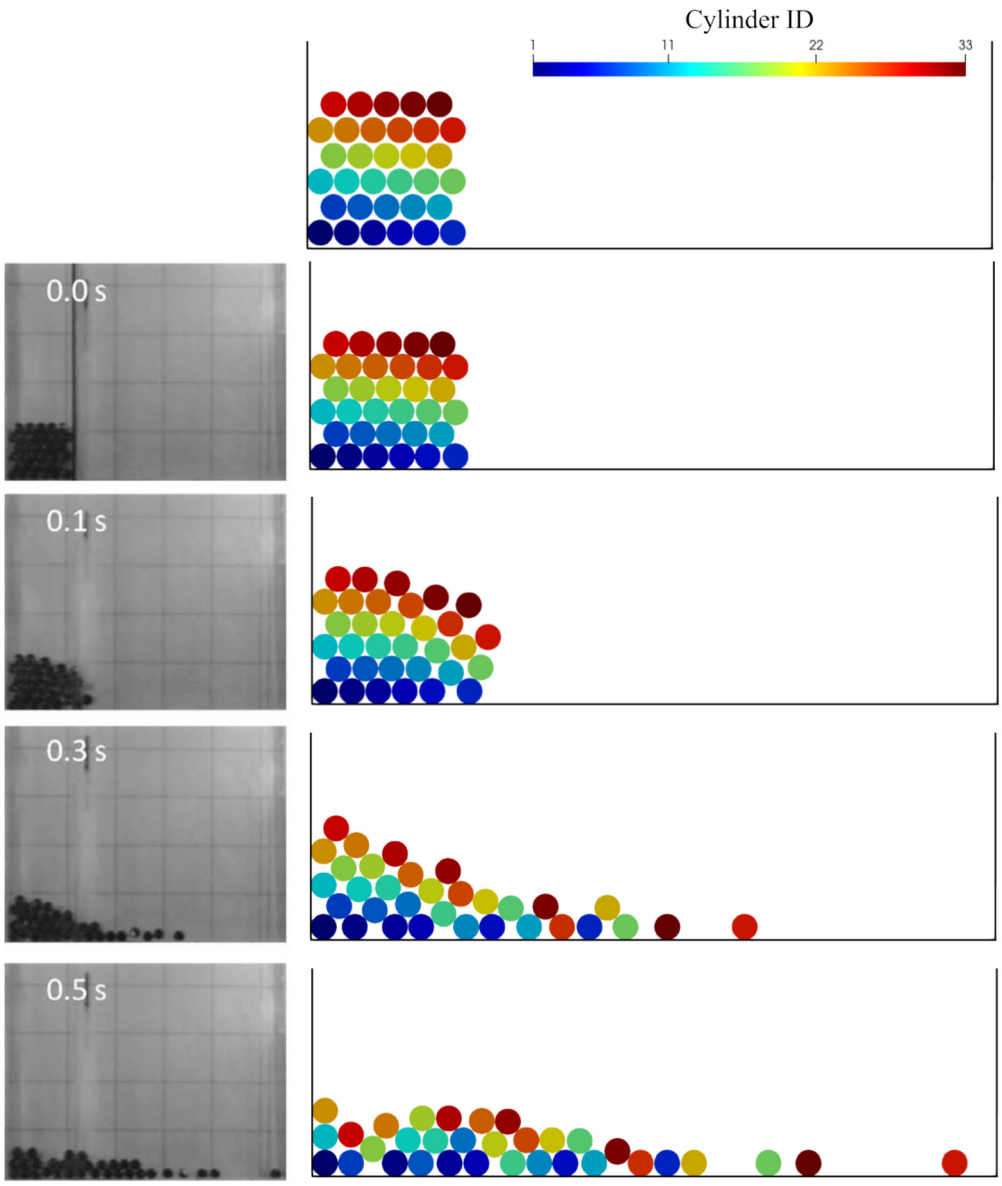

Fig. 8. Experimental [80] and numerical comparison of the transient behaviour of a six-layer pile of cylinders collapsing under gravity (left column: experiment; right column: simulation).

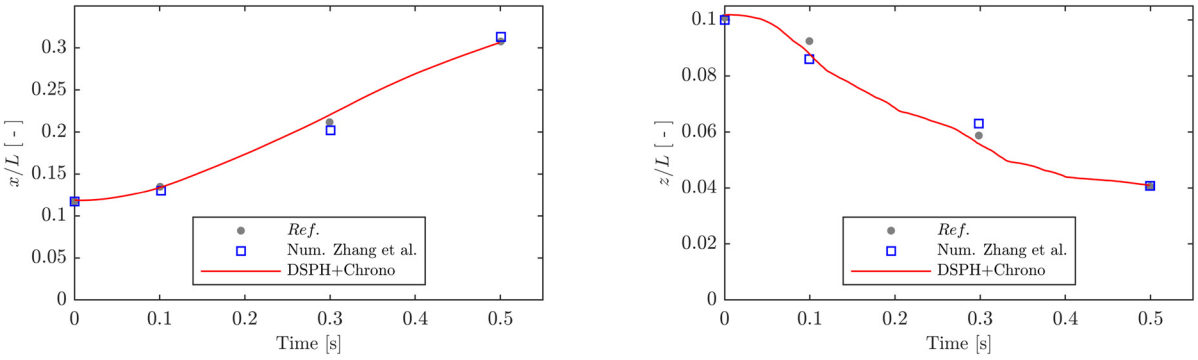

Fig. 9. Position of the centre of mass of the solid system (average) in the horizontal (left) and vertical (right) directions, compared to the reference and numerical solutions from Zhang et al. [80]. The data is made dimensionless by considering the width and height of the tank L=0.26 m.

ditionally, the arriving time of the first cylinder coming in contact with the right-hand side tank wall is compared for the simulations and experiments, considering 6, 8, 10, and 12 rows of cylinders (33, 44, 55, and 66 cylinders each, respectively). The comparison is provided in Fig. 11, and it highlights a good level of consistency of the reported numerical data with the experimental target, and are in line with the results of the numerical framework proposed in Zhang et al. [80] (compared in Fig. 11) and Ng et al. [80] (not re-

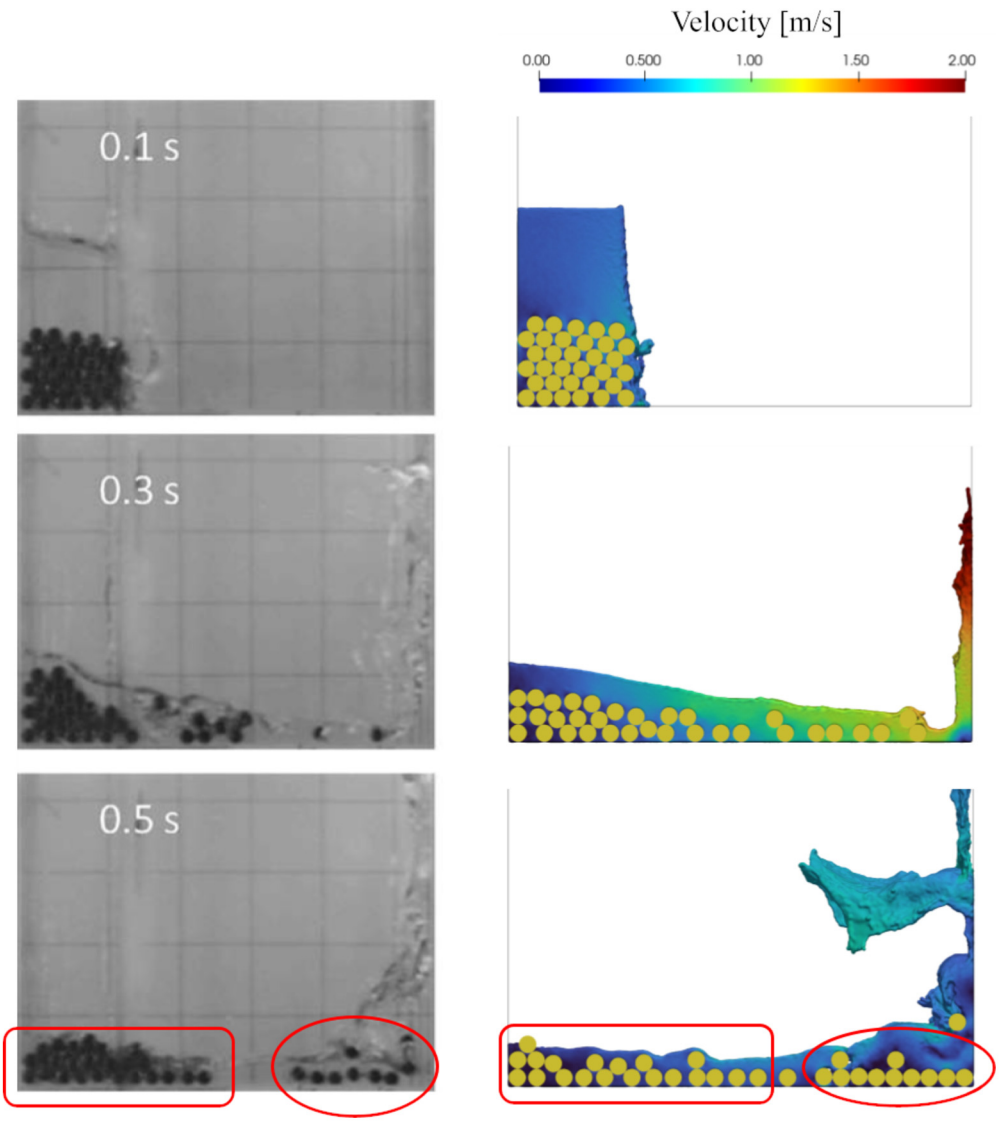

Fig. 10. Experimental [80] and numerical comparison of the transient behaviour of a six-layer pile of cylinders and water collapsing under gravity (left column: experiment; right column: simulation).

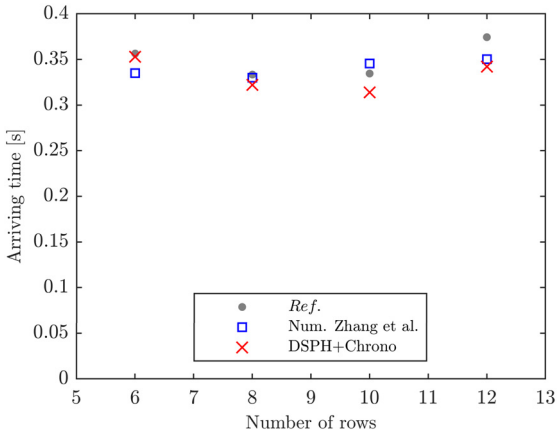

Fig. 11. Arrival time of the first cylinder to the right wall for cases with 6, 8, 10, and 12 rows of cylinders, compared to the reference and numerical solutions from Zhang et al. [80].

ported here). The model provides good estimations of the system evolution for the first two cases with 6 and 8 rows, respectively, seemingly reporting more accurate results when the fluid simulation fidelity is paramount. Conversely, when the contact accuracy becomes more relevant, the model underestimates the time at the first cylinder touch, nevertheless within an acceptable range.

6.3. Multibody dynamics

Among the multibody dynamics features, the following experimental setup, proposed by Arnold et al. [81], allows validating the dynamic constraints provided by the elements defined as hinge and linear spring in the previous dissertation. Two cases are presented, a gravity pendulum and spring (vertical) pendulum, respectively, where the geometry of the main mass stays the same but with different mechanical configurations, both of which tested in air and water.

The mass of the two configurations is given by a cubic-shaped block of resin (ρ=1220 kg/m^3) of edge L=60.0 mm. For the gravity pendulum, the motion of this mass hinges about the pivot point A (Fig. 12) is connected through a quite slender aluminium rod (cross section 2.0×16.7 mm, density ρ=2700 kg/m^3), which is chosen so that the CoG of the cube is set 200 mm away from the point A (L_{cube}). Theoretically, the oscillating period of such setup should be

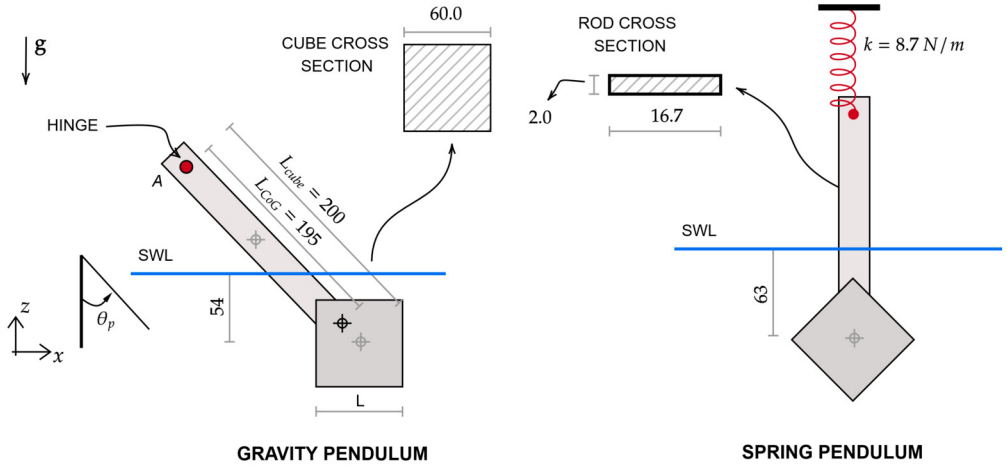

Fig. 12. Physical dimensions and initial configurations for the gravity pendulum (left) and the spring pendulum (right) setups (all dimensions in mm).

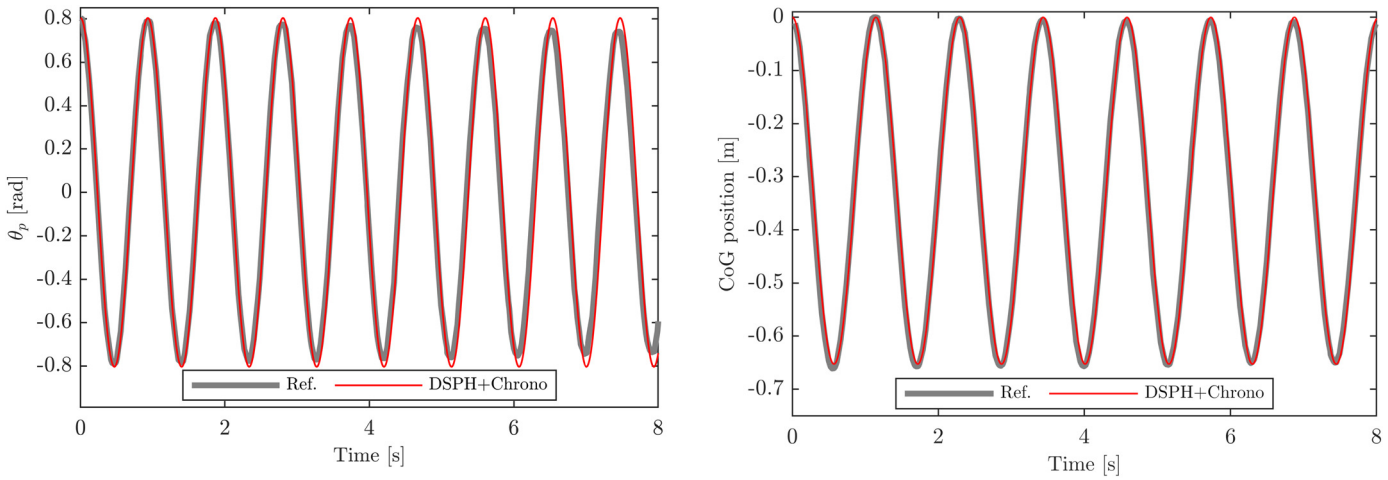

Fig. 13. Comparison between numerical and experimental [81] amplitude of gravity pendulum (left) and the spring pendulum (right) in air (vacuum for the numerical setup).

T_{theory}=0.933 s for an initial amplitude of 0.80 rad. The spring pendulum involves the same compound geometry (cube and rod), but it is configured such that the CoG of the cube is at its lowest position (stable position); the upper edge of the rod is connected to a spring of stiffness k=8.72 N/m, which provides restoring force to the system when it moves out of this initial configuration. In fact, when the spring pendulum is tested, the spring length corresponds to its rest length. For this second setup, the undamped theoretical period for the vertical motion is defined as $2\pi\sqrt{m/k} = 1.146$ s, where m is the total mass (cube and rod) and k is stiffness of the system, corresponding to the spring stiffness in this case.

The numerical modelling of the mass, cube and rod, which is primarily used by Project Chrono to build the coupled simulation, is tackled by creating two solid shapes as presented in Fig. 12 being the assignment completed by the density values given to each element. Starting from this, the model automatically computes the mass, CoG, and inertia for the compound geometry, given that the cube and the rod configure a unitary rigid instance. In addition, a relative joint that connects all the six DOFs is used for this purpose. After, a hinge joint constrains point A to experience only rotation for the gravity pendulum, whereas a linear spring configures a motion restriction for the spring pendulum. Prior to considering the case that comprises a fully developed fluid-structure interaction, it is worth validating stand-alone cases with no fluids at all.

For a more complete understanding of the data collected in the two panels of Fig. 13, it is important to mention that the cases reported in the reference research labelled “in air” are herein used for comparing the numerical solution corresponds to a simulation in vacuum. The hinge connection implemented in the gravity pendulum setup is set as ideal, that is, no torsional (frictional or viscous) damping is added to the dynamics of the system, whereas the real one surely does. The time evolution of the CoG of the cube is reported in Fig. 13 (left), in which the experimental and the numerical time series are compared. By contrasting the two shapes, one can immediately notice that the numerical model predicts a harmonic non-damped pattern, which is consistent with theoretical expectation. The oscillating period for the system is really accurate, having a relative error smaller than 0.5% (T_{Exp}=0.932 s vs. T_{Num}=0.931 s). The small deviation from the expected period is mainly due to two recognisable issues: firstly, the mass of the rod that slightly slows down oscillations by taking the CoG of the system closer to the pivot point, and secondly to the presence of a non-negligible damping effect on the vibration period being the hypothesis of undamped motion not fully satisfied. The spring pendulum free oscillation results are reported in Fig. 13 (right), in which the vertical CoG position of the cube is depicted for the numerical model response contrasting with experimental data. The two-time series are in very close agreement for what accounts amplitude and period; a quite small misalignment appears towards the end of the chart, which highlights the presence, albeit small, of some damping phenomenon in the experimental case most likely induced by air damping. Note that for this configuration the damping is relatively small due to the lower velocity of the mobile shape and to its aerodynamic shape. For this configuration, the experi-

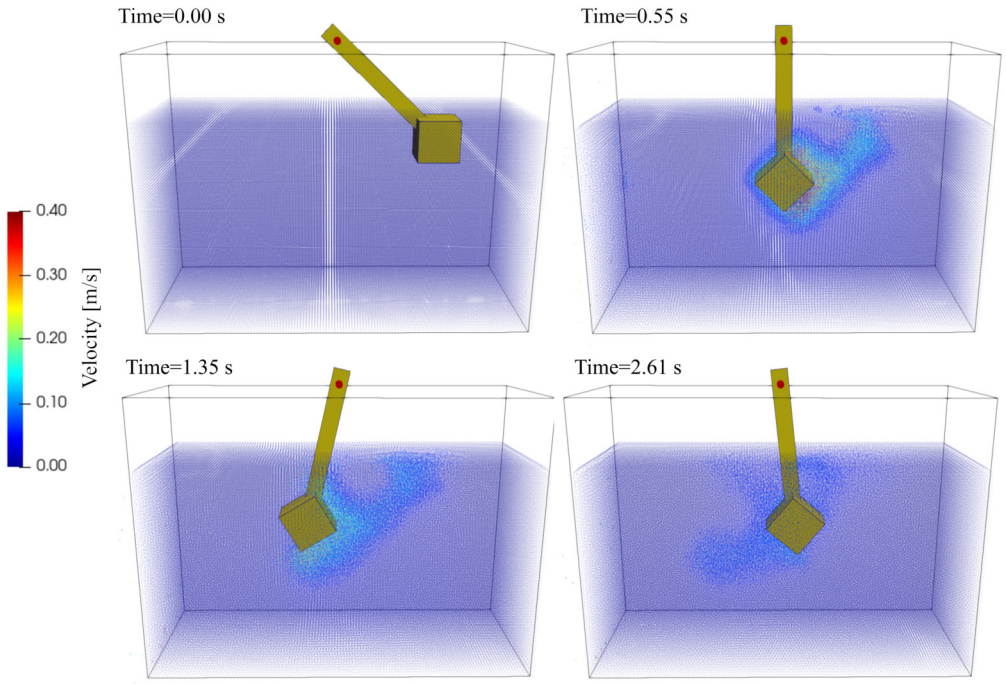

Fig. 14. 3-D visualizations of the gravity pendulum in water during the first cycle for the case with dp=L/15. The particle colouring highlights the fluid velocity magnitude.

mental and the numerical periods show a perfect match, with a relative error of 0.1% probably due to the round-off implemented for reporting the experimental figures (T_{Exp}=1.144 s vs. T_{Num}=1.146 s); however, the latter value corresponds to the period evaluated through the formula reported above. It is important to highlight that the particle size hardly affects the response of the mechanical system as long as the SPH resolution is consistent with the smallest dimension of the geometry being modelled. The coupling in fact works in such a way that the mechanical system response is only dependent on the quality of the geometry and/or mechanical properties that are shared with the multiphysics library. When, however, the mechanical system interacts with fluid particles, the initial particle interspacing plays a paramount role because it defines the accuracy of the interchanged forces.

The dynamics of the gravity pendulum beforehand validated is now tested in water. The position of the resin cube with respect to the fluid free surface is shown in Fig. 12, and it is such that the top surface of the cube is parallel to the free surface (initial amplitude θ_p=0.84 rad), and with an initial draft of 84 mm. The initial positioning of the cube comes from careful consideration about the hydrodynamic interaction of the shape, to have controlled eddy-shedding features for the sake of data interpretation; this also ensures numerical reproducibility by lowering the uncertainties related to turbulent phenomena. The tank in which the numerical test takes place is a 54×24-cm parallelepiped, with water depth of 30 cm (this last is fully compliant with the experimental one). The fluid is simulated using the physical parameters that correspond to the temperature experimental conditions, i.e., water density ρ=998.5 kg/m^3, kinematic viscosity υ_0=1.26·10^{-6} m^2/s (fresh water at 11.3 °C). The speed of sound is artificially lowered to c_s=150 m/s, which gives a reasonable fluid behaviour for the investigated problem. Fig. 14 shows four instants of the simulation with dp=L/15, in which the particles are coloured according to the magnitude of the velocity field.

Fig. 15 compares the experimental and numerical time evolution of pendulum motion amplitude. The figure reports data for four numerical simulations, which use the following dp values: L/15, L/25, and L/50. Additionally, Table 5 provides a more comprehensive and precise comparison of the features of the experimental and numerical results, namely the oscillating period at each cycle (T) and the related damping ratio (ξ). It is important to mention at this stage that due to the relatively coarse resolution employed for the first two cases, the particles that belong to the geometry of the rod do not possess sufficient information to apply the mDBC technique, thus they are treated as DBC. This will induce small deviations from the real behaviour, confirmed by the data supplied in Table 5.

Table 5
Experimental and numerical comparison of the period and damping ratio during the first four cycles for the gravity pendulum in water.

Case	T_1 [s]	T_2 [s]	T_3 [s]	T_4 [s]	ξ_1	ξ_2	ξ_3	ξ_4
Exp.	2.68	2.64	2.59	2.69	0.096	0.038	0.039	0.016
L/15	3.11	3.14	3.00	2.82	0.120	0.053	0.049	0.034
L/25	2.83	2.77	2.89	2.97	0.112	0.055	0.051	0.112
L/50	2.81	2.71	2.56	2.62	0.097	0.059	0.042	0.021

The test commences by releasing the gravity pendulum from an initial 45-degree angle (0.80 rad); the cube completes the first half cycle in close agreement, reaching the maximum negative amplitude almost in the same time frame. Soon after, some deviations are noticeable within the reference solution and the numerical data. On account of the first three dps, the oscillating period, which is greatly affected by fluid-imposed dissipation, is overestimated (ref. to Table 5) so gathering a delay of half a cycle by the end of the proposed chart. The observed slow-down in the motion of the pendulum may be caused by the relatively low level of resolution for the hydrodynamics interaction and that could be a contributing factor to the excessive damping in the first cycle as well. In fact, when higher system resolution increases, the model response compares well with the reference solution – still missing the amplitude of the first cycle – whereas the curves show similar and constant damping ratios throughout the remaining oscillations. As the resolution of the system improves, so does the accuracy of the fluid-solid interaction, giving more consistency and smoothness to the cycles, thus providing quite accurate amplitude prediction, mostly caused by the preservation of the damping effect. The numerical prediction stays close to the reference solution

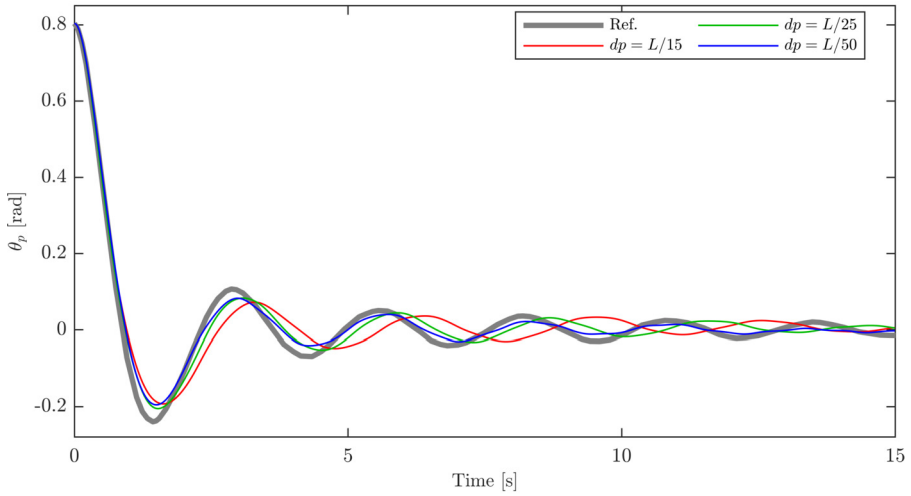

Fig. 15. Comparison between numerical and experimental [81] amplitude for the gravity pendulum in water.

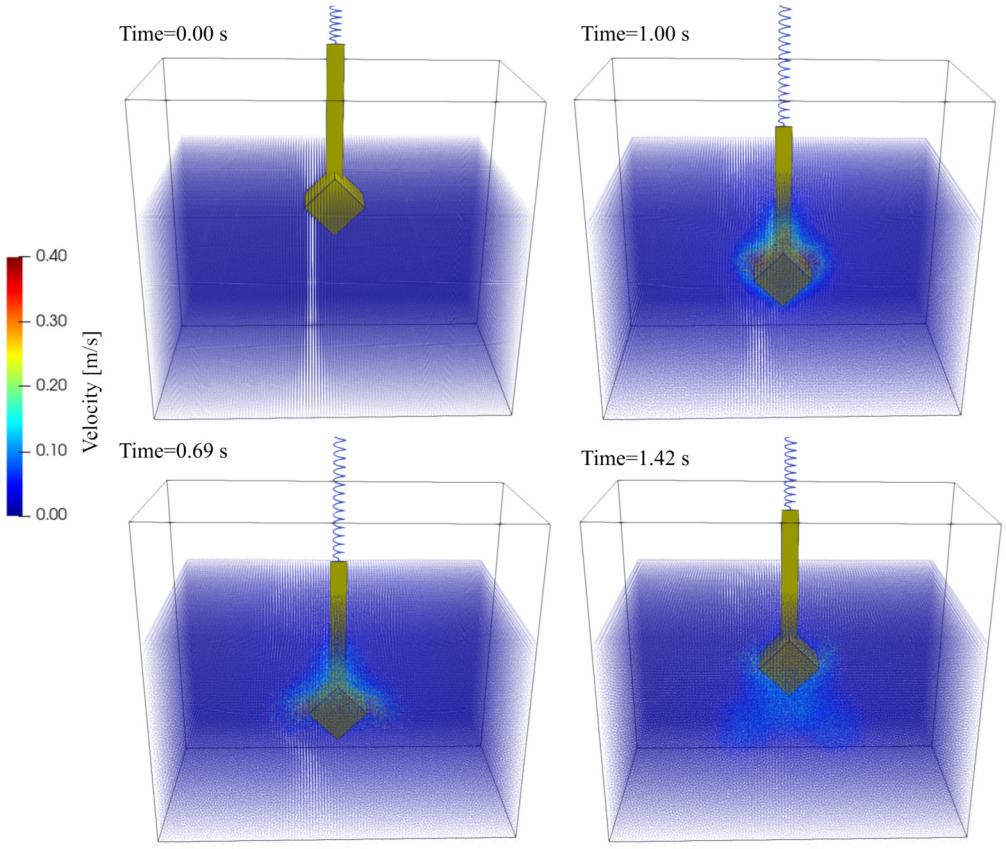

Fig. 16. 3-D visualizations of the spring pendulum in water during the first cycle for the case with dp=L/15.

when the amplitude becomes small in comparison to the particle size, which entails a proper force estimation across the surfaces of the cube.

The spring pendulum is simulated in water considering the initial setup proposed in Fig. 12. The cube is placed into a water box of 48×36 cm, water depth of 30 cm (as in the experimental setup) and draft of 93 mm. Note that the tank employed for this test is wider than the one used in the previous setup to accommodate the displaced fluid. Using the same turbulence model as in the previous, the physical parameters that correspond to the experimental conditions are water density ρ=998.4 kg/m^3, kinematic viscosity υ_0=1.18·10^{-6} m^2/s (fresh water at 15.9 °C). Three simulations are performed considering the same initial interparticle distances presented before; likewise, the rod SPH particles are not included. Fig. 16 depicts four instants of the simulation corresponding to the lowest simulated resolution (dp=L/15), in which the particle colour is proportional to the magnitude of the velocity field.

Fig. 17 presents the time evolution of the vertical displacement of the compound geometry (cube and rod), considering L/15 and L/25 to set the case resolutions, and the experimental reference (gray line), whereas Table 6 provides a detailed comparison for the first four oscillations, providing the period (T) and the relative damping ratio (ξ). The first oscillation, for all

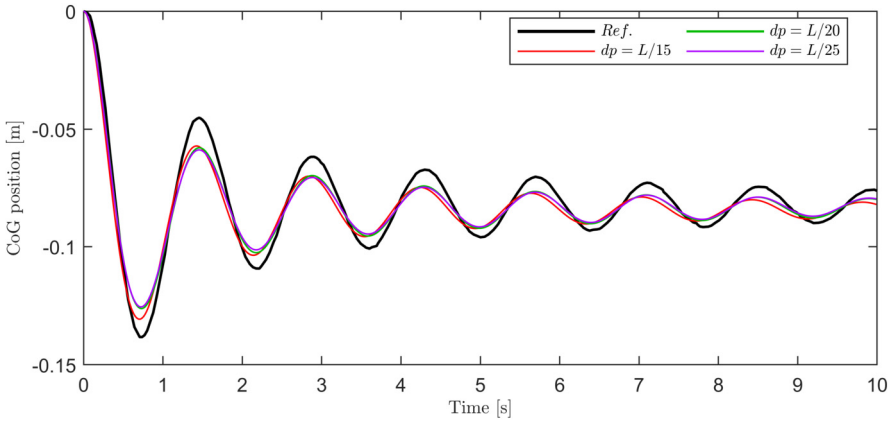

Fig. 17. Comparison between numerical and experimental [81] amplitude for the spring pendulum in water.

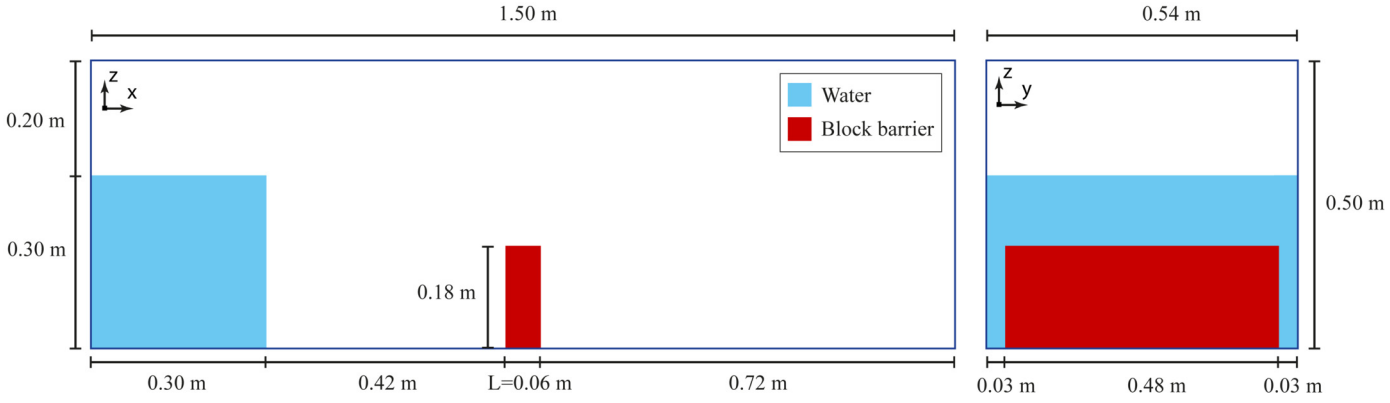

Fig. 18. Schematic of the benchmark used to test the performance of the models: side view (left) and front view (right).

Table 6
Experimental and numerical comparison of the period and damping ratio during the first four cycles for the spring pendulum in water.

Case	T_1 [s]	T_2 [s]	T_3 [s]	T_4 [s]	ξ_1	ξ_2	ξ_3	ξ_4
Exp.	1.45	1.39	1.39	1.39	0.093	0.059	0.045	0.037
L/15	1.40	1.40	1.39	1.39	0.109	0.068	0.054	0.047
L/25	1.42	1.41	1.40	1.41	0.101	0.061	0.044	0.034

the presented resolutions, does not recover the maximum motion amplitude, undershooting it by almost 15%, confirmed by the higher damping ratio for the first cycle. What follows is then a motion in almost complete agreement with the reference solution (T_{Exp}=1.39 s vs. $T_{L/25}$=1.40 s, relative error 0.5%), having similar damping ratios for the second and third oscillations ($\xi_{Exp(2-3)}$=0.059 vs. $\xi_{L/25(2-3)}$=0.061) and consistent with the experimental one throughout the entire simulations. For the rough resolution, although a much more accurate amplitude prediction is achieved, it provides shorter oscillating periods that resolve in a phase lag evident after the first few cycles. The numerical prediction moves away from the reference solution when the amplitude becomes small in comparison to particle size, which entails a greater fluid energy dissipation, causing minor skewness in the cycle shape. This phenomenon reduces its intensity as the resolution increases, suggesting that more resolute setups can reduce this unwanted dissipation. However, since the model delivers satisfactorily agreement with $L/25$, solutions with finer resolutions are not proposed. Other features worth noticing are the equilibrium floating line of two simulations; they perfectly match both the theoretical expectation and the experimental data, with little to no deviation.

7. Performance analysis

This section presents several benchmarks to assess the performance of the two-way coupling. For all the cases proposed in this section, an artificial viscosity treatment is used, so Eq. (6) is included to the momentum equation (4), where the artificial viscosity coefficient is α=0.02 and h/dp=2.0. The use of this treatment is due to expected flow behaviour for the physics that developed during fluid propagation. These cases are composed of a fluid column (water) and a block wall that comprises several rigid bodies (blocks) that can move freely inside the tank. The gravity-driven column of water moves along the tank (i.e., x direction) and impacts the blocks that, at the same time, can collide to each other and to the surfaces of the tank. As mentioned at the beginning of this section, the fluid is simulated using the artificial viscosity whereas the collisions are solved with the DEM-C (non-smooth contacts) approach. The blocks are defined with a mass of 0.216 kg and the material properties of PVC (polyvinyl chloride), that is, restitution coefficient e=0.60, friction coefficient μ=0.45, whereas the tank is built with the properties of steel material, which can be defined by e=0.80 and μ=0.45. Fig. 18 shows a general schematic of the cases, providing a side view (left) and a front view (right) where the block wall shape (red) represents the volume occupied by 24 blocks; note that the thickness of the block wall is L=0.06 m.

The target application seeks to offer a similar behaviour of the block barrier using different resolutions in both models. To test the DualSPHysics performance, the dp value is modified and so, the number of particles varies according to it. On the other hand, Project Chrono solves the collision detection considering the geometry of the blocks, where the number of contact faces that compose the geometry of each block plays an important role in terms

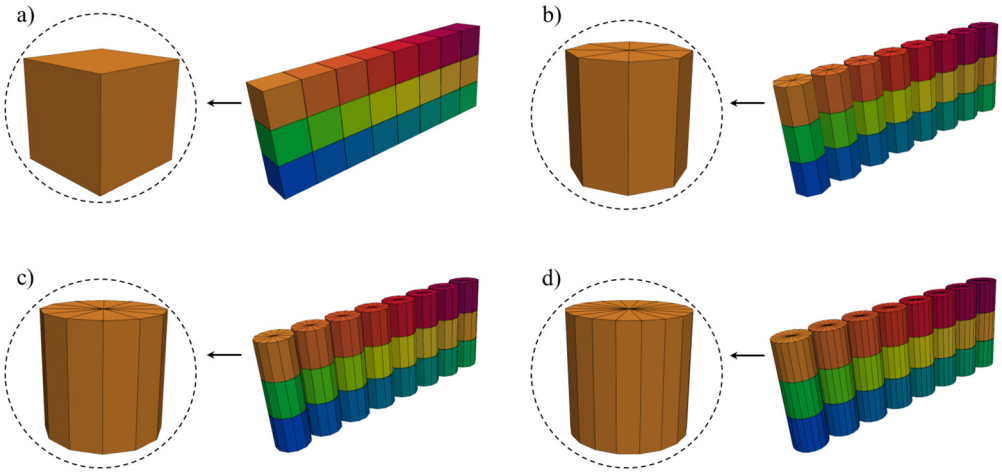

Fig. 19. Geometries of the blocks that compose the breakwater, where the blocks can be built as 6-face cube (a); 24-face cylinder (b); 36-face cylinder (c); or 54-face cylinder (d).

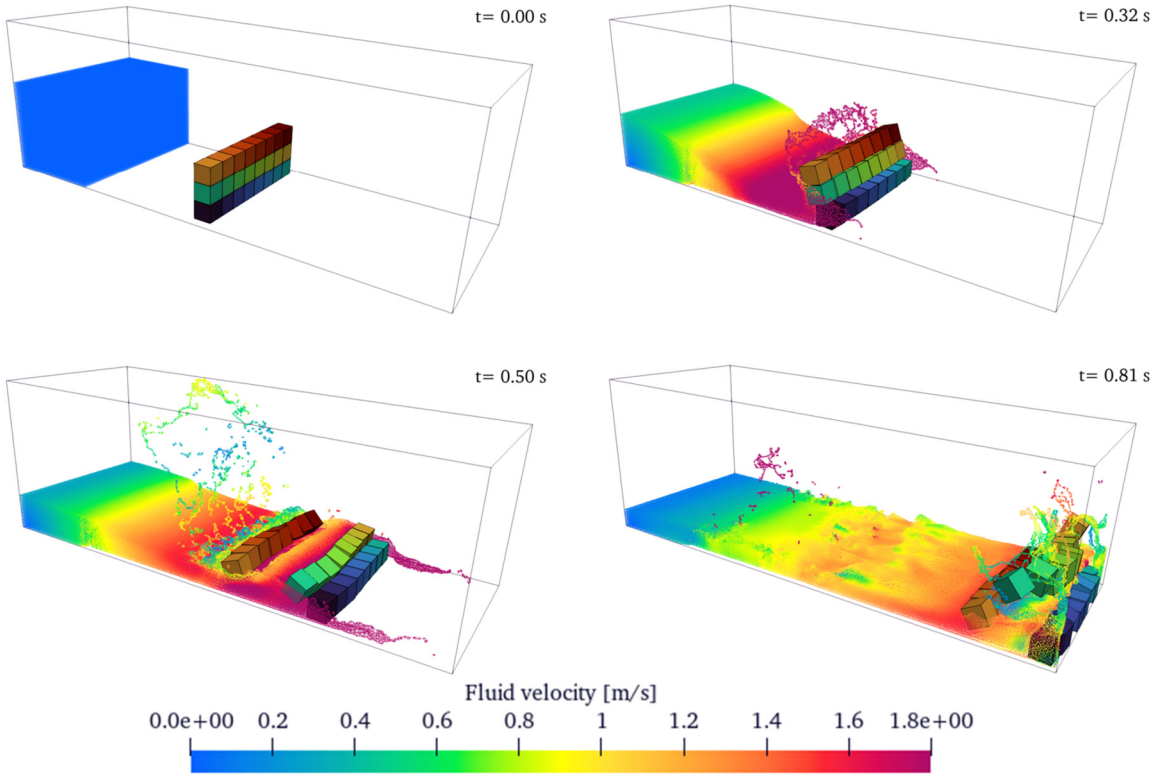

Fig. 20. Four instants of the simulation of case B.0 with fluid impacting a breakwater built with 24 6-face-cubes using $dp=L/15$.

of performance. Thus, to test the multiphysics library performance, four types of geometries are used to shape the blocks' bulk, each of them possessing a different number of faces (see Fig. 19); nevertheless, the breakwater always comprises 24 blocks. Therefore, the proposed cases can be split into two different groups considering the model to analyse in terms of performance: i) SPH model; and ii) multiphysics library.

The simulations are carried out on an Intel(R) Xeon(R) Platinum 8168 CPU and a graphic card NVIDIA Tesla V100-PCIE-32GB. All of configurations were executed by using the GPU solver for DualSPHysics and a single-core CPU for Project Chrono. The cases are identified by: i) B.0 is the base case shared for both groups of simulations; ii) D.*x* refers to the cases to test the DualSPHysics performance; and iii) C.*x* refers to the cases to test the Project Chrono performance; *x* is the sequence number under each group of simulations.

Fig. 20 depicts the base case (B.0) carried out, which involves a physical time t=1.00 s, and where several instants of the simulation can be seen. The first frame portrays the initial setup; then, the instant when the water column impacts the block barrier; the third shows how the first row of blocks is pushed forward; and finally, all the blocks are lumped close to the back-wall of the tank.

The first set of simulations is focused on the SPH-based solver performance analysis, where different SPH resolutions are used to modify the total number of particles of the domain while keeping the 6-face 24 blocks (see Fig. 19 (a)) to build the breakwater. Table 7 shows the setups carried out for this group, in which all the cases contain a total number of faces equals to 149. Note that the value of faces includes the 5 contact faces of the tank (the top face

Table 7
DualSPHysics performance cases by varying the number of particles.

Identifier	*dp*	Particles per block	Total particles	SPH steps	DualSPHysics runtime [s]	Chrono runtime [s]	Total runtime [s]	% Chrono
D.1	*L*/05	125	77368	10264	34	342	376	90.9
D.2	*L*/10	1000	425397	23000	223	609	839	72.6
B.0	*L*/15	3375	1233000	39076	947	981	1929	50.9
D.3	*L*/20	8000	2686223	49107	2650	1135	3785	30.0
D.4	*L*/24	13824	4437171	62918	5731	1451	7182	20.2

Table 8
Performance Project Chrono by varying the number of contact faces.

Identifier	Block type	Total faces	SPH steps	DualSPHysics runtime [s]	Chrono runtime [s]	Total runtime [s]	% Chrono
B.0	6-faces cube	149	39076	947	981	1928	50.9
C.1	24-faces cylinder	581	37026	921	1329	2251	59.1
C.2	36-faces cylinder	869	39257	981	2188	3169	69.1
C.2	54-faces cylinder	1301	38382	1017	3629	4646	78.1

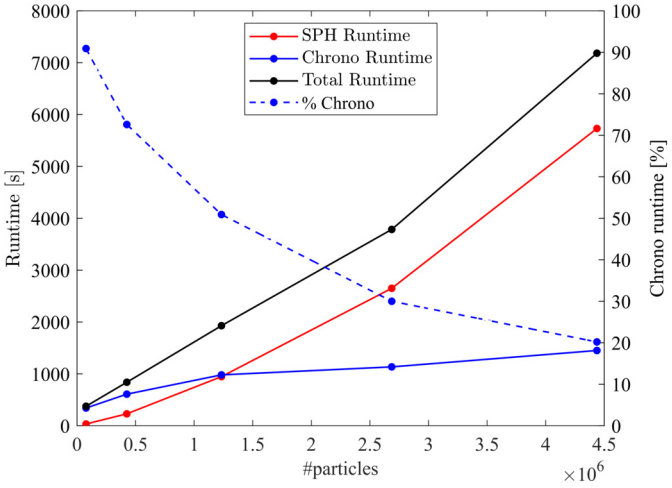

Fig. 21. Results of the performance test cases to analysis the performance of DualSPHysics and Project Chrono for different SPH resolutions.

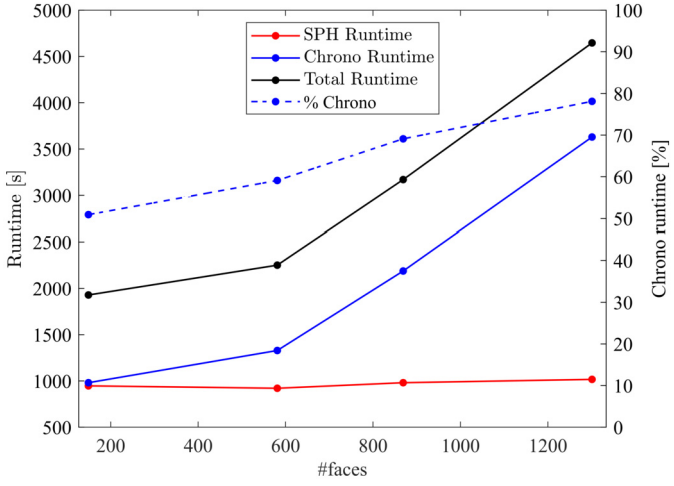

Fig. 22. Results of the performance test cases to analysis the performance of DualSPHysics and Project Chrono for different number of contact faces in the multiphysics library.

is not considered in the simulations) since the blocks also collide with the tank.

Fig. 21 shows the results of the first five cases proposed (in Table 7) considering the runtime according to the number of particles simulated. The solid red line corresponds to the runtime for solving the fluid-solid interaction by the SPH model, the solid blue line is the runtime for the solid-solid interaction by the multiphysics library, and the solid black line represents the total runtime of the simulation. In addition, the dashed blue line shows the quota (%) that Project Chrono consumes during the simulation. The number of particles has an impact on the SPH model in terms of performance, but on the contrary, the multiphysics library shows to be hardly affected. However, since the solid blue line does show a mild positive slope, the runtime of the Project Chrono is slightly different when the number of particles increases, which is probably because of the increasing number of SPH steps (column 5 in Table 7) that is not constant for each simulation due to the use of a variable Δt_{SPH} in the SPH solver, which provokes the number of calls to the multiphysics library to solve a time step to increase, causing additional overhead. However, considering that the time quota consumed by Project Chrono (blue dashed line in Fig. 21) goes from the 90.9% for the case with the least number of particles to the 20.2% for the case with the highest number of particles, it can be concluded that the number of particles exerts a direct influence on the SPH solver and has a minor influence on the Project Chrono runtime.

The second set of simulations is focused on the collision detection performance analysis, where different geometries are used to define the breakwater and so the number of collision points or faces is varied while keeping the SPH resolution constant. Table 8 shows the setups carried out for this second set, where the number of blocks is equals to 24 and the *dp*=*L*/15 for all cases.

Fig. 22 shows the results from the second set of simulations (in Table 8), where the runtime of the SPH model (solid red line), the runtime of the multiphysics library (solid blue line), the total runtime of the simulation (solid black line), and the percentage that the collision detection takes (dashed blue line). The runtime of Project Chrono to solve the collision detection, and so time consumed by the multiphysics library, increases according to the number of faces that compose the geometry of the simulated blocks. On the other hand, the runtime of DualSPHysics is not affected at all by this approach because the number of particles is the component that has a greater impact on the SPH runtime, and Project Chrono response does not affect the definition of the Δt_{SPH}. Therefore, the number of faces that a geometry possesses plays an important role in terms of performance when it is handled by the multiphysics library to evaluate collision detection. Particularly, it can be noted that when the number of faces doubles, so does the

runtime indicating a linear face-runtime relationship that holds within the investigated range.

8. Conclusions

With the presented coupling formulation, the SPH-based DualSPHysics solver takes a big step towards its general usability and versatility, widening the relevance of the code to a great extent. It allows merging the general descriptions of fluids and complex mechanisms within the same framework, presenting a much wider range of applicability without having to implement new pieces of code. The Lagrangian nature of the overall structure that derives from this coupling places the proposed system at the edge since it exploits the advantages of tracking fluid free-surfaces, and the high stability to impulse loads and sudden changes in position of the computational nodes. The validation benchmarks show that the model can be used to reproduce some of the relevant features that characterise real mechanical systems, such as impacts, time-dependent mechanical constraints, and multi-body system dynamics, which can interact with fluid.

Four benchmarks have been proposed for the coupling validation procedure. Apart from the stand-alone tests, the coupled model has proved capable of reproducing solid interactions when fluid forces are predominant in the simulations with sufficient accuracy, even when tens of rigid bodies are involved. Simple mechanical functions, such as linear springs and hinges, have been validated against experimental data demonstrating that the adopted turbulence model can capture the expected energy dissipation that fluids can exert on to mildly moving objects; the geometry buoyancy is correctly estimated by means of the proposed setup, overcoming previous issues with boundary geometry consistency. Furthermore, the computational cost has seen a drastic reduction from the latest applications of the model to solve similar problems [54], still providing comparable accuracy; this improvement was mainly achieved by combining the coupling with the Project Chrono library with the new mDBC technique, which involves that lower resolution is needed to obtain equivalent levels of precision. The SPH solver supposes the highest computational cost due to the high number of particles that it usually needs to reach an adequate resolution for the problem. However, the computation time of Project Chrono may be predominant in special cases where the SPH resolution is low, and the number of collision faces is very high.

The SPHERIC has formulated some of the main goals of present and future research in an attempt to improve the applicability of the SPH technique to a variety of physical and engineering problems. The proposed work directly contributes to the SPH Grand Challenge (GC#4 - Coupling to other methods) [6] by proposing a novel, general approach based on force-exchange interface algorithm that can be extended beyond the scope of the presented work (open-source release), and, in principle, to couple any other libraries within Lagrangian-based frameworks. Additionally, the authors point out that the special effort required to develop this code was pursued with the needs of end-users in mind, by providing practical information on how to use the code. This tool contributes to the challenge of applicability in the industry, (GC#5 - Applicability to industry) [6] thanks to the combination of different models in a transparent way for the user, allowing increasingly complex simulations to be carried out in a simple way. The use of coupling techniques, such as the one proposed here, allows reducing the resolutions used in each model to maintain reasonable execution times for simulations of real cases, and this work demonstrates how reasonable simulation time (using accessible hardware support) is achieved by exploiting the features made available by the latest advances in the SPH formulations. Specifically, the companion package released alongside this paper contains several templates regarding the use of DualSPHysics for the simulation of devices for renewable energy devices; examples are underway with validations of power take-off systems for wave energy converters, and other power capturing devices for which the coupled dynamics becomes essential to the evaluation of their efficiency and survivability.

The coupling strategy followed in this work facilitates the development tasks for including other features or modules available in Project Chrono, which will increase the capabilities of the tool. This advantage is mainly due to the use of a general-purpose communication interface (DSPHChronoLib) to exchange data between DualSPHysics and Project Chrono, which keeps a *low-coupling* strategy between both models, which means that new changes or features implemented on any side would not affect the operation of the other model. For example, as future work, this coupling will be extended to use other features included in Project Chrono such as non-linear Finite Element Analysis (FEA) module to solve flexible multibody systems, and hence, to solve fluid-structure interactions within an SPH-FEA coupled model.

Declaration of competing interest

The authors declare that they have no known competing financial interests or personal relationships that could have appeared to influence the work reported in this paper.

Data availability

I have shared the data/code at the Attach File step.

Acknowledgement

Funding for open access charge: Universidade de Vigo/CISUG, Spain. This work was supported by the project SURVIWEC PID2020-113245RB-I00 financed by MCIN/AEI/10.13039/501100011033 and by the project ED431C 2021/44 "*Programa de Consolidación e Estructuración de Unidades de Investigación Competitivas" financed by Xunta de Galicia, Consellería de Cultura, Educación e Universidade*. This study forms part of the Marine Science programme (ThinkInAzul) supported by *Ministerio de Ciencia e Innovación and Xunta de Galicia* with funding from European Union NextGenerationEU (PRTR-C17.I1) and European Maritime and Fisheries Fund.

I. Martínez-Estévez acknowledges funding from *Xunta de Galicia* under "*Programa de axudas á etapa predoutoral da Consellería de Cultura, Educación e Universidades da Xunta de Galicia*" (ED481A-2021/337). O. García-Feal was funded by Spanish "Ministerio de Universidades" and European Union – NextGenerationEU through the "Margarita Salas" post-doctoral grant. The authors wish to acknowledge the support provided by the Project Chrono developers: Prof. Dan Negrut and Dr. Radu Serban (University of Wisconsin–Madison, US), and Prof. Alessandro Tasora (University of Parma, Italy). The list of authors of the DualSPHysics code is published on its website (https://dual.sphysics.org/developers/) and the Copyright can be seen in the license file of the code (https://github.com/DualSPHysics/DualSPHysics/blob/master/LICENSE). The list of authors of the Project Chrono code is shown on its website (https://projectchrono.org/about/) and its Copyright can be seen in the license file of the code (https://github.com/projectchrono/chrono/blob/main/LICENSE). DSPHChronoLib code has been developed by the following authors: I. Martínez-Estévez, J.M. Domínguez, R. Canelas, B. Tagliafierro, O. García-Feal, A.J.C. Crespo and M. Gómez-Gesteira; and its Copyright is available in *DualSPHysics-Chrono/src_extra/DSPH-Chrono-Lib/LICENSE*.

DualSPHysics and DSPHChronoLib are released under the GNU Lesser General Public License (LGPL). Project Chrono is released under BSD-3-Clause License.

References

[1] A. Amicarelli, S. Manenti, R. Albano, G. Agate, M. Paggi, L. Longoni, D. Mirauda, L. Ziane, G. Viccione, S. Todeschini, A. Sole, L.M. Baldini, D. Brambilla, M. Papini, M.C. Khellaf, B. Tagliafierro, L. Sarno, G. Pirovano, Comput. Phys. Commun. 250 (2020) 107157, https://doi.org/10.1016/j.cpc.2020.107157.

[2] H. Gotoh, A. Khayyer, Coast. Eng. J. 60 (2018) 79–103, https://doi.org/10.1080/21664250.2018.1436243.

[3] D. Violeau, B.D. Rogers, J. Hydraul. Res. 54 (2016) 1–26, https://doi.org/10.1080/00221686.2015.1119209.

[4] A. Khayyer, B.D. Rogers, A.-M. Zhang, Appl. Ocean Res. 118 (2022) 103028, https://doi.org/10.1016/j.apor.2021.103028.

[5] S. Manenti, D. Wang, J.M. Domínguez, S. Li, A. Amicarelli, R. Albano, Water 11 (2019) 1875, https://doi.org/10.3390/w11091875.

[6] R. Vacondio, C. Altomare, M. De Leffe, X. Hu, D. Le Touzé, S. Lind, J.-C. Marongiu, S. Marrone, B.D. Rogers, A. Souto-Iglesias, Comput. Part. Mech. 8 (2021) 575–588, https://doi.org/10.1007/s40571-020-00354-1.

[7] Y. You, A. Khayyer, X. Zheng, H. Gotoh, Q. Ma, Appl. Ocean Res. 110 (2021) 102508, https://doi.org/10.1016/j.apor.2020.102508.

[8] M. Antuono, P.N. Sun, S. Marrone, A. Colagrossi, Comput. Fluids 216 (2021) 104806, https://doi.org/10.1016/j.compfluid.2020.104806.

[9] J.R.C. King, S.J. Lind, A.M.A. Nasar, J. Comput. Phys. 415 (2020) 109549, https://doi.org/10.1016/j.jcp.2020.109549.

[10] A.M.A. Nasar, G. Fourtakas, S.J. Lind, J.R.C. King, B.D. Rogers, P.K. Stansby, J. Comput. Phys. 444 (2021) 110563, https://doi.org/10.1016/j.jcp.2021.110563.

[11] P. Rastelli, R. Vacondio, J.C. Marongiu, G. Fourtakas, B.D. Rogers, Comput. Methods Appl. Mech. Eng. 393 (2022) 114716, https://doi.org/10.1016/j.cma.2022.114716.

[12] S.-H. Park, Y.B. Jo, Y. Ahn, H.Y. Choi, T.S. Choi, S.-S. Park, H.S. Yoo, J.W. Kim, E.S. Kim, Front. Energy Res. 8 (2020), https://doi.org/10.3389/fenrg.2020.00086.

[13] D. Valdez-Balderas, J.M. Domínguez, B.D. Rogers, A.J.C. Crespo, J. Parallel Distrib. Comput. 73 (2013) 1483–1493, https://doi.org/10.1016/j.jpdc.2012.07.010.

[14] L. Yang, M. Rakhsha, W. Hu, D. Negrut, J. Comput. Phys. 458 (2022) 111079, https://doi.org/10.1016/j.jcp.2022.111079.

[15] A. Mokos, B.D. Rogers, P.K. Stansby, J.M. Domínguez, Comput. Phys. Commun. 196 (2015) 304–316, https://doi.org/10.1016/j.cpc.2015.06.020.

[16] G. Fourtakas, B.D. Rogers, Adv. Water Resour. 92 (2016) 186–199, https://doi.org/10.1016/j.advwatres.2016.04.009.

[17] J.M. Domínguez, G. Fourtakas, C. Altomare, R.B. Canelas, A. Tafuni, O. García-Feal, I. Martínez-Estévez, A. Mokos, R. Vacondio, A.J.C. Crespo, B.D. Rogers, P.K. Stansby, M. Gómez-Gesteira, Comput. Part. Mech. 9 (2022) 867–895, https://doi.org/10.1007/s40571-021-00404-2.

[18] O. García-Feal, A.J.C. Crespo, M. Gómez-Gesteira, Comput. Part. Mech. 9 (2022) 897–910, https://doi.org/10.1007/s40571-020-00386-7.

[19] M. Gomez-Gesteira, B.D. Rogers, A.J.C. Crespo, R.A. Dalrymple, M. Narayanaswamy, J.M. Dominguez, Comput. Geosci. 48 (2012) 289–299, https://doi.org/10.1016/j.cageo.2012.02.029.

[20] M. Gomez-Gesteira, A.J.C. Crespo, B.D. Rogers, R.A. Dalrymple, J.M. Dominguez, A. Barreiro, Comput. Geosci. 48 (2012) 300–307, https://doi.org/10.1016/j.cageo.2012.02.028.

[21] J.M. Domínguez, A.J.C. Crespo, M. Gómez-Gesteira, J.C. Marongiu, Int. J. Numer. Methods Fluids 67 (2011) 2026–2042, https://doi.org/10.1002/fld.2481.

[22] A.J.C. Crespo, J.M. Domínguez, B.D. Rogers, M. Gómez-Gesteira, S. Longshaw, R. Canelas, R. Vacondio, A. Barreiro, O. García-Feal, Comput. Phys. Commun. 187 (2015) 204–216, https://doi.org/10.1016/j.cpc.2014.10.004.

[23] J.M. Domínguez, A.J.C. Crespo, M. Gómez-Gesteira, Comput. Phys. Commun. 184 (2013) 617–627, https://doi.org/10.1016/j.cpc.2012.10.015.

[24] J. O'Connor, J.M. Domínguez, B.D. Rogers, S.J. Lind, P.K. Stansby, Comput. Phys. Commun. 273 (2022) 108263, https://doi.org/10.1016/j.cpc.2021.108263.

[25] C. Altomare, A. Tafuni, J.M. Domínguez, A.J.C. Crespo, X. Gironella, J. Sospedra, J. Mar. Sci. Eng. 8 (2020) 826, https://doi.org/10.3390/jmse8100826.

[26] J. González-Cao, C. Altomare, A.J.C. Crespo, J.M. Domínguez, M. Gómez-Gesteira, D. Kisacik, Comput. Fluids 179 (2019) 604–612, https://doi.org/10.1016/j.compfluid.2018.11.021.

[27] T. Suzuki, O. García-Feal, J.M. Domínguez, C. Altomare, Comput. Part. Mech. 9 (2022) 1003–1015, https://doi.org/10.1007/s40571-022-00468-8.

[28] S. Wang, J. González-Cao, H. Islam, M. Gómez-Gesteira, C. Guedes Soares, Ocean Eng. 256 (2022) 111386, https://doi.org/10.1016/j.oceaneng.2022.111386.

[29] C. Altomare, J.M. Domínguez, G. Fourtakas, Comput. Part. Mech. 9 (2022) 863–866, https://doi.org/10.1007/s40571-022-00499-1.

[30] P.A. Cundall, O.D.L. Strack, Geotechnique 29 (1979) 47–65, https://doi.org/10.1680/geot.1979.29.1.47.

[31] F. Fleissner, T. Gaugele, P. Eberhard, Multibody Syst. Dyn. 18 (2007) 81, https://doi.org/10.1007/s11044-007-9066-2.

[32] W. Hu, M. Rakhsha, L. Yang, K. Kamrin, D. Negrut, Comput. Methods Appl. Mech. Eng. 385 (2021) 114022, https://doi.org/10.1016/j.cma.2021.114022.

[33] A. Tasora, M. Anitescu, J. Comput. Nonlinear Dyn. 5 (2010), https://doi.org/10.1115/1.4001371.

[34] J. O'Connor, B.D. Rogers, J. Fluids Struct. 104 (2021) 103312, https://doi.org/10.1016/j.jfluidstructs.2021.103312.

[35] A. Khayyer, Y. Shimizu, H. Gotoh, K. Nagashima, Appl. Math. Model. 94 (2021) 242–271, https://doi.org/10.1016/j.apm.2021.01.011.

[36] D.S. Morikawa, M. Asai, Comput. Methods Appl. Mech. Eng. 381 (2021), https://doi.org/10.1016/j.cma.2021.113832.

[37] Y.B. Jo, S.-H. Park, H.S. Yoo, E.S. Kim, Int. J. Multiph. Flow 153 (2022) 104125, https://doi.org/10.1016/j.ijmultiphaseflow.2022.104125.

[38] S. Dunatunga, K. Kamrin, J. Fluid Mech. 779 (2015) 483–513, https://doi.org/10.1017/jfm.2015.383.

[39] M. Rakhsha, C.E. Kees, D. Negrut, Fluids 6 (2021) 460, https://doi.org/10.3390/fluids6120460.

[40] M. Rakhsha, L. Yang, W. Hu, D. Negrut, Multibody Syst. Dyn. 53 (2021) 29–57, https://doi.org/10.1007/s11044-021-09784-y.

[41] D. Markauskas, H. Kruggel-Emden, R. Sivanesapillai, H. Steeb, Powder Technol. 305 (2017) 78–88, https://doi.org/10.1016/j.powtec.2016.09.052.

[42] H. Gotoh, A. Khayyer, Y. Shimizu, Appl. Ocean Res. 115 (2021) 102822, https://doi.org/10.1016/j.apor.2021.102822.

[43] L. Zou, J.Z. Sun, Z. Sun, Z.B. Yu, H.B. Zhao, Eur. J. Mech. B, Fluids 92 (2022) 49–64, https://doi.org/10.1016/j.euromechflu.2021.09.006.

[44] D. Markauskas, H. Kruggel-Emden, Adv. Powder Technol. 30 (2019) 2997–3009, https://doi.org/10.1016/j.apt.2019.09.007.

[45] R.B. Canelas, A.J.C. Crespo, J.M. Domínguez, R.M.L. Ferreira, M. Gómez-Gesteira, Comput. Phys. Commun. 202 (2016) 131–140, https://doi.org/10.1016/j.cpc.2016.01.006.

[46] R.B. Canelas, J.M. Domínguez, A.J.C. Crespo, M. Gómez-Gesteira, R.M.L. Ferreira, J. Hydraul. Eng. 143 (2017) 06017012, https://doi.org/10.1061/(ASCE)HY.1943-7900.0001331.

[47] Y. He, A.E. Bayly, A. Hassanpour, F. Muller, K. Wu, D. Yang, Powder Technol. 338 (2018) 548–562, https://doi.org/10.1016/j.powtec.2018.07.043.

[48] M. Asai, Y. Li, B. Chandra, S. Takase, Comput. Methods Appl. Mech. Eng. 377 (2021) 113681, https://doi.org/10.1016/j.cma.2021.113681.

[49] K. Wu, D. Yang, N. Wright, Comput. Struct. 177 (2016) 141–161, https://doi.org/10.1016/j.compstruc.2016.08.012.

[50] Y. Sun, G. Xi, Z. Sun, J. Fluids Struct. 90 (2019) 379–395, https://doi.org/10.1016/j.jfluidstructs.2019.07.005.

[51] S. Capasso, B. Tagliafierro, I. Martínez-Estévez, J.M. Domínguez, A.J.C. Crespo, G. Viccione, Comput. Part. Mech. 9 (2022) 969–985, https://doi.org/10.1007/s40571-021-00451-9.

[52] A. Tasora, R. Serban, H. Mazhar, A. Pazouki, D. Melanz, J. Fleischmann, M. Taylor, H. Sugiyama, D. Negrut, in: T. Kozubek, R. Blaheta, J. Šístek, M. Rozložník, M. Čermák (Eds.), High Performance Computing in Science and Engineering, Springer International Publishing, Cham, 2016, pp. 19–49, https://doi.org/10.1007/978-3-319-40361-8_2.

[53] Z. Wei, B.L. Edge, R.A. Dalrymple, A. Hérault, Ocean Eng. 183 (2019) 332–349, https://doi.org/10.1016/j.oceaneng.2019.04.029.

[54] R.B. Canelas, M. Brito, O.G. Feal, J.M. Domínguez, A.J.C. Crespo, Appl. Ocean Res. 76 (2018) 88–97, https://doi.org/10.1016/j.apor.2018.04.015.

[55] N. Quartier, P. Ropero-Giralda, J.M. Domínguez, V. Stratigaki, P. Troch, Water 13 (2021) 384, https://doi.org/10.3390/w13030384.

[56] P. Ropero-Giralda, A.J.C. Crespo, R.G. Coe, B. Tagliafierro, J.M. Domínguez, G. Bacelli, M. Gómez-Gesteira, Energies 14 (2021) 760, https://doi.org/10.3390/en14030760.

[57] P. Ropero-Giralda, A.J.C. Crespo, B. Tagliafierro, C. Altomare, J.M. Domínguez, M. Gómez-Gesteira, G. Viccione, Renew. Energy 162 (2020) 1763–1776, https://doi.org/10.1016/j.renene.2020.10.012.

[58] B. Tagliafierro, I. Martínez-Estévez, J.M. Domínguez, A.J.C. Crespo, M. Göteman, J. Engström, M. Gómez-Gesteira, Appl. Energy 311 (2022) 118629, https://doi.org/10.1016/j.apenergy.2022.118629.

[59] B. Tagliafierro, M. Karimirad, I. Martínez-Estévez, J.M. Domínguez, G. Viccione, A.J.C. Crespo, Energies 15 (2022) 3993, https://doi.org/10.3390/en15113993.

[60] J.M. Domínguez, A.J.C. Crespo, M. Hall, C. Altomare, M. Wu, V. Stratigaki, P. Troch, L. Cappietti, M. Gómez-Gesteira, Coast. Eng. 153 (2019) 103560, https://doi.org/10.1016/j.coastaleng.2019.103560.

[61] H. Wendland, Adv. Comput. Math. 4 (1995) 389–396, https://doi.org/10.1007/BF02123482.

[62] E.Y.M. Lo, S. Shao, Appl. Ocean Res. 24 (2002) 275–286, https://doi.org/10.1016/S0141-1187(03)00002-6.

[63] R.A. Dalrymple, B.D. Rogers, Coast. Eng. 53 (2006) 141–147, https://doi.org/10.1016/j.coastaleng.2005.10.004.

[64] J.J. Monaghan, Annu. Rev. Astron. Astrophys. 30 (1992) 543–574, https://doi.org/10.1146/annurev.aa.30.090192.002551.

[65] G. Fourtakas, J.M. Dominguez, R. Vacondio, B.D. Rogers, Comput. Fluids 190 (2019) 346–361, https://doi.org/10.1016/j.compfluid.2019.06.009.

[66] B.J. Leimkuhler, S. Reich, R.D. Skeel, in: J.P. Mesirov, K. Schulten, D.W. Sumners (Eds.), Mathematical Approaches to Biomolecular Structure and Dynamics, Springer, New York, NY, 1996, pp. 161–185, https://doi.org/10.1007/978-1-4612-4066-2_10.

[67] J.J. Monaghan, R.a.F. Cas, A.M. Kos, M. Hallworth, J. Fluid Mech. 379 (1999) 39–69, https://doi.org/10.1017/S0022112098003280.

[68] A.J. Crespo, M. Gómez-Gesteira, R.A. Dalrymple, Comput. Mater. Continua 5 (2007) 173–184.

[69] C. Altomare, J.M. Domínguez, A.J.C. Crespo, J. González-Cao, T. Suzuki, M. Gómez-Gesteira, P. Troch, Coast. Eng. 127 (2017) 37–54, https://doi.org/10.1016/j.coastaleng.2017.06.004.
[70] F. Zhang, A. Crespo, C. Altomare, J. Domínguez, A. Marzeddu, S. Shang, M. Gómez-Gesteira, J. Hydrodyn. 30 (2018) 95–105, https://doi.org/10.1007/s42241-018-0010-0.
[71] A. English, J.M. Domínguez, R. Vacondio, A.J.C. Crespo, P.K. Stansby, S.J. Lind, L. Chiapponi, M. Gómez-Gesteira, Comput. Part. Mech. 9 (2022) 911–925, https://doi.org/10.1007/s40571-021-00403-3.
[72] S. Marrone, M. Antuono, A. Colagrossi, G. Colicchio, D. Le Touzé, G. Graziani, Comput. Methods Appl. Mech. Eng. 200 (2011) 1526–1542, https://doi.org/10.1016/j.cma.2010.12.016.
[73] J.J. Monaghan, A. Kos, N. Issa, J. Waterw. Port Coast. Ocean Eng. 129 (2003) 250–259, https://doi.org/10.1061/(ASCE)0733-950X(2003)129:6(250).
[74] M. Machado, P. Moreira, P. Flores, H.M. Lankarani, Mech. Mach. Theory 53 (2012) 99–121, https://doi.org/10.1016/j.mechmachtheory.2012.02.010.
[75] J. Fleischmann, R. Serban, D. Negrut, P. Jayakumar, J. Comput. Nonlinear Dyn. 11 (2015), https://doi.org/10.1115/1.4031197.
[76] M. Anitescu, A. Tasora, Comput. Optim. Appl. 47 (2010) 207–235, https://doi.org/10.1007/s10589-008-9223-4.
[77] A. Pazouki, M. Kwarta, K. Williams, W. Likos, R. Serban, P. Jayakumar, D. Negrut, Phys. Rev. E 96 (2017) 042905, https://doi.org/10.1103/PhysRevE.96.042905.
[78] T. Hagemeier, D. Thévenin, T. Richter, https://doi.org/10.48550/arXiv.2009.02250, 2020.
[79] K.C. Ng, A. Alexiadis, H. Chen, T.W.H. Sheu, J. Fluids Struct. 106 (2021) 103369, https://doi.org/10.1016/j.jfluidstructs.2021.103369.
[80] S. Zhang, S. Kuwabara, T. Suzuki, Y. Kawano, K. Morita, K. Fukuda, J. Comput. Phys. 228 (2009) 2552–2565, https://doi.org/10.1016/j.jcp.2008.12.005.
[81] M. Arnold, M. Kretschmer, J. Koch, P.W. Cheng, F. Biskup, J. Ocean Wind Energy 2 (2015), https://doi.org/10.17736/jowe.2015.mkr02.

4.2 Coupling an SPH-based solver with an FEA structural solver to simulate free surface flows interacting with flexible structures

The second article is entitled "**Coupling an SPH-based solver with an FEA structural solver to simulate free surface flows interacting with flexible structures**" by **Martínez-Estévez, I.**, Tagliafierro, B., El Rahi, J., Domínguez, J. M., Crespo, A. J. C., Troch, P., & Gómez-Gesteira, M. Published in the journal *Computer Methods in Applied Mechanics and Engineering* in 2023.

Table 2. Information of the journal Computer Methods in Applied Mechanics and Engineering from 2022 JCR.

	Journal information
Journal	*Computer Methods in Applied Mechanics and Engineering*
Online ISSN	*1879-2138*
Country	*Netherlands*
Editorial	*Elsevier*
Impact factor	*7,2*
Quartile	*Q1 (Engineering, Multidisciplinary)*

Available online at www.sciencedirect.com
ScienceDirect
Comput. Methods Appl. Mech. Engrg. 410 (2023) 115989
Computer methods in applied mechanics and engineering
www.elsevier.com/locate/cma

Coupling an SPH-based solver with an FEA structural solver to simulate free surface flows interacting with flexible structures

I. Martínez-Estévez[a,*], B. Tagliafierro[b], J. El Rahi[c], J.M. Domínguez[a], A.J.C. Crespo[a], P. Troch[c], M. Gómez-Gesteira[a]

[a] *Environmental Physics Laboratory, CIM-UVIGO, Universidade de Vigo, Spain*
[b] *Laboratori d'Enginyeria Marítima, Universitat Politècnica de Catalunya - BarcelonaTech (UPC) Barcelona, Spain*
[c] *Department of Civil Engineering, Ghent University, Belgium*

Received 9 December 2022; received in revised form 23 February 2023; accepted 3 March 2023
Available online 27 March 2023

Abstract

This work proposes a two-way coupling between a Smoothed Particle Hydrodynamics (SPH) model-based named DualSPHysics and a Finite Element Analysis (FEA) method to solve fluid–structure interaction (FSI). Aiming at having a computationally efficient solution via spatial adjustable resolutions for the two phases, the SPH-FEA coupling herein presented implements the Euler–Bernoulli beam model, based on a simplified model that incorporates axial and flexural deformations, to introduce a solid solver in the DualSPHysics framework. This approach is particularly functional and very precise for slender beam elements undergoing large displacements, and large deformations can also be experienced by the structural elements due to the non-linear FEA implementation via a co-rotational formulation. In this two-way coupling, the structure is discretised in the SPH domain using boundary particles on which the forces exerted by fluid phases are computed. Such forces are passed over to the FEA structural solver that updates the beam shape and, finally, the particle positions are subsequently reshuffled to represent the deformed shape at each time step. The SPH-FEA coupling is validated against four reference cases, which prove the model to be as accurate as other approaches presented in literature.

Keywords: FSI; SPH; FEA; Euler–Bernoulli; DualSPHysics; Project Chrono

1. Introduction

Multiphysics simulations are now becoming mainstream for industry in many application fields, one of which is fluid–structure interaction (FSI) [1]. According to the investigated effect, different classes of problems can be identified under the FSI, in which the physics may strongly differ and whose coupled effects are not negligible. FSI refers to aeroelastic or hydroelastic problems characterised by strong interaction between fluid phases and flexible structures that combined lead to deformations that, in turn, dynamically influence the response of the other medium [2,3]. Other common cases in which FSI becomes relevant are either when structures are extremely *compliant* and so, they closely follow the fluid dynamics and experience large deformations. Another common case is when

* Corresponding author.
E-mail address: ivan.martinez.estevez@uvigo.es (I. Martínez-Estévez).

https://doi.org/10.1016/j.cma.2023.115989

free-surface flows impact deformable structures with sudden changes in pressure, often resulting in portions of fluid being scattered throughout. Relevant examples here come from the simulation of biological systems [4] and impulsive loads on structures [5]. Whatever the instance, the evolution of the fluid and the deformation of the structure should be taken into account seamlessly to preserve the veracity of the numerical prediction.

Traditionally, FSI problems were addressed through mesh-based methods, often considering a partitioned approach and thus, using appropriate Finite Element Methods (FEM) to treat the fluid and the structure separately [6]. However, the fluid mesh should follow the movement of the solid, making the use of remeshing tools essential. Computational costs and convergence issues have led to consider meshless approaches for the fluid phase. Lagrangian particle methods appear to be particularly advantageous for investigating FSI problems due to their meshless nature, which easily allows large deformations and tracking interfaces between the different phases with precision [7]. As the Smoothed Particle Hydrodynamics (SPH) technique is relatively new, SPH-FEM coupling is a recent approach to model FSI [8]: this hybrid method exploits the strengths of both models. Some applications of this methodology are presented in Fourey et al. [9]. A multi-resolution SPH-FEM method for FSI was presented by Chen et al. [10], where the multi-resolution technology can be applied for discretising the fluid and the structure.

Fully Lagrangian approaches have been used for the FSI applications, where both fluids and solids are modelled within the same SPH framework, although employing different techniques. Sun et al. [11] proposed a coupling between a multiphase solver δ-SPH for fluid and a total Lagrangian SPH for the solid solver, which was improved and described in Sun et al. [12]. In addition, a particular mechanical relationship dictating the motion of the rigid bodies such that they mimic flexible elements was described in Capasso et al. [13]. A GPU implementation was presented in O'Connor and Rogers [14], proposing a unified SPH framework for FSI applications. Ren et al. [15] described and validated a fully SPH-based solver to study complex fluid motion with high non-linearity against flexible structures. Other approaches coupled SPH with Discrete Element Method (DEM) such as the one presented in Nasar et al. [16].

One example is the coupled Enhanced Incompressible SPH (ISPH) fluid solver with an SPH-based solid solver presented in Khayyer et al. [17], which provides full validation of the SPH-based solid solver. Similarly, Morikawa and Asai [18] presented a two-way coupling between an Explicit Incompressible SPH (EISPH) fluid solver and an SPH solid solver to deal with FSI problems.

As suggested by the available literature, the use of the SPH method to deal with FSI problems has been growing large and progressing at a very fast pace (see [7]). However, it is well known that particle-based methods, at least when considered in their primordial implementations [19] with a traditional SPH gradient formulation, have to deal with high-frequency non-physical noise pressure. The SPH methods that are influenced by this problem are the so-called weakly compressible SPH (WCSPH), in which an equation of state is solved to obtain the pressure, usually with a stiff relationship that bounds pressure and density fields [20]. A great deal of research has been carried out to face this issue, and the very first algorithm is known as artificial viscosity [21]. One of the most widely accepted pressure enhancers defines a numerical artefact to smooth the density field and it was presented in Antuono et al. [22], lately extended further by Khayyer et al. [23]. As a matter of fact, small particle oscillations do not jeopardise the overall quality of the numerical method as a whole, but it can nonetheless be an issue when an SPH-based solver is embedded in so-called weak coupling schemes with other solvers: this is relevant to FSI applications. Meringolo et al. [24] investigated the limitations of the WCSPH method and provided a filter to mitigate the acoustic noise. On the other hand, other approaches based on SPH, like the ISPH aforementioned, which base the solution of the pressure field on a projection method [25], are inherently devoid of this problem since fluid incompressibility is enforced and guaranteed by solving a Poisson's equation although it presents other drawbacks [26].

The open-source DualSPHysics [27] code is the SPH-based method used in the present work. This code can be freely downloaded from the website www.dual.sphysics.org. It was developed to simulate free-surface flows and their interaction with fixed and floating structures within an international collaborative work between several universities and research centres. DualSPHysics is a highly parallelised implementation of SPH that allows to exploit the capabilities of both multi-core central processing units (CPUs) and graphics processing units (GPUs) [28]. On the other hand, Project Chrono [29] is a multiphysics simulation engine that can be compiled as a library to be coupled as a third-party application, which handles flexible structures and allows solid–solid body interactions with frictional contacts in very large multibody systems with mechanical constraints, among other multiple functionalities. A first coupling between DualSPHysics and Project Chrono was presented in Canelas et al. [30], where a complete system of mechanical constraints was validated by comparing numerical and experimental results for an oscillating

wave surge converter device. Recently, Martínez-Estévez et al. [31] presented an extension of the first coupling DualSPHysics-Chrono, including new features to deal with solid–solid interaction, where the coupling strategy using a general-purpose communication interface (the so-called DSPHChronoLib) to handle the exchange of data between both solvers is described. Within the field of renewable energy, many successful applications have been presented over the last years with the coupled code [32,33].

A new structured version of the DualSPHysics code coupled to the multiphysics library Project Chrono is presented here. Project Chrono implements a non-linear Finite Element Analysis (FEA) method that can deal with flexible structures. As mentioned before, it also supports collision detection algorithms between rigid and flexible bodies and allows simulating multibody dynamics where mechanical constraints can be applied on the bodies. Therefore, in this work, a two-way coupling SPH-FEA is proposed in order to solve FSI, in which the governing equations to solve fluid are handled by the SPH-based model, whereas the FEA solves the structural dynamics. This novel approach comprises several advantages in comparison with other methods: (i) co-operative framework; (ii) resolution independence; (iii) performance and resource optimisation; and (iv) extended capabilities. Considering the first one, the novel methodology presented in this work preserves the accuracy and robustness of the two solvers employed in a co-operative framework. This is, in fact, one of the main advantages of this coupling since the pros of using a meshless SPH method to solve the fluid (adaptable and accurate) are aggregated to those of using a mesh-based mechanical solver (light and precise). Secondly, this methodology allows the possibility of using distinct spatial resolutions for each model, providing a key distinctive feature: *uncoupled resolutions*. The basis of this concept is that even though both models are synchronised and communicate to each other during the simulation, they solve their own systems separately in different environments and the resolutions employed are independent. Considering the performance, the equations to solve the structure using the FEA module of Project Chrono are less expensive in terms of computational cost than approaches using fully Lagrangian solvers. Finally, the multiphysics library Project Chrono provides a wide range of features that promotes the possibility of including more functionalities and so, to extend the capabilities of the coupled model. One example is the use of frictional contact surfaces in FEA meshes in very large multibody systems, where mechanical constraints can be also defined to restrict the movement of flexible elements.

For this first implementation, the FEA solver is coupled by linking the structural element that describes a linear elastic beam known as the Euler–Bernoulli beam model and restricted to 2D. This implies that the method as such cannot deal with stocky elements due to model limitations or experience out-of-plane deformations as the third dimension is not taken into account. The mentioned model is very convenient to test and validate the general structure of the coupling, including its accuracy, robustness and flexibility, as it is computationally inexpensive, and a range of closed-form solutions can be found for academic cases. Nevertheless, it is expected that the co-simulating environment helps to improve the applicability of the proposed SPH framework to industrial applications to a much greater extent.

The contents of this paper are organised as follows: Section 2 shows the main formulation included in the SPH model; Section 3 presents the FEA method integrated in the multiphysics library; Section 4 describes the coupling procedure between both models; Section 5 shows several benchmarks carried out in order to validate the coupling; and finally, Section 6 draws the conclusions of this work.

2. Smoothed particle hydrodynamics solver

This section introduces the main formulation implemented in the DualSPHysics [27] SPH-based numerical model, the novel approach for the boundary conditions and the time step integrator used in this code.

2.1. SPH principle

SPH is a meshless method that discretises a continuum on a set of particles, in which the equations of fluid dynamics are solved. The physical quantities of each particle are obtained as an interpolation of the quantities of its neighbouring particles. The contribution of their neighbours is computed by using a weighting function or kernel (W), whose area of influence is defined by a smoothing length (h). Then, an integral approximation of any function $F(\boldsymbol{r})$ represents the SPH basis by following:

$$F(\boldsymbol{r}) = \int F(\boldsymbol{r}') W(\boldsymbol{r} - \boldsymbol{r}', h)\, d\boldsymbol{r}' \tag{1}$$

being $\boldsymbol{r}$ the position of the point where the function is computed and $\boldsymbol{r}'$ is the position at each time step. Thus, the function F is approximated, in discrete form, by the interpolation of the contribution of all particles belonging to the compact support of the kernel function, following:

$$F\left(\boldsymbol{r}_a\right) \approx \sum_b F\left(\boldsymbol{r}_b\right) \frac{m_b}{\rho_b} W\left(\boldsymbol{r}_a - \boldsymbol{r}_b, h\right) \tag{2}$$

where the subscripts a and b refer to the target particle and the neighbouring particle, respectively, m is the mass and ρ is the density. On the other hand, the weighting function $W(\boldsymbol{r}, h)$, chosen in this work, is the Quintic Wendland kernel [34] that is defined as:

$$W\left(q\right) = \alpha_D \left(1 - \frac{q}{2}\right)^4 \left(2q + 1\right), 0 \leq q \leq 2 \tag{3}$$

being $q = r_{ab}/h$ the non-dimensional distance between particles, r_{ab} is the distance between particles a and b, and α_D is set to $10/7\pi h^2$ in two-dimensional space (2-D).

Note that in DualSPHysics, particles are initially created at the same initial spacing (dp). This spacing is used to define the smoothing length of the simulations. In this work, the smoothing length is $h = 1.2dp$, so that the kernel interaction $2h$ distance is $2.4dp$.

2.2. Governing equations

The discrete form of the Navier–Stokes (N–S) equations is used to govern the motion of the particles in a fluid dynamics system. The momentum equation in Lagrangian form can be written as:

$$\frac{d\boldsymbol{v}_a}{dt} = -\sum_b m_b \left(\frac{p_b + p_a}{\rho_b \rho_a}\right) \nabla_a W_{ab} + \boldsymbol{\Gamma}_a + \boldsymbol{g}, \tag{4}$$

$$\boldsymbol{\Gamma}_a = \sum_b m_b \frac{4\upsilon_0 \boldsymbol{r}_{ab} \cdot \nabla_a W_{ab}}{\left(\rho_a + \rho_b\right)\left(r_{ab}^2 + 0.01h^2\right)} \boldsymbol{v}_{ab} + \sum_b m_b \left(\frac{\tau_a^{ij} + \tau_b^{ij}}{\rho_b \rho_a}\right) \nabla^i W_{ab} \tag{5}$$

where t is the simulation time, $\boldsymbol{v}$ is the velocity, p is the pressure, $\boldsymbol{g}$ is the gravity acceleration and W_{ab} is the kernel function. The dissipation treatment ($\boldsymbol{\Gamma}_a$) is included to the momentum equation, which uses a laminar viscosity (first term) approximated by Lo and Shao [35], and a sub-particle scale model (SPS) (second term) described by Dalrymple and Rogers [36] in which a Favre averaging in a weakly compressible approach is used. The term υ_0 denotes the kinematic viscosity (set to 10^{-6} m^2/s) of the fluid and τ is the SPS stress tensor in Einstein notation in coordinate directions i and j according to:

$$\tau^{ij} = \overline{\upsilon^i \upsilon^j} - \overline{\upsilon^i}\ \overline{\upsilon^j} \tag{6}$$

modelled by an eddy viscosity closure as:

$$\frac{\tau^{ij}}{\rho} = 2\upsilon_{SPS}\left(S^{ij} - \frac{1}{3}S^{ii}\delta^{ij}\right) - \frac{2}{3}C_L \Delta^2 \delta^{ij} \left|S^{ij}\right|^2 \tag{7}$$

being $\upsilon_{SPS} = [C_{SM}\Delta]^2 |S^{ij}|^2$ the turbulent eddy viscosity, $C_{SM} = 0.12$ is the Smagorinsky's constant, $C_L = 0.0066$, Δ is the initial particle spacing and $|S^{ij}| = 1/2(2S^{ij}S^{ij})^{1/2}$, and S^{ij} is an element of the SPS strain tensor. Details of the implementation can be found in the reference paper Domínguez et al. [27].

On the other hand, the continuity equation in discrete form can be expressed following:

$$\frac{d\rho_a}{dt} = \sum_b m_b \boldsymbol{v}_{ab} \cdot \nabla_a W_{ab} + D, \tag{8}$$

$$D = 2\delta h c_s \sum_b \left(\rho_{ba}^T - \rho_{ab}^H\right) \frac{\boldsymbol{r}_{ab} \cdot \nabla_a W_{ab}}{r_{ab}^2} \frac{m_b}{\rho_b} \tag{9}$$

Here, the density diffusion term (D) is added to the continuity equation to reduce fluctuations in the density field, following the formulation presented in Fourtakas et al. [37], in which superscripts T and H represent the total and hydrostatic component of the density, respectively. The approach employed for the density diffusion treatment in this work is based on the formulation presented in Molteni and Colagrossi [38], but introducing a correction for

which the dynamic density is replaced with the total density (ρ^T). The term c_s is the numerical speed of sound and being δ the coefficient that controls this diffusion term (set to 0.1). Thus, for a weakly compressible fluid, the hydrostatic pressure difference of particles a and b is computed as:

$$p_{ab}^H = \rho_0 g z_{ab} \tag{10}$$

where z_{ab} is the vertical distance between particles a and b. Despite the use of a formulation based on the one described in Molteni and Colagrossi [38] carries some inconsistencies near the wall boundaries, the use of total density improves the behaviour of the pressure near the wall boundaries as it was demonstrated by Fourtakas et al. [37]. It should be noted that in Antuono et al. [39] a general approach is described, known as δ-SPH, which ensures the consistency of the density fluid at free surface, but it implies the computation of a normalised density gradient, whereas in Fourtakas et al. [37] it is not needed to perform that extra calculation and their approach works accurately for gravity-dominated flows with significantly lower computational cost.

DualSPHysics code includes a weakly compressible SPH formulation to solve the fluid pressure, and therefore, the pressure (p) is obtained from the particle density (ρ) by using the following equation of state:

$$p = \frac{c_s^2 \rho_0}{\gamma_p} \left[\left(\frac{\rho}{\rho_0} \right)^{\gamma_p} - 1 \right] \tag{11}$$

where $\rho_0 = 1000$ kg/m^3 is the reference density of the fluid and $\gamma_p = 7$ is the polytropic constant.

2.3. Boundary conditions

DualSPHysics implements the modified Dynamic Boundary Conditions (DBC) method (the so-called mDBC) proposed by English et al. [40], which is a modification of the original DBC method formerly presented in Crespo et al. [41] and originally conceived by [42]. The boundary particle arrangement within the mDBC implementation is done following the same strategy of the DBC (see [41]). However, a boundary interface is created some distance from the innermost layer of boundary particles, usually at $dp/2$ for simple shapes. An example of this novel method is depicted in Fig. 1, in which the boundary interface is represented with a black line. A ghost node (cross) is created in the fluid domain for each boundary particle (the so-called target boundary particle in Fig. 1), following the procedure proposed by Marrone et al. [43]. Normal vectors (arrows) are defined from the boundary particles to the boundary interface, pointing in the fluid domain direction. Then, the ghost node is projected according to its normal vector. When flat boundaries are modelled, the ghost node is mirrored across the boundary interface; otherwise for boundary particles placed in a corner, the ghost node is mirrored through this corner into the fluid domain.

Following this novel methodology, boundary particles obtain the fluid properties computed through a corrected SPH approximation at the ghost node, where the density field is evaluated considering the procedure proposed by Liu and Liu [44]. Then, the density of the ghost node (ρ_g) is obtained as:

$$\rho_g = \frac{\sum_j \rho_j W_{gj} \frac{m_j}{\rho_j}}{\sum_j W_{gj} \frac{m_j}{\rho_j}} \tag{12}$$

When the ghost node incorporates the new density value, the density of the boundary particle (ρ_b) is obtained by following:

$$\rho_b = \rho_g + \left(r_b - r_g \right) \cdot \left[\partial_x \rho_g ; \partial_y \rho_g ; \partial_z \rho_g \right] \tag{13}$$

where r_b is the position of the boundary particle, r_g is the position of the associated ghost node, and $[\partial_x \rho_g ; \partial_y \rho_g ; \partial_z \rho_g]$ is the gradient computed at the ghost node considering a first-order consistent SPH interpolation [44]. This approach offers a more accurate and smoother pressure field. More details can be found in [40].

In DualSPHysics, the basic equations of rigid body dynamics are implemented in order to simulate the motion of fluid-driven objects [45]. The motion of a fluid-driven object is derived by considering its interaction with fluid and its own weight. In this SPH code, the rigid bodies are considered as a fluid-driven object composed by boundary particles k. Thus, the net force exerted by the fluid is computed on each boundary particle of the object according

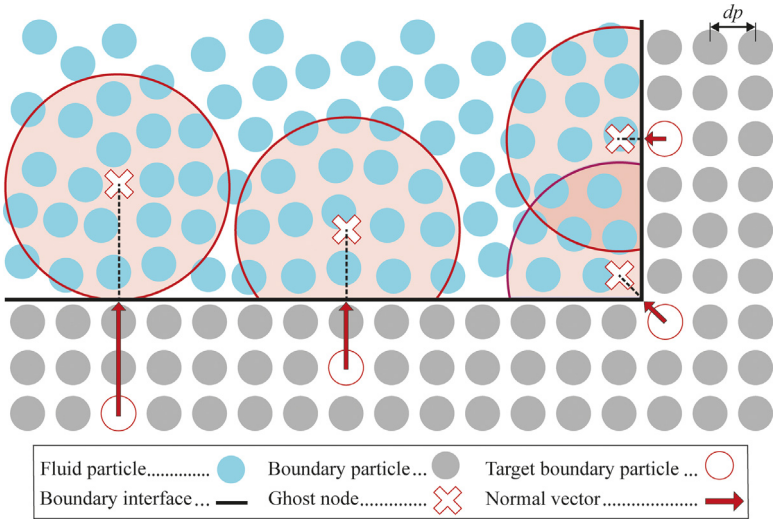

Fig. 1. Projection of ghost nodes when the mDBC method is applied.

to the sum of the contributions of all surrounding fluid particles. Therefore, each boundary particle k experiences a force per unit mass given by:

$$\boldsymbol{f}_k = \sum_a \boldsymbol{f}_{ka} \tag{14}$$

where $\boldsymbol{f}_{ka}$ is the force per unit mass exerted by the fluid particle a on the boundary particle k.

2.4. Time integrator scheme

DualSPHysics implements the symplectic position Verlet (the so-called Symplectic) time integrator scheme [46], which is an explicit and second-order accurate in time scheme. For brevity, the governing equations can be written as:

$$\frac{d\boldsymbol{v}_a}{dt} = \boldsymbol{f}_a; \ \frac{d\rho_a}{dt} = R_a; \ \frac{d\boldsymbol{r}_a}{dt} = \boldsymbol{v}_a \tag{15}$$

When viscous density forces and density evolution are present in DualSPHysics, the velocity is required at the $(n + 1/2)$ step. Therefore, a velocity Verlet half step is used to compute the required velocity for the acceleration and density evolution for $\boldsymbol{f}(\boldsymbol{r}_{n+1/2})$ and $R(\boldsymbol{r}_{n+1/2})$, respectively. Then, the scheme implemented in DualSPHysics is given by:

$$\begin{aligned}
\boldsymbol{r}_a^{n+1/2} &= \boldsymbol{r}_a^n + \tfrac{\Delta t_{SPH}}{2}\boldsymbol{v}_a^n, \\
\boldsymbol{v}_a^{n+1/2} &= \boldsymbol{v}_a^n + \tfrac{\Delta t_{SPH}}{2}\boldsymbol{f}_a^n, \\
\boldsymbol{v}_a^{n+1} &= \boldsymbol{v}_a^n + \Delta t_{SPH}\boldsymbol{f}_a^{n+1/2}, \\
\boldsymbol{r}_a^{n+1} &= \boldsymbol{v}_a^n + \Delta t_{SPH}\left(\tfrac{\boldsymbol{v}_a^{n+1}+\boldsymbol{v}_a^n}{2}\right)
\end{aligned} \tag{16}$$

Finally, the density evolution is computed according the half time step of the symplectic position Verlet scheme by following [47], whose form is given by:

$$\begin{aligned}
\rho_a^{n+1/2} &= \rho_a^n + \tfrac{\Delta t_{SPH}}{2}R_a^n, \\
\rho_a^{n+1} &= \rho_a^n + \tfrac{2-\varepsilon_a^{n+1/2}}{2+\varepsilon_a^{n+1/2}}
\end{aligned} \tag{17}$$

being $\varepsilon_a^{n+1/2} = -\left(\frac{R_a^{n+1/2}}{\rho_a^{n+1/2}}\right)\Delta t_{SPH}$

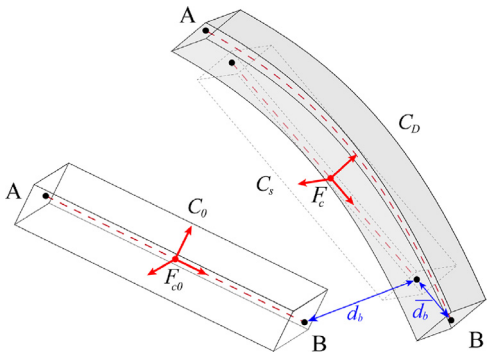

Fig. 2. Concept of the co-rotational formulation implemented in Project Chrono (inspired by [52]).

DualSPHysics implements a variable time step (Δt_{SPH}) that is controlled by a CFL (Courant–Friedrich–Lewy) condition, in which the force term (Δt_f) and the viscous diffusion term (Δt_{cv}) follow [48], and are defined as:

$$\Delta t_f = \min_a \left(\sqrt{h / \left| \frac{d\boldsymbol{v}_a}{dt} \right|} \right); \quad \Delta t_{cv} = \min_a \frac{h}{c_s + \max_b \frac{|h\boldsymbol{v}_a \cdot \boldsymbol{r}_a|}{r_{ab}^2 + 0.01^2}} \tag{18}$$

So, the final value of the integrator time step is given by:

$$\Delta t_{SPH} = 0.2 \min \left(\Delta t_f, \Delta t_{cv} \right) \tag{19}$$

Details on the implementation of the time integrator scheme and the variable time step in DualSPHysics are given in [27].

3. FEA structural solver

The core module of Project Chrono (*Chrono::Engine*) supports the modelling of non-linear Finite Element Analysis (FEA) to solve flexible multibody systems [29]. In this work, the flexible elements are solved with the co-rotational (CR) approach, whose theory can be seen for instance in Belytschko and Glaum [49], and Felippa and Haugen [50]. The CR concept is a Finite Element Method (FEM) that allows large displacements and rotations, but strains and deformations must be small when linear systems are considered. However, Project Chrono implements a non-linear FEA via CR formulation where large deformations are allowed in structural elements, such as the classical three-dimensional (3-D) Euler–Bernoulli beam, based on the work presented in Rankin and Nour-Omid [51].

In this CR implementation, a floating coordinate system (F_c) is considered to follow the deformed shape of the elements, where a reference configuration (C_0) of the element is used to compute the deformed state (C_D) from a superposition between C_0 to the so-called *floating* or *shadow configuration* (C_s). In addition, a local small-strain deformation is included from C_s to C_D [52]. Fig. 2 depicts the concept of the CR formulation as implemented in this multiphysics library. Assuming that the flexible elements are discretised as 3-D beams composed of two end-nodes (denoted by A and B) and six degrees of freedom (DOFs) at each node, the initial frame position is placed in the midpoint of the two nodes.

Project Chrono computes the global stiffness matrix ($\boldsymbol{K_e}$) and the global force ($\boldsymbol{f_e}$) vector of the beam element from the local components $\overline{\boldsymbol{K}_e}$ and $\overline{\boldsymbol{f}_e}$, which represent the local stiffness matrix and the local force vector, respectively. Note that the overlined terms indicate quantity in the local reference system. First of all, the local displacement ($\overline{\boldsymbol{d}}$) is defined by considering the components that can produce a deformation in the beam:

$$\overline{\boldsymbol{d}} = \left(\overline{\boldsymbol{d}}_A, \overline{\boldsymbol{\theta}}_A, \overline{\boldsymbol{d}}_B, \overline{\boldsymbol{\theta}}_B \right) \tag{20}$$

where $\overline{\boldsymbol{d}}_A$ and $\overline{\boldsymbol{d}}_B$ are the local displacements, and $\overline{\boldsymbol{\theta}}_A$ and $\overline{\boldsymbol{\theta}}_B$ are the local finite rotations referred to the end nodes of the beam. Details of this formulation are given in Crisfield et al. [53], and in Tasora and Masarati [52].

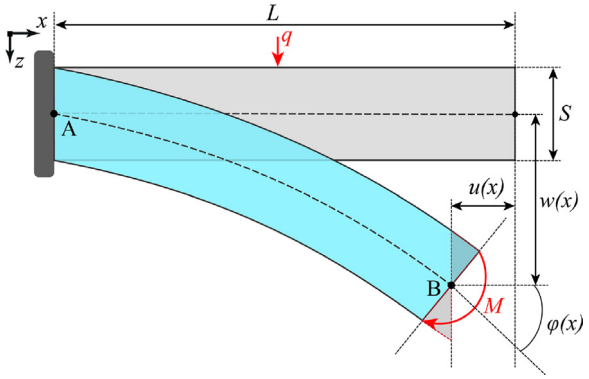

Fig. 3. Schematic of the Euler–Bernoulli beam theory in 2-D.

Once $\overline{\boldsymbol{d}}$ is obtained, the local nodal forces ($\overline{\boldsymbol{f}_{in}}$) are computed from the local stiffness matrix and the local displacements using:

$$\overline{\boldsymbol{f}_{in}} = \overline{\boldsymbol{K}_{\boldsymbol{e}}}\,\overline{\boldsymbol{d}} \tag{21}$$

Finally, $\overline{\boldsymbol{f}_{in}}$ and $\overline{\boldsymbol{K}_{\boldsymbol{e}}}$ are transformed from the local system into global coordinates following the approach presented in [50] and in [52]. The method can be applied to beam elements composed of two nodes and 6-DOFs such as the classical Euler–Bernoulli beams available in Project Chrono.

3.1. Euler–Bernoulli beam

The classical Euler–Bernoulli beam theory is used to provide a simplified framework for anticipating the response of structural elements. As such, finite elements can be modelled and solved under the Euler–Bernoulli theory to compute the deformation of beams considering their internal stress (see for instance [54]). A 3-D beam is usually identified as a geometrical structure in which one of its dimensions is much larger than the other two, being the largest dimension considered the axis of the beam and the cross-section normal to the axis. Fig. 3 shows a schematic of a Euler–Bernoulli beam, in this case, represented in 2-D, being A the fixed end-node and B the free-end node.

In this work, the main kinematic formulae about the Euler–Bernoulli beams are presented in the following:

$$w = w\,(x) \tag{22}$$

$$\varphi\,(x) = -\frac{dw\,(x)}{dx} \tag{23}$$

where x is the axis direction of the beam, w is the displacement orthogonal to the axis or axial displacement, and φ is the rotation or sectional displacement with respect to the axial direction of the beam. Eq. (23) implicitly contains the condition that uniquely characterises the Euler–Bernoulli approach in which the kinematic of each cross section strictly forms a 90-degree angle with the deflected shape of the beam.

The governing equation to solve the deflection of a homogeneous (i.e., same material) and uniform (i.e., same cross section within A and B) beam is defined as:

$$q\,(x) = -\varphi\,(x)\left(EI\frac{d\varphi\,(x)}{dx}\right) \tag{24}$$

where $q(x)$ is the transversal load, E the Young's Modulus, and I the second moment of the inertia of the cross-section, being the product EI called flexural rigidity.

Assuming the structure is modelled as a co-rotated Euler–Bernoulli beam, the translation $u(x)$ of the element depends on Eq. (23), which contains the displacements and rotations of the end nodes. The state is used to compute the deflection φ along the axis and then, when the deflection is known, the bending moment function (M) can be evaluated with the following equation:

$$M\,(x) = -EI\left(\frac{d\varphi\,(x)}{dx}\right) \tag{25}$$

The normal stress along the cross section (σ_{xx}) induced by bending moment (M) can be evaluated using the Navier's hypothesis [55] that gives:

$$\sigma_{xx}(x) = -\frac{M(x)}{I} y \tag{26}$$

where y is the distance between the point of interest (may not belong to the cross-section) and the beam axis along the height of the cross section. This definition yields a linear relationship between distance from the neutral axis and the considered point.

The Euler–Bernoulli defined as such provides a very advantageous tool that requires little computational overhead and little data transfer. Nevertheless, the model has certainly got limitations, and they generate from the particular conditions in which the theory thrives. In particular, the model cannot accurately capture the kinematic of beams for which shear forces are relevant and can only capture linearly distributed stress patterns. It can nonetheless accurately and reliably proxy slender beams, as it will be shown in Section 5.

3.2. Time integrator scheme

The implicit time integrator Hilber–Hughes–Taylor (HHT) proposed by Hilber et al. [56] is available in Project Chrono. This time integrator scheme is able to deal with structural dynamic systems using a set of second-order Ordinary Differential Equations (ODE). Therefore, the HHT scheme can be used to simulate flexible structures within the FEA approach. This scheme generalises the Newmark's algorithm proposed by Newmark [57] for second-order ODE systems. Details of the implementation of HHT and Newmark's in Project Chrono are given in Negrut et al. [58]. Then, the system using Newmark's algorithm is integrated in time:

$$\boldsymbol{M}\frac{d^2\boldsymbol{q}}{dt^2} + \boldsymbol{C}\frac{d\boldsymbol{q}}{dt} + \boldsymbol{K}\boldsymbol{q} = \boldsymbol{F_e}(t) \tag{27}$$

where $\boldsymbol{M}$, $\boldsymbol{C}$ and $\boldsymbol{K}$ are mass, damping and stiffness matrices, respectively, and $\boldsymbol{F_e}$ is the vector of external forces, which varies in time t, whereas $\boldsymbol{q}$ represents the configuration of the system as a set of generalised coordinates. In this work, $\boldsymbol{F_e}$ constitutes the communication interface that realises the connection with the externally computed loads from the SPH particle interaction. The Newmark's scheme is solved assuming the following integration formulae:

$$\boldsymbol{q}^{n+1} = \boldsymbol{q}^n + \Delta_{Ch}\frac{d\boldsymbol{q}^n}{dt} + \frac{\Delta_{Ch}^2}{2}\left[(1-2\beta)\frac{d^2\boldsymbol{q}^n}{dt^2} + 2\beta\frac{d^2\boldsymbol{q}^{n+1}}{dt^2}\right], \tag{28}$$

$$\frac{d\boldsymbol{q}^{n+1}}{dt} = \frac{d\boldsymbol{q}^n}{dt} + \Delta_{Ch}\left[(1-\gamma)\frac{d^2\boldsymbol{q}^n}{dt^2} + \gamma\frac{d^2\boldsymbol{q}^{n+1}}{dt^2}\right] \tag{29}$$

where the terms β and γ are the parameters to govern the numerical dissipation of the algorithm, which can be defined as:

$$\gamma \geq \frac{1}{2}; \quad \beta \geq \frac{\left(\gamma + \frac{1}{2}\right)^2}{4} \tag{30}$$

Eqs. (28) and (29) are used to discretise the equations of motion (Eq. (27)) at time t^{n+1} by using an integration time step (Δt_{Ch}), and following:

$$\boldsymbol{M}\frac{d^2\boldsymbol{q}^{n+1}}{dt^2} + \boldsymbol{C}\frac{d\boldsymbol{q}^{n+1}}{dt} + \boldsymbol{K}\boldsymbol{q}^{n+1} = \boldsymbol{F_e}\left(t^{n+1}\right) \tag{31}$$

This method becomes second-order accurate when the values $\gamma = 1/2$ and $\beta = 1/4$ are considered. However, it does not introduce any numerical damping in the solution, making it impractical to address problems where high-frequency oscillations can disturb the system's solution [58]. This indeed is the main drawback of the Newmark's family of integrators: they are not able to provide second-order accuracy along with desirable level of numerical damping. Conversely, the HHT method stands out because it overcomes the issue of its predecessor due to it is unconditionally stable, preserves the numerical damping properties, and achieves second-order accuracy [58]. It includes an extra dissipation quotient (so-called α) to Eq. (31), which makes it an optimal and accurate method, if wisely employed, when some numerical damping is required to damp out high-order mode of vibration effects,

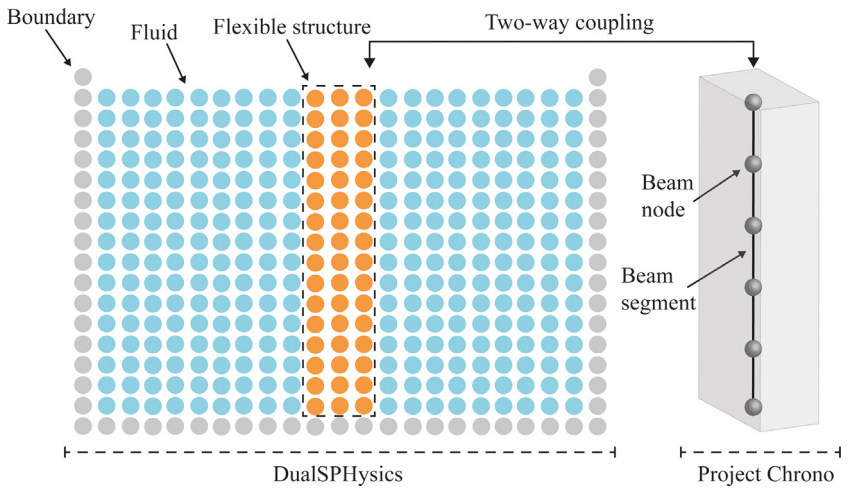

Fig. 4. Discretisation of the domain in DualSPHysics and Project Chrono.

which often arise in flexible structure with high multiplicity of connected elements. The equation of motion for the HHT scheme can be written as:

$$\boldsymbol{M}\frac{d^2\boldsymbol{q}^{n+1}}{dt^2} + (1+\alpha)\,\boldsymbol{C}\frac{d\boldsymbol{q}^{n+1}}{dt} - \alpha\boldsymbol{C}\frac{d\boldsymbol{q}^{n}}{dt} + (1+\alpha)\,\boldsymbol{K}\boldsymbol{q}^{n+1} - \alpha\boldsymbol{K}\boldsymbol{q}^{n} = \boldsymbol{F}_{\boldsymbol{e}}\left(\tilde{t}^{n+1}\right), \tag{32}$$

$$\tilde{t}^{n+1} = t^n + (1+\alpha)\,\Delta_{Ch} \tag{33}$$

where $\alpha \in [-1/3, 0]$ and the parameters to govern the numerical dissipation of HHT algorithm are defined, following [58], by:

$$\gamma = \frac{1}{2} - \alpha; \quad \beta = \frac{(1-\alpha)^2}{4} \tag{34}$$

Therefore, the HHT scheme works as the Newmark's when $\alpha = 0$ (i.e., $\gamma = 1/2$ and $\beta = 1/4$) as it clearly indicates that there is no numerical damping applied and is second order accurate. Otherwise, numerical dissipation is present for $\gamma > 1/2$, and the larger the value of α, the more damping is induced in the numerical solution. In this work, the HHT integrator has been used to solve the structure with $\alpha = 0$ since no dissipation is required for the cases reproduced in the validation section (see in Fourey et al. [9]).

4. SPH-FEA coupling

The novel implementation presented in this manuscript is based on a two-way coupling of the SPH model with the FEA structural solver described in Section 3. The DualSPHysics code solves the fluid–fluid and fluid–solid interactions, and the behaviour of the deformable object is simulated using the FEA structural solver integrated in Project Chrono. The entire domain is described using subsets of particles within the SPH solver, including the flexible structure as a set of boundary particles. On the other hand, within the FEA solver, the structure is built with a set of segments (N) that connects nodes ($N + 1$). The segments are modelled using beam elements under the Euler–Bernoulli formulation (Section 3.1), whereas the beam nodes are 3-D finite element nodes with 6-DOFs. Fig. 4 shows the discretisation of the domain in both models (DualSPHysics and Project Chrono).

DualSPHysics and Project Chrono exchange data to simulate the fluid–elastic structure interactions within a two-way procedure via a communication interface, where DualSPHysics controls the communication making calls to Project Chrono. The data exchange process can be split into two event flows: (i) initial setup; and (ii) time step integration. These events are explained in the following subsections.

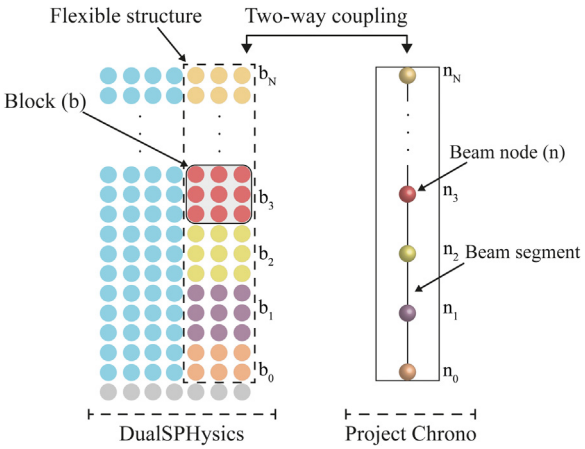

Fig. 5. Initial setup of the flexible structure in DualSPHysics and Project Chrono.

4.1. Initial setup flow

Initially, DualSPHysics transfers to Project Chrono the density of the structure (ρ), number of structure segments (N), damping coefficient (c), Young's Modulus (E), and Poisson's ratio (ν) to model the elastic structure. After that, Project Chrono returns the vector with the initial positions of the nodes ($\boldsymbol{R}_0$). Once the initial setup is completed, the structure is built and discretised in both the SPH and the FEA domains. The SPH solver divides the flexible structure into $N + 1$ blocks. The concept of block represents a set of particles of the structure that will be linked to a FEA beam node. Fig. 5 shows the initial setup where the blocks are identified with b_i and the beam nodes with n_i, being $i \in [0, N]$ the index of the blocks and nodes. The approach followed in this work is such that the SPH solver computes linear forces exerted by the fluid on the blocks and the FEA structural solver simulates the movement and the deformation of the flexible structure by applying those forces on the beam nodes. It should be noted that the model presented here does not account the torsional forces exerted by the fluid since it is focused on 2-D simulations yet, where the torsion of the beam is neglected.

4.2. Time integration flow

In the time step integration flow, both models exchange data in order to solve fluid–structure interaction. Then, the advance of a SPH time step (Δt_{SPH}) is solved, which is repeated until the maximum simulation time is achieved (t_{MAX}). The process of simulating a Δt_{SPH} can be split into three steps: (i) compute the linear forces ($\boldsymbol{F}$) on the structure; (ii) solve the movement of the structure ($\boldsymbol{R}$); and (iii) update the magnitudes of the structure particles. The coupled model presented in this work is based on the coupling strategy presented in Martínez-Estévez et al. [31] by using the general-purpose communication interface DSPHChronoLib to handle the data exchange process between DualSPHysics and Project Chrono. The use of this interface as a link between both solvers facilitates the development tasks since it follows a *low coupling* strategy, which means that new changes or features implemented in either solver would not affect the operation of the other [31]. A complete schematic of the flow events is shown in Fig. 6.

The three steps involved during the simulation are depicted in Fig. 7 and explained here in detail:

(i) DualSPHysics computes the particle interaction by solving the SPH governing equations (4) and (8) considering the fluid–structure interaction and linear ($d\boldsymbol{V}/dt$) and angular ($d\boldsymbol{\Omega}/dt$) accelerations are obtained. The SPH model computes the linear forces on the structure particles by solving the Eq. (14). Then, the linear forces ($\boldsymbol{F}_i$) on each block b_i are computed as the sum of all the forces of the particles belonging to it. Therefore, the vector includes the total force exerted by the fluid on the block b_i. Thus, the forces computed on the block b_i, will be applied on the node n_i.

(ii) DualSPHysics transfers $\boldsymbol{F}_i$ to Project Chrono through DSPHChronoLib. The FEA structural solver applies $\boldsymbol{F}_i$ on its respectively node n_i and solves the movement of the structure. This process usually takes several

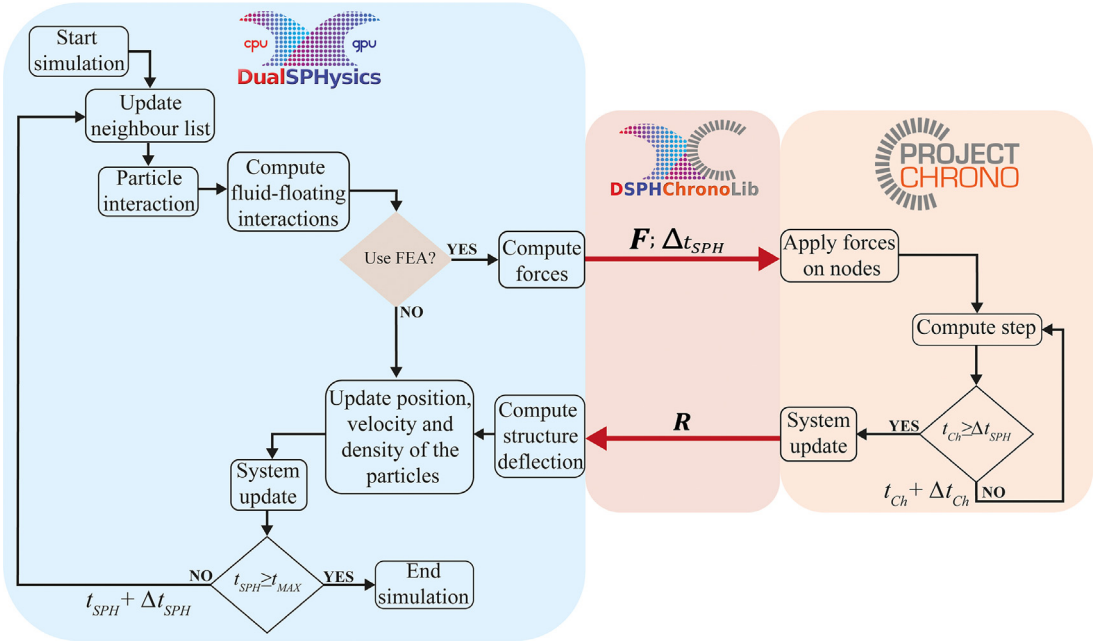

Fig. 6. Scheme of the two-way time step integration flow of the coupled model.

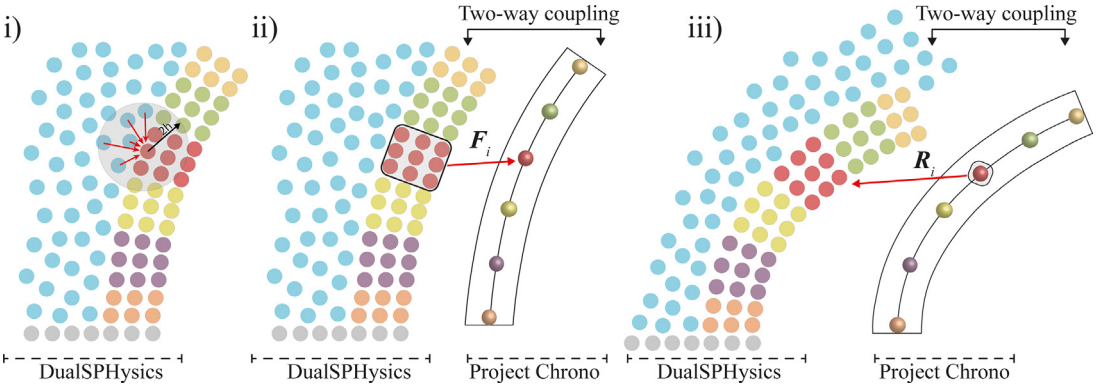

Fig. 7. Main steps during the time step integration of the two-way coupling between DualSPHysics and Project Chrono to solve fluid–structure interactions.

internal integration time steps (Δt_{Ch}), and therefore, it goes on until the loop exit condition is satisfied ($t_{Ch} \geq \Delta t_{SPH}$) and Project Chrono updates the system. The behaviour of the flexible structure is considered to obtain the variable Δt_{SPH} (computed in Eq. (19)) since the velocity of its particles is taken account in Eq. (18). Note that t_{Ch} is not the absolute internal time of the simulation in the multiphysics library, hence it is relative to each Δt_{SPH} that is solved.

(iii) Project Chrono transfers back the node positions ($\boldsymbol{R}_i$) to DualSPHysics through DSPHChronoLib. Then, DualSPHysics computes the deformation of the shape in SPH and updates the position ($\boldsymbol{r}$), velocity ($\boldsymbol{v}$), density (ρ) and pressure (p) of all particles. At this point, the system is ready to be updated and to solve the next time step, if any.

5. Validation cases

The literature revised in the introduction provides examples of benchmark cases useful for accuracy comparison. In this section, four benchmarks are presented in order to validate the proposed coupled model for FSI: (i) freely

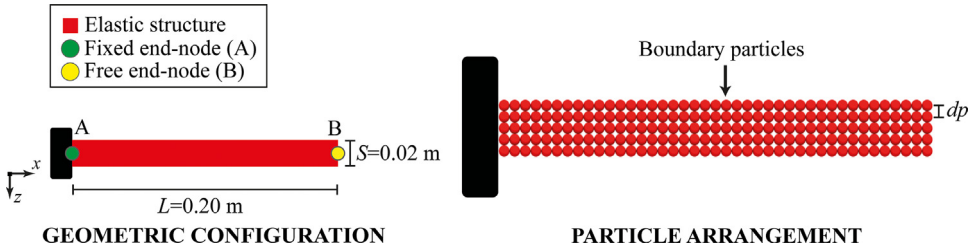

Fig. 8. Geometric configuration and initial particle arrangement of the cantilevered beam for an SPH resolution $dp = S/4$.

oscillating cantilevered beam; (ii) hydrostatic water column on an elastic beam; (iii) breaking water column with an elastic gate; and (iv) breaking water column impacting an elastic obstacle. All the simulations included in this section are carried out on a personal computer with AMD Ryzen 9 5950X CPU and a graphic card NVIDIA RTX A5000. The SPH solver of DualSPHysics is executed on the GPU while Project Chrono is solved on a single-core CPU thread.

5.1. A freely oscillating cantilevered beam

Prior to presenting proper FSI cases, a first benchmark is herein used to ascertain the agreement of the structure solution under dynamic conditions, which allows validating the management of the coupled library by the main code DualSPHysics. The undamped, dynamic response of a cantilevered beam subjected to an initial velocity distribution is compared to an analytical solution that was derived from the theory of thin plates developed by Landau and Lifshitz [59]. Fig. 8 shows the geometry of the cantilevered beam that is composed of two end-nodes (A and B), whose dimensions are length $L = 0.20$ m and thickness $S = 0.02$ m and its elastic material properties are Young's modulus $E = 1.68$ MPa, Poisson's ratio $\nu = 0.40$, and density $\rho = 1000$ kg/m^3. The motion of a freely oscillating plate at its free-end (node B in Fig. 8), described by its middle plane line in a 2-D framework, is given into closed form as:

$$w\,(L,t) = \frac{\psi c_s}{\omega} \cdot \cos\left(\omega t\right) \tag{35}$$

where w is the displacement in the complementary direction to the axis, ψ is a scaling factor (set to 1/100), being $c_s = \sqrt{K/\rho}$ the speed of sound of the material, $K = E/(3(1-2\nu)$ the bulk modulus and ω the circular frequency of oscillation defined as:

$$\omega = k_w^2 \sqrt{\frac{EIT}{12\rho\left(1-\nu^2\right)}} \tag{36}$$

where k_w is the wave number that corresponds to the first mode (i.e., $k_w = 1.875/L$), I is the beam area moment of inertia of the cross section.

The boundary conditions imposed to the beam to realise a clamped-free-end static scheme are:

$$w\,(A) = 0; \quad \frac{\partial w}{\partial x}\,(A) = 0; \quad \frac{\partial^2 w}{\partial x^2}\,(B) = 0; \quad \frac{\partial^3 w}{\partial x^3}\,(B) = 0 \tag{37}$$

whereas an initial velocity field is imposed to the beam's axis as:

$$\frac{\partial w\,(x)}{\partial t} = \psi c_s \frac{f\,(x)}{f\,(x=L)} \tag{38}$$

in which $f\,(x)$ is defined according to the following function:

$$\begin{aligned} f\,(x) = {} & (\cos k_w L + \cosh k_w L)\,(\cosh k_w x - \cos k_w L) \\ & + (\sin k_w L - \sinh k_w L)\,(\sinh k_w x - \sin k_w x) \end{aligned} \tag{39}$$

Note that the Neumann boundary conditions are enforced at (internal) node level, meaning that the vertical velocity profile is discretised according to the node position along the axis and so this approach asymptotically tends to the continuous distribution when the number of nodes (segments) increases.

Table 1
Performance of the freely oscillating cantilevered beam case for $dp = S/4$.

dp	Structure particles	Fluid particles	Segments (N)	SPH steps	DualSPHysics runtime [s]	Chrono runtime [s]	Total runtime [s]	% Chrono
$S/4$	205	–	10	44 195	104	30	134	22
$S/4$	205	–	20	44 195	106	33	139	24
$S/4$	205	–	30	44 195	108	42	150	28

Fig. 8 visualises the initial solid layout for the beam and the initial particle setup corresponding to the initial interparticle distance $dp = S/4$. According to the coupling procedure presented in Section 4, regardless of the fluid presence, the initial value of dp must guarantee a minimum width of one particle per segment so that there is consistency between the geometric beam configuration in both spaces. However, this test case does not involve the solution of any fluid phase and the structure is completely resolved within the Project Chrono subroutine thus giving no relevance to the particle discretisation.

It is important to underline that to compare the results of a Euler–Bernoulli beam model to plate theory's, a correction must be implemented to account for the different hypotheses on which the two theories develop to predict the steady-state solution for thin elements. In the first place, the slenderness of the beam herein considered (i.e., $\propto L/S$) classifies as slender, and for which the Euler–Bernoulli theory should be providing good estimation of the overall kinematics. However, the same geometric configuration gives rise to two different flexural rigidities that differ for a constant value introduced by further deformability of the planar model, as it was proposed in [60] and recently demonstrated and validated in [13]. The computation of the correction follows:

$$\hat{E} = \frac{E}{1-\nu^2} \tag{40}$$

where $\hat{E}$ represents the corrected value to be used to define the axial and flexural stiffness that are passed to the structural solver. Using the value defined by means of Eq. (40) allows to use the solution of Eq. (35) as reference.

To assess the accuracy and precision of the structural model, three simulations with $N = 10$, 20, and 30 segments are respectively run, and the results are collected in Fig. 9 in terms of dimensionless tip deflection in time (node B) using the theoretical maximum motion amplitude $(\psi c_s)/\omega = 0.0025$ m (see Eq. (35)). Note that with the maximum deflection being small in comparison to the beam length, the validity of the theoretical solution obtained using the linear theory is ensured. The beam tip deflection matches the theoretical target for each case, showing hardly any dispersion among the considered FEM resolutions. The agreement is quantified here measuring the L_1 error for the amplitude and the period when $N = 30$ is used. A proper reproduction of the displacement function is shown, with a frequency error of about 3% ($\omega_{theory} = 20.82$ rad/s against $\omega_{num} = 20.27$ rad/s) an overall error on the amplitude around 1.5%, which specifically accounts for an almost 2%-error for the positive peaks and a 0.2% for the negative peaks.

Table 1 shows the different setups of the freely oscillating cantilevered beam carried out for a physical time $Time = 1.50$ s. All cases are configured with the same SPH resolution ($dp = S/4$). However, the number of segments (N) is modified in order to validate the structural behaviour of the FEA solver. It should be noticed that only structure particles are created in this benchmark, so the relevant computational cost to be studied is the consumed one by the multiphysics library. The data reported in the table show that DualSPHysics takes the same computational time as the number of steps remain the same, whereas the number of segments to be solved prevalently affects the Chrono runtime.

5.2. A hydrostatic water column on an elastic beam

A first validation in which FSI phenomenon is relevant is carried out in this section although the physics of this test does not comprise violent collisions and sudden variation of motion. This means that the solution to the problem may be retrieved by uncoupling fluid and structure response still getting high accuracy. In fact, this test case was originally proposed by Fourey [61], as a theoretical configuration to settle a solution of practical interest to compare with. Anyway, it serves well the scope of this section, providing a fair benchmark to evaluating the precision of the numerical solver.

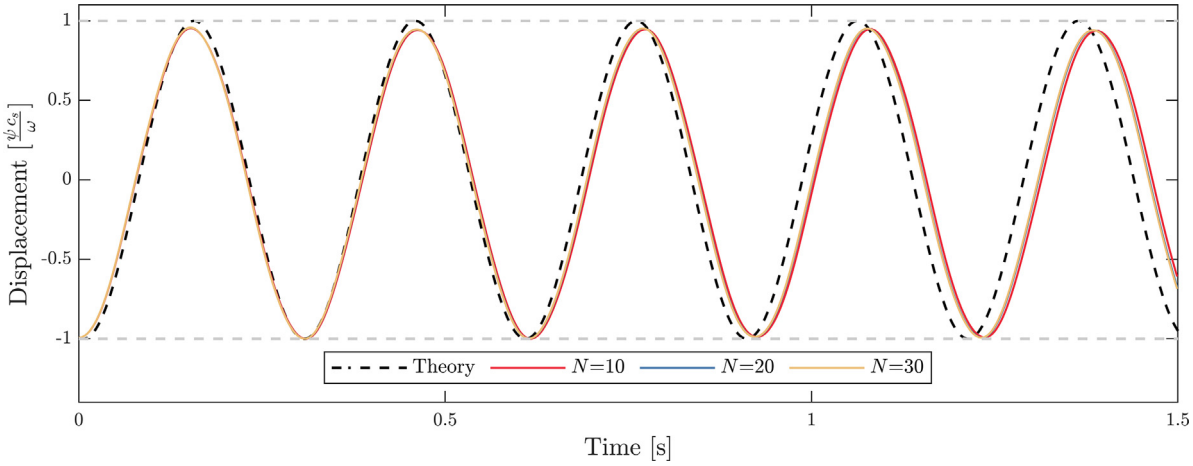

Fig. 9. Time histories of the dimensionless tip deflection (given as a function of the maximum theoretical displacement) of the plate for different number of segments.

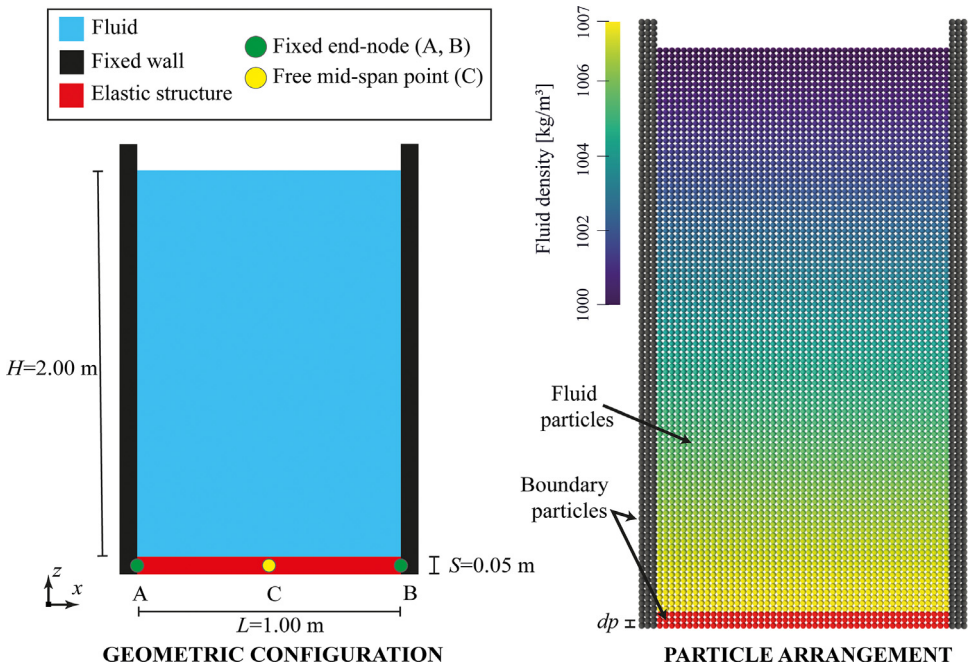

Fig. 10. Initial configuration the hydrostatic water column over an elastic beam and the initial particle arrangement in which the fluid and boundary particles are indicated for the SPH resolution $dp = S/2.5$.

Fig. 10 proposes a schematic sketch of the setup geometry. By assuming that the hydrostatic water column, whose height is $H = 2.00$ m, is at equilibrium on a double-clamped aluminium plate (beam), it allows calculating a closed-form solution of the problem in its initial configuration (straight line). In addition, density $\rho = 1000$ kg/m^3, speed of sound $c_s = 50$ m/s and gravity acceleration as -9.81 m/s^2 are considered. The water column is propped by a 5-centimetre thick ($S = 0.05$ m) and 100-centimetre long ($L = 1.00$ m) aluminium plate, defined with Young's modulus $E = 67.5$ GPa, Poisson's ratio $\nu = 0.34$, and density $\rho = 2700$ kg/m^3. Thus, the deflection of the beam at its mid-span point C, considering that the beam is clamped on both sides (points A and B), is given by:

$$w\,(L/2) = \frac{1}{384} g \frac{(\rho H + \rho_a T)\, L^4}{E_a I_a} \tag{41}$$

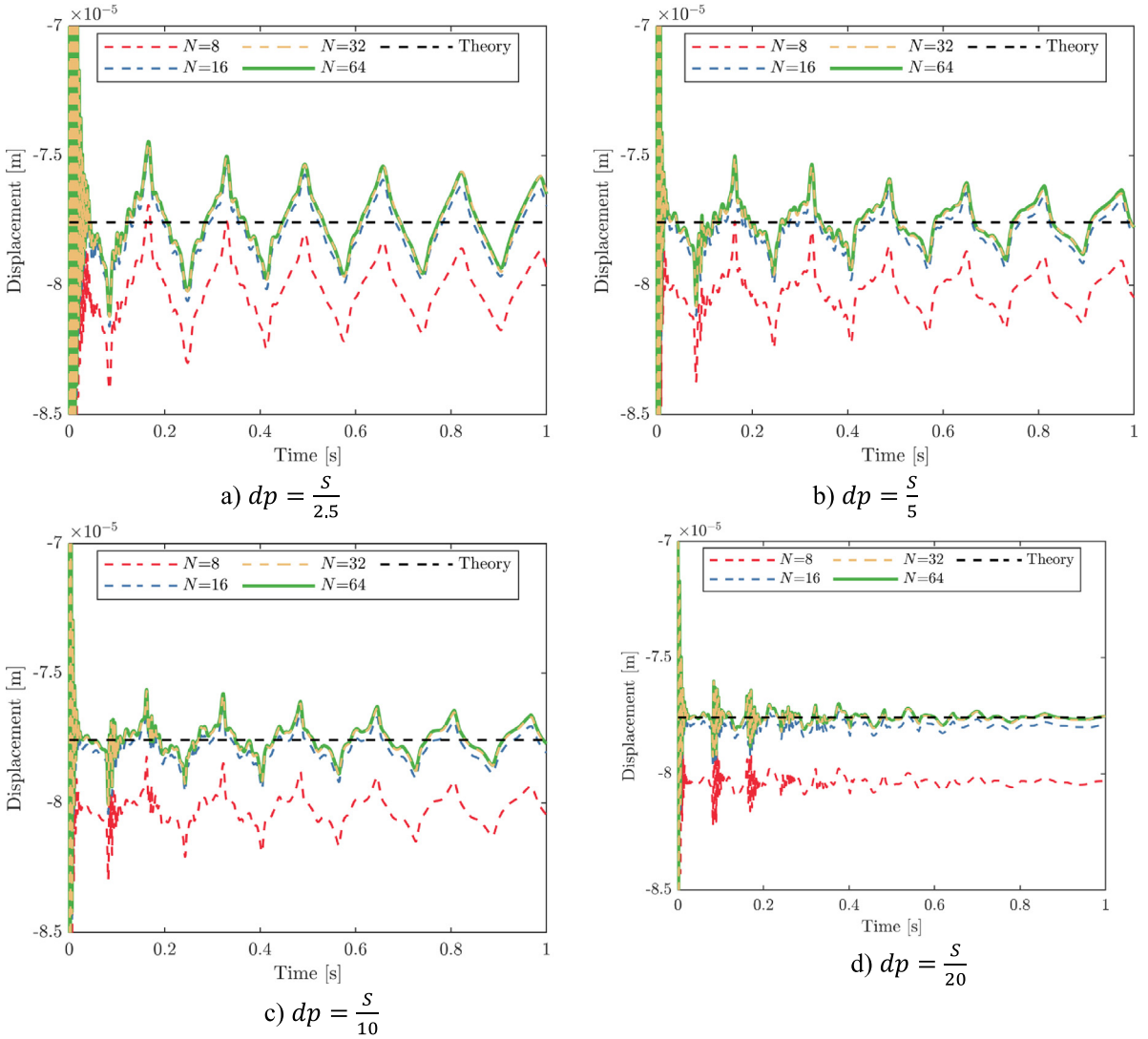

Fig. 11. Displacement history for the mid-span point C for different particle resolutions and number of segments compared to the theoretical solution.

where I_a is the moment of inertia of the beam area. For the problem at hand, Eq. (41) gives a vertical deflection of -77.5 μm, which is itself small, so it resolves to little or no overall movement in the water column. The magnitude of the theoretical displacement, which is several orders of magnitude smaller than the length of the beam, reinforces the quality of the hypotheses on which the utilised beam model grounds, providing a very accurate reference to compare with. It is important to note that for this case there is no need to apply the correction proposed in Eq. (40) because the reference solution is developed with respect to the beam theory rather than the plate theory.

The magnitude of the beam's deflection at its mid-span point (C) justifies the use of this benchmark for defining the accuracy and precision of most FSI coupling procedures. Focusing more on the stability of the technique being used [9,14,17], its use is essentially due to the availability of a highly reliable analytical solution. On this account, it should be emphasised that the use of the double precision for data transfer was critical to correctly capture the plate displacement, being the displacement of the beam many orders of magnitude smaller than the size of the domain.

The dataset is structured in Fig. 11 and corresponds to the outcome of the SPH-FEA coupled model for four different FEM resolutions (number of segments $N = 8$, 16, 32, and 64). Each chart refers to a different initial particle size, respectively, $dp = S/2.5$ (a), $dp = S/5$ (b), $dp = S/10$ (c), and $dp = S/20$ (d), reporting the displacement of

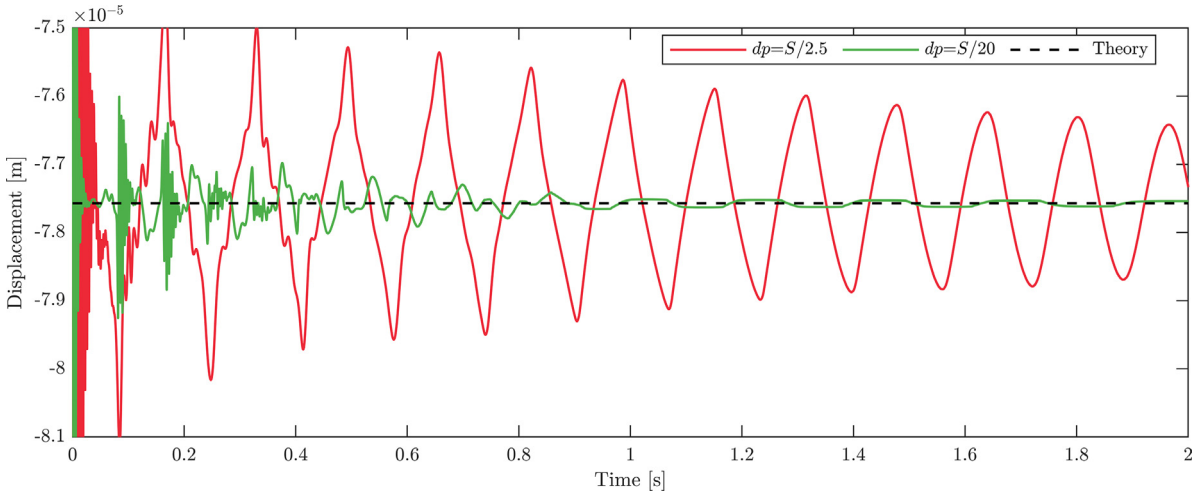

Fig. 12. Particle resolution convergence study for the displacement history at the mid-span point C for 64 FEM segments compared to the theoretical solution.

the control point C against the analytical solution given by Eq. (41), and all the simulations comprise a one-second duration. In this case, when the system response depends on data exchanged between the two solvers, the number of segments mildly affects the accuracy of the whole setup even when boosting the system resolution. This could possibly be due to the low mobility of the fluid particles, which resolves in relatively high accuracy in the fluid force computation regardless of dp. Although the case with $N = 8$ provides low precision, showing a consistent offset from the reference solution of about 3 μm, it exhibits the same overall features of the cases with higher number of segments. Lastly, $N = 16$, $N = 32$, and $N = 64$ provide greater precision, with the latter two fully capturing the analytical solution, as can be clearly seen in panel (d).

Fig. 12 provides an overview on the convergence issue posed by the initial particle resolution dp, while keeping the same number of segments ($N = 64$) for the double-clamped beam. Two main peculiarities of the problem can be clearly appreciated when the problem is solved using the proposed coupling: the particle resolution is game changing in the accuracy and stability of the water column as smaller particle sizes are indicative of less noisy pressure fields. Despite the particle resolution, the fluid forces are well computed in all the cases and thus leading to the same vertical force distributions that eventually provoke the same mid-span deflections.

A better understanding, indeed, on the damped oscillatory nature of the beam mid-point displacement can be grasped by considering the four snapshots in Fig. 13: each one pictures the state of the fluid tank and the beam, with $dp = S/2.5$, at different time steps taken during $Time = 0.001$ s (a), $Time = 0.021$ s (b), $Time = 0.041$ s (c), and $Time = 0.061$ s (d). The time-window covers a range of 0.080 s that corresponds to the return period of occurrence of the spikes that appear in Fig. 11. The cyclic behaviour, marked by large oscillations and clearly visible for coarser particle spacings, is induced by a shock wave, which is likely generated by the initial set down experienced by the beam, propagating vertically in the tank. If one considers that the disturbance is generated at time zero (panel (a) in Fig. 13), the periodicity of the spikes matches perfectly with the travelled distance, which is twice the water column height ($2H$) over the fluid speed of sound c_s. The particle resolution affects the system response since finer particle resolutions allow damping out the pressure disturbance much quickly, resulting in shorter times necessary to stabilise the beam vibrations induced by the pressure wave.

Lastly, Fig. 14 shows a comparison between the pressure measured right above the mid-span point C in the fluid tank for the two resolutions (and $N = 64$) considered above with the analytical pressure computed for still water and no plate deformation. The pressure time histories are affected by the shock wave that forms at time zero, when the water column settles on to the elastic beam. As the particle resolution decreases, the pressure fluctuations seem to reduce as well, and the damping effect provided by the fluid formulation is able to filter out the energy contented of this acoustic wave.

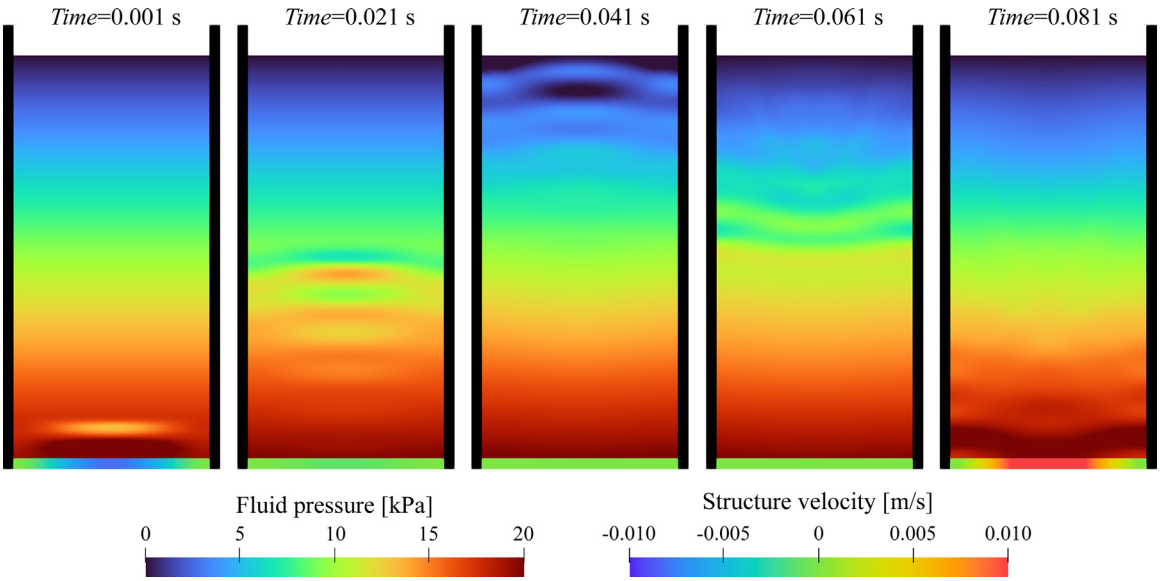

Fig. 13. Snapshots of a one-period pressure wave propagation within the fluid tank with $dp = S/20$, where fluid particles are coloured by pressure whereas solid particles by vertical velocity.

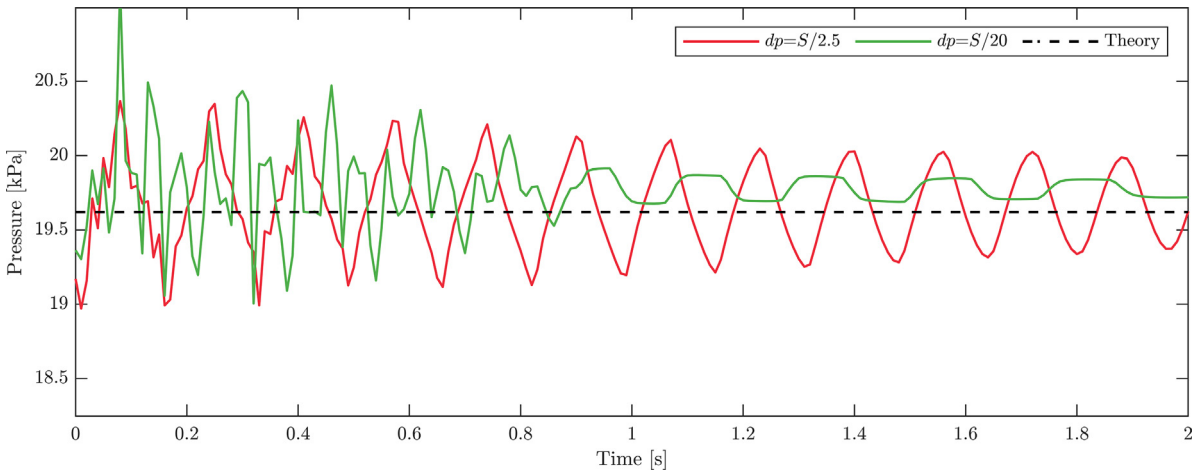

Fig. 14. Fluid pressure time evolution for the mid-span point C for different particle resolutions and $N = 64$ compared to the theoretical solution.

Fig. 15 shows two snapshots corresponding to the fluid pressure and beam stress at the initial state (*Time* = 0 s) and after a while when the system is at the equilibrium (*Time* = 1.00 s), for which pressure field matches the initial state. The initial stage of the water settling on the aluminium beam consists of the water column in its configuration dictated by the presence of gravity alone, whereas the beam is initialised as if gravity were not applied yet. As shown before, the exchange of data process commences soon after the first SPH time step, after which the fluid–structure system starts interacting. The right-hand visual representation proposes the fluid pressure and the beam stress fields for a state at which static conditions have been reached. The stress along the beam (σ_{xx}) shows to be distributed in perfect accordance with the theoretical response of a double clamped beam under a uniform load condition. At the two clamped section, where the beam Boundary Conditions are enforced, the upper fibres are engaged in tension (negative values), whereas the mid cross section proposes a reverse fibre configuration by having the lower ones in tension. Note that the position of the inflection points, in which stress are close to zero (green areas), is perfectly captured as they locate at $0.211L$ from the closest fixed cross section. It is worth mentioning

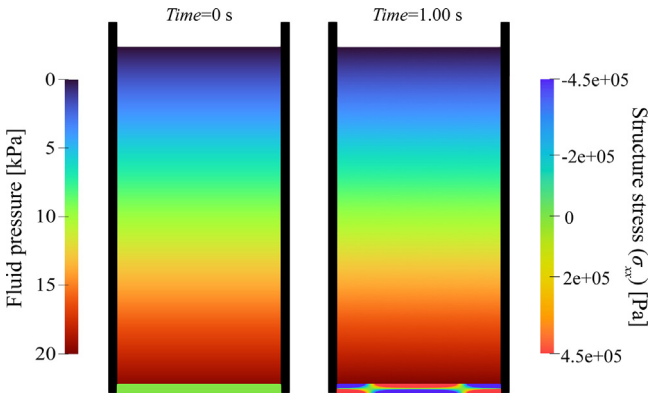

Fig. 15. Snapshots of the simulation considering the fluid pressure and beam stress of the initial state (left) and when the system is at equilibrium (right).

that although the initial shock wave is still travelling, the induced under/over pressure does not cause detectable stress variations in the beam, essentially due to the low magnitude of those pressure oscillations (see Fig. 14).

The accuracy of the coupling is tested with respect to the energy conservation of the structural solver provided by the non-linear FEA solver. As a matter of fact, this case provides proper background for this type of validation considering the total elastic strain energy stored by Euler–Bernoulli beam. With reference to Fig. 3 regarding the nomenclature, the internal energy (U_I) can be defined as:

$$U_I = \frac{1}{2}\int_0^L EI\left(\frac{d^2w}{dx^2}\right)^2 dx \tag{42}$$

Eq. (42) provides, in time, the energy stored by the beam element, and it can be compared with the work done by the external forces. Hence, by considering the work of the external entities acting on a double clamped beam, it can be calculated in a closed form by considering the static displacement function:

$$w\,(x) = -x\frac{q(1-x)(L^2x^2 - L^3x)}{24EIL^2} \tag{43}$$

being $q = (\rho H + \rho_a T)$. By integrating Eq. (42) over the length of the beam, the work of the distributed load is:

$$U_E = \frac{L^5 q}{1440EI} \tag{44}$$

Fig. 16 shows the time evolution of the beam internal energy for an increasing number of beam segments while keeping fixed the SPH particle size to $dp = S/20$, and the numerical model response is compared with the theoretical solution (0.433 J) proposed in Eq. (44). Here, due to the scope of this last test, the simulations are executed for 10.0 s. The chart, proposed in a logarithmic time scale, allows following in detail the initial load process. As mentioned before, the process starts with the beam in a neutral position. At the time the first-time step is computed, the fluid experiences the gravity pull and, therefore the fluid mass finds the beam reactive forces during its fall. Due to the impulsive force that is transferred to the beam, the first instants of the simulation (for all the cases) see a strong increase in the maximum deformation of the beam that, as it can be noticed from the chart, corresponds to a spike in beam internal energy. The first five visibly decaying cycles (up to $Time = 0.02$ s) can be used to characterise the dynamic response of the beam as they are close to the first period of vibration of the system formed by the beam and the part of water it interacts with. The evident damped cyclic response is provided by an energy dissipation that occurs in the fluid phase. From this time on, and up to $Time = 0.080$ s, the beam reaches its equilibrium configuration that matches the theoretical value. Thus, the pressure wave, previously generated by the settling process (see Fig. 13), reaches again the beam-to-fluid interface, thus provoking very small vibrations throughout the beam. The frequency at which those new vibrations take place is close to the previous one, but not exactly the same as the hydrodynamic stiffness offered by the water interface is reduced due to the very small

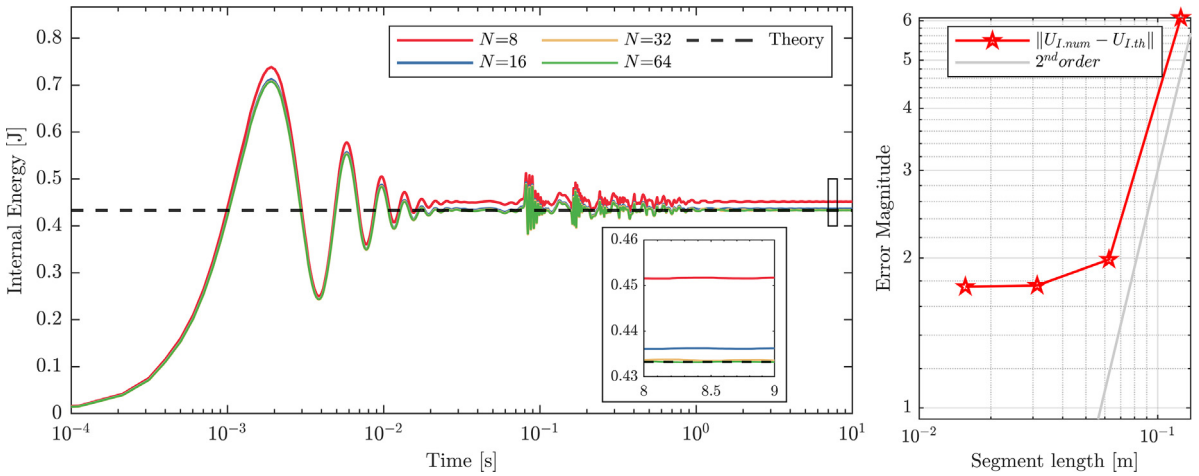

Fig. 16. Total strain energy of the beam compared to the theoretical solution: time history and convergence study.

Table 2
Performance of the hydrostatic water column on an elastic beam case for $N = 64$.

dp	Structure particles	Fluid particles	Segments (N)	SPH steps	DualSPHysics runtime [s]	Chrono runtime [s]	Total runtime [s]	% Chrono
S/2.5	153	6409	64	7383	45	42	87	48
S/5	606	23 106	64	14 775	97	78	175	45
S/10	2211	87 201	64	29 549	192	124	316	39
S/20	8421	338 391	64	59 096	337	183	520	35

overpressure magnitudes. This process iterates for about one second, after which the beam stays steady at its equilibrium position, at which the U_I is consistent with the theoretical value, highlighted by the zoomed view on the time-window from *Time* 8.00 to 9.00 s. For the sake of reference, a similar investigation on the inner energy content of the beam is proposed in [17,62]. The right-hand side of Fig. 16 proposes a converge study by measure of the L_2 error for whole time series, and those values are then reported with respect to the length of segment the beam is discretised with. The chart proposes a close-to-second order convergence rate when moving from the 8 to 16 segments, which is consistent with the time stepper HHT. However, the chart also proves that moving towards finer discretizations does not yield the same rate of convergence. This can be possibly explained by the fact that the resolution of the fluid phase is unchanged, so the overall coupling model hits its saturation state.

The performance results presented in this section include only the combination of each solver's resolution selected with the best of the other solver. Thus, Table 2 shows the performance results of the simulations for different values of *dp* while the number of segments is kept constant ($N = 64$). It can be noticed that the number of particles is varying and, as it increases, the total runtime grows accordingly. Although the resolution of Project Chrono does not change, its runtime is slightly different when the number of particles rises. This trend is possibly due to the increasing number of SPH steps, which is not constant for each simulation because the SPH solver uses a variable integration time step (Δt_{SPH}) that depends on the resolution (h in Eq. (18)). Therefore, when the number of calls to the multiphysics library to solve a time step rises, it causes an additional overhead even though the percentage (%) of time consumed by Chrono is within a narrow range for each case.

On the other hand, Table 3 shows the performance results of the simulations for different values of segments (N), in which the SPH resolution does not change ($dp = S/20$). For all the cases, the number of particles is the same, while the DualSPHysics runtime and the number of SPH steps do not remain constant. More specifically, the runtime of DualSPHysics can indirectly be affected by the number of segments since the SPH solver has to compute the fluid forces for each FEA beam node ($N + 1$) (see Section 4.2). Thus, when the number of segments increases, even if for a constant value of *dp*, the DualSPHysics runtime can be also affected. On the other hand, the number

Table 3
Performance of the hydrostatic water column on an elastic beam case for $dp = S/20$.

dp	Structure particles	Fluid particles	Segments (N)	SPH steps	DualSPHysics runtime [s]	Chrono runtime [s]	Total runtime [s]	% Chrono
$S/20$	8421	338 391	8	59 095	289	45	334	14
$S/20$	8421	338 391	16	59 097	290	52	342	15
$S/20$	8421	338 391	32	59 093	292	77	369	21
$S/20$	8421	338 391	64	59 096	337	183	520	35

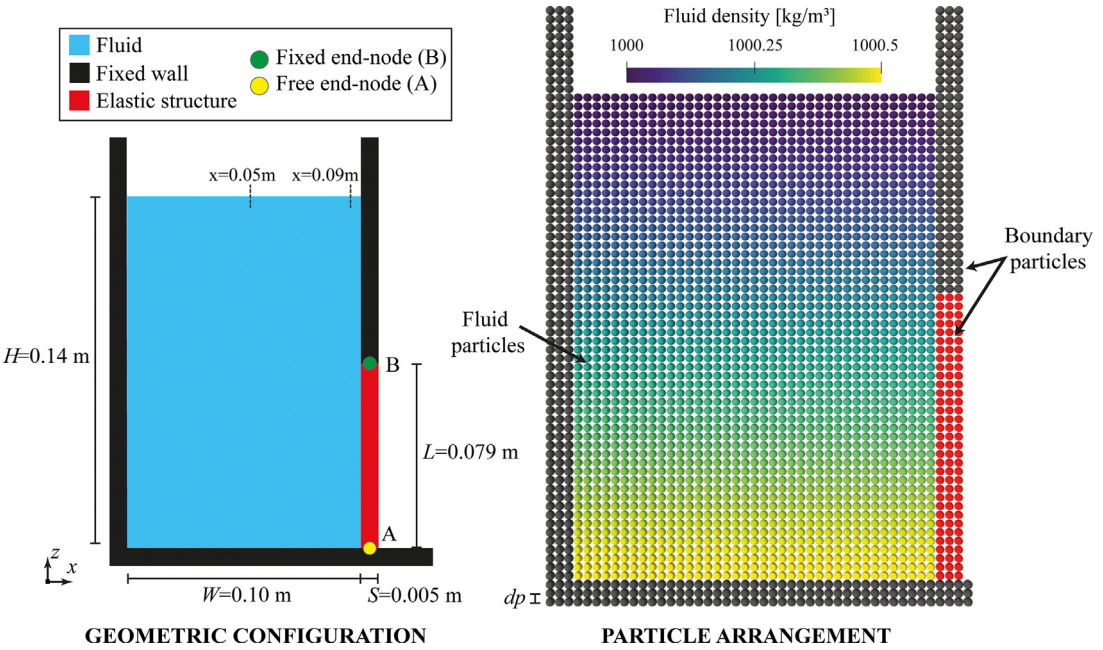

Fig. 17. Initial configuration of the elastic gate, the breaking water column, and its particle discretisation for the SPH resolution $dp = S/2$.

of SPH steps is slightly different since the variable time step used in the SPH solver is computed according to the maximum particle velocity. Therefore, any variation in the response of the FEA model when solving the structure can provoke changes in the Δt_{SPH}. Finally, it can be noticed that the execution time of Project Chrono and the percentage (%) of elapsed time consumption rises according to the number of segments.

5.3. A breaking water-column with an elastic gate

The third case makes use of an experimentally tested setup that was first presented in Antoci et al. [63], in which the experimental set-up and results in a two-dimensional fashion are provided. The schematic of the setup is given in Fig. 17, where a water column, with dimensions height $H = 0.14$ m and width $W = 0.10$ m, is confined between vertical walls. The vertical wall on the right terminates with a 7.90-mm elastic gate (length $L = 0.079$ m, thickness $S = 0.005$ m), clamped to the upper part of a fixed support (node B) and otherwise free to deflect in any direction. Moreover, density $\rho = 1000$ kg/m^3, speed of sound $c_s = 50$ m/s, and gravity acceleration as -9.81 m/s^2 are considered. The elasticity of the gate is modelled using a beam element as proposed by the SPH-FEA scheme to reproduce the deformation induced by the fluid pressure. As final note, it is important to mention that the experimental data (beam free-end and water level in the tank time histories) given in [63] evidently refers to a 3-D case. However, the setup was conceived and ran expecting that the response of the system was not affected by the extension in the third dimension (i.e., width of the tank), so that a bi-dimensional cross section

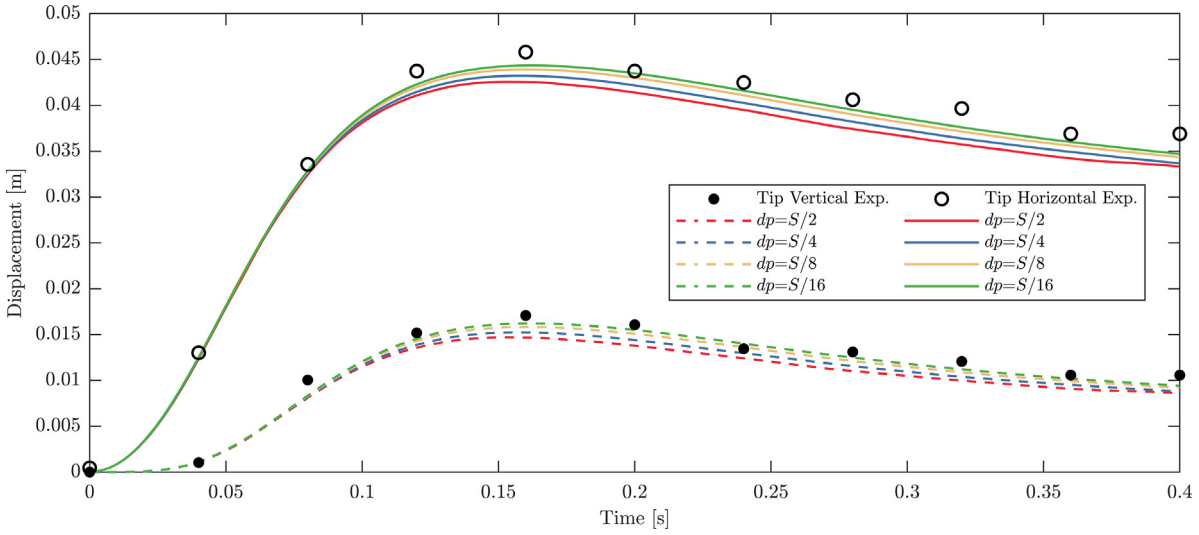

Fig. 18. Horizontal and vertical displacement histories for the tip of the beam (point A) for different particle resolutions and $N = 32$ compared to the experimental reference [63].

Table 4
RMSE estimation between experimental and numerical results for horizontal and vertical displacement of the tip of the beam (point A).

Displacement	Horizontal				Vertical			
dp	*S/2*	*S/4*	*S/8*	*S/16*	*S/2*	*S/4*	*S/8*	*S/16*
RSME	0.0027	0.0022	0.0016	0.0012	0.0017	0.0014	0.0010	0.0008

could well represent the overall system evolution. Fig. 17 reports a vertical cross section of the system along an axis of symmetry for the system, which is used to configure the 2-D numerical environment for this investigation. To support this assumption, apart from the accuracy that the 2-D model in [63] showed, other researchers have made comparison between 2-D and 3-D cases [64,65], de facto recollecting very small deviations between the two solutions.

In this investigation, the parameters that describe the flexible element configuration have been set in accordance with the reference one (i.e., material density $\rho = 1100$ kg/m^3, Poisson's ratio $\nu = 0.50$), except for some details that are given in the following. Firstly, the rubber plate was approximated by [63] as a linear elastic model with Young's modulus $E = 12$ MPa and Poisson's ratio $\nu = 0.40$. However, in the present work, a more compelling modelling procedure was enforced following the mechanical stress–strain characterisation performed by and reported in [66]. This has led structural solvers with advanced capabilities to implement a hyper-elastic material relationship, and thus improving the model accuracy [8,9,64,67]. Nevertheless, the simulations performed using this coupling employ a linear elasticity model and thus, it is only possible to constrain the beam response to obey an initial Young's modulus defined as the secant modulus from the stress–strain relationship at a strain of 0.02 (available in Fourey et al. [9]), giving back a value of $E = 6.50$ MPa. Lastly, the beam has been modelled with $N = 32$ for all the cases.

The accuracy of the numerical model is investigated by analysing the results shown in Figs. 18 and 19, and also considering the results provided in Table 4. In Fig. 18, the beam tip displacement in the vertical (dashed lines) and the horizontal (solid lines) directions is obtained from four different simulations and compared against the experimental reference. The objective of this plot is to provide an evaluation of the accuracy sensitivity to the particle resolution, as for each simulation a decreasing particle size is used. It can be noticed that the results tend to converge to the reference data when increasing the resolution. Therefore, the four resolutions provide a consistent beam response to the fluid kinematics.

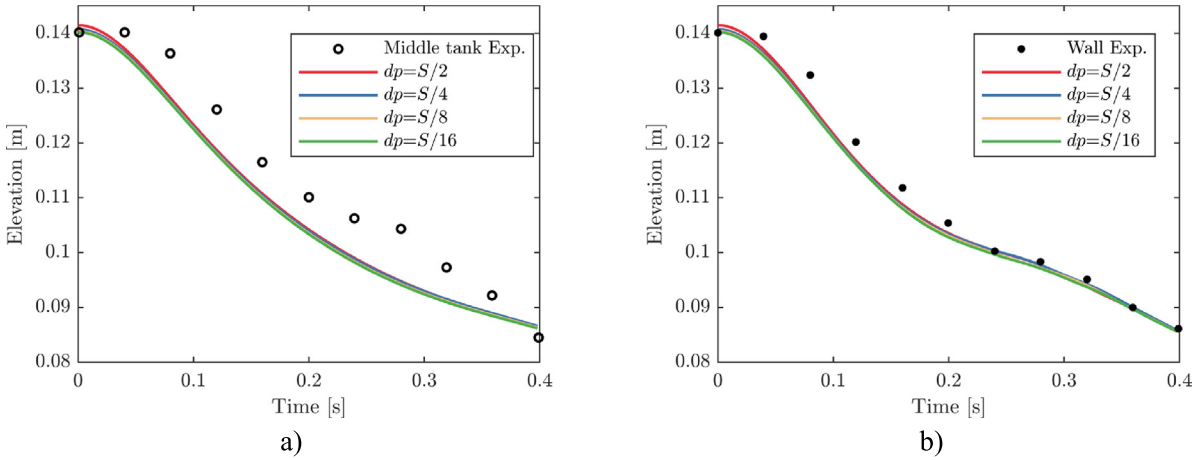

Fig. 19. Water level evolution for different particle resolutions in the middle of the tank (a) and just behind the gate (b).

As anticipated, Table 4 sides the description of this case providing a quantitative assessment of the performance of the model by using the root-mean square error (RMSE) estimator. Thus, the continuous representation provided in Fig. 18 for the numerical model results is first discretised into a set of ten data points that temporally correspond to the experimental sampling time. The RMSE operator processes the dataset and provides the figures that are reported in the following table, for both horizontal and vertical displacement. The results show that the RMSE value decreases with increasing resolution for both horizontal and vertical displacements of the tip. Therefore, studied numerical configurations provide a similar accuracy on account of the experimental solution and provide a clear convergence trend to the reference experimental solution as well.

Fig. 19 shows a comparison of the water level in the middle of the tank (x = 0.05 m) and close to the gate's wall (x = 0.09 m), with only the lowest resolution deviating from the numerical trend established by the others. From the two charts in Fig. 19, it is clear that the numerical model is able to capture the overall water discharge phenomenon, except for a persistent in-time overestimation. On this account, the reference paper [63] reports a similar deviation for the water level evolution at the two locations, explaining that the faster water discharge observed in the numerical model would likely be due to an excess of initial deformation in the beam. Conversely, another investigative work by [9] that provides a similar comparison, suggested that there might be a time shift between the reference displacement and the water level data. The authors lean for the latter reasoning since a slight time shift in the water discharge would deliver much closer agreement and, at the same time, since it is more plausible on account of the accuracy shown by the model in retracing the gate motion.

In closing, six rendered views of the simulations are proposed in Fig. 20 for six-time steps where the two separated colour bars indicate the fluid pressure and structure stress, respectively. They correspond to the beginning of the water discharge (first row), where the beam experiences sudden changes in the beam stress distribution, then the level of stress becomes gradually steadier as the water discharge increases. From the fourth (second row) it can be noticed that the beam achieves a sort of stationary posture, where the fluid forces are at equilibrium with the elastic recentring force of the system (Fig. 18 from *Time* = 0.16 s). Note that the beam stress field here is almost unchanged from one snapshot to the other, and this reflects the small variation in maximum displacement.

Furthermore, Fig. 21 shows the instant of the simulation when the tip of the elastic structure reaches its maximum deflection (*Time* = 0.16 s), where the fluid pressure and the stress field for the elastic gate are represented considering the SPH resolution *dp* = S/16. This much more zoomed visualisation of the numerical configuration captured at a given time offers the possibility to appreciate the quality of the resolved pressure field, which is very smooth. Such smoothness is preserved at the discharge cross section that develops soon after the tip of the beam, where a new free surface and the pressure gradient is the highest. On the other hand, the zoomed representation of the beam confirms equally high quality in the stress response. The spectrum of the colour bar that indicates beam stress in such that blue refers to the tension and red, compression. Two main features may be immediately apparent from the figures, and they are a direct consequence of the employed model to describe the beam. First, the range is perfectly

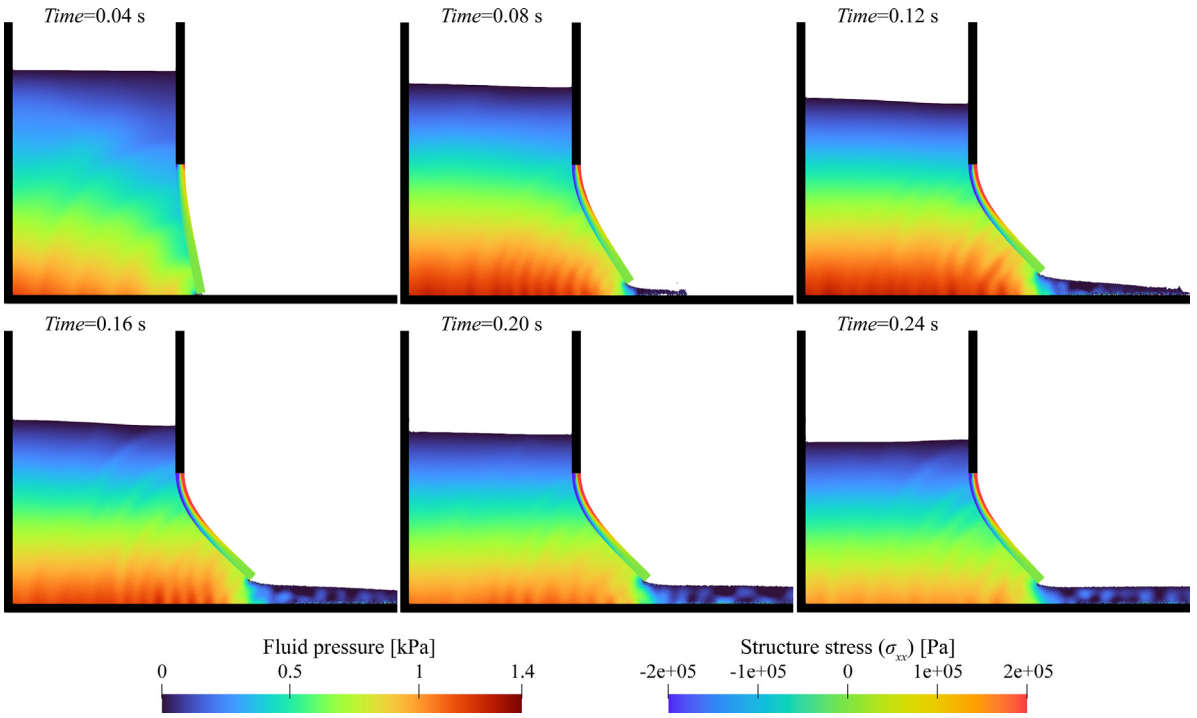

Fig. 20. Snapshots of the simulation of the elastic gate with $dp = S/16$ in which the fluid pressure and structure stress are represented.

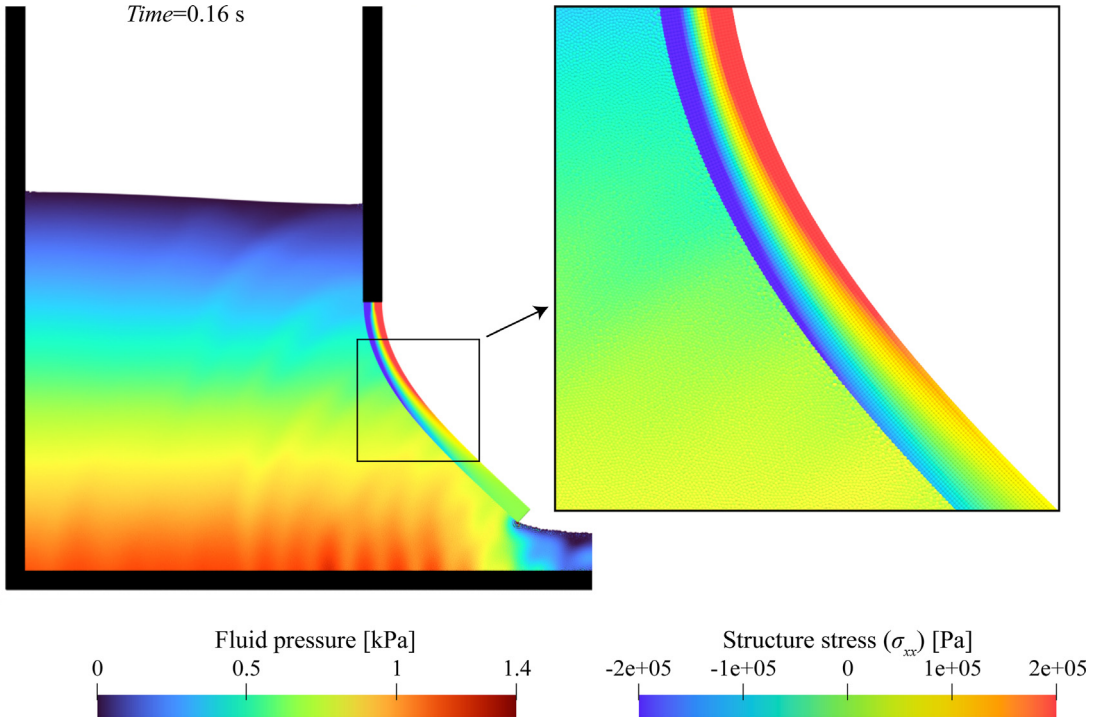

Fig. 21. Fluid pressure and structure stress at $Time = 0.16$ s of the elastic gate case where the structure experiences the maximum deflection.

Table 5
Performance of the breaking water-column with an elastic gate case for $N = 32$.

dp	Structure particles	Fluid particles	Segments (N)	SPH steps	DualSPHysics runtime [s]	Chrono runtime [s]	Total runtime [s]	% Chrono
S/2	99	2184	32	30 724	108	126	235	54
S/4	320	8848	32	61 547	300	251	551	45
S/8	1143	35 612	32	122 761	641	466	1106	42
S/16	4318	142 912	32	244 922	1609	995	2604	38

symmetric, and it results from the fact that fluid actions are (axial and longitudinal ones) computed using the SPH boundary particles, but then they are applied to the nodes located on the axis of the beam. Secondly, there is a layer of particles, located in the middle of the beam (neutral axis) that does not experience any stress due to the fact that only the bending moment is considered, thus not having axial forces. Note that the selected range for σ_{xx} allows describing fully the stress value spectrum and thus comparison can be visually made to other references such as (Zhang et al. [68]).

Table 5 shows the performance results for the third benchmark presented in this work, defining four different SPH resolutions ($dp = S/2$, $dp = S/4$, $dp = S/8$ and $dp = S/16$). In all the cases, the beam is modelled with $N = 32$, and a physical time $Time = 0.40$ s is simulated. When the number of particles simulated increases, due to the use of progressively finer interparticle spacings, both the DualSPHysics runtime and the SPH time steps proportionally increase. Likewise, as it can be noticed from the seventh column, the Project Chrono runtime is influenced in spite of having a constant resolution of the FEA solver. This occurs due to the growing number of calls to the FEA solver that corresponds to the SPH steps. This fact is clear when the percentage of time consumed by Project Chrono is considered, which is quite similar in all cases.

5.4. A dam break impacting a flexible obstacle

In contrast with the testing performed prior within this paper, the nature of the fourth benchmark comprises a much violent fluid–structure interaction, characterised by large displacements and harsh accelerations of the solid phase with respect to the fluid one. The test proposed by Liao et al. [69] comprises a breaking water column impacting a rubber plate in a 3-D confined environment, in which multi-phase effects become relevant for the correct simulation of the obstacle displacement. Within the scope of this research, the impact of the water column and the flow over the flexible obstacle is taken as a reference up to 0.80 s because the multiphase water–air interaction that happens after cannot be captured by the present solver. The sketch of the problem is given in Fig. 22. In the experiment, the elastic baffle is made of rubber with thickness $S = 0.004$ m, length $L = 0.090$ m, density $\rho = 1161.54$ kg/m^3, and Young's modulus $E = 3.50$ MPa. The plate is placed vertically at 0.40 m away from the right-hand side of the water column, and it is deployed such a way that the cross section indicated by point A can be considered the only boundary surface clamped to the experimental water tank. On the other hand, point B is considered representative of the free end of this cantilevered plate. It is important to mention at this stage that the plate width takes up the whole width of the tank (0.10 m), and as so happens, this is very handy as the dynamics of the system is well represented by its middle plane, providing the basis for testing numerical solvers considering 2-D environments. During the test, the motion of the baffle was monitored using a visual tracking system, and the motion for three markers was recorded; in the following, data that refers to Marker 1 (0.0875 m above the tank bottom) is used for comparison purposes.

For the numerical model, the water column height $H = 0.20$ m is discretised with density $\rho = 997$ kg/m^3 and using a speed of sound $c_s = 50$ m/s. It is kept still up to time zero, when the removable gate starts moving upward at an imposed velocity that corresponds to the motion law given in the reference work. The flexible plate comprises $N = 32$ Euler–Bernoulli beam segments with the following properties: a corrected Young's modulus $\hat{E} = 4.39$ MPa is obtained from Eq. (40) and Poisson's ratio $\nu = 0.45$. The numerical discretisation for a resolution that corresponds to $dp =$ S/4 (1 mm) is visualised in Fig. 22.

Four SPH resolutions are considered ($dp = S/4$, $dp = S/8$, $dp = S/16$ and $dp = S/32$), while keeping a fixed number of segments ($N = 32$) to solve this benchmark numerically. The response of the solver for the four cases listed before is arranged in a chart and reported in Fig. 23 by comparing the experimental data for the horizontal

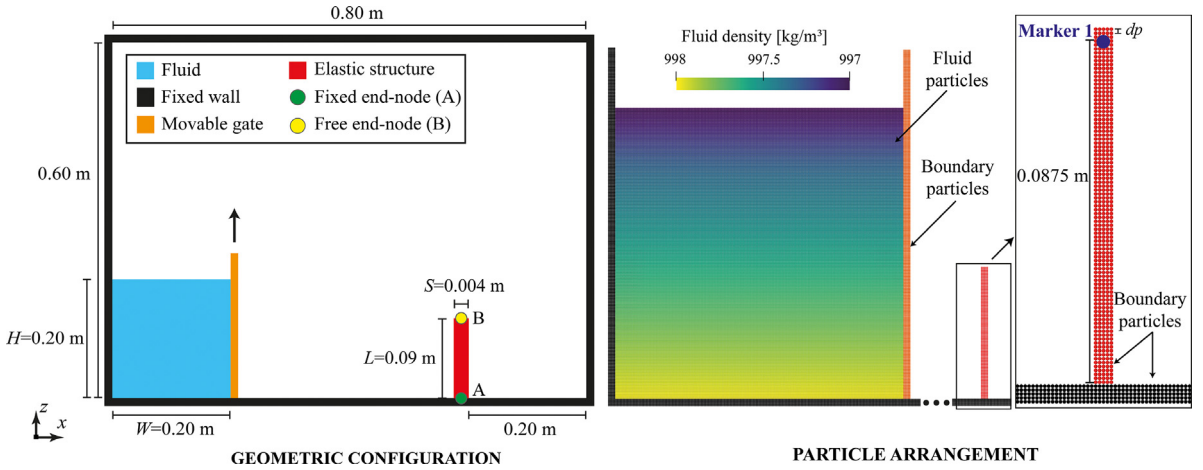

Fig. 22. Initial configuration of the dam break impacting a flexible obstacle and its particle discretisation for the SPH resolution $dp = S/4$.

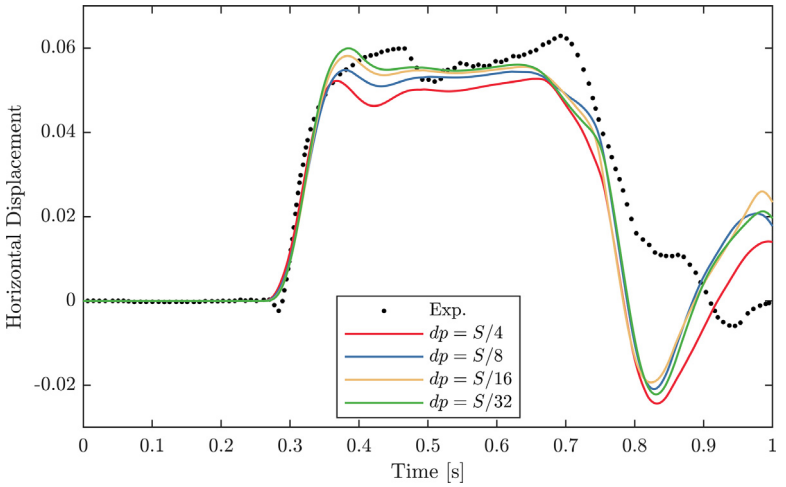

Fig. 23. Horizontal displacement histories for the tip of the beam (Marker 1) for different particle resolutions (dp) and $N = 32$ compared to the experimental reference [69].

displacement of Marker 1 [69] against the same quantity computed from the numerical simulations. The description of this test case is further completed by Fig. 24 that shows six visualisations at relevant steps, which collect particle information on the fluid pressure (colour bar on the left) and structure stress (colour bar on the right).

The model predicts the response of the beam under the free-surface flow impact up to $Time = 0.50$ s, whereas it drops in agreement due to the influence of the air phase on the overall dynamic of the fluid phase, as suggested by previous literature dealing with this case. A more detailed discussion can be found in Liao et al. [69] and in Sun et al. [11] on the effect of multi-phase interaction on the accuracy of this specific problem. Regardless, this benchmark is very useful to test the stability and accuracy of FSI solvers. The proposed one shows similar features to other single-phase solvers (see for instance Khayyer et al. [70] and O'Connor & Rogers [14]). More specifically, the impact instant, which mostly depends on the accuracy of the fluid phase is well captured by providing a consistent and precise instant for the four resolutions around $Time = 0.27$ s (first frame of Fig. 24). From this point on, the impact of the waterfront resolves in sudden beam deformations, which start cumulating as the tip of the beam goes towards its maximum deformation. Around $Time = 0.32$ s (second frame of Fig. 24), the fluid mass is deflected by the beam, which in turn, experiences a deformed shape comprising two changes in curvature. However, the accuracy during this phase indicates quite remarkable sensitivity to the fluid resolution, as the displacement of the beam tends

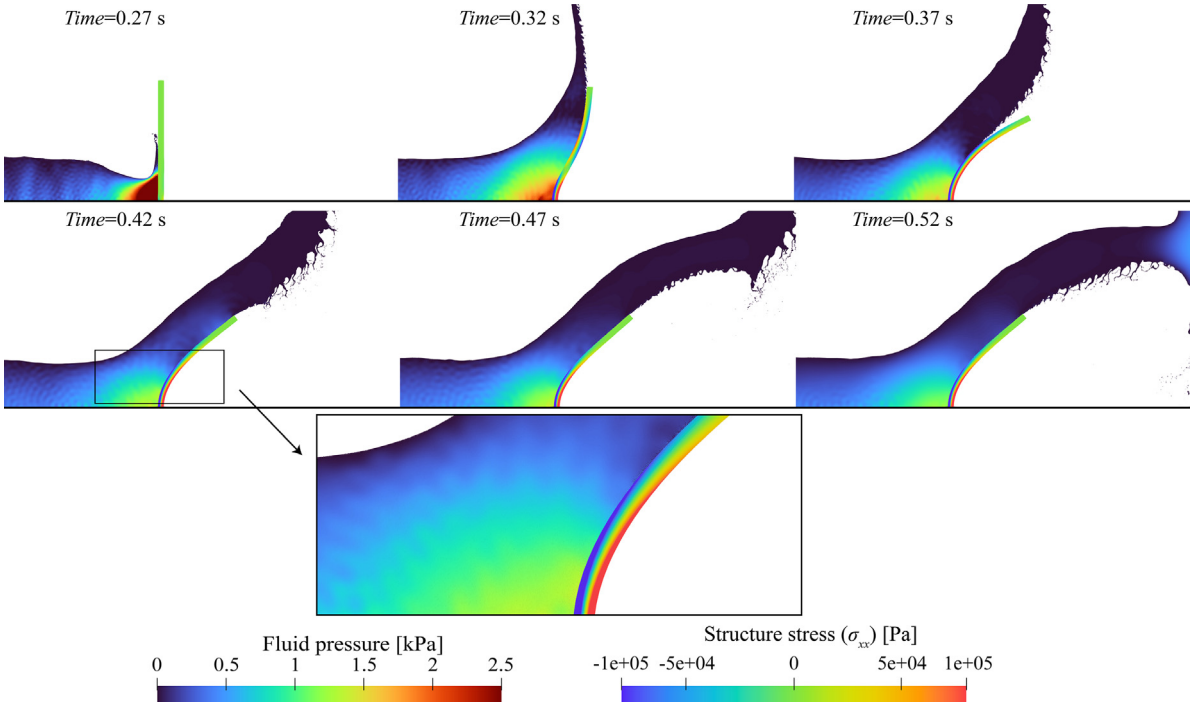

Fig. 24. Snapshots of the simulation of dam break impacting a flexible obstacle with $dp = S/32$ in which the fluid pressure and structure stress are represented.

towards a maximum displacement of around 0.06 m, and this is highlighted in the third frame of Fig. 24. The beam, at this instant, has shifted its deformed shape to show a linear bending moment distribution. Note that the tip of the beam has slightly detached the fluid main flow due to a *backlash* effect. The ensuing phase is characterised by a sort of steady state due to a substantial constant flow that maintains an almost constant state of stress in the beam, as shown in the fourth and fifth frames in Fig. 24. Lastly, the sixth frame in Fig. 24 determines the point at which the multiphase air–water interaction begins due to the trapped air below the flow that is still in contact with the lateral wall. However, this does not become apparent in terms of beam deflection till $Time = 0.60$ s when the horizontal displacement diverges from the reference solution. After this, the response of the system is no longer consistent since the air trapped in the cavity that forms downstream of the beam heavily affects the hydrodynamics of the system [11]. It is also included a zoomed view of the snapshot that corresponds to $Time = 0.42$ s, where it can be seen the representation of the stress along the beam.

Table 6 shows the performance results for the fourth benchmark presented in this work, where a physical time $Time = 1.00$ s is simulated. The four different SPH resolutions ($dp = S/4$, $dp = S/8$, $dp = S/16$ and $dp = S/32$) are performed, while the beam is modelled with $N = 32$ for all the cases. It can be noticed that when the number of particles simulated increases, due to the use of higher SPH resolutions, both the DualSPHysics runtime and the SPH time steps increase accordingly. Moreover, the Project Chrono runtime is slightly affected by the SPH resolution, due to the growing number of calls to the FEA solver that corresponds to the SPH steps. However, the percentage of time consumed by Project Chrono decreases when the number of particles increase. Regarding the highest SPH resolution reported here ($dp = S/32$), which corresponds to more than 2.5 million of fluid particles, the computational cost of solving the structure is 15% of the total runtime.

6. Conclusions and future work

This paper has presented a novel SPH-FEA solver coupling between the open source DualSPHysics and the Project Chrono library. The outcome software leverages the meshless SPH method to deal with the resolution of

Table 6
Performance of the flexible obstacle case for $N = 32$.

dp	Structure particles	Fluid particles	Segments (N)	SPH steps	DualSPHysics runtime [s]	Chrono runtime [s]	Total runtime [s]	% Chrono
S/4	455	40 401	32	158 938	1299	619	1918	32
S/8	1629	160 801	32	322 158	3864	1120	4984	22
S/16	6137	641 601	32	676 281	8824	2252	11 076	20
S/32	23 793	2 563 200	32	1 342 800	35 990	6406	42 396	15

the Navier–Stokes' equations to simulate fluid phases, whereas the non-linear FEM-based FEA module herein solves the dynamics of elastic structures. The proposed coupled method offers many advantages for the simulations of FSI problems thanks to the blending of the two solvers. On the one hand, the strength of the SPH-based fluid solver, very powerful in addressing violent flows and dealing with free-surface flows. On the other, the relatively inexpensive Euler–Bernoulli beam model and the Lagrangian capabilities of the Corotational framework for flexible elements capable of accommodating large displacements. Ultimately, it is important to mention that the structure of the two-way algorithm herein presented, in which the two systems communicate via exchanging forces and positions, has demonstrated to be extremely robust and thus providing a key distinctive feature to this new implementation: *uncoupled resolutions*.

Following an increasing level of complexity, four standardised validation cases have been proposed as references to validate the numerical framework. Firstly, the numerical prediction for a freely oscillating cantilevered beam, in which the motion is induced by very specific initial conditions, was validated contrasting with an analytical solution. The comparison shows a satisfactory matching, though overestimating the fundamental (or first) period of vibration of the structural system within a 2-% range, whereas perfectly capturing the motion amplitude. This initial investigation was critical for assessing minimum requirements to optimise the beam mesh, and the accuracy that the structural solver requires to perform the subsequent validation tasks.

Secondly, a proper case of fluid interacting with a structure has been set up. Despite its simplicity, a double-clamped horizontal beam supporting a pseudo-static water column has revealed to be extremely useful in estimating the model precision, as widely recognised in the reported literature. Again, a theoretical solution, based on legitimated hypotheses, provides the reference framework to compare with, and the proposed model shows accuracy in estimating the beam mid-point displacement. Additionally, the energy dissipation of the structural integrator has been thoroughly checked for long simulations. The results provided another metric to highlight the accuracy and precision of the solver, but in more general terms, they allow us to remark the coupling strategy ensures the energy conservation of the system. The results sourced from the performed simulations highlight the pros of having the uncoupled-resolution feature, which, in principle, allows to tune the model in accordance with the expected response of the system, thus smartly allocating the computational resources.

Thirdly, the discharge of a water reservoir adjusted by a flexible gate has been simulated following the experimental setup investigated in [63]. The surface of the elastic element (the gate) interacts with a medium-speed flow that also develops relevant interactions between the beam's displacement and the fluid transient states. Relatively low fluid resolutions delivered good agreement on account of a well-resolved beam kinematics, and, as the results showed, the first investigated case fails in estimating the beam deflection only when the particle size hampers the correct prediction of the water discharge, essentially correlated to the fluid resolution.

Lastly, the fourth case achieves the maximum level of complexity among the cases presented in this paper. A breaking water column runs over a flexible beam which in an initial phase deflects the flow that then chaotically scatters across the whole closed environment. Again, the numerical model successfully predicts the overall FSI system dynamics, while proving very resilient to such extreme spatial changes. The sensitivity analysis that was performed by considering both solid and fluid phases proved that even cases with a very limited number of particle layers can suffice. It should be noted that the air phase was not simulated in this work. Therefore, the reported numerical results are not in perfect agreement when the influence of the air phase on the overall dynamic of the fluid phase plays an important role, as discussed in [11].

In this work, the proposed coupling has been described and used with respect to a two-dimensional environment, but its extension to a 3-D one should be theoretically possible. Future work will comprise the implementation and validations of the presented framework for 3-D simulations, for which the effect of rotational forces or torques on the

nodes will be considered for experiencing bending and torsion in the beam. To sum up, the extension will keep using Euler–Bernoulli-based beam elements that, in spite of being capable of describing only particular physical systems, can provide an excellent balance between the solid solver computational cost and the quality of the outcome. It is expected that the impact of computational performance of the structural solver will greatly diminish when moving to full 3-D simulations, as its cost will mostly stay the same while the fluid simulation runtime will be dominant.

In addition, future implementation will contain a builder for structural systems that can comprise multiple beams assembled together to form any structure configuration, on which the use of the Rayleigh damping model will be activated. As it is the writing of this paper, multiphysics simulations comprising free surface flows and flexible elements in 3D are still restricted to academic cases and have not yet seen applications to engineering problems mainly due to their prohibitive computational cost.

Declaration of competing interest

The authors declare that they have no known competing financial interests or personal relationships that could have appeared to influence the work reported in this paper.

Data availability

Data will be made available on request.

Acknowledgements

Funding for open access charge: Universidade de Vigo/CISUG, Spain. This work was supported by the project SURVIWEC PID2020-113245RB-I00 financed by Ministerio de Ciencia e Innovación (MCIN/AEI/10.13039/501100011033) and by the project ED431C 2021/44 *"Programa de Consolidación e Estructuración de Unidades de Investigación Competitivas" financed by Xunta de Galicia*, *Consellería de Cultura, Educación e Universidade*. This study forms part of the Marine Science programme (ThinkInAzul) supported by *Ministerio de Ciencia e Innovación and Xunta de Galicia* with funding from European Union NextGenerationEU (PRTR-C17.I1) and European Maritime and Fisheries Fund. Grant TED2021-129479A-I00 funded by Ministerio de Ciencia e Innovación (MCIN/AEI/10.13039/501100011033) and by the "European Union NextGenerationEU/PRTR".

I. Martínez-Estévez acknowledges funding from *Xunta de Galicia* under *"Programa de axudas á etapa predoutoral da Consellería de Cultura, Educación e Universidades da Xunta de Galicia"* (ED481A-2021/337). J. El Rahi is a Ph.D. fellow (fellowship 1115821N) of the Research Foundation Flanders (FWO). B. Tagliafierro acknowledges financial support for this publication by the Fulbright Schuman Program, which is administered by the Fulbright Commission in Brussels and jointly financed by the U.S. Department of State, and the Directorate-General for Education, Youth, Sport and Culture (DG.EAC) of the European Commission. Its contents are solely the responsibility of the authors and do not necessarily represent the official views of the Fulbright Program, the Government of the United States, or the Fulbright Commission in Brussels. The authors wish to acknowledge the support provided by the Project Chrono developers: Prof. Dan Negrut and Dr. Radu Serban (University of Wisconsin–Madison, US), and Prof. Alessandro Tasora (University of Parma, Italy).

References

[1] M.S. Shadloo, G. Oger, D. Le Touzé, Smoothed particle hydrodynamics method for fluid flows, towards industrial applications: Motivations, current state, and challenges, Comput. Fluids 136 (2016) 11–34, http://dx.doi.org/10.1016/j.compfluid.2016.05.029.

[2] M.-C. Hsu, Y. Bazilevs, Fluid–structure interaction modeling of wind turbines: simulating the full machine, Comput. Mech. 50 (2012) 821–833, http://dx.doi.org/10.1007/s00466-012-0772-0.

[3] R. Roul, A. Kumar, Fluid-structure interaction of wind turbine blade using four different materials: Numerical investigation, Symmetry 12 (2020) 1467, http://dx.doi.org/10.3390/sym12091467.

[4] F.-B. Tian, H. Dai, H. Luo, J.F. Doyle, B. Rousseau, Fluid–structure interaction involving large deformations: 3D simulations and applications to biological systems, J. Comput. Phys. 258 (2014) 451–469, http://dx.doi.org/10.1016/j.jcp.2013.10.047.

[5] S. Bailoor, A. Annangi, J.H. Seo, R. Bhardwaj, Fluid–structure interaction solver for compressible flows with applications to blast loading on thin elastic structures, Appl. Math. Model. 52 (2017) 470–492, http://dx.doi.org/10.1016/j.apm.2017.05.038.

[6] D.J. Benson, Computational methods in Lagrangian and Eulerian hydrocodes, Comput. Methods Appl. Mech. Eng. 99 (1992) 235–394, http://dx.doi.org/10.1016/0045-7825(92)90042-I.

[7] A. Khayyer, H. Gotoh, Y. Shimizu, On systematic development of FSI solvers in the context of particle methods, J. Hydrodyn. 34 (2022) 395–407, http://dx.doi.org/10.1007/s42241-022-0042-3.
[8] Z. Li, J. Leduc, J. Nunez-Ramirez, A. Combescure, J.-C. Marongiu, A non-intrusive partitioned approach to couple smoothed particle hydrodynamics and finite element methods for transient fluid–structure interaction problems with large interface motion, Comput. Mech. 55 (2015) 697–718, http://dx.doi.org/10.1007/s00466-015-1131-8.
[9] G. Fourey, C. Hermange, D. Le Touzé, G. Oger, An efficient FSI coupling strategy between Smoothed Particle Hydrodynamics and Finite Element methods, Comput. Phys. Commun. 217 (2017) 66–81, http://dx.doi.org/10.1016/j.cpc.2017.04.005.
[10] C. Chen, W.-K. Shi, Y.-M. Shen, J.-Q. Chen, A.-M. Zhang, A multi-resolution SPH-FEM method for fluid–structure interactions, Comput. Methods Appl. Mech. Eng. 401 (2022) 115659, http://dx.doi.org/10.1016/j.cma.2022.115659.
[11] P.N. Sun, D. Le Touzé, A.-M. Zhang, Study of a complex fluid–structure dam-breaking benchmark problem using a multi-phase SPH method with APR, Eng. Anal. Bound. Elem. 104 (2019) 240–258, http://dx.doi.org/10.1016/j.enganabound.2019.03.033.
[12] P.-N. Sun, D. Le Touzé, G. Oger, A.-M. Zhang, An accurate FSI-SPH modeling of challenging fluid–structure interaction problems in two and three dimensions, Ocean Eng. 221 (2021) 108552, http://dx.doi.org/10.1016/j.oceaneng.2020.108552.
[13] S. Capasso, B. Tagliafierro, I. Martínez-Estévez, J.M. Domínguez, A.J.C. Crespo, G. Viccione, A DEM approach for simulating flexible beam elements with the Project Chrono core module in DualSPHysics, Comput. Part. Mech. 9 (2022) 969–985, http://dx.doi.org/10.1007/s40571-021-00451-9.
[14] J. O'Connor, B.D. Rogers, A fluid–structure interaction model for free-surface flows and flexible structures using smoothed particle hydrodynamics on a GPU, J. Fluids Struct. 104 (2021) 103312, http://dx.doi.org/10.1016/j.jfluidstructs.2021.103312.
[15] Y. Ren, A. Khayyer, P. Lin, X. Hu, Numerical modeling of sloshing flow interaction with an elastic baffle using SPHinXsys, Ocean Eng. 267 (2023) 113110, http://dx.doi.org/10.1016/j.oceaneng.2022.113110.
[16] A.M.A. Nasar, B.D. Rogers, A. Revell, P.K. Stansby, Flexible slender body fluid interaction: Vector-based discrete element method with Eulerian smoothed particle hydrodynamics, Comput. Fluids 179 (2019) 563–578, http://dx.doi.org/10.1016/j.compfluid.2018.11.024.
[17] A. Khayyer, H. Gotoh, H. Falahaty, Y. Shimizu, An enhanced ISPH–SPH coupled method for simulation of incompressible fluid–elastic structure interactions, Comput. Phys. Commun. 232 (2018) 139–164, http://dx.doi.org/10.1016/j.cpc.2018.05.012.
[18] D.S. Morikawa, M. Asai, Coupling total Lagrangian SPH–EISPH for fluid–structure interaction with large deformed hyperelastic solid bodies, Comput. Methods Appl. Mech. Eng. 381 (2021) 113832, http://dx.doi.org/10.1016/j.cma.2021.113832.
[19] J.J. Monaghan, Smoothed particle hydrodynamics, Rep. Progr. Phys. 68 (2005) 1703, http://dx.doi.org/10.1088/0034-4885/68/8/R01.
[20] E.-S. Lee, C. Moulinec, R. Xu, D. Violeau, D. Laurence, P. Stansby, Comparisons of weakly compressible and truly incompressible algorithms for the SPH mesh free particle method, J. Comput. Phys. 227 (2008) 8417–8436, http://dx.doi.org/10.1016/j.jcp.2008.06.005.
[21] J.J. Monaghan, R.A. Gingold, Shock simulation by the particle method SPH, J. Comput. Phys. 52 (1983) 374–389, http://dx.doi.org/10.1016/0021-9991(83)90036-0.
[22] M. Antuono, A. Colagrossi, S. Marrone, D. Molteni, Free-surface flows solved by means of SPH schemes with numerical diffusive terms, Comput. Phys. Commun. 181 (2010) 532–549, http://dx.doi.org/10.1016/j.cpc.2009.11.002.
[23] A. Khayyer, Y. Shimizu, T. Gotoh, H. Gotoh, Enhanced resolution of the continuity equation in explicit weakly compressible SPH simulations of incompressible free-surface fluid flows, Appl. Math. Model. 116 (2023) 84–121, http://dx.doi.org/10.1016/j.apm.2022.10.037.
[24] D.D. Meringolo, A. Colagrossi, S. Marrone, F. Aristodemo, On the filtering of acoustic components in weakly-compressible SPH simulations, J. Fluids Struct. 70 (2017) 1–23, http://dx.doi.org/10.1016/j.jfluidstructs.2017.01.005.
[25] S.J. Cummins, M. Rudman, An SPH projection method, J. Comput. Phys. 152 (1999) 584–607, http://dx.doi.org/10.1006/jcph.1999.6246.
[26] A. Skillen, S. Lind, P.K. Stansby, B.D. Rogers, Incompressible smoothed particle hydrodynamics (SPH) with reduced temporal noise and generalised Fickian smoothing applied to body–water slam and efficient wave–body interaction, Comput. Methods Appl. Mech. Eng. 265 (2013) 163–173, http://dx.doi.org/10.1016/j.cma.2013.05.017.
[27] J.M. Domínguez, G. Fourtakas, C. Altomare, R.B. Canelas, A. Tafuni, O. García-Feal, I. Martínez-Estévez, A. Mokos, R. Vacondio, A.J.C. Crespo, B.D. Rogers, P.K. Stansby, M. Gómez-Gesteira, DualSPHysics: from fluid dynamics to multiphysics problems, Comput. Part. Mech. 9 (2022) 867–895, http://dx.doi.org/10.1007/s40571-021-00404-2.
[28] J.M. Domínguez, A.J. Crespo, M. Gómez-Gesteira, Optimization strategies for CPU and GPU implementations of a smoothed particle hydrodynamics method, Comput. Phys. Commun. 184 (2013) 617–627.
[29] A. Tasora, R. Serban, H. Mazhar, A. Pazouki, D. Melanz, J. Fleischmann, M. Taylor, H. Sugiyama, D. Negrut, Chrono: An open source multi-physics dynamics engine, in: T. Kozubek, R. Blaheta, J. Šístek, M. Rozložník, M. Čermák (Eds.), High Performance Computing in Science and Engineering, Springer International Publishing, Cham, 2016, pp. 19–49, http://dx.doi.org/10.1007/978-3-319-40361-8_2.
[30] R.B. Canelas, M. Brito, O.G. Feal, J.M. Domínguez, A.J.C. Crespo, Extending DualSPHysics with a Differential Variational Inequality: modeling fluid-mechanism interaction, Appl. Ocean Res. 76 (2018) 88–97, http://dx.doi.org/10.1016/j.apor.2018.04.015.
[31] I. Martínez-Estévez, J.M. Domínguez, B. Tagliafierro, R.B. Canelas, O. García-Feal, A.J.C. Crespo, M. Gómez-Gesteira, Coupling of an SPH-based solver with a multiphysics library, Comput. Phys. Commun. 283 (2023) 108581, http://dx.doi.org/10.1016/j.cpc.2022.108581.
[32] P. Ropero Giralda, A. Crespo, B. Tagliafierro, C. Altomare, J.M. Domínguez, M. Gómez-Gesteira, G. Viccione, Efficiency and survivability analysis of a point-absorber wave energy converter using DualSPHysics, Renew. Energy 162 (2020) 1763–1776, http://dx.doi.org/10.1016/j.renene.2020.10.012.
[33] B. Tagliafierro, I. Martínez-Estévez, J.M. Domínguez, A.J.C. Crespo, M. Göteman, J. Engström, M. Gómez-Gesteira, A numerical study of a taut-moored point-absorber wave energy converter with a linear power take-off system under extreme wave conditions, Appl. Energy 311 (2022) 118629, http://dx.doi.org/10.1016/j.apenergy.2022.118629.
[34] H. Wendland, Piecewise polynomial, positive definite and compactly supported radial functions of minimal degree, Adv. Comput. Math. 4 (1995) 389–396, http://dx.doi.org/10.1007/BF02123482.

[35] E.Y.M. Lo, S. Shao, Simulation of near-shore solitary wave mechanics by an incompressible SPH method, Appl. Ocean Res. 24 (2002) 275–286, http://dx.doi.org/10.1016/S0141-1187(03)00002-6.
[36] R.A. Dalrymple, B.D. Rogers, Numerical modeling of water waves with the SPH method, Coast. Eng. 53 (2006) 141–147, http://dx.doi.org/10.1016/j.coastaleng.2005.10.004.
[37] G. Fourtakas, J.M. Dominguez, R. Vacondio, B.D. Rogers, Local uniform stencil (LUST) boundary condition for arbitrary 3-D boundaries in parallel smoothed particle hydrodynamics (SPH) models, Comput. Fluids 190 (2019) 346–361, http://dx.doi.org/10.1016/j.compfluid.2019.06.009.
[38] D. Molteni, A. Colagrossi, A simple procedure to improve the pressure evaluation in hydrodynamic context using the SPH, Comput. Phys. Commun. 180 (2009) 861–872, http://dx.doi.org/10.1016/j.cpc.2008.12.004.
[39] M. Antuono, A. Colagrossi, S. Marrone, Numerical diffusive terms in weakly-compressible SPH schemes, Comput. Phys. Commun. 183 (2012) 2570–2580, http://dx.doi.org/10.1016/j.cpc.2012.07.006.
[40] A. English, J.M. Domínguez, R. Vacondio, A.J.C. Crespo, P.K. Stansby, S.J. Lind, L. Chiapponi, M. Gómez-Gesteira, Modified dynamic boundary conditions (mDBC) for general-purpose smoothed particle hydrodynamics (SPH): application to tank sloshing, dam break and fish pass problems, Comput. Part. Mech. 9 (2022) 911–925, http://dx.doi.org/10.1007/s40571-021-00403-3.
[41] A.J. Crespo, M. Gómez-Gesteira, R.A. Dalrymple, Boundary conditions generated by dynamic particles in SPH methods, Comput., Mater. Continua. 5 (2007) 173–184.
[42] R.A. Dalrymple, O. Knio, SPH Modelling of Water Waves, (2012) 779–787. http://dx.doi.org/10.1061/40566(260)80.
[43] S. Marrone, M. Antuono, A. Colagrossi, G. Colicchio, D. Le Touzé, G. Graziani, δ-SPH model for simulating violent impact flows, Comput. Methods Appl. Mech. Eng. 200 (2011) 1526–1542, http://dx.doi.org/10.1016/j.cma.2010.12.016.
[44] M.B. Liu, G.R. Liu, Restoring particle consistency in smoothed particle hydrodynamics, Appl. Numer. Math. 56 (2006) 19–36, http://dx.doi.org/10.1016/j.apnum.2005.02.012.
[45] R.B. Canelas, J.M. Domínguez, A.J.C. Crespo, M. Gómez-Gesteira, R.M.L. Ferreira, A Smooth Particle Hydrodynamics discretization for the modelling of free surface flows and rigid body dynamics, Int. J. Numer. Methods Fluids 78 (2015) 581–593, http://dx.doi.org/10.1002/fld.4031.
[46] B. Leimkuhler, C. Matthews, Introduction, in: B. Leimkuhler, C. Matthews (Eds.), Molecular Dynamics: With Deterministic and Stochastic Numerical Methods, Springer International Publishing, Cham, 2015, pp. 1–51, http://dx.doi.org/10.1007/978-3-319-16375-8_1.
[47] A.N. Parshikov, S.A. Medin, I.I. Loukashenko, V.A. Milekhin, Improvements in SPH method by means of interparticle contact algorithm and analysis of perforation tests at moderate projectile velocities, Int. J. Impact Eng. 24 (2000) 779–796, http://dx.doi.org/10.1016/S0734-743X(99)00168-2.
[48] J.J. Monaghan, A. Kos, Solitary waves on a cretan beach, J. Waterw., Port, Coast., Ocean Eng. 125 (1999) 145–155, http://dx.doi.org/10.1061/(ASCE)0733-950X(1999)125:3(145).
[49] T. Belytschko, L.W. Glaum, Applications of higher order corotational stretch theories to nonlinear finite element analysis, Comput. Struct. 10 (1979) 175–182, http://dx.doi.org/10.1016/0045-7949(79)90085-3.
[50] C.A. Felippa, B. Haugen, A unified formulation of small-strain corotational finite elements: I, Theory, Comput. Methods Appl. Mech. Eng. 194 (2005) 2285–2335, http://dx.doi.org/10.1016/j.cma.2004.07.035.
[51] C.C. Rankin, B. Nour-Omid, The use of projectors to improve finite element performance, Comput. Struct. 30 (1988) 257–267, http://dx.doi.org/10.1016/0045-7949(88)90231-3.
[52] A. Tasora, P. Masarati, Analysis of rotating systems using general-purpose multibody dynamics, in: P. Pennacchi (Ed.), Proceedings of the 9th IFToMM International Conference on Rotor Dynamics, Springer International Publishing, Cham, 2015, pp. 1689–1701, http://dx.doi.org/10.1007/978-3-319-06590-8_139.
[53] M.A. Crisfield, U. Galvanetto, G. Jelenić, Dynamics of 3-D co-rotational beams, Comput. Mech. 20 (1997) 507–519, http://dx.doi.org/10.1007/s004660050271.
[54] O.A. Bauchau, J.I. Craig, Euler–Bernoulli beam theory, in: O.A. Bauchau, J.I. Craig (Eds.), Structural Analysis, Springer Netherlands, Dordrecht, 2009, pp. 173–221, http://dx.doi.org/10.1007/978-90-481-2516-6_5.
[55] J.M. Gere, S.P. Timoshenko, Mechanics of Materials, Springer US, Boston, MA, 1991.
[56] H.M. Hilber, T.J.R. Hughes, R.L. Taylor, Improved numerical dissipation for time integration algorithms in structural dynamics, Earthq. Eng. Struct. Dyn. 5 (1977) 283–292, http://dx.doi.org/10.1002/eqe.4290050306.
[57] N.M. Newmark, A method of computation for structural dynamics, Trans. Am. Soc. Civ. Eng. 127 (1962) 1406–1433, http://dx.doi.org/10.1061/TACEAT.0008448.
[58] D. Negrut, R. Rampalli, G. Ottarsson, A. Sajdak, On an implementation of the hilber-hughes-taylor method in the context of index 3 differential-algebraic equations of multibody dynamics (DETC2005-85096), J. Comput. Nonlinear Dyn. 2 (2006) 73–85, http://dx.doi.org/10.1115/1.2389231.
[59] L.D. Landau, E.M. Lifshitz, Theory of Elasticity: Volume 7, Pergamon Press, 1970.
[60] S. Timoshenko, S. Woinowsky-Krieger, Theory of Plates and Shells, McGraw-hill, New York, 1959.
[61] G. Fourey, Développement D'Une Méthode de Couplage Fluide Structure SPH Eléments Finis En Vue de Son Application à L'Hydrodynamique Navale (Ph.D.thesis), Ecole Centrale de Nantes, 2012.
[62] F. Xie, W. Zhao, D. Wan, MPS-DEM coupling method for interaction between fluid and thin elastic structures, Ocean Eng. 236 (2021) 109449, http://dx.doi.org/10.1016/j.oceaneng.2021.109449.
[63] C. Antoci, M. Gallati, S. Sibilla, Numerical simulation of fluid–structure interaction by SPH, Comput. Struct. 85 (2007) 879–890, http://dx.doi.org/10.1016/j.compstruc.2007.01.002.
[64] M.-J. Li, Y. Lian, X. Zhang, An immersed finite element material point (IFEMP) method for free surface fluid–structure interaction problems, Comput. Methods Appl. Mech. Eng. 393 (2022) 114809, http://dx.doi.org/10.1016/j.cma.2022.114809.

[65] Z.-F. Meng, A.-M. Zhang, J.-L. Yan, P.-P. Wang, A. Khayyer, A hydroelastic fluid–structure interaction solver based on the Riemann-SPH method, Comput. Methods Appl. Mech. Eng. 390 (2022) 114522, http://dx.doi.org/10.1016/j.cma.2021.114522.

[66] C. Antoci, Simulazione Numerica Dell'Interazione Fluido-Struttura Con la Tecnica SPH, Vol. 100 (Ph.D. thesis), Universita di Pavia, 2006, Ph. D. thesis.

[67] M. McLoone, N.J. Quinlan, Coupling of the meshless finite volume particle method and the finite element method for fluid–structure interaction with thin elastic structures, Eur. J. Mech. B/Fluids 92 (2022) 117–131, http://dx.doi.org/10.1016/j.euromechflu.2021.12.001.

[68] G. Zhang, W. Zhao, D. Wan, Partitioned MPS-FEM method for free-surface flows interacting with deformable structures, Appl. Ocean Res. 114 (2021) 102775, http://dx.doi.org/10.1016/j.apor.2021.102775.

[69] K. Liao, C. Hu, M. Sueyoshi, Free surface flow impacting on an elastic structure: Experiment versus numerical simulation, Appl. Ocean Res. 50 (2015) 192–208, http://dx.doi.org/10.1016/j.apor.2015.02.002.

[70] A. Khayyer, N. Tsuruta, Y. Shimizu, H. Gotoh, Multi-resolution MPS for incompressible fluid-elastic structure interactions in ocean engineering, Appl. Ocean Res. 82 (2019) 397–414, http://dx.doi.org/10.1016/j.apor.2018.10.020.

4.3 A numerical study of a taut-moored point-absorber wave energy converter with a linear power take-off system under extreme wave conditions

The third article is entitled "**A numerical study of a taut-moored point-absorber wave energy converter with a linear power take-off system under extreme wave conditions**" by Tagliafierro, B., **Martínez-Estévez, I.**, Domínguez, J. M., Crespo, A. J. C., Göteman, M., Engström, J., & Gómez-Gesteira, M. Published in the journal Applied Energy in 2022.

Table 3. Information of the journal Applied Energy from 2022 JCR.

	Journal information
Journal	*Applied Energy*
Online ISSN	*1872-9118*
Country	*United Kingdom*
Editorial	*Elsevier*
Impact factor	*11,2*
Quartile	*Q1 (Engineering, Chemical)*

Applied Energy 311 (2022) 118629

Contents lists available at ScienceDirect

Applied Energy

journal homepage: www.elsevier.com/locate/apenergy

A numerical study of a taut-moored point-absorber wave energy converter with a linear power take-off system under extreme wave conditions

Bonaventura Tagliafierro [a], Iván Martínez-Estévez [b], José M. Domínguez [b], Alejandro J.C. Crespo [b,*], Malin Göteman [c], Jens Engström [c], Moncho Gómez-Gesteira [b]

[a] Department of Civil Engineering, University of Salerno, Fisciano, SA, Italy
[b] Environmental Physics Laboratory, CIM-UVIGO, Universidade de Vigo, Ourense, Spain
[c] Department of Electrical Engineering, Uppsala University, Uppsala, Sweden

ARTICLE INFO

Keywords:
Uppsala WEC
Embedded focused waves
NewWave
Extreme events
DualSPHysics
MoorDyn+
Project Chrono
CFD

ABSTRACT

Probably the biggest challenge for wave energy is to ensure survival in harsh offshore conditions, in order to reduce costs for offshore repair operations and downtime, and achieve economic viability. This work presents a reliable numerical tool that can be used to study the dynamics and survivability of wave energy converters in violent wave conditions, possibly cutting down the costs of experimental campaigns. Within the Smoothed Particle Hydrodynamics framework, this research identifies a detailed procedure to model a taut-moored point-absorber wave energy converter together with its inherent power take-off device, which seamlessly exploits its functions of energy harvesting and load bearing. A validation of the DualSPHysics code is provided by contrasting the numerical outcome with a thorough set of data obtained in physical tests with extreme waves, showing that the time-integrated numerical model can capture with good accuracy all the physics involved. The computational fluid dynamics tool is employed to perform a survivability study, modeling high-return period wave conditions for marine structures, and providing guidelines on how to create the numerically best setup to be used for design purposes. A real-like irregular sea state representation, comprising 500 waves, was used to draw insightful indications for the structure optimization to increase the structure's life expectancy, or conversely, to reduce the initial and operational costs.

1. Introduction

A point-absorber wave energy converter (WEC) consists of a floating buoy, whose wave-activated motion is converted into electricity by means of a power take-off (PTO) system [1]. Modeling of these structures should account for device kinematics, hydrodynamics, electromechanics, including different levels of details [2]. Furthermore, their potential should be evaluated when deployed in wave energy farms in which bodies are either interconnected with various technologies [3] or embedded in other systems [4], and their mutual interaction studied according to efficiency of the array layouts [5]. Due to the increased awareness of potential energy availability, offshore areas are becoming increasingly attractive for engineers and investors to implement WECs — this, however, comes at a cost of greater vulnerability to extreme events.

Thanks to knowledge transfer and to purposely developed research projects, wave energy is now on the verge of being competitive on the global market (some latest examples can be found in [6]). As PTO systems are becoming more sophisticated and complex, the investigative tools should evolve to be able to capture the whole behavior of such devices, which, in general, operate without any clear distinctions between harvesting and survival modes. Likewise, the total cost of energy often has been reduced by maximizing energy production of WECs, overly relying on simplified design practices [7], and disregarding other factors such as capital costs and *operation and maintenance* costs, which has led to seeking locations where the power carried by waves is abundant. This can lead to detrimental repercussions on the total lifetime cost, which is summarized in [8]: "there is increasing reason to believe that the first successful WECs may be better off eschewing the hunt for world's largest waves". The same concept was also expressed by [9], in which by utilizing a more comprehensive methodology for assessing the Levelized Cost of Electricity (LCoE), it is demonstrated that areas with less wave power availability can reduce the capital costs.

On the one hand, for what concerns the power production mode, practical approaches [10] and linear models are widely exploited by

* Corresponding author.
E-mail address: alexbexe@uvigo.es (A.J.C. Crespo).

https://doi.org/10.1016/j.apenergy.2022.118629
Received 25 October 2021; Received in revised form 30 December 2021; Accepted 24 January 2022
Available online 11 February 2022

the industry to obtain a sensible reduction in the cost of wave energy through optimization [11], that is, maximizing the energy output. This phase is conveniently dealt with by using potential flow models [12], often linear and for inviscid fluids, which can be used to reproduce the response of WECs under operational sea states. Potential flow-based models comprise a vast variety of solutions (see, for example, [13,14], and [15]), providing fast and relatively accurate answers suitable for investigating performance within serviceability limit states (SLS); however, they do require assumptions to include viscous effects and wave superposition. Some authors have pointed out the great limitations of such approaches [16], issuing several warnings on their use for analyses where highly non-linear interactions take place [7]; however, they can be skillfully used to pinpoint with more precision the conditions (combinations of factors) that are more likely to produce certain scenarios [17].

Structures with significant dynamic response require stochastic modeling of the sea surface and its kinematics by time series, entailing the use of time-domain analyses. Real sea states are best described by irregular wave models, either linear or non-linear. On top of this, other environmental conditions such as wind, tides, and currents can affect the magnitude of the corresponding loads. Unless a tailored design procedure is identified for each specific WEC, it is generally prescribed to use a time-domain simulation of at least three hours to completely represent an extreme event, containing approximately 1000 waves [18], thus providing a statistically treatable significant series of datum points. However, the length of the series is strongly dependent on the quantity being investigated and the nature of failure (e.g., fatigue analysis) [19]. Certain applications may be reliable enough with 300 waves [20], however there is not yet a general rule.

Unfortunately, identifying the conditions that are likely to produce the maximum effects (loads) will require a full understanding of how winds, waves, and currents impact on the system dynamics and subsequently the loads. Within a stochastic framework [21], the environmental variables should be combined, using combinations of their expected values according to their probability of occurring simultaneously. As such, for a system with a large number of degrees of freedom, the number of combinations may well go to the hundreds, hampering the straightforward use of computationally expensive CFD simulations. Approaching the solution of this problem through physical testing is not an option either, for the system would lack any flexibility to respond to combined environmental actions (e.g., waves and currents) and/or changes in the structural configuration (e.g., a damaged connection). Presently, the best way to tackle this problem is through a multi-tier design procedure [22], which may start with linear approaches and frequency-domain analyses, and then proceed with mid-fidelity simulations to narrow the range of environmental conditions [17,23].

Survivability analyses, on the other hand, need more complex and sophisticated models that can guaranteeing high-fidelity modeling procedures in order to solve the dynamics of the system as a whole. For handling WEC simulations, CFD (Computational Fluid Dynamics) methods represent the best option: they do not require heavy preventive assumptions on the fluid mechanics, solving the fluid motion by means of the Navier–Stokes equations in spatial domain and in time, and either meshbased or mesh-less approach can be used (see [24]). Several examples of WEC simulations using CFD frameworks have proven the viability of this approach when the PTO apparatus is also included, following a variety of models (for example, [25–27], or [28]). The significant limitation of the use of CFD tools for the design phases of WECs is their computational cost.

Regardless of the scenario, for CFD simulations of WECs, the Smoothed Particle Hydrodynamics (SPH) method represents a viable approach [24] with the appropriate degree of flexibility in reproducing moving objects under violent fluid motion [29], overcoming mesh distortion issues presented by mesh-based solvers. Nevertheless, few applications can be found in the literature as reviewed in [29,30]. Here, the open-source DualSPHysics code [31], based on the SPH method, becomes a suitable option. Its highly parallelized structure harnesses the computing power of graphics processing unit (GPU) cards, allowing for a speed-up up to 100 when compared with CPU calculations, and has demonstrated accuracy equivalent to well-known meshbased models [32]. Thanks to the coupling with the Project Chronov [33] and MoorDyn+ libraries (based on MoorDyn [34]), the DualSPHysics framework can embed multi-featured complex mechanisms typically deployed in WECs, such as the features of the WEC under study in this work. DualSPHysics has been proven to simulate with accuracy a great variety of WECs: an oscillating wave surge converter with mechanical constraints was validated in [35] under regular wave conditions; complete dynamic investigations of heaving point absorbers [26,36–38]; and fixed oscillating water column devices have been studied [39,40].

The Uppsala WEC [41] has been considered as a reference case in this research; it operates according to the principles that hold for floating oscillating body devices, which are mainly designed to operate offshore (often in deep-water conditions). The concept was devised in the early 2000s and installed for the first pilot wave power plants deploying this technology [41]; it was physically tested under constrained focused waves and irregular waves in [42]. The device has been used ever since as a benchmark for numerical model validation, including consideration of the electromechanics of the PTO. Table 1 reports on the body of research that has leveraged the Uppsala WEC concept to widen understanding of the economic viability of moored point absorbers, expanding upon the previous background for extreme wave modeling [43]. All the pieces of research utilized mesh-based CFD software (i.e., OpenFOAM, IHFOAM and ANSYS Fluent) to investigate the performance of the Uppsala WEC under various extreme wave conditions.

However, the software that has complemented the experimental investigation needs highly skilled operators (OpenFOAM, IHFOAM) due to the modification in the source code to model the dynamics of the linearly-constrained PTO and the mooring line. Furthermore, despite the progress made in recent years, mesh-based CFD software is often challenged by simulations that entail the use of costly overset mesh for solving violent wave conditions [7,16,47]. Developing and validating new, reliable numerical simulation methods based on meshfree methods is of utmost importance.

This work proposes, for the first time, the application of an SPH-based model for the Uppsala WEC model. The proposed CFD software overcomes the above-mentioned problems by being fully integrated with two external libraries for simulating mechanical systems (e.g., linear PTOs) and mooring lines, and by being mesh-less. The DualSPHysics code is used to study a taut-moored point-absorber WEC with a linear PTO system under extreme wave conditions, investigating the various quantities that are vital for the Ultimate-Limit State (ULS) safety checks of this type of structures under high return-period events. The paper is arranged as follows: Section 2 describes in detail the basics of the mathematical foundation of the SPH method and its implementation in the code distribution herein used; Section 3 presents the code augmentation achieved through coupling techniques that allow leveraging specialized libraries within the same framework; Sections Section 4 presents the experimental setup for the Uppsala WEC whereas Section 5 describes the numerical configuration and proposes a general procedure for reproducing similar devices as well, in particular PTO calibrations; Section 6 validates the numerical model, for two distinct PTO configurations, under embedded focused waves. Finally, Section 7 presents long time series CFD simulations representing a real sea-state condition with 500 waves that impact the Uppsala WEC. Section 8 closes this work by synthesizing the main achievements.

2. DualSPHysics code

2.1. SPH basis

The SPH method is mathematically built up on a convolution integral approximation: any function F can be defined by:

$$F(\boldsymbol{r}) = \int F(\boldsymbol{r}')W(\boldsymbol{r}-\boldsymbol{r}')\mathrm{d}\boldsymbol{r}', \tag{1}$$

Table 1
Research papers reporting on the numerical hydrodynamics performance of the Uppsala University WEC under various scenarios.

Reference	Numerical model	Validation with	Type of waves	Validated data	Scope
[44]	VOF-RANS (OpenFOAM)	Exp.	Regular and focused waves	Incident wave, Motion, Line force	Survivability
[25]	Analytical, VOF-RANS (OpenFOAM and ANSYS Fluent)	EXP	Regular and focused waves	Motion, Line force	Survivability
[45]	BEM, VOF-RANS (ANSYS Fluent)	EXP and NUM	Irregular waves	Incident wave, Motion, Line force	Survivability under irregular waves
[46]	VOF-RANS (OpenFOAM)	EXP	Regular and focused waves	Motion, Line force	Survivability under tsunami waves
[28]	VOF-RANS (IHFOAM)	EXP	Focused waves	Motion, Line force	Survivability with focused waves

BEM: Boundary Element Method; VOF-RANS: Volume of Fluid-Reynolds-averaged Navier–Stokes' (equations); EXP: Experiments; NUM: Numerical data.

where W is the kernel function [48], $\boldsymbol{r}$ is the position vector of the point where the function is being computed, $\boldsymbol{r}'$ is the position vector of another computational point (or particle). The function F is approximated by interpolating particle contributions; a summation is performed all over the particles within the compact support of the kernel:

$$F(\boldsymbol{r_a}) \approx \sum_b F(\boldsymbol{r_b}) W(\boldsymbol{r_a} - \boldsymbol{r_b}, h) \frac{m_b}{\rho_b}, \tag{2}$$

where a is the interpolated particle, b is a neighboring particle, m and ρ being the mass and the density, respectively, m_b/ρ_b the volume associated with the neighboring particle b, and h is the smoothing length. For the sake of consistency, the kernel function W must fulfill several properties, such as positivity on the compact support, normalization, and monotonically decreasing with distance [49]. The weighting function used in this work is the piecewise polynomial Quintic Wendland (QW) kernel [50]:

$$W(q) = \alpha_D \left(1 - \frac{q}{2}\right)^4 (2q+1), \quad \text{with:} \quad 0 \le q \le 2, \tag{3}$$

where α_D is a real number that ensures the kernel normalization property:

$$\int W(|\boldsymbol{r} - \boldsymbol{r}'|) d\boldsymbol{r}' = 1,$$

$q = r/h$ is the non-dimensional distance between particles, r is the distance between a certain particle a and another particle b, and

$$h = 1.20\sqrt{3} dp$$

is the smoothing length in which dp is the initial inter-particle spacing. In this work, the QW kernel is used to compute interactions of particles at a distance up to the value of $2h$.

2.2. Governing equations

In fluid mechanics, the SPH method is used to discretize a volume of fluid as a set of particles and the Navier–Stokes (N–S) equations dictate their motion. In the Lagrangian framework, the differential form of momentum N–S Eqs. (4) and the continuity Eq. (5) can be written in their discrete version using the kernel function:

$$\frac{d\boldsymbol{v_a}}{dt} = -\sum_b m_b \left(\frac{P_a + P_b}{\rho_a \rho_b} + \Pi_{ab}\right) \nabla_a W_{ab} + \boldsymbol{g}, \tag{4}$$

$$\frac{d\rho_a}{dt} = \rho_a \sum_b \frac{m_b}{\rho_b} \boldsymbol{v}_{ab} \nabla_a W_{ab} + 2\delta hc \sum_b (\rho_b - \rho_a) \frac{\boldsymbol{v}_{ab} \nabla_a W_{ab}}{\boldsymbol{r}_{ab}^2} \frac{m_b}{\rho_b}, \tag{5}$$

where t is the time, $\boldsymbol{v}$ is the velocity, P pressure, $\boldsymbol{g}$ is the gravitational acceleration, ∇_a is the gradient operator, W_{ab} the kernel function, whose value depends on the distance between a and b, δ is a parameter that governs the diffusive term, $\boldsymbol{r}_{ab} = \boldsymbol{r}_a - \boldsymbol{r}_b$ with $\boldsymbol{r}_k$ being the position of the particle k, and c is the speed of sound.

The artificial viscosity term, Π_{ab}, is added in the momentum equation based on the Neumann–Richtmeyer artificial viscosity, aiming to reduce oscillations and stabilize the SPH scheme, following the work of [49]. In addition, the term δ controls the density diffusion term (last term in Eq. (5)) that is implemented in DualSPHysics, which works as a high frequency numerical noise filter improving the stability of the scheme by smoothing the density. The formulation is based on the density diffusion terms introduced by [51] and further developed under the name of *delta-SPH* in [52]. For the simulations performed in this work, the second term in the right-hand side of the continuity Eq. (5) is solved according to the formulation proposed in [53], which considers the only the dynamic density to control the intensity of the diffusive term.

A relationship between density and pressure bonds the system of equations. DualSPHysics uses a weakly compressible SPH formulation (WCSPH) for modeling Newtonian fluids and, for such formulation, Tait's equation of state is used to determine fluid pressure, P, from particle density. Following [54], it can be expressed as [55]:

$$P = \frac{c^2 \rho_0}{\gamma} \left(\left(\frac{\rho}{\rho_0}\right)^\gamma - 1\right), \tag{6}$$

where ρ_0 is the reference fluid density, γ is the polytropic constant. The fluid compressibility is adjusted so that c can be artificially lowered to assure reasonable values for the timesteps.

2.3. Rigid body dynamics and SPH

A full SPH model can deal with rigid bodies by computing the total force contributions of the surrounding fluid. In DualSPHysics, the motion of objects interacting with fluid particles is handled by the basic equations of rigid body dynamics. The geometries of these objects are discretized by filling the volume they occupy with boundary particles; for those particles it is assumed that they behave following the dynamics of each body's center of mass. Each boundary particle k experiences a force per unit mass given by:

$$\boldsymbol{f}_k = \boldsymbol{g} + \sum_{b \in \text{fluid}} \boldsymbol{f}_{kb}. \tag{7}$$

$\boldsymbol{f}_{kb}$ is the force per unit mass exerted by the fluid particle b on the boundary particle k. For the motion of a rigid body, the basic equations of rigid body dynamics can then be used:

$$\boldsymbol{M} \frac{d\boldsymbol{V}}{dt} = \sum_{k \in \text{body}} m_k \boldsymbol{f}_k, \tag{8}$$

$$\boldsymbol{I} \frac{d\boldsymbol{\Omega}}{dt} = \sum_{k \in \text{body}} m_k (\boldsymbol{r}_k - \boldsymbol{r}_0) \times \boldsymbol{f}_k, \tag{9}$$

where $\boldsymbol{M}$ is the matrix mass of the object, $\boldsymbol{I}$ is the matrix moment of inertia, $\boldsymbol{V}$ is the velocity, $\boldsymbol{\Omega}$ the angular velocity, and $\boldsymbol{r}_0$ the center of mass; $\times$ indicates the cross product. Eqs. (8) and (9) are integrated in time to predict the values of $\boldsymbol{V}$ and $\boldsymbol{\Omega}$ at the beginning of the next time step. Each boundary particle within the body has a velocity given by:

$$\boldsymbol{v_k} = \boldsymbol{V} + \boldsymbol{\Omega} \times (\boldsymbol{r_k} - \boldsymbol{r_0}). \tag{10}$$

Finally, the boundary particles within each rigid body are moved by integrating Eq. (10) in time. This approach has been checked out by [56], which shows that linear and angular momentum are conservative properties. Validations about buoyancy-driven motion are performed in [57], where DualSPHysics is tested for solid objects larger than the smallest flow scales and with various densities; [58] provides a validation for the motion of a freely floating box under linear waves.

2.4. Modified dynamic boundary conditions

DualSPHysics implements the Dynamic Boundary Condition (DBC), proposed by [59], as a standard method for the definition of the boundary conditions. The DBC treatment has demonstrated to work properly when applied to cases of wave propagation and wave run-up of armor block breakwaters with complex geometries [60]. However, a novel formulation was proposed by [61] in order to improve the initial DBC formulation, eliminating the creation of large gaps when the transition from non-wet to wet bounds takes place.

The modification of DBCs (the so-called mDBCs) works with the same particle arrangement defined for its parent version, but the interacting boundary surface is located between the outermost particle layers of the body and the fluid domain. Once the geometry has been characterized by normal vectors, this latter location is used to mirror ghost nodes into the fluid domain and hence evaluating the fluid properties at that virtual position; eventually, these properties are used to correct the SPH approximation when a fluid particle interacts with an mDBC particle, as it was already performed in [62,63].

3. Coupling with external libraries

Multyphysics simulations rely on coupling strategies between different pieces of software to create a unique environment in which different differential systems of equations are separately solved. This strategy is implemented in DualSPHysics by creating a fully Lagrangian 3D *world* that contains the geometry for the whole system. As discussed, the fluid phase is managed by the internal SPH solver described in Section 2; the dynamics of rigid bodies, comprising also the solid–solid contacts, is managed by the Project Chrono library [33], whereas the effects of mooring lines on floating structures is addressed by the MoorDyn+ library [64]. Mooring lines are vital for offshore structures (some examples can be found in [65,66]) for their capability of providing connections spanning long distances; their small usage of material is due to a combination of high-resistance material and the absence of bending-induced stress. These features are indeed needed to reproduce the response of PTO systems and to account for the various connectivity among the parts of WECs, and/or of WEC arrays.

3.1. Coupling with project Chrono library

The Project Chrono library has been implemented into the original DualSPHysics framework, creating an integrated interface for simulating structure–structure interaction as well [67]. The library is primarily developed to handle very large systems of 3D rigid bodies [68], with interactions among them. The coupling allows for arbitrarily shaped bodies to be considered, and the solver can integrate externally applied forces and torques, and the effects of kinematic-type restrictions, dynamic-type restrictions. Appendix A provides a description of the contact tracing method and of the spring–damper element, which are the functions utilized in this study.

3.2. Coupling with MoorDyn+

The two-way coupling presented in [58] is used for the simulations in this work. The open-source MoorDyn+ library solves the mooring dynamics using the lumped-mass approach inherited from the first version of MoorDyn [34]. An exhaustive description of the theory implemented for this work is presented in Appendix B.

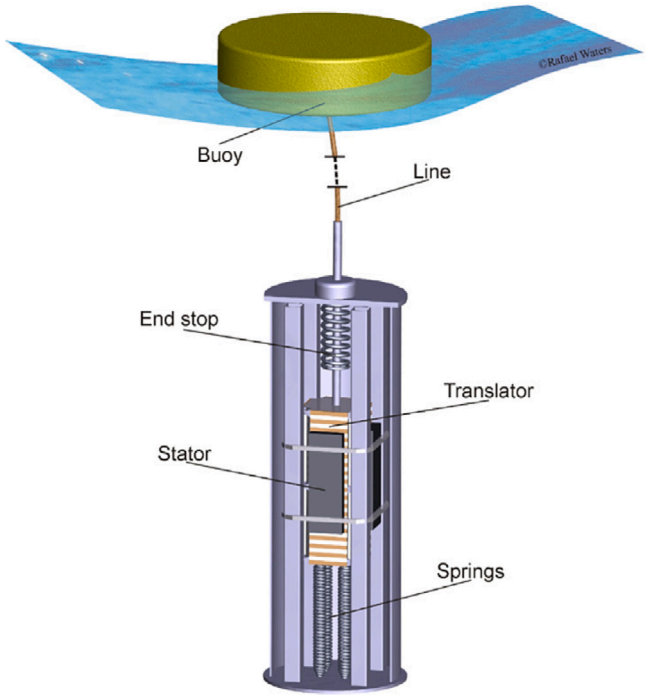

Fig. 1. Schematic of the Uppsala WEC [41] with a cylinder buoy. The various components of the PTO systems are tagged according to the function they are designed for.
Source: [25].

4. Experimental setup

A 1/20th-scale model WEC (Froude similarity) was studied in a wave tank in [42], with features reminiscent of the Uppsala WEC. For the validation proposed in this work, the setup that made use of a cylindrical float (refer to Fig. 1) is chosen. The buoy is taut-moored to a mass that is constrained to move only along the vertical direction; a line connects the buoy with the translator. As opposed to the mainstream rotating generators, in fact, the Uppsala WEC proposes a linear generator directly driven from the rectified motion of a floating buoy. The relative motion between the *translator* and the *stator* produces a moving magnetic field, which induces a current in the coils located in the latter. Often, the translator comprises a series of *SN* magnets with alternate polarities, whereas the stator hosts the copper coils. This mechanism, within the experimental setup, is simulated via a friction paddle with an adjustable normal force. The gravity field provides some part of the recentering force that is necessary to restrict the motion of the buoy. When, however, the wave exceeds a certain threshold, the translator is further restrained in its motion by an end-stop spring. This system also works as a booster for the translator's backup movement: the energy stored by compressing the spring is released when the cycle reverses, thus increasing the kinetic energy of the translator.

The data and the geometry considered in the following sections are presented in [25,42]. The tests at the Coastal Ocean and Sediment Transport (COAST) at Plymouth University (UK) were carried out with a cylinder float, which is identified by *CYL* in [25,42]; the characteristics of the geometry are given in Table 2. For the validation purposes within this research, reference is made to the extreme wave event *embedded focused waves*, which is also used in [25] for carrying out survivability analysis through numerical modeling of the Uppsala WEC. In particular, the data for the event defined by wave height $H = 7.20$ m (model scale $H = 0.36$ m) and wave period $T = 10.70$ s (model scale $T = 2.393$ s) is considered, for two different runs, in which the PTO friction damping is 5.00 kN and 59.00 kN, respectively (model scale

Table 2
Buoy dimensions of the Uppsala WEC.

	Symbol	1:20 model	Unit
Buoy radius	R	0.085	m
Buoy draft	D	0.032	m

Table 3
Damping definition.

Label	Full scale	1:20 model	Unit
C0	5000	0.63	N
C2	59 000	7.38	N

0.63 N and 7.38 N); the two cases are summarized in Table 3. These are chosen for being representative of two antithetical conditions: Case **C0** is the case where supposedly the harvesting function was deactivated — of course, some energy is damped out by the physical system that consists of pulleys and rails. Case **C2**, on the other hand, foresees the use of a breaking system that was activated by screws with a predefined, adjustable load, which adds a controlled damping value to the previous one. In this work, the different nature of the energy dissipation as described above is accounted for.

5. Numerical configuration

General setting

The numerical model is built upon the experimental setup reported in [42], herein using the 1:20th model scale thus making direct comparison to the available raw data.

The Uppsala WEC working principle combines a free-floating buoy with a linear magnet generator (PTO), which is attached on a ballasted platform and located at sea-floor level. The motion of the float is transmitted to the translator through a mooring line, making then the dynamics of the whole system quite complex and heavily dependent on the behavior of each part. Hence, the proposed model fully exploits the features made available by the two coupled libraries: Chrono and MoorDyn+. Several instances are combined to shape the system that can mimic the behavior of the PTO when connected to a float through a mooring line. In the following, a general overview of the numerical model geometry is given.

Using the schematic depicted in Fig. 1 as a template, Fig. 2 shows a mechanical model (left) and a 3D perspective view of the assembly (right) of the WEC, in which the different parts are labeled from *A*-*F*. Table 4 provides a synthetic description of the system regarding the elements and the libraries that handle their dynamics. Note that the only part interacting with fluid particles is the buoy (A). Although the elements from *B*–*F* are shown in the same 3D environment, they do not interact with water, much like the physical moving parts in the real case, which were installed aside the wave tank. Instead, accounting for the mooring line, in spite of the fact that such elements can interact with waves in a theoretical way, the line motion only depends on the fairlead and anchor positions, and the gravity acceleration. The line-to-water interaction is neglected here.

The solid surfaces of the float (A in Fig. 2), where the most important part of the fluid–solid interaction takes place, consist of a set of boundary particles that are solved according to the mDBC algorithm that is presented in Section 2.4. The inertia of the buoy, which is not reported in the reference material, is computed by considering that the mass is uniformly distributed along the outer plastic shell, with a thickness defined in hindsight to comply with the total mass. It goes that the center of gravity of the buoy lies at the centroid location of the solid.

The mooring line is modeled here as a set of masses linearly joined by spring–damper items, following the approach presented in [69]. Element B in Fig. 2 relates, in a non-linear fashion, the motion of the

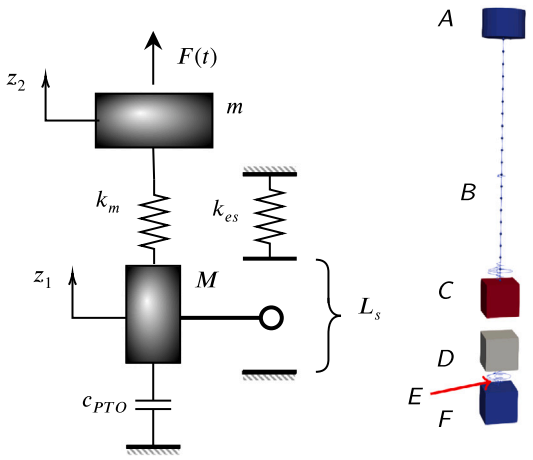

Fig. 2. Mechanical model of the PTO system with a moored buoy (left) and perspective visualization of the PTO assembly in the numerical model (right). The meaning of the symbols is given in Table 7, whereas the Latin letters from A–F are explained in Table 4.

Table 4
Instances and relative handler for the simulation of the Uppsala WEC.

Label	Function	Instance	Manager
A	Buoy	Moving	Chrono
B	Taut line	Mooring line	MoorDyn+
C	End-stop	Moving Spring Contact	Chrono Chrono Chrono SMC
D	Translator	Moving Contact	Chrono Chrono SMC
E	Energy	Damper	Chrono
F	End-stop	Contact	Chrono SMC

buoy to the translator D. The line is initialized as a connection between the initial draft of the float and the bottom of the wave tank, which leads to an unstretched length $L_{us} = 2.468$ m. The stiffness of the line, which is given by the product of elasticity modulus and cross-sectional area (EA_l) is retrieved from the information given in [42]. [25] reports that an 8-meter-long polymer line (unstretched length $L_0 = 8.00$ m [25]) was used to connect the buoy to a mass that was supposed to mimic the translator; the line stretched 1% at a load of $F = 60$ N, thus giving:

$$K_{line.exp} = \frac{F}{0.010 L_0} = 750 \text{ N/m},$$

which represents the stiffness of the whole line, amounting to 6000 N of axial stiffness (EA). However, the numerical model only foresees one line that connects the buoy, at its draft, to the translator that virtually starts from the bottom of the flume. Here, to consider the same effects in terms of line stiffness, the line axial stiffness EA_l is set to $L_{us} \cdot K_{line.exp} = 1830$ N.

Once the geometry of the line along its mechanical properties are defined, it is possible to proceed to assign the parameters to model the mooring line through the lumped-mass approach, according to the definitions given in Appendix B. Table 5 depicts the input values that are used to set up the line into the MoorDyn+ solver.

Note that the *Model time step* (dt_M) is defined according to the following relationship:

$$dt_M \leq \frac{10}{f_n}, \tag{11}$$

where f_n identifies the critical frequency in the spring–mass system that describes the mooring line; its definition is given in Appendix B.5.

The PTO system that is employed in the Uppsala WEC functions as both harvesting device and safety system, having no clear definition

Table 5
Input parameters used for the definition of the mooring line.

Element	Symbol	Quantity	Unit
Cross sectional stiffness	EA_l	1830	N
Nominal diameter*	D_N	2	mm
Spring constant	k_m	0.750	kN/m
Segments	N	40	–
Density in air*	ρ_l	1500	kg/m^3
Weight in fluid	W_l	0.015	N
Natural frequency (Eq. (30))	f_n	98.4	kHz
Model time step	dt_M	7.0e−05	s

*The given values for these variable are plausible ones, not having any counterparts in the reference paper.

Table 6
Definition of the PTO generator damping models for the numerical simulations.

Label	F_μ	c_{PTO}
C0	0.000 N	2.795 Ns/m
C2	6.755 N	2.795 Ns/m

of the two phases. Here, it comprises three solid objects, two moving (C and D) and one fixed (F) (Fig. 2 and Table 4). The translator D is bounded in its vertical motion by the upper and the lower end-stops C and F, respectively, the former being movable and the latter fixed. The interaction between $D-C$ and $D-F$ is possible thanks to the contact tracing functionalities that are described in Appendix A.1. When the translator D impacts the massless end-stop system C, its vertical motion is modified by the presence of a spring element, which exerts an elastic force according to the following relationship:

$$F_{Spring}(t) = k_{es} \cdot (l(t) - l_{es}) \tag{12}$$

where $l(t)$ is the spring length and l_{es} is the equilibrium length of the *end-stop*.

The harvesting tool that is used in the physical tests is here represented by element E. For the aims of this work, as also stated before, the validation is performed considering two different setups for the generator (ref. Table 3). In particular, for case **C0**, described in [42] as the case in which no energy was harvested, a value that was representative of internal energy dissipation was utilized. To better represent this phenomenon, a velocity-proportional damping model is proposed. The damper element E in fact obeys the following relationship:

$$F_{Damper} = c_{PTO}\dot{z} - \text{sign}(\dot{z})F_\mu, \tag{13}$$

where c_{PTO} is the viscous damping coefficient, F_μ is the friction force given by the product of the friction coefficient and the transverse load. Table 6 reports the parameters that are used to reproduce the generator damping for Cases **C0** and **C2** in the SPH model starting from the values depicted in Section 3. Note that the Case **C0**, in spite of being defined as with *no damping*, needs to include some energy dissipation function in its definition to account for the internal resistance to the motion given by the various pieces of equipment that were used in the physical tests. For the aims of this research, the internal friction described above was modeled as velocity-proportional damping since it was found to be in better agreement with experimental evidence. The values reported in Table 6 are retrieved by using standard scaling procedures [70].

PTO calibration

Prior to validating the whole system, a first calibration of the proposed numerical model of the Uppsala WEC is performed against an analytical solution built upon the mechanical scheme shown in Fig. 2; this first phase takes place in a dry setting, as the fluid phase is completely absent. Since the goal of this section is the validation of contact tracing features and line behavior, only the **C0** case is used here, thus keeping its description more agile to be described through analytical models. The dynamics of the evolving system are assumed in

Table 7
Input parameters used for the analytical model.

Element	Symbol	Quantity	Unit
Buoy mass	m	0.712	kg
Line stiffness	k_m	0.750	kN/m
End-stop stiffness	k_{es}	1.940	kN/m
End-stop spring length	l_{es}	0.030	m
Translator mass	M	0.780	kg
Free Stroke	L_s	0.170	m
Internal damping	c_{PTO}	2.625	Ns/m

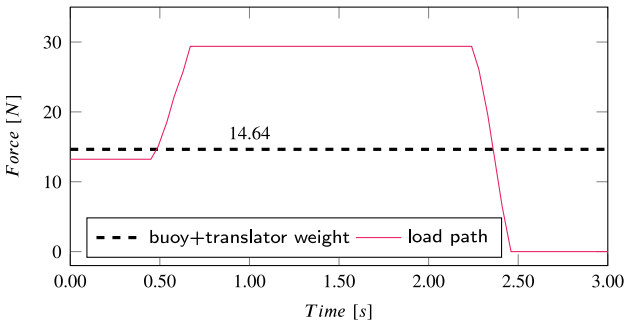

Fig. 3. Force time history used for the model calibration; the black dashed line reports the buoy and the translator weight.

the vertical direction only, and that the initial position of the translator is at its lowest ($-L_s/2$). The mooring line is simulated by a spring assuming that it will always be engaged in tension during this test. Note that this assumption will be satisfied by defining a particular external force time-history. The following equations describe the mechanical model:

$$\begin{cases} M\ddot{z_1} + c_{PTO}\dot{z_1} + K(z_1)(z_2 - z_1) = -Mg, \\ m\ddot{z_2} + k_m(z_1 - z_2) = mg + F(t), \end{cases} \tag{14}$$

where M is the mass of the translator, c_{PTO} is the applied damping, g is the magnitude of the gravity acceleration, m is the mass of the buoy, k_m is the stiffness of the line, and $F(t)$ is the applied force; z_1 and z_2 are the position of the translator and the float, respectively. $K(z_1)$ represents the stiffness of the inner system and takes into account the presence of the end-stopping system. It can be defined by the following step function:

$$K = \begin{cases} k_m & \text{if } |z_1| < L_s/2; \\ k_m + k_{es} & \text{if } |z_1| \geq L_s/2; \end{cases} \tag{15}$$

where k_{es} is the stiffness of the end-stop system.

The contact between the translator and the end-stop is handled only numerically and considering that there is a sudden variation in the stiffness of the system; a similar approach can be found in [25]. The time series of the driving force $F(t)$ is shown in Fig. 3: it is built to comply with the assumptions made beforehand. The initial 0.50 s of the time series report a constant force 10% lower than the weight of the system (that is, *Buoy mass+Translator mass*): this initial gap is necessary for the numerical model to reach an equilibrium position, where the line is taut and the translator at rest on the lower end-stop. The initial force in the line was found to be around 8 N.

Comparison of the numerical model response and the analytical solution is made in Fig. 4, where the solution of Eq. (14) is computed by integrating the system with a Runge–Kutta method fourth-order accurate. Three different simulations are performed with the numerical model, considering the effects of the initial inter-particle distance (dp) and the parameter $O_{contact}$ (overlap threshold) that assigns the accuracy of the external feature of the considered geometry for the contact tracing algorithm (inward and outward envelope). The overlapping threshold is defined in terms of dp. Despite being managed by the

Table 8
Parametric analysis for the model calibration.

Label	dp [m]	$O_{contact}$ $[dp]$
①	R/4	0.50
②	R/4	0.10
③	R/5	0.10

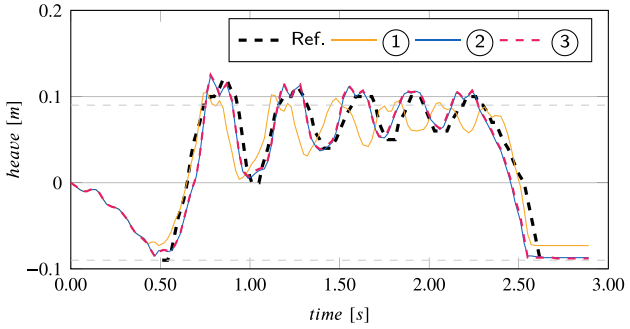

Fig. 4. PTO model calibration. The heave motion evolution of the model for the three cases collected in Table 8 are compared against the analytical predictions.

CHRONO SMC solver, the envelope shape offset is important for the accuracy of the collision detection: when the outer envelope shape far exceeds the actual geometry, a large gap can appear. On the other hand, envelope shapes too close can cause boundary penetration, which may cause *sticky* contact effects.

Table 8 reports the three cases that are used for the calibration of the parameters that matter for the contact tracing solver. Here, two initial resolutions are considered ($R/4$ and $R/5$), and two overlap threshold values. By comparing the evolution of the three cases with the reference solution, it can be concluded that the numerical model is able to reproduce the main characteristics of the PTO system, accounting for the role the elasticity of the mooring line plays along with its motion restriction. In such instances, however, the dynamics of the line is only considered in its linear range, which is an assumption that is violated when a real application is of interest. Nevertheless, this case serves well for the solely purpose of assessing the sensitivity of the model to the two parameters. It can be noticed that the parameter $O_{contact}$ is to be set meticulously. Case ① forms a large gap between the expected rest position – at $L_s/2$ – and the actual position of the translator. This is due to a repulsive effect generated by an excessive offset between the parent geometries of the translator and the end-stop, which as well results in a considerable difference in phase. Nevertheless, Case ② and Case ③ prove that the model can provide a reliable solution, not dependent on the initial inter-particle distance. A small gap is still appearing, which is considered to not affect the quality of the results, being the response of the system in phase with the target solution.

To conclude the calibration procedure, it can be observed that when the overlapping threshold $O_{contact}$ is small enough, the surface interaction is solved with accuracy and the system solution converges. For the following simulations, the parameter $O_{contact}$ is set to 0.10 dp. Furthermore, two simulations with $dp = R/6$ and $dp = R/7$, and $O_{contact} = 0.10\ dp$, were performed as well, providing the same accuracy as in the case with $dp = R/5$, and $O_{contact} = 0.10$; for the sake of readability of the chart, the time responses are not reported.

Wave tank

DualSPHysics allows deploying a set of built-in functions that are useful to design a suitable numerical tank that complies with the experimental conditions, without strictly reproducing the geometry. In fact, the tests in the COAST Laboratory were run in a wave basin of 35× 15.5 m, 2.5 m deep. A schematic of the numerical tank is presented in Fig. 5, in which the lateral and the top view are sketched. The tank has seen a dramatic reduction in length and width, but the depth complies with the experimental one to not alter the wave profile. The tank can be shortened thanks to using a piston-type wavemaker equipped with an active wave absorption system (AWAS) that guarantees the correct input incident wave, following the implementation proposed in [71]. The input motion at this position is generated from the incident wave gauged during the physical tests. The width of the tank is shrunk to three times the diameter of the floater, and to prevent lateral reflection, a numerical damping zone (shaded area in top view Fig. 5) that employs a quadratic decay function is applied in the y–direction [71]. Furthermore, to avoid any drag effects due to the presence of lateral solid walls, periodic boundary conditions are applied [72]. Downstream of the buoy there is an 1:3 anti-reflective beach which, boosted with numerical damping, provides a reflection coefficient lower than 3%.

6. Validation

6.1. Propagation of extreme waves

Purposing the model for the validation of the whole WEC, a first step is taken towards the validation of the wave tank in generating and propagating waves. This procedure is also common practice for assessing the accuracy of physical systems prior to running any tests. The extreme sea-state condition model that is employed to validate the SPH model is generated through a focused wave train which is constrained (embedded) into a regular wave background. The surface elevation of one such experimental test is reported in Fig. 6 (gray line), taken from [42]. The authors report that the test was carried out prior to including the float into the flume, and the wave elevation was measured at the buoy's location with a resistive wave gauge. In order to retrieve the wave characteristics to build the wavemaker motion, the signal is decomposed via a spectral analysis based on the Fourier Transform (FT) (via FFT). The regular body of the wave train, boxed in Fig. 6, has a wave period of $T_{reg} = 2.403$ s and a wave height of $H_{reg} = 0.27$ m whereas the focused part, as well boxed in the same figure, has $T_{focus} = 2.604$ s and $H_{focus} = 0.38$ m; both spectra are reported in Fig. 6. With these parameters for the regular wave train, joint with the 2.50-m water depth, it is possible to assert that the wave is traveling in intermediate water with a wave length of $L_{reg} = 8.50$ m, and that it can be ranked second order Stokes' wave. The phase between the regular background and the focused group is given as $\phi = \pi$.

The motion of the paddle is computed as follows. The regular wave body motion for 2nd order Stokes' waves is managed by an internal tool that is provided along with the software [71], which allows convenient use of an AWAS system to control over the quality of the generated waves. The unidirectional crest-focused wave is defined according to the *NewWave* theory [73]. The NewWave linear theory was firstly proposed by [74] defining the free-surface elevation $\eta(x,t)$ with respect to the sea-state power density spectrum $S_n(\omega)$, as linear superposition of N wave modes. For a so-called crest-focused wave group, it goes:

$$\eta(x,t) = \sum_{n=0}^{N} a_n cos(k_n(x - x_f) - \omega_n(t - t_f)), \tag{16}$$

where x_f and t_f are the focusing position and focusing time, respectively. The amplitude of each component is given by:

$$a_n = \frac{A_{cr} S_n(\omega) \Delta\omega_n}{\sum_n S_n(\omega) \Delta\omega_n}, \tag{17}$$

where $\Delta\omega_n$ is the frequency increment, and $A_{cr} = \sqrt{2m_0 \ln(N)}$, where m_0 is the zeroth moment of the spectrum, is the linear crest amplitude. Note that the crest amplitude at $A_{cr}(x_f, t_f)$ equals the maximum wave height H_{focus}. Investigation carried out by [73] suggested that wave group generated by wavemakers that move according to the NewWave linear theory may lead to the introduction of spurious waves into the generated spectrum (see also [26]). To prevent this, the theory developed by [75] for second-order wave generation is used to correct the

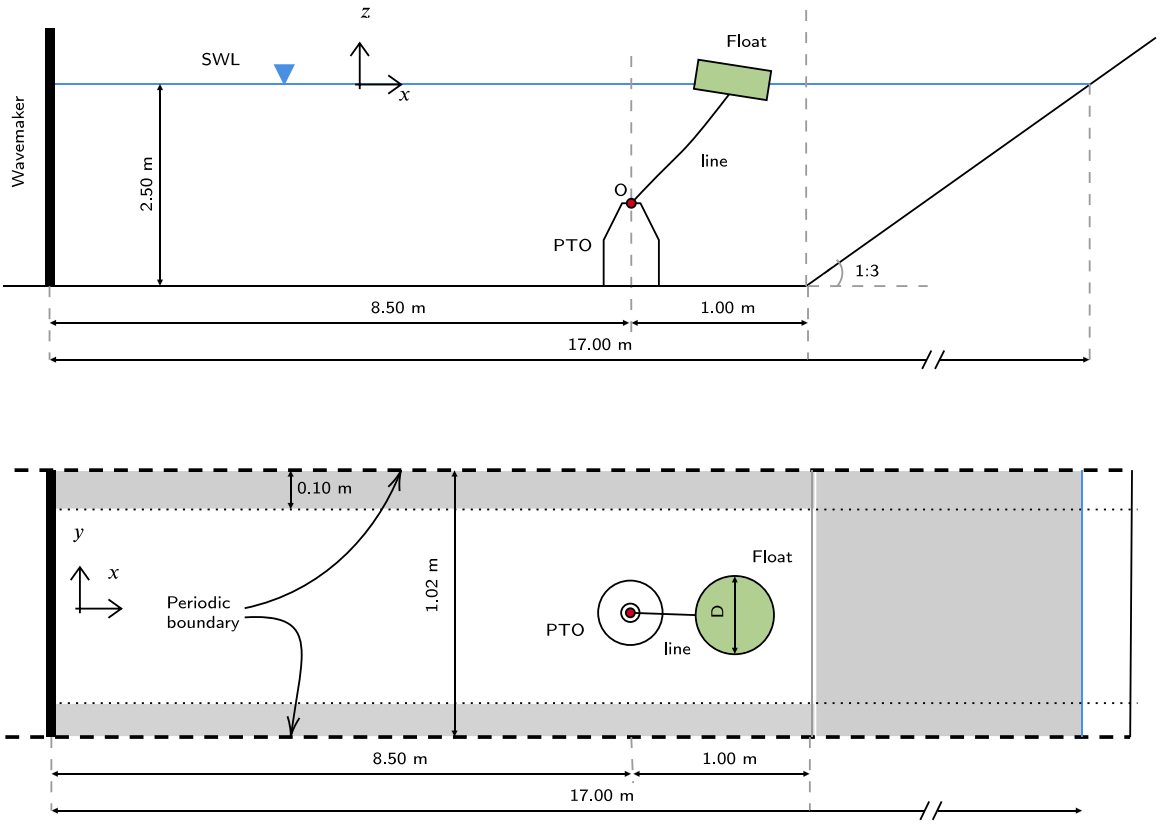

Fig. 5. Lateral and top views of the numerical tank for embedded focused wave tests. Following the experimental configuration, the point O is actually located at $z = -2.50$ m: its representation is only for the sake of clarity.

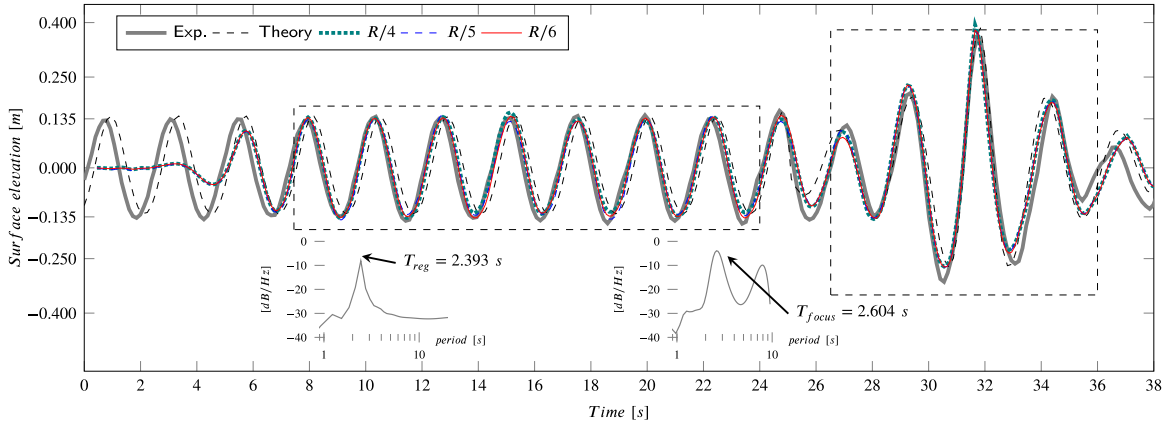

Fig. 6. Experimental, theoretical, and numerical surface elevations of the embedded focused wave. The two dashed boxes highlight the portion of the signal (Exp.) that is used to compute the spectra reported as insets.

motion input. Examples of focused waves simulation with DualSPHysics can be found in [26,76].

The paddle motion for the focused wave group is hence generated by considering $N = 1000$, which is also suggested in [73,77], and by generating a Joint North Sea Wave Observation Project (JONSWAP) [78] power density spectrum with a peak period $T_p = T_{focus}$ and a significant wave height $H_{m0} = 1.90 \cdot H_{reg}$. The wave group focuses at $x_f = 1L$, which corresponds to the initial position of the buoy, when the shortest wave in the spectrum reaches such position.

A standalone fluid validation is performed contrasting the obtained incident waves against the theoretical expectation for the surface elevation (Theory) and the physical data (Exp.), reported in Fig. 6. By visually comparing the experimental measurements to the expectation, it can be noticed that the latter does not fully comply with the former solely for some slight differences around *time* = 26 s, likely due to a misalignment where the two signals join. The outcome of the numerical model is reported in the same chart for three different particle resolutions, namely $R/4$, $R/5$, and $R/6$. Although it is customary to refer to the height of the wave for wave validations, the particle resolution is set based on the size of the float, thus preparing the model for future applications. The surface elevation evolution retraces with accuracy the target one with a few exceptions: around the point where two wave trains are spliced together, and around the two main troughs of the focusing group. At this stage it becomes important for the reader to keep this detail in mind because it can make the quality of the results below clearer.

Prior to moving to the full validation, a non-dimensional error estimator is defined to provide solid figures on the system accuracy. The

Table 9
Estimated errors for the wave tank in propagating extreme waves.

dp [m]	W	$E_{T.reg}$	$E_{T.focus}$
$R/4$	0.843	1.8%	2.2%
$R/5$	0.862	1.6%	2.2%
$R/6$	0.877	1.6%	2.1%

index of agreement W, which was redefined by [79] over a previous definition given in [80]. It can account for amplitude differences and is of course sensitive to phase misalignment; W for a specific signal X_{num} with respect to a certain reference solution (X_{exp}) is estimated as follows:

$$W = 1 - \frac{\sum_{j=1}^{N_X}(|X_{num.j} - X_{exp.j}|)}{\sum_{j=1}^{N_X}(|X_{num.j} - \mu_{exp}| + |X_{exp.j} - \mu_{exp}|)} \tag{18}$$

where N_X is the number of elements in the array X_{num}, and $\mu_{exp} = mean(X_{exp})$. The values provided by Eq. (18) are capped by +1 that indicates that the two signals are coincident. In this work, a scoring classification proposed in [81] for a similar index is used to rate the achieved accuracy. The proposed terminology, which pairs quantitative figures provided by Eq. (18) to qualitative descriptions; the classification defines as *excellent* for values of W between 0.9 and 1.0, *very good* between 0.8 and 0.9, *good* between 0.7 and 0.8, *fair* or *reasonable* between 0.5 and 0.7, *poor* between 0.3 and 0.5, and *bad* lower than 0.3.

The quantifier in Eq. (18) is utilized to assess the accuracy of the model in generating and propagating constrained focused waves, and the results are reported in the second column of Table 9. The lengths of the compared time series comprise seven fully developed waves and the entire focused ground, as framed in Fig. 6 by the dashed rectangles and having the experimental data as reference solution. In addition, Table 9 depicts two extra columns that report error estimations in terms of period (and phase) for regular waves ($E_{T.reg}$) and for the focused group ($E_{T.focus}$). Overall, the tank presented in this section achieves a high degree of accuracy in reproducing the wave train, and it scores as *very good* according to [81]'s scale.

6.2. Validation of the full WEC

The validation procedure concludes by simulating the full physical setup numerically, using the test array depicted in Table 10; the two tests **C0** and **C2** are repeated three times considering different *dp*s. The results of these six simulations are presented in Figs. 7 and 8, respectively for the case with no applied damping **C0** and the case that mimics the energy harvesting phase **C2**. The investigated quantities are the heave and surge motion of the buoy, which are referred to its center of gravity, and the line force computed as the force at the fairlead connection to the translator mass. Before describing the results, it is important to remark that the *same* particle spacing is used to discretize the initial geometry of the solids. Additionally, Table 10 indicates the number of fluid particles per each simulation (fifth column) and the required runtime (sixth column) for solving the specified physical time (in parentheses) using the GPU accelerated version of the code.

The buoy motion (heave and surge, (a) and (b) in Figs. 7 and 8), respectively) shows overall good agreement in terms of period for both cases and for the three particle resolution, whereas the amplitude needs further discussion. Making reference to Fig. 7, the heave evolution matches perfectly with the experimental one, regardless of *dp*. On the other hand, the surge motion is consistently underestimated during the regular wave train; such a tendency is still in place while the focused train is hitting the float, but showing a slight horizontal average drift. A similar pattern can be observed in [44], where the same device is simulated, under the same wave conditions, with the meshbased fluid solver integrated in OpenFOAM; this work concluded that the surge underestimation was (excerpted from the [44]) "partly attributed to the fact that the [numerical] model neglects the line elasticity". In disagreement with this conclusion, the evidence produced by the proposed model shows that by neglecting the line stiffness it cannot fully explain the observed discrepancy. Moving on to Fig. 8, the heave motion initially follows the experimental trend; when, however, a form of steady state is reached, the heave is consistently overestimated for the regular wave train, whereas it fully agrees during the focused part. For what concerns the surge motion, the response shows similar features to the previous case.

Table 10
Case array for the WEC validation under embedded focused waves.

Label	F_μ	c_{PTO}	dp [m]	Particles [10^6]	Runtime[a]
C0	0.000 N	2.795 Ns/m	R/4	1.815	15 h (38.00 s)
			R/5	3.438	32 h (38.00 s)
			R/6	6.158	75 h (38.00 s)
C2	6.755 N	2.795 Ns/m	R/4	1.815	13 h (33.20 s)
			R/5	3.438	30 h (33.20 s)
			R/6	6.158	64 h (33.20 s)

[a]The values exposed in this column refer to simulations performed on a GPU NVidia RTX2080Ti.

Table 11
Estimated errors for the float motion (Heave and Surge) and the line force.

Label	dp [m]	W Heave	W Surge	W line force
C0	R/4	0.799	0.701	0.629
	R/5	0.815	0.724	0.628
	R/6	0.830	0.759	0.671
C2	R/4	0.631	0.712	0.640
	R/5	0.659	0.725	0.656
	R/6	0.658	0.709	0.717

The forces estimated in the line remain in agreement with the experimental references. For the case with no damping (Fig. 7(c)), the model provides an accurate response on account of both the time evolution and the overall magnitude of the peaks. During regular waves, the system shapes a pattern very close to the experimental trend, and the quality of the signal improves as the particle resolution does. In contrast with the motion of the buoy, the force evolution for the case with damping, **C2**, can be qualified as sufficiently accurate for the following aspects. First, the main peak is well caught, proving again that the particle resolution of the model can improve the quality of the results; however, the secondary peaks of the focused wave show a partial overestimation. Secondly, the regular part results in a different periodic pattern, which agrees with the reference data but for a spike in the aftermath of the wave crest.

A final picture of the numerical model performance is given in Table 11. The definition of W (Eq. (18)) is run over the numerical time series reported in Figs. 7 and 8; the error is defined with reference to the experimental time series. For Case ***C*0** the model predicts quite well the heave motion, whereas the surge shows a consistent underestimation that makes it score as *good* (ref. [81]); the predicted time series for the line forces proves to be in *fair* agreement with the reference one. For Case ***C*2**, the model provides an overestimated time series for the heave motion, scoring as *reasonable*, whereas the surge motion and the line forces show similar figures as for ***C*0**.

Further insights about the performance of the Uppsala WEC can be inferred from the charts shown in Figs. 9 (translator and end-stop displacements, and line stretching) and 10 (translator velocity). The three charts report key information about the internal dynamics of the PTO system and the stretching function of the mooring line for the cases **C0** and **C2** with an initial particle spacing of $R/6$. The motion of the translator, which takes places along the z-direction, is mostly driven by the heave component of the buoy's motion due to the particular bound that the mooring line creates. A plausible figure for the work done by the surge component is around 2% of the overall work done by the

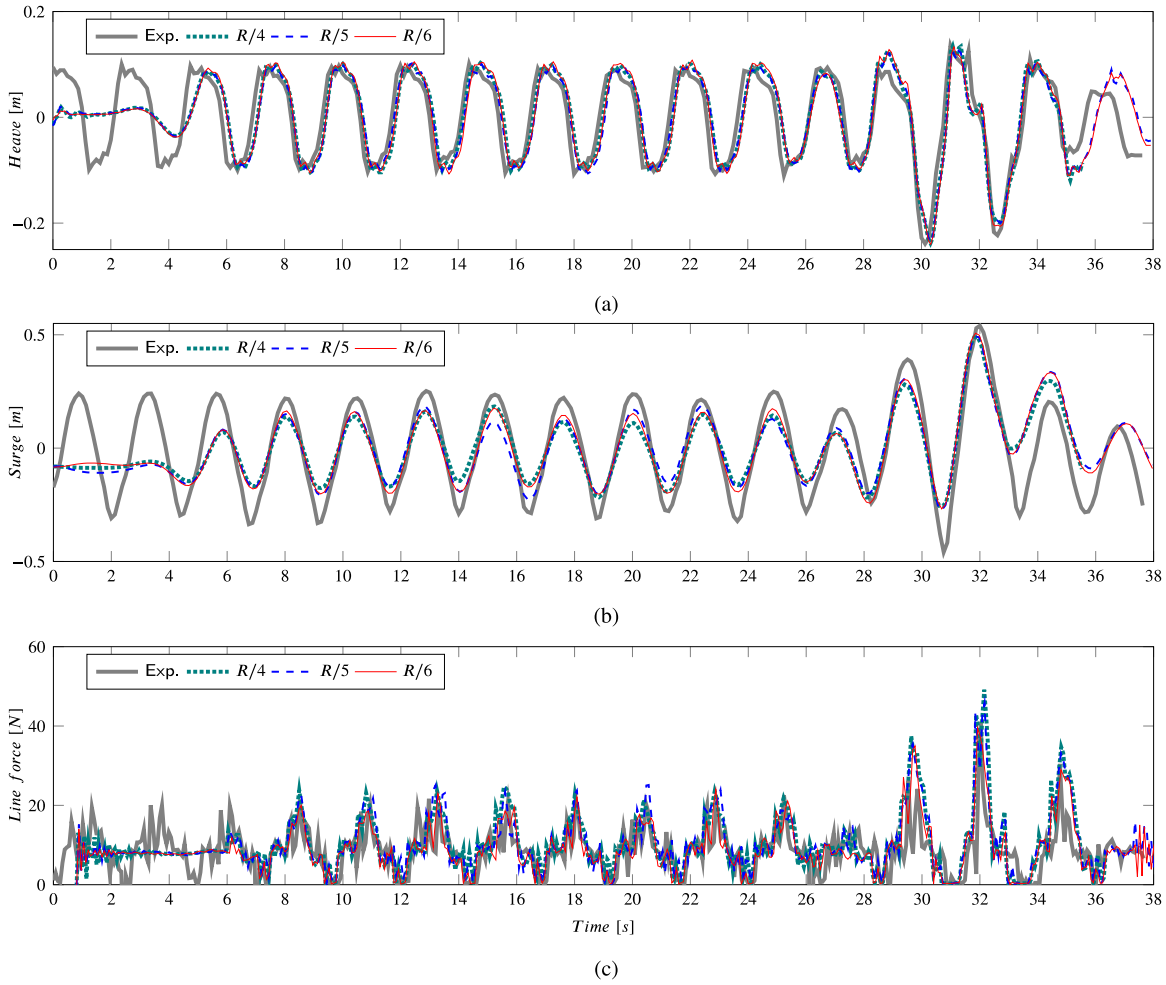

Fig. 7. Experimental and numerical buoy position in heave (a) and surge (b) motion, and line force (c) for the case with no PTO frictional damping (***C0***) reported in Table 8.

heave. The two charts 9(a) and 9(b) report the stretching evolution of the line that is computed as $L(t)-L0$, being $L(t)$ the length of the line in time. Note that in both panels, at the beginning of the simulations, the line stretches around 2 cm reaching equilibrium for a tension of around 9 N (refer to the first 3 s in 7(c) and 8(c)). For the case with no damping (Fig. 9(a)), the line stretches almost in unison with the motion of the translator, and some spikes appear when the translator hits the end-stop, which can be paired with the spikes shown in Fig. 10. On average, the magnitude of the stretch seldom exceeds the equilibrium value, due to the absence of resistance in the translator motion. On the other hand, the presence of a damping function in the PTO (Fig. 8(c)) strongly changes the stretching function: the line is engaged with higher tension for the moment the translator starts its motion, showing fainter peaks at the moments of impact.

Fig. 11 reports six frames of the simulation **C0** when the main peak of the focused train is striking the buoy; the first row depicts the velocity field interpolating values over the particles surrounding the float, and the second shows the y-component of the vorticity field over the computational nodes. Three instants of the simulation are captured here, namely when the main crest of the focused wave approaches the float (a) and (d); the crest is at buoy's location (b) and (e); and immediately after the crest overtakes the float (c) and (f), in the moment when the line force peaks. In addition, the frames point out the non-breaking nature of the waves described by the numerical model, which reduces the likelihood of slamming loads onto the float outer surface (for more see: [28]). The vorticity field shows the effects of the interaction of the body with the surrounding fluid, highlighting a high mass transport around the hull of the device. As a whole, the device is utterly submerged during this event, thus hampering the presence of slamming loads.

By discussing the quantities not reported in the experimental pool of data, useful information can be deduced. First of all, the presence of a damping function helps in reducing the magnitude of the forces that are generally experienced on the internal components of the power take-off and on the mooring line, thanks to the smoothing effect of the magnetic field on the dynamics of the translator. The line sees a more stable stretching function, which, in turn, implies a force trend more suitable for investigating fatigue cycles. However, the peak force is hardly altered by the presence of the damper, due to similar peak speeds at the moment of impact of the end-stop during the main peak of the focused wave. Finally, it can be concluded that higher snatching forces are expected when the line retakes tension, due to the combination of the inertia of the translator and the frictional force of the damping system.

Trying to hypothesize the reasons for the mismatching in some of the previously exposed quantities, it is possible to highlight some of differences in the physical and numerical configurations, the most important of which is the mass distribution on the geometry of the float. This conclusion is strengthened by the agreement shown in Fig. 8(a) when the motion is driven by the focused wave group: in this circumstance, the pitching motion becomes negligible due to the type of forces involved and only the shape of buoy can affect the magnitude of the force. Another source of discrepancy may arise from the wave-line interaction which can affect the magnitude of the force, albeit neglected in this work. It is worth mentioning that the artificial viscosity treatment used for this validation may have played a meaningful role in the

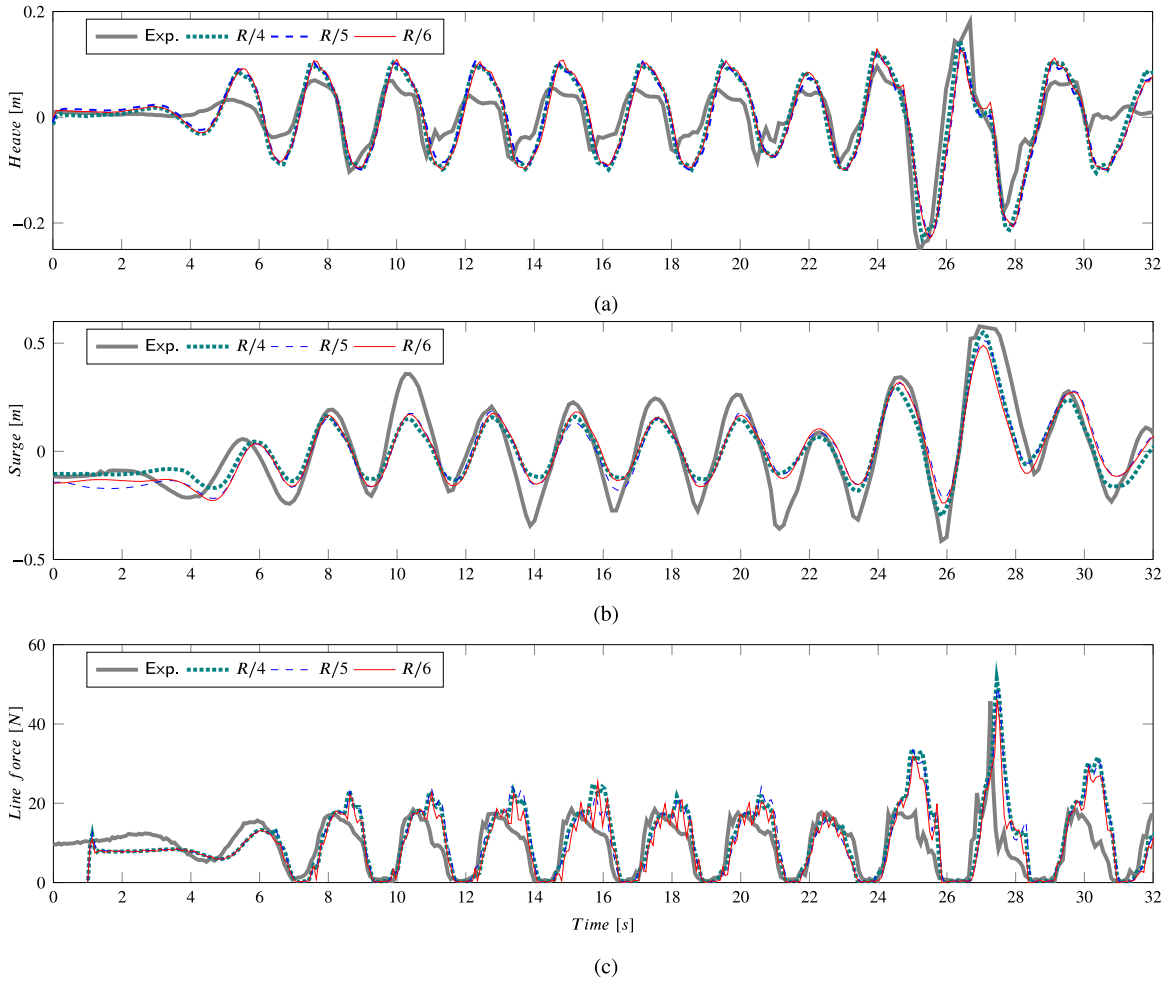

Fig. 8. Experimental and numerical buoy position in heave (a) and surge (b) motion, and line force (c) for the case with PTO frictional damping (***C2***) reported in Table 8.

phenomenon under discussion. However, further research is needed to identify the nature of this numerical–experimental mismatching, which occurred for the simulations presented in this work and it was observed in [44] as well.

7. Study with irregular waves

Extreme loads are typically defined as the maximum loads that can be expected during a specific duration, e.g., the n-year design loads. The return period must be defined according to the nominal life of the structure and to the expected failure mode [21]. As such, for the aim of the following analyses, the considered wave condition is not indicative of any specific safety check (more on this in EN1998 [21]); instead, it is used as a proxy for showing the general capabilities of the proposed tool. As a matter of fact, also specified in the reference research [25,42], the chosen event corresponds to a return period of 80 years at the Wave Hub site, located in southwest UK. This event was not chosen for a specific purpose, being not linked to any specific safety check thereafter performed (i.e., the Limit State was not identified).

The study performed in this section determines the dynamic response of the Uppsala WEC under irregular sea states, representative of realistic, extreme conditions. The time series of irregular waves is generated using a JONSWAP power density spectrum by means of an internal tool [82]. A stretched algorithm as described in [71] is used to define the band-width of the irregular wave train that has significant wave height H_{m0} = 0.27 m and peak period T_p = 2.393 s in 2.50-m water depth. To obtain a series of 500 waves, 1200 s of physical time are used to run the simulation; hence, the computational time is balanced by performing the following analyses (with and without device) discretizing the domain with an initial inter-particle distance $R/5$ (ref. Table 10), resulting in a computational time of roughly 800 h (30 days). This initial particle spacing provides sufficient accuracy as shown Table 11.

The same configuration of the numerical tank presented and validated in Section 5 (Wave tank) is utilized for wave generation and propagation. The motion of the piston is internally computed to match the time series, and corrected in time by an AWAS system. The accuracy of the system's generation and propagation capabilities is assessed through a simulation devoid of the device; the wave surface elevation at the buoy's location is gauged and analyzed by means of an FTT. Fig. 12 depicts the reference wave density spectrum, the theoretical one, and the numerical one. This comparison shows that the system produces the target free-surface elevation with sufficient accuracy, capturing the peak period with a 3%-error and slightly overshooting the H_{m0} value of about 4%.

The whole numerical domain validated in Section 6 is used to express the extreme forces as function of the PTO configuration. According to the values of the applied damping shown in [42], four test cases (**I0-I3**) are defined to evaluate the response of the system under irregular waves. The configuration of the damper for each case is presented in Table 12. To better adhere real PTO system working principles, the Coulomb-like damping is no longer included here, thus using solely a velocity-proportional one. The parameter c_h is deemed to be representative of the energy conversion process that takes place into the PTO (adjustable), whereas c_{PTO} simulates the internal dissipative

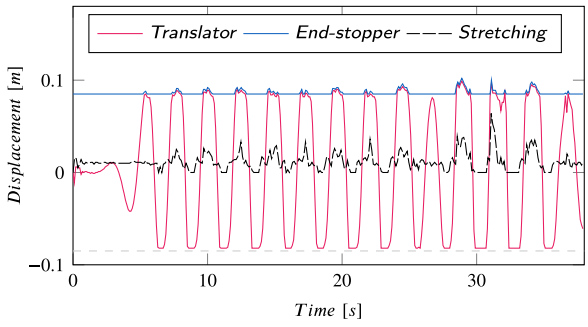

(a)

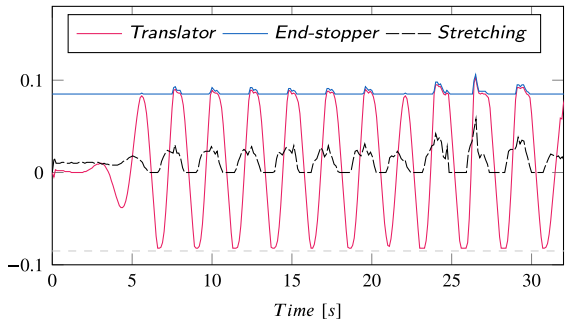

(b)

Fig. 9. Translator and end-stop displacements evolution, and line stretching function during case **C0** (a) and **C2** (b) reported in Table 8, for the initial particle spacing $R/6$. The dashed gray lines report the lower bound of the end-stopping system, which is fixed.

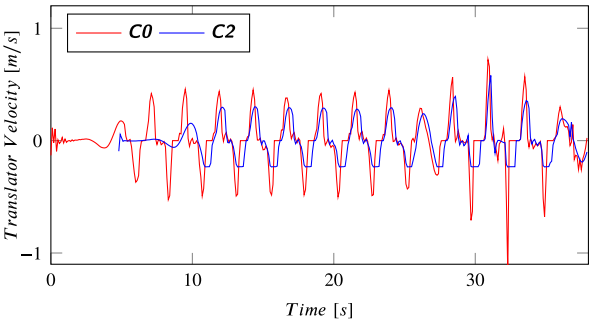

(a)

Fig. 10. Translator velocity evolution during case **C0** and **C2** reported in Table 8, for the initial particle spacing $R/6$.

Table 12
Definition of the generator damping for the numerical model analysis under irregular waves.

Label	c_h	c_{PTO}
I0	0.000 Ns/m	2.795 Ns/m
I1	3.333 Ns/m	2.795 Ns/m
I2	6.755 Ns/m	2.795 Ns/m
I3	9.725 Ns/m	2.795 Ns/m

mechanisms, shared among all the cases (fixed). Note that the Coulomb-to-viscous transformation is performed according to the scale factors given in [70].

The output of the numerical model for the four configurations presented in Table 12 is post-processed according to the following query. The wave height evolution measured in front of the device in each test is partitioned into single periods T_i with a down-zero-crossing function; the zero-cross procedure has been set to include in each time window a trough and the ensuing crest. In agreement with the identification of each zero-cross interval, the other quantities are partitioned as well. Specifically, within each T_i, the wave height A_i is calculated as the straight sum of the minimum and maximum absolute values of the free-surface elevation function; mins and maxs are then also combined to define another quantity, $H_i^2 = H_{max.i}^2 + H_{min.i}^2$ that may be considered as representative of the wave energy content; using the available information of the translator motion, the PTO absorbed power per period $P_i = c_h \int \dot{z}^2 dt$ is built; finally, the velocity evolution of the translator is used to retrieve the peak velocity per period $V_i = max(|\dot{z}|)$. Furthermore, the line force in each T_i is taken as the force peak within the identified time window, that is, $F_i = max(F_{line})$.

The charts proposed in Figs. 13(a) and 13(b) make use of the subsets of data computed in the preceding step. The former employs the wave height A_i and the peak force F_i, and it shows a scatter plot for each duo of wave height-peak force for the two extreme cases ***I0*** and ***I3*** in terms of damping. The second chart proposes an extreme value analysis of the peak force F_i through the exceedance probability function for the line forces of the four irregular wave tests ***I0*** − ***I3***. The main body of forces is linearly correlated to the wave height, clearly identifying a threshold where the slope of the relationship dramatically increases. This point (around $A_i \approx 0.27$ m) corresponds to the activation of the end-stopping system. Being the threshold higher than the total stroke due to the fact that the mean period of the hitting waves is not nearly close to the fundamental heave period of the system, which refers to the structure without end-stopping system. As pointed out by previous research on the same device [25,42,44], the main effect of increasing the PTO is to mild the extreme actions on to the system, which is consistently reported in this research as well. By comparing the trend of each data set (dashed lines in Fig. 13(a)), this aforementioned result is more visible. This is also straightened by the pattern of the lines reported in Fig. 13(b), which substantially show that the configuration with no damping is more likely to experience higher forces.

The data used in the extreme value analysis (Fig. 13) can provide an estimate of the maximum loads that might be expected to occur for the specified return periods. It is clear that the system benefits from the increase in internal damping for what accounts extreme values, for example, of the line forces. As a drawback, however, the damping shifts the force plateaus around smaller wave amplitudes — this fact concerns the most when fatigue analysis of the system is performed. A thorough design of the line diameter, material, and kind of fairlead connections should account for both conditions, as such fulfilling all the design requirements at once. A final piece of insight can be gained from inspecting the dependence of the exceedance probability on the PTO damping: it suggests that a value in between the cases **I1** and **I2** could provide the right balance between the serviceability and the survivability safety checks (safety and function).

Complementary to the previous analyses, a final part of this investigation deals with an in-depth examination of the dataset presented at the beginning of this section. For the four cases **I0-I3**, Fig. 14 charts the measured line peak forces against the individual wave height of the incident wave A_i (first column); the sum of the squared crest and trough H_i^2 (second column); the PTO absorbed power per period $P_i = c_{PTO} \int \dot{z}^2 dt$ (third column); and the maximum translator velocity per period $V_i = max(|\dot{z}|)$ (fourth column). Each scatter plot is fitted by a least-squares line and includes the Pearson correlation coefficient $\rho = \rho(F, Q)$, where F arrays the F_i scalars, and Q arrays the four variables (i.e., A_i, H_i^2, P_i, and V_i).

Fig. 14 suggests that the damping increases the linearity of the system's response, considered in terms of forces, for the four defined quantities. The first two rows show a high dispersion of the scatter plots as well around the fitting lines, whereas rows three and four show a more stable behavior and both the wave height and the wave energy could be used to make predictions about the evolution of the system for

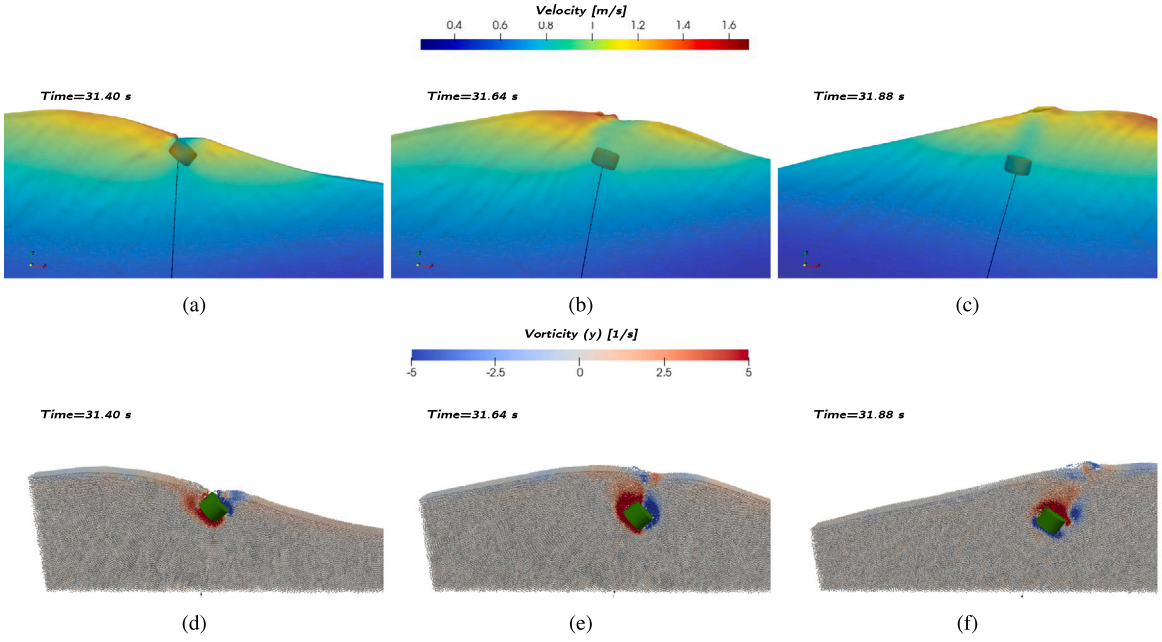

Fig. 11. 3D visualization of the numerical simulation **C0** for the resolution $R/6$. The snapshots represent three instants of it, respectively: the main crest of the focused wave approaching the float (a) and (d); when the crest is at buoy's location (b) and (e); and just after the crest (c) and (f), when the line force peaks. The colorbar above each row of frames reports the velocity magnitude for the surfaces, and the vorticity for the particle array around the float.

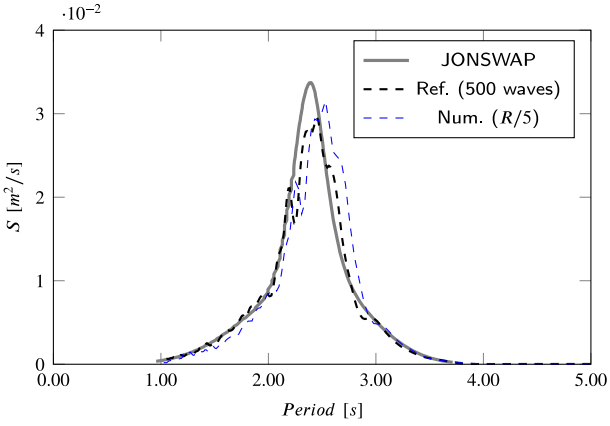

Fig. 12. Wave spectra for the case of irregular waves, comparison between the JONSWAP spectrum (T_p = 2.393 s, H_{m0} = 0.27 m, depth= 2.50 m), the reference one obtained with 500 wave periods, and the numerical one (resolution $R/5$) obtained from a simulation without the device.

modified conditions. The first two columns, which could be seen as a re-arrangement of the data in Fig. 13, prove that when a relevant value of the PTO damping is included in the system, its response correlates well with the external cause. The fourth column, instead, reveals that the peak velocity of the translator sensibly reduces with the increase of damping, meaning that the nature of the peak force is not related to translator hitting the end-stop, which can be taken as the instant when the velocity peaks, but rather to the end-stop spring reaching its maximum compression.

The following conclusions can be drawn from the extreme analysis presented in this section. The Uppsala WEC surely benefits from utilizing a greater value for the PTO damping: in the first place, more power is harvested by the system for smaller wave amplitudes and this may increase its revenue assuming that the system is connected to the grid; secondly, the reduced mobility of the translator inside the PTO can diminish detrimental effects on to the casing and, in turn, on the foundation. However, this effect is relegated to certain

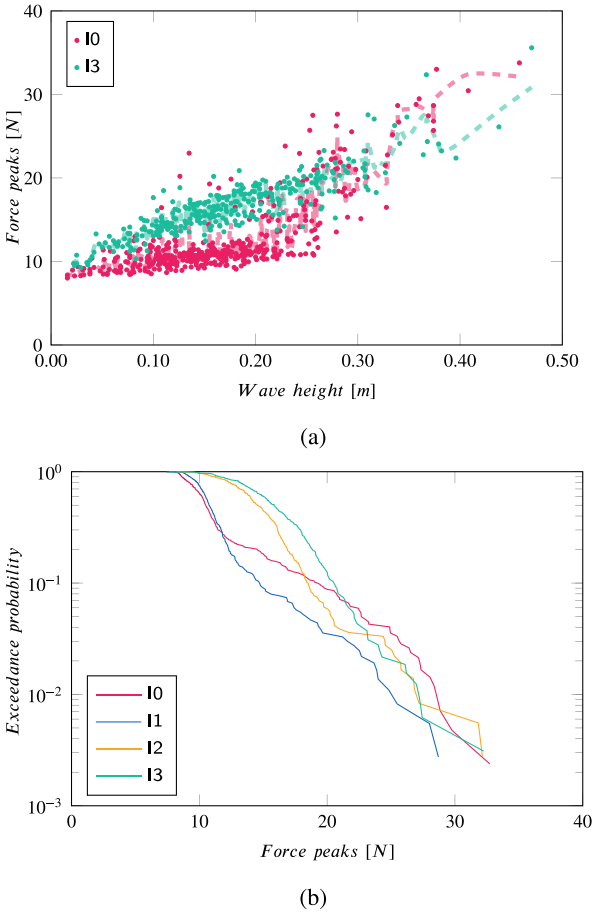

Fig. 13. (a) Measured force peaks for the four irregular wave tests ***I0*** and ***I3***, plotted against the individual wave height of the numerical incident wave. The dashed lines represent the running average of each set of data and are included to improve the chart readability. (b) Extreme value analysis through the exceedance probability function for the line forces of the four irregular wave tests ***I0*** – ***I3***.

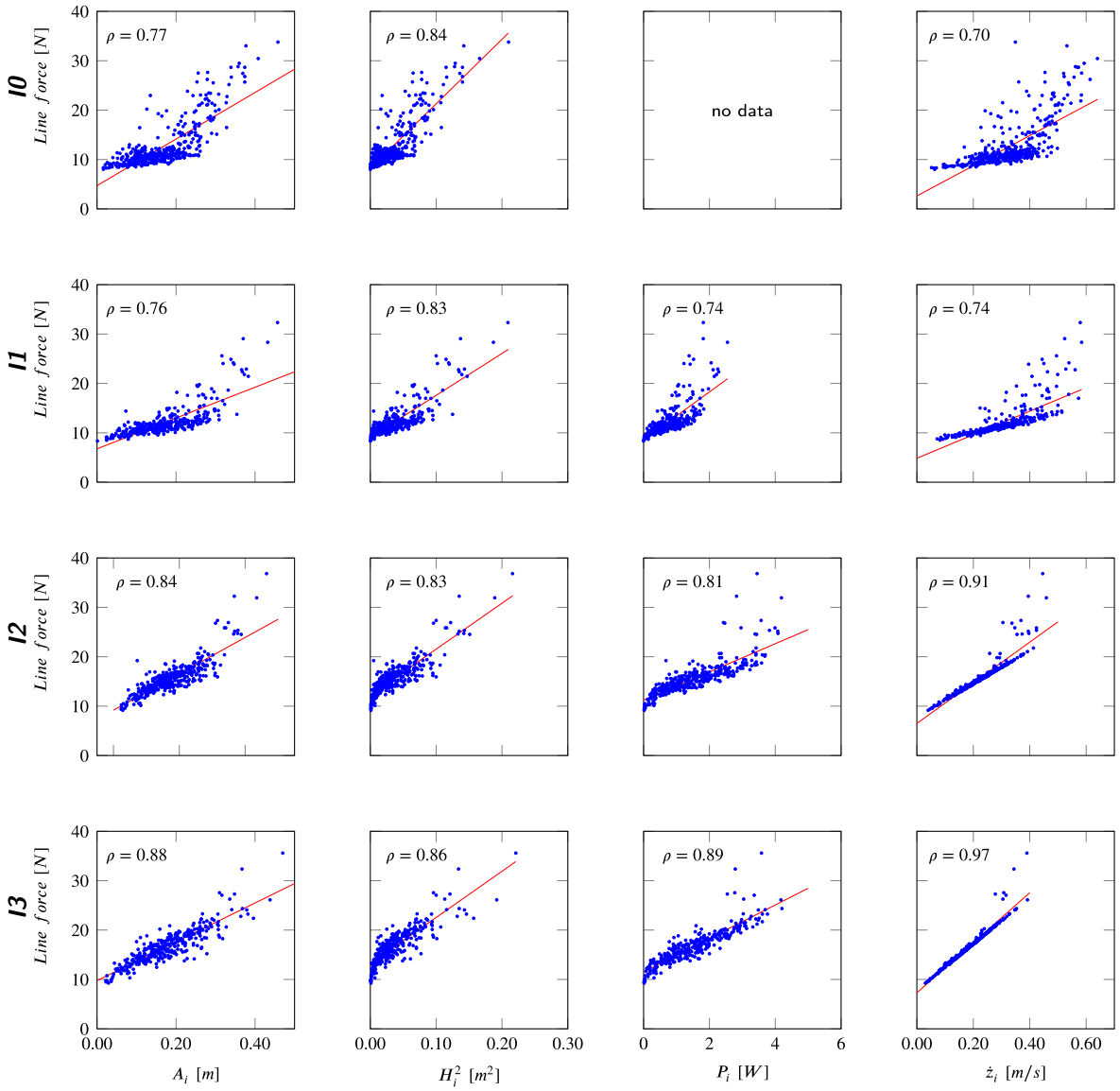

Fig. 14. Measured force peaks in irregular wave test $I0-I3$ plotted against the individual wave height of the incident wave A_i (first column); the squared individual wave height H_i^2 (second column); the PTO absorbed power per period $c_h \int \dot{z}^2 dt$ (third column); and the maximum translator velocity per period $\dot{z}$ (fourth column). Each scatter plot reports the value of the Pearson correlation coefficient ρ and a least-squares (red) line.

values of damping and only for extreme forces. It turns out that the harvesting function performance and the lifespan of the mooring system are interlocked. The optimization of the system must account for this feature, balancing the expected line load in the various conditions.

The end-stopping system could also see improvement. Its spring represents a booster during energy harvesting, but the primary duty of this element is to protect the system against extreme events. Hence, a way to reduce the peaks of the force would be to reduce the stiffness of the spring, which entails a longer spring length and with cascading effects on the design of the structure as a whole; it could also include a viscous damper, thus making it more similar to a shock-absorber.

8. Conclusions

Using the Uppsala WEC as a benchmark, this work has validated an open-source piece of software that combines the functionality of two different computing libraries. The time evolution of the incident wave, of the heave and surge motion, and the line force for two different PTO configurations are validated with contrasting experimental data. It showed that the mesh-less nature of the Smoothed Particle Hydrodynamics method has the right degree of maturity in handling survivability simulations of floating devices meant for wave energy conversion. Compared to meshbased solvers, violent and sudden changes in device configuration and fluid mechanics do not affect the stability and convergence of the system. Overall, DualSPHysics represents a useful asset for studying the kinematics of marine structures, and it can complement the set of tools already available for investigating wave energy converters.

The dataset presented in this research paper demonstrates that the proposed numerical model can capture the experimental behavior of the Uppsala WEC point absorber with sufficient accuracy, envisaging its use for analyses beyond this initial configuration. The proposed numerical method has shown to be apt for the simulation of real wave energy converters under extreme conditions. The validation was performed using the Uppsala WEC, which is composed of a float, a mooring line, and a complete power take-off system located at the sea floor, which includes end-stopping systems. The calibration and validation procedure could also be used to model devices with features similar to those of the Uppsala WEC, where the complex interaction of mooring

lines, mechanical constraints, and, of course, fluids themselves cannot be disregarded, rather must be included to get reliable information.

This work suggests that the Uppsala WEC performance can be improved. The management of the PTO internal damping turns out to be critical to enhancing the capability of the device, for short- and long-term conditions, and could be used to increase the robustness and resilience of the system. In fact, a system with self-adjustable internal damping, variable in time and in accordance with prior knowledge of the sea state actually impacting the device, may increase the device's life expectancy. The end-stopping system could see improvement as well. Although during the simulations carried out for this research the free stroke never exceeded the maximum allowable stroke, spring stiffness may be downgraded and coupled with a damper; this may reduce the harvesting capabilities of the system, but it will surely reduce the overall maximum actions.

Computational costs notwithstanding, a high-fidelity model, such as the one presented in this paper, can be used to run long simulations, considering complete sea states, and considering the high efficiency of the DualSPHysics framework, it is doable even without using HPC systems. Indeed, the expense of CFD simulations is well balanced by the accuracy that they can provide. The execution of these tests numerically leads to further knowledge of the system response with a high degree of detail, while the reproduction of the PTO system with a highly non-linear response, closely resembling real ones, allows investigating the response of the system in energetic sea-state conditions. This can provide feedback on possible strategies to be used to avoid oversizing while maintaining comparable degrees of reliability.

The applicability of numerical models to solving engineering problems is now beyond question. However, the convergence and stability problems that can arise when using state-of-the-art tools are not the only obstacles to using them to simulate wave energy converters. Passive and active control systems are a common practice for improving power capture performance; numerical simulations of dedicated hardware and software require a further improvement of the proposed code. On the validity and reliability of the results obtainable from the proposed model, it can be stated that the scale of the device that was used for validation purposes is relatively high, so much so that it can be expected that they have comparable effects from the fluid viscous forces (see [83]). Additional challenges arise from the way the power take-off is simulated. For example, when scaling the results to full, the pulley system used in the experiments has no full-scale analogs in the offshore environment and the mooring line elastic properties are generally different, although it may be selected to be consistent with the dynamic properties of real counterparts (see [84]). However, more research is needed to improve the reliability of scaling procedures for point-absorbing wave energy converters.

CRediT authorship contribution statement

Bonaventura Tagliafierro: Conceptualization, Validation, Investigation, Methodology, Formal analysis, Data curation, Visualization, Writing – original draft. **Iván Martínez-Estévez:** Software, Resources, Writing – review & editing. **José M. Domínguez:** Software, Resources, Writing – review & editing. **Alejandro J.C. Crespo:** Conceptualization, Validation, Visualization, Methodology, Formal analysis, Data curation, Investigation, Writing – original draft, Supervision, Resources, Funding acquisition. **Malin Göteman:** Investigation, Validation, Data curation, Writing – review & editing. **Jens Engström:** Investigation, Validation, Data curation, Writing – review & editing. **Moncho Gómez-Gesteira:** Methodology, Visualization, Supervision, Writing – review & editing, Project administration, Resources, Funding acquisition.

Declaration of competing interest

The authors declare that they have no known competing financial interests or personal relationships that could have appeared to influence the work reported in this paper.

Acknowledgments

Funding for open access charge: Universidade de Vigo/CISUG, Spain. This work was supported by the project SURVIWEC PID2020-113245RB-I00 financed by MCIN/ AEI /10.13039/ 501100011033 and by the project ED431C 2021/44 "Programa de Consolidación e Estructuración de Unidades de Investigación Competitivas" financed by Xunta de Galicia, Consellería de Cultura, Educación e Universidade, Spaon. This work was also partially supported by COST Action CA17105 WECANet "A pan-European Network for Marine Renewable Energy with a Focus on Wave Energy", supported by COST (European Cooperation in Science and Technology) which is funded by the Horizon 2020 Framework Programme of the European Union. COST is a funding agency for research and innovation networks.

B. Tagliafierro acknowledges funding from Italian Ministry for Education, University and Research (MIUR) as part of the program "Dottorati Innovativi a caratterizzazione industriale" (ID DOT 1328490-3), funded by the European Union (Structural Funding ERDF-ESF for "Research and Innovation" 2014–2020). I. Martínez-Estévez acknowledges funding from Xunta de Galicia, Spain under "Programa de axudas á etapa predoutoral da Consellería de Cultura, Educación e Universidades da Xunta de Galicia" (ED481A-2021/337). M. Göteman and J. Engström acknowledge funding from the Centre of Natural Hazards and Disaster Science, Sweden, STandUP for Energy and the Swedish Energy Authority (project number 47264-1). The authors wishes to express their gratitude to the IT team's support (EPhysLab, University of Vigo) in using the HPC system at http://monkey-island.uvigo.es. The authors are grateful to Dr. Corrado Altomare (Polytechnic University of Catalonia) for his insightful comments.

Appendix A. Coupling with project Chrono

A.1. Collision algorithm: smooth-contact code

Nonfluid objects are schematized as a set of particles; their motion is imposed by the system of Eqs. (9)–(10), being the cause defined in (7). When the distance between two approaching particles of two different floating objects is within the interaction radius, another branch of the code is demanded to estimate the forces that develop at contact. For the application presented in this study, the soft-sphere discrete element method (DEM) implemented in the Project Chrono library is employed; this approach considers the outer envelope surface of bodies to be deformable, which entails that the surfaces can overlap during their collision to a certain extent. Following the Project Chrono library coupling, the smooth-contact code (SMC) available from version Chrono-4.0.0 with a single-core module (DEM penalty-based in [33]).

Due to the particular motion imposed to the colliding rigid bodies, in the following, a description of the contact force that develops in the normal direction of collision is given. In fact, tangential forces are negligible and restricted to second-order deformations due to the motion of the PTO system being modeled in this work. The colliding objects (translator and the two end-stoppers (ref. to Fig. 2)) are restricted to move along the same axis.

The normal contact force $\boldsymbol{F}_n$, according to the model presented by [85]:

$$\boldsymbol{F}_n = k_n \delta_n^{\frac{3}{2}} \hat{\boldsymbol{n}} - c_n \delta_n^{\frac{3}{2}} v_n, \tag{19}$$

where k_n is the normal stiffness, c_n is the normal damping, v_n is the normal component of the relative velocity at the point of contact, δ_n is the normal overlap, and $\hat{\boldsymbol{n}}$ is the unit vector pointing from one particle center to the other. The quantities k_n and c_n are defined automatically by the Chrono module starting from the user-defined modulus of elasticity E_v, Poisson's ratio ν_c and coefficient of restitution e. More details are given in [86].

The extent of overlap, relative collision velocity, and other material properties are used to calculate the forces and torques acting on the bodies. Then, particle positions and velocities are updated by resolving all forces and torques in the N-body system (Eqs. (8) and (9)).

A.2. Mechanical restrictions: spring damper

The translational degrees of freedom between rigid instances can include reactive forces according to their relative motion. The element that is able to exert this force is called *spring–damper* element. Let i and j be two points belonging to two bodies, respectively; the relative force can be defined such that:

$$F_{sd} = c_{sd}\boldsymbol{v}_{ij} \cdot \hat{\boldsymbol{t}}_{sd} + k_{sp}\boldsymbol{r}_{ij} \cdot \hat{\boldsymbol{t}}_{sd} - f_{sd}\hat{\boldsymbol{t}}_{sd}, \tag{20}$$

where c_{sd}, k_{sd}, and f_{sd} are the viscous damping coefficient, stiffness, and friction damping that are implemented in the element, respectively; $\boldsymbol{r}_{ij}$ and $\boldsymbol{v}_{ij}$ are the relative position and velocity between points i and j. The term

$$\hat{\boldsymbol{t}}_{sd} = \frac{\boldsymbol{r}_j - \boldsymbol{r}_i}{|\boldsymbol{r}_j - \boldsymbol{r}_i|}, \tag{21}$$

is the direction along which the force is applied; $\boldsymbol{r}_i$ and $\boldsymbol{r}_j$ identify the position of the points. Note that no predictive algorithm is used for the final position of the connected nodes, thus the force is identified at each time step within one loop.

Appendix B. Coupling with MoorDyn+

B.1. Lumped-mass mooring line model

The lumped-mass approach consists in partitioning the entire *unstretched* length of a line (L_0) into N equally long segments, generating an $N + 1$ number of nodes. The position of each node that makes up the line in an absolute reference system is stored as $\boldsymbol{r}_i$, with i spanning over $i = 1...N + 1$. The properties of each segment are inherited from the overall geometry of the line, which is defined by the parameters: $l = L_0/N$; volume-equivalent area ($A = \pi/4d^2$, being d the volume-equivalent diameter), density(ρ), net mass $m_i = Al(\rho - \rho_w)$, being ρ_w the water density), elasticity modulus (E), and internal damping coefficient (C_{int}). An important assumption is made on the kinematics of the node: the tangential direction is defined as:

$$\hat{\boldsymbol{t}}_i = \frac{\boldsymbol{r}_{i^+} - \boldsymbol{r}_{i^-}}{|\boldsymbol{r}_{i^+} - \boldsymbol{r}_{i^-}|}, \tag{22}$$

where $\boldsymbol{r}_{i^+}$ and $\boldsymbol{r}_{i^-}$ identify the position of the proceeding and the following nodes in the line, respectively. It must be noticed that this procedure cannot be applied to the boundary nodes.

B.2. Internal forces

The system of equations that is ultimately solved to identify the position of each node is built by considering the internal forces coming from the two connected segments. Based on the hypothesis that each segment behaves as a spring–damper element, the internal forces net buoyancy W, can be defined as follows.

$$\boldsymbol{W}_{i^+} = m_i * \boldsymbol{g}, \tag{23}$$

$$\boldsymbol{T}_{i^+} = EA\epsilon_{i^+}\frac{\boldsymbol{r}_{i^+} - \boldsymbol{r}_i}{|\boldsymbol{r}_{i^+} - \boldsymbol{r}_i|} \cup \epsilon_{i^+} > 0, \tag{24}$$

$$\boldsymbol{C}_{i^+} = C_{int}A\dot{\epsilon}_{i^+}\frac{\boldsymbol{r}_{i^+} - \boldsymbol{r}_i}{|\boldsymbol{r}_{i^+} - \boldsymbol{r}_i|} \cup \epsilon_{i^+} > 0, \tag{25}$$

where $\boldsymbol{g}$ is the vector of gravity acceleration, ϵ_{i^+} and $\dot{\epsilon}_{i^+}$ are respectively the strain and the strain rate in the segment $_{i^+}$. It is important to stress that the constraints imposed over the rate and the strain rate makes the line only engaged in tension. The model herein used also does not account for bending and torsional stiffness that may be important to model more complex classes of mooring devices.

B.3. External forces

The MoorDyn library implements the effects of the line motion in still water by applying the hydrodynamic drag forces, which are solely proportional to the absolute node velocity $\dot{\boldsymbol{r}}_i$. The virtual geometry of each segment interacting with water is considered cylindrical and fully rigid. The transverse load on the line is calculated by using the approach proposed by [87], which yields:

$$\boldsymbol{D}_{t,i} = -\frac{1}{2}\rho_w \pi d l C_{dt} \|(\dot{\boldsymbol{r}}_i \cdot \hat{\boldsymbol{t}}_i)\hat{\boldsymbol{t}}_i\|(\dot{\boldsymbol{r}}_i \cdot \hat{\boldsymbol{t}}_i)\hat{\boldsymbol{t}}_i, \tag{26}$$

$$\boldsymbol{D}_{trans,i} = \frac{1}{2}\rho_w d l C_{dn} \|(\dot{\boldsymbol{r}}_i \cdot \hat{\boldsymbol{t}}_i)\hat{\boldsymbol{t}}_i - \dot{\boldsymbol{r}}_i\|((\dot{\boldsymbol{r}}_i \cdot \hat{\boldsymbol{t}}_i)\hat{\boldsymbol{t}}_i - \dot{\boldsymbol{r}}_i), \tag{27}$$

where C_{dt} and C_{dn} are the tangential and the transverse drag coefficients, respectively.

The added mass force at each node, when considering the tangential and the transverse contributions, can be expressed as:

$$\boldsymbol{m}_{a,i} = \rho_w Al[C_{an}(\boldsymbol{I} - \hat{\boldsymbol{t}}_i\hat{\boldsymbol{t}}_i^T) + C_{at}\hat{\boldsymbol{t}}_i\hat{\boldsymbol{t}}_i^T], \tag{28}$$

where C_{an} is the added mass coefficient in the transverse direction, C_{at} is the tangential added mass coefficient, $\boldsymbol{I}$ is the 3×3 identity matrix.

B.4. Mass and integration

The second-order system of equations that accounts for the mooring line dynamic can be written as follows:

$$\begin{aligned}(\boldsymbol{m}_i + \boldsymbol{m}_{a,i})\ddot{\boldsymbol{r}}_i = \boldsymbol{T}_{i^+} - \boldsymbol{T}_{i^-} + \boldsymbol{C}_{i^+} - \boldsymbol{C}_{i^-} + \boldsymbol{W}_i + \boldsymbol{D}_{t,i} + \\ + \boldsymbol{D}_{trans,i} \text{ for } i = 2...N,\end{aligned} \tag{29}$$

where $\boldsymbol{m}_i = Al\rho\boldsymbol{I}$. The system is closed by the boundary conditions given at the cable-end nodes (fairleads or fixed), which represent the interfaces over which the MoorDyn library and the DualSPHysics code communicate. In fact, as it is shown in [58], the coupling sets a cosimulating environment, where two simulations run in separate tasks. MoorDyn+ solves the $3(N + 1)$ equations using a constant-time-step second-order Runge–Kutta integrator.

B.5. Stability and segment damping

One of the main drawbacks of the lumped-mass approach to model cable in general is the introduction of higher modes of vibration along the axis of the line, which may give rise to nonphysical node oscillation. This problem is worked around in the formulation presented in [34] by finely setting the value C_{int} that can damp out components with frequencies close to the smallest one. The phenomenon has a natural frequency defined as:

$$f_n = \frac{1}{\pi l}\sqrt{\frac{E}{\rho}}. \tag{30}$$

Eq. (30) shows that the natural frequency depends on the user defined parameter N, being $l = L_0/N$. The radicand only accounts for the material being modeled that for the case of polyester fiber ($E \approx 1$ GPa and $\rho \approx 1000$ kg/m^3) yields to $f_n \cong 10/l$ Hz. This segment vibration is hence damped out by introducing a line internal damping (B [N s]) that almost makes the system critically damped (ξ close to 1) at f_n and it can be obtained through:

$$B = \xi l\sqrt{E\rho}. \tag{31}$$

The numerical treatment that is deployed to avoid having the line response dominated by resonance generated by the discretization could have an impact on the dynamics of interest if the dominant frequencies are close to f_n.

References

[1] Falcão AFdO. Wave energy utilization: A review of the technologies. Renew Sustain Energy Rev 2010;14(3):899–918. http://dx.doi.org/10.1016/j.rser.2009.11.003.

[2] Li Y, Yu Y-H. A synthesis of numerical methods for modeling wave energy converter-point absorbers. Renew Sustain Energy Rev 2012;16(6):4352–64. http://dx.doi.org/10.1016/j.rser.2011.11.008, URL: https://www.sciencedirect.com/science/article/pii/S1364032111005351.

[3] Gomes RP, Gato LM, Henriques JC, Portillo JC, Howey BD, Collins KM, Hann MR, Greaves DM. Compact floating wave energy converters arrays: Mooring loads and survivability through scale physical modelling. Appl Energy 2020;280:115982. http://dx.doi.org/10.1016/j.apenergy.2020.115982, URL: https://www.sciencedirect.com/science/article/pii/S030626192031429X.

[4] Muliawan MJ, Karimirad M, Gao Z, Moan T. Extreme responses of a combined spar-type floating wind turbine and floating wave energy converter (STC) system with survival modes. Ocean Eng 2013;65:71–82. http://dx.doi.org/10.1016/j.oceaneng.2013.03.002, URL: https://www.sciencedirect.com/science/article/pii/S002980181300111X.

[5] Göteman M, Giassi M, Engström J, Isberg J. Advances and challenges in wave energy park optimization—A review. Front Energy Res 2020;8:26. http://dx.doi.org/10.3389/fenrg.2020.00026, URL: https://www.frontiersin.org/article/10.3389/fenrg.2020.00026.

[6] Clemente D, Rosa-Santos P, Taveira-Pinto F. On the potential synergies and applications of wave energy converters: A review. Renew Sustain Energy Rev 2021;135:110162. http://dx.doi.org/10.1016/j.rser.2020.110162, URL: https://www.sciencedirect.com/science/article/pii/S1364032120304536.

[7] Penalba M, Davidson J, Windt C, Ringwood JV. A high-fidelity wave-to-wire simulation platform for wave energy converters: Coupled numerical wave tank and power take-off models. Appl Energy 2018;226:655–69. http://dx.doi.org/10.1016/j.apenergy.2018.06.008, URL: https://www.sciencedirect.com/science/article/pii/S0306261918308754.

[8] Coe RG, Ahn S, Neary VS, Kobos PH, Bacelli G. Maybe less is more: Considering capacity factor, saturation, variability, and filtering effects of wave energy devices. Appl Energy 2021;291:116763. http://dx.doi.org/10.1016/j.apenergy.2021.116763, URL: https://www.sciencedirect.com/science/article/pii/S0306261921002701.

[9] Lavidas G, Blok K. Shifting wave energy perceptions: The case for wave energy converter (WEC) feasibility at milder resources. Renew Energy 2021;170:1143–55. http://dx.doi.org/10.1016/j.renene.2021.02.041, URL: https://www.sciencedirect.com/science/article/pii/S0960148121002093.

[10] Coe RG, Bacelli G, Forbush D. A practical approach to wave energy modeling and control. Renew Sustain Energy Rev 2021;142:110791. http://dx.doi.org/10.1016/j.rser.2021.110791, URL: https://www.sciencedirect.com/science/article/pii/S1364032121000861.

[11] Garcia-Teruel A, DuPont B, Forehand DI. Hull geometry optimisation of wave energy converters: On the choice of the objective functions and the optimisation formulation. Appl Energy 2021;298:117153. http://dx.doi.org/10.1016/j.apenergy.2021.117153, URL: https://www.sciencedirect.com/science/article/pii/S0306261921005845.

[12] Cummins W. The impulse response function and ship motions. David Taylor model basin reports, Department of the Navy: Hydromechanics Laboratories; 1962.

[13] Beatty SJ, Hall M, Buckham BJ, Wild P, Bocking B. Experimental and numerical comparisons of self-reacting point absorber wave energy converters in regular waves. Ocean Eng 2015;104:370–86. http://dx.doi.org/10.1016/j.oceaneng.2015.05.027, URL: https://www.sciencedirect.com/science/article/pii/S0029801815002115.

[14] Penalba M, Kelly T, Ringwood J. Using NEMOH for modelling wave energy converters: A comparative study with WAMIT. In: 12th European wave and tidal energy conference (EWTEC). 2017, URL: http://mural.maynoothuniversity.ie/12466/.

[15] Rahmati M, Aggidis G. Numerical and experimental analysis of the power output of a point absorber wave energy converter in irregular waves. Ocean Eng 2016;111:483–92. http://dx.doi.org/10.1016/j.oceaneng.2015.11.011, URL: https://www.sciencedirect.com/science/article/pii/S0029801815006241.

[16] Davidson J, Giorgi S, Ringwood JV. Linear parametric hydrodynamic models for ocean wave energy converters identified from numerical wave tank experiments. Ocean Eng 2015;103:31–9. http://dx.doi.org/10.1016/j.oceaneng.2015.04.056, URL: https://www.sciencedirect.com/science/article/pii/S0029801815001432.

[17] van Rij J, Yu Y-H, Guo Y, Coe RG. A wave energy converter design load case study. J Mar Sci Eng 2019;7(8). http://dx.doi.org/10.3390/jmse7080250, URL: https://www.mdpi.com/2077-1312/7/8/250.

[18] Det Norske Veritas. Recommended practice: Environmental conditions and environmental loads. Oslo, Norway: DNV; 2007.

[19] Romano A, Bellotti G, Briganti R, Franco L. Uncertainties in the physical modelling of the wave overtopping over a rubble mound breakwater: The role of the seeding number and of the test duration. Coast Eng 2015;103:15–21. http://dx.doi.org/10.1016/j.coastaleng.2015.05.005, URL: http://www.sciencedirect.com/science/article/pii/S0378383915000915.

[20] Boccotti P. Idraulica marittima. UTET univertità; 2004.

[21] Gulvanessian H, Calgaro J-A, Holický M, Gulvanessian H. Designers' guide to eurocode: Basis of structural design. 2nd ed.. ICE Publishing; 2012, http://dx.doi.org/10.1680/bsd.41714, URL: https://www.icevirtuallibrary.com/doi/abs/10.1680/bsd.41714. arXiv:https://www.icevirtuallibrary.com/doi/pdf/10.1680/bsd.41714,

[22] Trueworthy A, DuPont B. The wave energy converter design process: Methods applied in industry and shortcomings of current practices. J Mar Sci Eng 2020;8(11). http://dx.doi.org/10.3390/jmse8110932, URL: https://www.mdpi.com/2077-1312/8/11/932.

[23] Coe R, Bacelli G, Wilson D, Patterson D. System identification of a heaving point absorber: Design of experiment and device modeling. Energies 2017;10:472. http://dx.doi.org/10.3390/en10040472.

[24] Penalba M, Giorgi G, Ringwood JV. Mathematical modelling of wave energy converters: A review of nonlinear approaches. Renew Sustain Energy Rev 2017;78:1188–207. http://dx.doi.org/10.1016/j.rser.2016.11.137.

[25] Sjökvist L, Wu J, Ransley E, Engström J, Eriksson M, Göteman M. Numerical models for the motion and forces of point-absorbing wave energy converters in extreme waves. Ocean Eng 2017;145:1–14. http://dx.doi.org/10.1016/j.oceaneng.2017.08.061, URL: https://www.sciencedirect.com/science/article/pii/S002980181730505X.

[26] Ropero-Giralda P, Crespo AJ, Tagliafierro B, Altomare C, Domínguez JM, Gómez-Gesteira M, Viccione G. Efficiency and survivability analysis of a point-absorber wave energy converter using DualSPHysics. Renew Energy 2020;162:1763–76. http://dx.doi.org/10.1016/j.renene.2020.10.012, URL: http://www.sciencedirect.com/science/article/pii/S0960148120315780.

[27] Lin Z, Chen H, Qian L, Ma Z, Causon D, Mingham C. Simulating focused wave impacts on point absorber wave energy converters. Proc Inst Civ Eng - Eng Comput Mech 2021;174(1):19–31. http://dx.doi.org/10.1680/jencm.19.00038, arXiv:https://doi.org/10.1680/jencm.19.00038.

[28] Katsidoniotaki E, Nilsson E, Rutgersson A, Engström J, Göteman M. Response of point-absorbing wave energy conversion system in 50-years return period extreme focused waves. J Mar Sci Eng 2021;9(3). http://dx.doi.org/10.3390/jmse9030345, URL: https://www.mdpi.com/2077-1312/9/3/345.

[29] Davidson J, Costello R. Efficient nonlinear hydrodynamic models for wave energy converter design—A scoping study. J Mar Sci Eng 2020;8(1). http://dx.doi.org/10.3390/jmse8010035, URL: https://www.mdpi.com/2077-1312/8/1/35.

[30] Windt C, Davidson J, Ringwood JV. High-fidelity numerical modelling of ocean wave energy systems: A review of computational fluid dynamics-based numerical wave tanks. Renew Sustain Energy Rev 2018;93:610–30. http://dx.doi.org/10.1016/j.rser.2018.05.020, URL: https://www.sciencedirect.com/science/article/pii/S1364032118303629.

[31] Domínguez J, Fourtakas G, Altomare C, Canelas R, Tafuni A, García Feal O, Martínez-Estévez I, Mokos A, Vacondio R, Crespo A, Rogers B, Stansby P, Gómez-Gesteira M. DualSPHysics: from fluid dynamics to multiphysics problems. Comput Part Mech 2021. http://dx.doi.org/10.1007/s40571-021-00404-2.

[32] González-Cao J, Altomare C, Crespo AJC, Domínguez JM, Gómez-Gesteira M, Kisacik D. On the accuracy of DualSPHysics to assess violent collisions with coastal structures. Comput Fluids 2019;179:604–12, URL: http://dx.doi.org/10.1016/j.compfluid.2018.11.021.

[33] Tasora A, Serban R, Mazhar H, Pazouki A, Melanz D, Fleischmann J, Taylor M, Sugiyama H, Negrut D. Chrono: An open source multi-physics dynamics engine. 2016, p. 19–49. http://dx.doi.org/10.1007/978-3-319-40361-8_2.

[34] Hall M. MoorDyn user's guide. 2018, [Online]: www.matt-hall.ca/moordyn.

[35] Brito M, Canelas R, García-Feal O, Domínguez J, Crespo A, Ferreira R, Neves M, Teixeira L. A numerical tool for modelling oscillating wave surge converter with nonlinear mechanical constraints. Renew Energy 2020;146:2024–43. http://dx.doi.org/10.1016/j.renene.2019.08.034.

[36] Tagliafierro B, Montuori R, Vayas I, Ropero-Giralda P, Crespo A, Domínguez J, Altomare C, Viccione G, Gòmez-Gesteira M. A new open source solver for modelling fluid-structure interaction: case study of a point-absorber wave energy converter with a power take-off unit. In: Proceedings of the 11th international conference on structural dynamics, Athens, Greece. 2020, http://dx.doi.org/10.47964/1120.9052.21578.

[37] Ropero-Giralda P, Crespo AJC, Coe RG, Tagliafierro B, Domínguez JM, Bacelli G, Gómez-Gesteira M. Modelling a heaving point-absorber with a closed-loop control system using the DualSPHysics code. Energies 2021;14(3). http://dx.doi.org/10.3390/en14030760, URL: https://www.mdpi.com/1996-1073/14/3/760.

[38] Quartier N, Ropero-Giralda P, Domínguez JM, Stratigaki V, Troch P. Influence of the drag force on the average absorbed power of heaving wave energy converters using smoothed particle hydrodynamics. Water 2021;13(3). http://dx.doi.org/10.3390/w13030384, URL: https://www.mdpi.com/2073-4441/13/3/384.

[39] Crespo A, Altomare C, Domínguez J, González-Cao J, Gómez-Gesteira M. Towards simulating floating offshore oscillating water column converters with smoothed particle hydrodynamics. Coast Eng 2017;126:11–26. http://dx.doi.org/10.1016/j.coastaleng.2017.05.001.

[40] Quartier N, Crespo AJ, Domínguez JM, Stratigaki V, Troch P. Efficient response of an onshore oscillating water column wave energy converter using a one-phase SPH model coupled with a multiphysics library. Appl Ocean Res 2021;115:102856. http://dx.doi.org/10.1016/j.apor.2021.102856, URL: https://www.sciencedirect.com/science/article/pii/S0141118721003278.

[41] Waters R, Stålberg M, Danielsson O, Svensson O, Gustafsson S, Strömstedt E, Eriksson M, Sundberg J, Leijon M. Experimental results from sea trials of an offshore wave energy system. Appl Phys Lett 2007;90(3):034105. http://dx.doi.org/10.1063/1.2432168.

[42] Göteman M, Engström J, Eriksson M, Hann M, Ransley E, Greaves D, Leijon M. Wave loads on a point-absorbing wave energy device in extreme waves. International ocean and polar engineering conference, All Days, 2015, ISOPE-I-15-593.

[43] Hann M, Greaves D, Raby A, Howey B. Use of constrained focused waves to measure extreme loading of a taut moored floating wave energy converter. Ocean Eng 2018;148:33–42. http://dx.doi.org/10.1016/j.oceaneng.2017.10.024, URL: https://www.sciencedirect.com/science/article/pii/S0029801817306261.

[44] Engström J, Sjökvist L, Göteman M, Eriksson M, Hann M, Ransley E, Greaves M. Buoy geometry and its influence on survivability for a point absorbing wave energy converter: Scale experiment and CFD simulations. School of Engineering, Computing and Mathematics; 2017, p. 4, URL: http://hdl.handle.net/10026.1/13620.

[45] Chen W, Dolguntseva I, Savin A, Zhang Y, Li W, Svensson O, Leijon M. Numerical modelling of a point-absorbing wave energy converter in irregular and extreme waves. Appl Ocean Res 2017;63:90–105. http://dx.doi.org/10.1016/j.apor.2017.01.004, URL: https://www.sciencedirect.com/science/article/pii/S0141118716302668.

[46] Sjökvist L, Göteman M. Peak forces on a point absorbing wave energy converter impacted by tsunami waves. Renew Energy 2019;133:1024–33. http://dx.doi.org/10.1016/j.renene.2018.10.092, URL: https://www.sciencedirect.com/science/article/pii/S0960148118312953.

[47] Davidson J, Costello R. Efficient nonlinear hydrodynamic models for wave energy converter design - a scoping study. J Mar Sci Eng 2020;8:35. http://dx.doi.org/10.3390/jmse8010035.

[48] Monaghan JJ. Smoothed particle hydrodynamics. Rep Progr Phys 2005;68(8):1703–59. http://dx.doi.org/10.1088/0034-4885/68/8/r01.

[49] Monaghan JJ. Smoothed particle hydrodynamics. Annu Rev Astron Astrophys 1992;30(1):543–74. http://dx.doi.org/10.1146/annurev.aa.30.090192.002551.

[50] Wendland H. Piecewise polynomial, positive definite and compactly supported radial basis functions of minimal degree. Adv Comput Math 1995;4(1):389–96. http://dx.doi.org/10.1007/BF02123482, URL: http://sro.sussex.ac.uk/id/eprint/24323/.

[51] Molteni D, Colagrossi A. A simple procedure to improve the pressure evaluation in hydrodynamic context using the SPH. Comput Phys Comm 2009;180(6):861–72. http://dx.doi.org/10.1016/j.cpc.2008.12.004.

[52] Antuono M, Colagrossi A, Marrone S. Numerical diffusive terms in weakly-compressible SPH schemes. Comput Phys Comm 2012;183(12):2570–80. http://dx.doi.org/10.1016/j.cpc.2012.07.006, URL: http://www.sciencedirect.com/science/article/pii/S0010465512002342.

[53] Fourtakas G, Vacondio R, Domínguez J, Rogers B. Improved density diffusion term for long duration wave propagation. In: Proceedings of the international SPHERIC workshop, Harbin, China. 2020.

[54] Monaghan JJ, Cas RAF, Kos AM, Hallworth M. Gravity currents descending a ramp in a stratified tank. J Fluid Mech 1999;379:39–69. http://dx.doi.org/10.1017/S0022112098003280.

[55] Batchelor GK. An introduction to fluid dynamics. Cambridge mathematical library, Cambridge University Press; 2000, http://dx.doi.org/10.1017/CBO9780511800955.

[56] Monaghan J, Kos A, Issa N. Fluid motion generated by impact. J Waterway Port Coast Ocean Eng 2003;129(6):250–9. http://dx.doi.org/10.1061/(ASCE)0733-950X(2003)129:6(250).

[57] Canelas RB, Domínguez JM, Crespo AJ, Gómez-Gesteira M, Ferreira RM. A smooth particle hydrodynamics discretization for the modelling of free surface flows and rigid body dynamics. Int J Numer Methods Fluids 2015;78(9):581–93. http://dx.doi.org/10.1002/fld.4031.

[58] Domínguez J, Crespo A, Hall M, Altomare C, Wu M, Stratigaki V, Troch P, Cappietti L, Gómez-Gesteira M. SPH simulation of floating structures with moorings. Coast Eng 2019;153:103560. http://dx.doi.org/10.1016/j.coastaleng.2019.103560.

[59] Crespo A, Gómez-Gesteira M, Dalrymple R. Boundary conditions generated by dynamic particles in SPH methods. Comput Mater Continua 2007;5(3):173–84.

[60] Zhang F, Crespo A, Altomare C, Domínguez J, Marzeddu A, Shang S-p, Gómez-Gesteira M. DualSPHysics: A numerical tool to simulate real breakwaters. J Hydrodyn 2018;30. http://dx.doi.org/10.1007/s42241-018-0010-0.

[61] English A, Domínguez J, Vacondio R, Crespo A, Stansby P, Lind S, Chiapponi L, Gómez-Gesteira M. Modified dynamic boundary conditions (mDBC) for general purpose smoothed particle hydrodynamics (SPH): application to tank sloshing, dam break and fish pass problems. Comput Part Mech 2021. http://dx.doi.org/10.1007/s40571-021-00403-3.

[62] Liu M, Liu G. Restoring particle consistency in smoothed particle hydrodynamics. Appl Numer Math 2006;56(1):19–36. http://dx.doi.org/10.1016/j.apnum.2005.02.012, URL: https://www.sciencedirect.com/science/article/pii/S0168927405000565.

[63] Fourtakas G, Dominguez JM, Vacondio R, Rogers BD. Local uniform stencil (LUST) boundary condition for arbitrary 3-D boundaries in parallel smoothed particle hydrodynamics (SPH) models. Comput & Fluids 2019;190:346–61. http://dx.doi.org/10.1016/j.compfluid.2019.06.009.

[64] Martínez-Estévez I. MoorDynPlus. 2021, https://github.com/imestevez/MoorDynPlus. Accessed: 2021-07-27.

[65] Davidson J, Ringwood JV. Mathematical modelling of mooring systems for wave energy converters—A review. Energies 2017;10(5). http://dx.doi.org/10.3390/en10050666, URL: https://www.mdpi.com/1996-1073/10/5/666.

[66] Xu S, Wang S, Guedes Soares C. Review of mooring design for floating wave energy converters. Renew Sustain Energy Rev 2019;111:595–621. http://dx.doi.org/10.1016/j.rser.2019.05.027, URL: https://www.sciencedirect.com/science/article/pii/S1364032119303399.

[67] Canelas R, Brito M, Feal O, Domínguez J, Crespo A. Extending DualSPHysics with a differential variational inequality: modeling fluid-mechanism interaction. Appl Ocean Res 2018;76:88–97. http://dx.doi.org/10.1016/j.apor.2018.04.015.

[68] Tasora A, Anitescu M. A matrix-free cone complementarity approach for solving large-scale, nonsmooth, rigid body dynamics. Comput Methods Appl Mech Engrg 2011;200(5):439–53. http://dx.doi.org/10.1016/j.cma.2010.06.030.

[69] Hall M, Goupee A. Validation of a lumped-mass mooring line model with deepcwind semisubmersible model test data. Ocean Eng 2015;104:590–603. http://dx.doi.org/10.1016/j.oceaneng.2015.05.035, URL: https://www.sciencedirect.com/science/article/pii/S0029801815002279.

[70] Giannini G, Temiz I, Rosa-Santos P, Shahroozi Z, Ramos V, Göteman M, Engström J, Day S, Taveira-Pinto F. Wave energy converter power take-off system scaling and physical modelling. J Mar Sci Eng 2020;8(9). http://dx.doi.org/10.3390/jmse8090632, URL: https://www.mdpi.com/2077-1312/8/9/632.

[71] Altomare C, Domínguez J, Crespo A, González-Cao J, Suzuki T, Gómez-Gesteira M, Troch P. Long-crested wave generation and absorption for SPH-based DualSPHysics model. Coast Eng 2017;127:37–54. http://dx.doi.org/10.1016/j.coastaleng.2017.06.004.

[72] Gomez-Gesteira M, Rogers B, Crespo A, Dalrymple R, Narayanaswamy M, Dominguez J. Sphysics – development of a free-surface fluid solver – Part 1: Theory and formulations. Comput Geosci 2012;48:289–99. http://dx.doi.org/10.1016/j.cageo.2012.02.029.

[73] Whittaker C, Fitzgerald C, Raby A, Taylor P, Orszaghova J, Borthwick A. Optimisation of focused wave group runup on a plane beach. Coast Eng 2017;121:44–55. http://dx.doi.org/10.1016/j.coastaleng.2016.12.001, URL: https://www.sciencedirect.com/science/article/pii/S0378383916304161.

[74] Tromans PS, Anaturk AR, Hagemeijer P. A new model for the kinematics of large ocean waves-application as a design wave. International ocean and polar engineering conference, All Days, 1991, arXiv:https://onepetro.org/ISOPEIOPEC/proceedings-pdf/ISOPE91/All-ISOPE91/ISOPE-I-91-154/2004345/isope-i-91-154.pdf. ISOPE-I-91-154.

[75] Madsen OS. On the generation of long waves. J Geophys Res (1896-1977) 1971;76(36):8672–83. http://dx.doi.org/10.1029/JC076i036p08672, URL: https://agupubs.onlinelibrary.wiley.com/doi/abs/10.1029/JC076i036p08672. arXiv:https://agupubs.onlinelibrary.wiley.com/doi/pdf/10.1029/JC076i036p08672.

[76] Carpintero Moreno E, Fourtakas G, Stansby P, Crespo A. Response of the multi-float WEC M4 in focussed waves using SPH. In: Proceedings of 4th international conference on renewable energies offshore, October 2020, Lisbon, Portugal. 2020.

[77] Ransley E, Greaves D, Raby A, Simmonds D, Hann M. Survivability of wave energy converters using CFD. Renew Energy 2017;109:235–47. http://dx.doi.org/10.1016/j.renene.2017.03.003, URL: https://www.sciencedirect.com/science/article/pii/S0960148117301799.

[78] Hasselmann K, Barnett T, Bouws E, Carlson H, Cartwright D, Enke K, Ewing J, Gienapp H, Hasselmann D, Kruseman P, Meerburg A, Muller P, Olbers D, Richter K, Sell W, Walden H. Measurements of wind-wave growth and swell decay during the joint north sea wave project (JONSWAP). Deut Hydrogr Z 1973;8:1–95.

[79] Willmott CJ, Robeson SM, Matsuura K. A refined index of model performance. Int J Clim 2012;32(13):2088–94. http://dx.doi.org/10.1002/joc.2419, URL: https://rmets.onlinelibrary.wiley.com/doi/abs/10.1002/joc.2419. arXiv:https://rmets.onlinelibrary.wiley.com/doi/pdf/10.1002/joc.2419.

[80] Willmott CJ, Ackleson SG, Davis RE, Feddema JJ, Klink KM, Legates DR, O'Donnell J, Rowe CM. Statistics for the evaluation and comparison of models. J Geophy Res: Oceans 1985;90(C5):8995–9005. http://dx.doi.org/10.1029/JC090iC05p08995, URL: https://agupubs.onlinelibrary.wiley.com/doi/abs/10.1029/JC090iC05p08995. arXiv:https://agupubs.onlinelibrary.wiley.com/doi/pdf/10.1029/JC090iC05p08995.

[81] Gruwez V, Altomare C, Suzuki T, Streicher M, Cappietti L, Kortenhaus A, Troch P. Validation of RANS modelling for wave interactions with sea dikes on shallow foreshores using a large-scale experimental dataset. J Mar Sci Eng 2020;8(9). http://dx.doi.org/10.3390/jmse8090650, URL: https://www.mdpi.com/2077-1312/8/9/650.

[82] Altomare C, Tagliafierro B, Dominguez J, Suzuki T, Viccione G. Improved relaxation zone method in SPH-based model for coastal engineering applications. Appl Ocean Res 2018;81:15–33. http://dx.doi.org/10.1016/j.apor.2018.09.013, URL: https://www.sciencedirect.com/science/article/pii/S0141118718303705.

[83] Orphin J, Nader J-R, Penesis I. Size matters: Scale effects of an OWC wave energy converter. Renew Energy 2021. http://dx.doi.org/10.1016/j.renene.2021.11.121, URL: https://www.sciencedirect.com/science/article/pii/S0960148121017171.

[84] Hughes SA. Physical models and laboratory techniques in coastal engineering. World Scientific; 1993, http://dx.doi.org/10.1142/2154, URL: https://www.worldscientific.com/doi/abs/10.1142/2154. arXiv:https://www.worldscientific.com/doi/pdf/10.1142/2154.

[85] Flores P, Machado M, Silva M, Martins J. On the continuous contact force models for soft materials in multibody dynamics. Multibody Syst Dyn 2012;25:357–75. http://dx.doi.org/10.1007/s11044-010-9237-4.

[86] Sunday C, Murdoch N, Tardivel S, Schwartz SR, Michel P. Validating N-body code chrono for granular DEM simulations in reduced-gravity environments. Mon Not R Astron Soc 2020;498(1):1062–79. http://dx.doi.org/10.1093/mnras/staa2454.

[87] Morison J, Johnson J, Schaaf S. The force exerted by surface waves on piles. J Pet Technol 1950;2(05):149–54. http://dx.doi.org/10.2118/950149-G, arXiv:https://onepetro.org/JPT/article-pdf/2/05/149/2238818/spe-950149-g.pdf.

CHAPTER 5

Discussion

This chapter describes the implementation and the simulations performed to validate the code, as well as its application to a real engineering problem studying a WEC under extreme waves. The content is presented in the following sections: i) rigid multi-body dynamics; ii) flexible structures; and iii) real engineering application. It should be noted that, the developments of source code included in DualSPHysics for this doctoral thesis, were implemented using C++ for the core code, but also optimised and accelerated using both OpenMP to exploit the parallelism of multi-core CPUs and CUDA to execute the code on massive parallel GPUs. However, for practical reasons, the results presented in this doctoral thesis and discussed in this section were carried out using only the GPU implementation of DualSPHysics.

5.1 Rigid multi-body dynamics

The first approach involves the two-way SPH-DEM coupling between DualSPHysics and Chrono to solve fluid-solid-solid interactions, including frictional contacts, and multibody dynamics systems that comprise mechanical constraints. For the first implementation, a new method to deal with collision detection, denoted as SMC, has been integrated into the coupling. Thus, two approaches are available in this coupling (SMC and NSC), which differ in terms of their capabilities, parameterisations, as well as in their computational complexity. In addition, a new formulation to reproduce frictional dampers, denoted as Coulomb dampers, has also been integrated into the code. These implementations and all the available features have been presented in Section 4.1, which has been published as a program paper (journal publication with the source code used). That article describes the main formulation, the features available in this coupled model, as well as the coupling strategy through a general-purpose communication interface (the so-called DSPHChronoLib). Therefore, the work presents a complete program documentation

of the three software tools (DualSPHysics, DSPHChronoLib and Chrono), showing the most important source files developed and used to connect both models in a single co-operative framework via DSPHChronoLib. Additionally, the article is published together with the source code, which is released under GNU Lesser General Public License (LGPL), guidelines for its compilation and usability, including the set of benchmarks presented in the article to reproduce the results. Next subsections contain the results and discussion of the validations performed for collision detection and multibody dynamics.

5.1.1 Collision detection

Several cases were proposed to validate the NSC and SMC methods for collision detection. The first case comprises a steel sphere that is completely submerged in liquid into a steel tank (see Section 4.1). The ball is dropped and eventually impacts the steel bottom of the tank. Therefore, for this benchmark, the trajectory of the ball is tracked, and the fluid-solid-solid interactions are computed and compared with experiments. The solid-solid interactions are solved with the new SMC method. A convergency study is performed for different SPH resolutions and results show the accuracy of both, the SPH solver to simulate the fluid-solid interaction and the DEM solver to reproduce the solid-solid interaction in comparison with the reference experimental data (Hagemeier et al., 2020). The root mean square error (RMSE) estimator is used to provide a quantitative measure of the accuracy of the produced results, providing an error of 0.0017 for the highest SPH resolution. On the other hand, the NSC method is validated for a multiple body collision (see Section 4.1). Several aluminium cylinders are stacked to form an unstable column of material, which eventually breaks due to gravity, releasing the cylinders and allowing them to be tracked. Two configurations were considered, one in dry conditions to validate the multi-body contacts, and the other, including the cylinders completely submerged in water to validate the fluid-solid-solid interactions. numerical results provide a quantitative estimation of the accuracy of the model compared to the experimental data (Zhang et al., 2009). The coupled code showed reasonably good behaviour, with small inconsistencies within a ±2% range that, however, it is an acceptable discrepancy considering the chaotic nature of the phenomenon.

5.1.2 Multi-body dynamics

Among the features of multi-body dynamics, the selected cases allow validating the dynamic constraints provided by elements defined as a rotational hinge and a linear spring-damper (see Section 4.1). Two cases are presented, a gravity pendulum (hinge) and spring pendulum (spring-damper), both tested in air and water, for which the amplitude movement was measured. The reference data was taken from. In this coupling, the mechanical system response is only dependent on the quality of the geometry and/or mechanical properties that are shared with Chrono when analysing the behaviour in dry conditions or in air. However, when the mechanical system interacts with fluid, the resolution of SPH plays an important role because the fluid forces are predominant. Numerical results for the tests in air are in perfect agreement with the reference data (Arnold et al., 2015) when comprising mechanical constraints for both the gravity and the spring pendulum and reporting a relative error smaller than 0.5% and 0.1%, respectively. After, for the tests in water, a convergence study has been conducted by varying the SPH resolution. Results show that the numerical model can predict the response of the system according to the experimental data used as reference, however, there are some discrepancies. For both the gravity and spring pendulum in water, a slow-down of the movement was observed, which translates into an underestimation of the amplitude of the movement. This issue could be due to the high damping of the fluid when solving the fluid-solid interaction. Note that as the SPH model resolution increases, so does the accuracy of the fluid-solid interaction. Therefore, it is assumed that the model is more consistent at higher resolutions and could provide more accurate results.

5.2 Flexible structures

The second approach involves a novel implementation of a two-way SPH-FEA coupling to solve FSI problems where the structure can experience large displacements and deformations (see Section 4.2). This implementation employs DualSPHysics and Chrono and takes advantage of the previously described coupling strategy, so newer developments presented here use the general-purpose communication interface DSPHChronoLib to exchange data between DualSPHysics

and Chrono. The article in Section 4.2 describes the main formulation of the SPH-based coded, as well as the formulation integrated into the FEM-based solver to simulate the flexible structure, which is considered as a Euler-Bernoulli beam. Additionally, the coupling strategy is also detailed showing the main processes that take place when solving a single step in this coupled SPH-FEA code. Furthermore, widely used benchmarks of other numerical models were considered to evaluate this coupled code for solving FSI phenomena. These test cases, which are described in the following subsections, can be grouped as structural dynamics and fluid-structure interactions.

5.2.1 Structural dynamics

A first benchmark is proposed to analyse the accuracy of the structure solution under dynamic conditions (see Section 4.2). The dynamic response of a cantilevered beam is subjected to an initial velocity distribution and numerical results are compared to an analytical solution derived from the theory of thin plates (Landau and Lifshitz, 1970). To evaluate the structural dynamics behaviour, a convergency study is conducted considering different FEM resolutions. Results show that the beam tip deflection matches the theoretical solution for each case, providing an overall error on the amplitude around 1.5%. The convergence study showed that there are little differences between the FEM resolutions considered. This means that there is no need to consider very fine FEM resolutions to obtain an accurate structural response of the beams using this implementation.

5.2.2 Fluid-structure interactions

Three benchmarks have been conducted to validate the full coupled model when FSI phenomena take place.

The first validation to study FSI consists of a hydrostatic water column on an elastic beam (see Section 4.2). This benchmark does not comprise violent impacts and sudden variation of motion of the structure, however, it is relevant to evaluate the accuracy of this coupled code. This test case was originally proposed as a theoretical setup (Fourey, 2012). The hydrostatic water column is at equilibrium on a double-clamped aluminium plate (beam). The beam deflection is measured at its

mid-span point and compared against the reference theoretical solution to evaluate the accuracy. In this case, the number of segments, what refers to FEM resolution, slightly affects the accuracy of the entire system even when increasing the SPH resolution. Therefore, using reasonable FEM resolutions, the numerical model fully captures the analytical solution. Considering the convergence analysis using different SPH resolutions, it is observed that the SPH resolution plays an important role in the accuracy and stability of the water column. In fact, finer resolutions are indicative of less noisy pressure fields due to the weakly compressible SPH formulation implemented in DualSPHysics.

The second case is a breaking water-column with an elastic gate, which is based on an experimentally tested setup (Antoci et al., 2007). The elasticity of the gate is modelled using a beam to reproduce the deformation induced by the fluid pressure due to the discharge of the breaking water-column. The accuracy of the numerical model is investigated by analysing the beam tip displacement in the vertical and the horizontal directions and compared against the experimental reference data. The objective of this analysis is to provide an evaluation of the accuracy sensitivity to the SPH resolution. It can be noticed that the results tend to converge to the reference data when increasing the resolution. A quantitative assessment of the performance of the model is carried by using the RMSE estimator. RMSE values are, using the highest resolution, 0.0012 and 0.0008 for the horizontal and vertical displacements, respectively. Regarding the numerical results, it can be concluded that the code is able to accurately reproduce FSI problems when the structure experiences deformations.

Finally, the third case is a dam break impacting a flexible obstacle. In contrast with the test cases proposed prior in this subsection, the nature of this benchmark involves a very violent FSI, characterised by large displacements (Liao et al., 2015). This test proposed comprises then a breaking water column impacting a rubber plate. It should be noted that for this case, multi-phase (air and fluid) effects are relevant for the appropriate simulation of the rubber plate behaviour. A convergence study of this setup using different SPH resolutions is performed. Results show that the coupled model predicts the response of the beam under the fluid flow impact. However, there is a disagreement of the numerical response

considering the reference data due to the influence of the air on the dynamics of the fluid, as mentioned above and suggested by the previous literature in relation to the present benchmark (Liao et al., 2015; Sun et al., 2019). Particularly, the moment of impact, when the air has little effect, is well captured, and provides a consistent and accurate response across the four SPH resolutions. This case shows the accuracy and capabilities of the proposed coupled model to study violent FSI involving large deformations and displacements of the structure. However, the response of the system is not consistent or accurate when the air effect is predominant. Therefore, to fully solve the phenomenon under study, it would be needed to use a multi-phase solver that account for both, the fluid and air.

5.3 Real engineering application

The third and final study was conducted in Section 4.3, where the three models (DualSPHysics, Chrono and MoorDyn+) worked together in a co-operative framework to perform a real engineering application. The aim of this investigation is to present a reliable numerical tool that can be used to study the dynamics and survivability of WECs in violent wave conditions, supporting the design stage and potentially helping to reduce the cost of experimental campaigns. This research provides a detailed procedure for modelling a taut-moored point-absorber WEC together with its PTO system, seamlessly exploiting its energy harvesting functions. Specifically, the Uppsala WEC (UWEC) (Waters et al., 2007) is used as a reference case in this study.

Next subsections describe the numerical setup and the simulations performed to validate the code and analyse the behaviour of the UWEC under extreme and realistic irregular wave conditions.

5.3.1 Numerical setup

The numerical model is defined considering an experimental setup, where a 1:20th model scale of the UWEC was used (Göteman et al., 2015). The UWEC operational principle comprises a fluid-driven floating buoy with a linear magnet generator representing the PTO. The PTO is embedded into a ballasted platform that

is located at the sea bottom. The buoy is a cylinder with radius (U_r) set to 0.085m, while the PTO system is modelled with Chrono using a moving piece that travels along a guide (translator). The translator is bounded in its vertical motion by an upper and lower end-stop, which are movable and fixed, respectively. The interaction between the translator and the end-stoppers is solved using the new SMC approach implemented in this work and introduced in Section 3.2.1. Additionally, when the translator impacts the upper end-stop system, its vertical movement is modified by the presence of a mechanical spring-damper element, which exerts an elastic force by defining only the stiffness component, computed according to Eq. (13), for which the viscous part (damping) is not considered. The harvesting tool is represented by a friction damper (Coulomb damper), whose novel implementation in this code was presented in Section 3.2.2, by computing the Eq. (14). A friction force coefficient (F_μ) is defined for the Coulomb damper, given by the product of the friction coefficient and the transverse load. It should be noted that for the proposed setup of the PTO system, a representative value of internal energy dissipation is defined. Therefore, a viscous damping coefficient (c_{PTO}) is added to Eq. (14) to reproduce a velocity-proportional damping model to fully simulate the harvesting tool of the UWEC following the reference experimental setup (Göteman et al., 2015) (see Section 4.3). On the other hand, the motion of the floating buoy is transmitted to the translator through a taut-mooring line. Thus, several of the main new features implemented in MoorDyn+ are required for this application, such as: i) the modelling of taut-mooring lines that are pretensioned; ii) the possibility of simulating several moored objects (buoy and translator); and iii) the definition of mooring lines to interconnect different movable objects (the buoy is attached to the translator). Furthermore, the UWEC device is analysed under wave conditions to validate the coupled code while it shows its potential to be applied for real engineering applications. Finally, DualSPHysics handles the wave generation and propagation by designing a numerical tank that includes a piston-type wavemaker equipped with an Active Wave Absorption System (AWAS) that guarantees the correct input incident wave. In addition, there is an anti-reflective beach with numerical damping, which provides a reflection coefficient lower than 3%. Therefore, the proposed model fully exploits the capabilities of DualSPHysics coupled to Chrono and MoorDyn+ to reproduce all the features of the UWEC.

5.3.2 Validation under extreme waves

A validation of the DualSPHysics code is provided by contrasting the numerical result with a thorough set of data obtained from physical tests with extreme waves (Göteman et al., 2015). A first step is taken to validate the wave tank for wave generation and propagation. A focused wave train, which is constrained (embedded) into a regular wave background, is generated to represent the extreme sea-state using the SPH-based code. A sensitive analysis using three different SPH resolutions ($U_r/4$, $U_r/5$ and $U_r/6$) is considered to validate the extreme wave generation and propagation within DualSPHysics, where U_r is the buoy radius. Results presented in Section 4.3 show that this CFD can accurately reproduce extreme waves with this methodology, giving a range of estimated error in terms of period between 1.6% and 1.8% for regular waves, and from 2.1% to 2.2% for focused waves in comparison with the experimental data.

The validation procedure continues by simulating the UWEC under the extreme wave conditions previously analysed. Two configurations are considered for the PTO of the device (C0 and C2, as reported in Section 4.3). The case C0 aims to reproduce the device where no applied damping is considered, whereas the C2 mimics the energy harvesting. For this set of simulations, the same three SPH resolutions ($U_r/4$, $U_r/5$ and $U_r/6$) are defined for each configuration. Then, six simulations are performed to validate the UWEC under extreme wave conditions. Results included in Section 4.3 provide a measure of the error of the numerical results for buoy movement and mooring line forces versus experimental data. The heave and surge motions of the buoy are given according to its centre of gravity and the mooring line force is computed as the force at the fairlead connection to the translator mass. For the case C0, the model predicts accurately the heave motion, which initially follows the regular trend and agrees during the focused part. On the other hand, the surge motion is consistently underestimated during the regular wave. This tendency is still present when the focused train hits the float. However, a slight horizontal drift of the buoy is observed after the impact of the focused wave. The forces estimated in the line remain in agreement with the experimental ones, for which the model provides an accurate response accounting both the time evolution and the overall magnitude of the peaks. Conversely, for the case C2, the

model provides an overestimated time series for the heave motion during the regular trend but agrees with the experimental data during the focused wave impact with the buoy. Results for the surge motion and the line forces are similar to the ones obtained from C0. However, it should be noted that for C2, the drift of the buoy is not observed in surge after the arrival of the focused waves (as seen for C0), agreeing with the experimental data. Regarding the discrepancies observed, it should be noted that the coupled model does not consider wave-mooring line interactions, which may affect the magnitude of the force. The omission of this capability may be a source of discrepancy and one of the reasons for the mismatch between numerical and experimental results. In conclusion, it can be assumed that the presence of a damping function helps in reducing the magnitude of the forces that the internal components of the PTO and the mooring line experience. In fact, the mooring line receives a more stable stretching function that smooths the peaks if comparing the setup with energy absorption with the case with no damping applied, C2 and C0, respectively. Therefore, this coupled model gives an acceptable response and becomes a feasible tool to investigate the behaviour of the WECs in general, and specifically, to support the design of the UWEC.

5.3.3 Realistic irregular sea state

The study presented in this subsection aims to provide solutions for the optimisation of the structure to increase the survivability of the structure or, conversely, to reduce the initial and operational costs. For that, a real-life representation of the irregular sea state is considered. The setup defines an environment comprising 500 irregular waves, which are representative of realistic extreme conditions. Moreover, in order to get closer to the real working principle of the PTO system, the Coulomb damper with its frictional force (F_μ) is no longer used as suggested for previous cases according to the experimental configuration (Göteman et al., 2015). Conversely, the friction damper is converted to a viscous one according to scale factors (Giannini et al., 2020) and using Eq. (13) to reproduce the system. The new damping coefficient aims to be representative of the energy conversion process that takes place in the PTO. Four test cases (I0-I3) are defined to evaluate the response of the system under these wave conditions. Each case defines

a different value for the damping coefficient (c_h) of the PTO, whereas the internal dissipative mechanism (c_{PTO}) is kept and shared among all the cases.

A final part of this investigation deals with an in-depth examination of the four cases, measuring the line peak forces against different magnitudes, where the most important are the PTO absorbed power and the maximum translator velocity. Results reported in Section 4.3 suggest that the use of damping (c_h) to absorb the energy of PTO movement, increases the linearity of the system response in terms of peak forces. The analysis of the PTO absorbed power proves that when a relevant value of the PTO damping is included in the system, its response has also a better linear correlation. The maximum translator velocity indicates that the peak velocity of the translator sensibly decreases as the damping increases, meaning that the nature of the peak force is not related to the translator hitting the end-stop.

The following conclusions can be drawn from the analysis presented in this subsection. The Uppsala WEC certainly benefits from the use of a higher value for PTO damping. First, more power is harvested by the system for smaller wave amplitudes, and this may increase its energy collection assuming that the system is operating. Secondly, the reduced mobility of the translator within the PTO can reduce the detrimental effects on the casing and on the foundations of the structure where the mechanical system is placed. However, this effect is only achieved with certain values of damping and only for extreme forces. It should be noted that the harvesting function performance and the useful life of the mooring system are related. In this way, the optimisation of the system should account for this feature, balancing the expected loads on the line. The end-stopping system could benefit from improvements. In fact, its spring is a reinforcement during energy harvesting, but its main purpose is to protect the system against extreme events when the translator impacts violently. One way to reduce the force peaks would be to reduce the stiffness of the spring damper or even incorporate a viscous damper, making it similar to a shock absorber. However, this solution could reduce the capacity of energy collection, but it would certainly increase the life expectancy of the device. The analysis of the numerical results shows valuable information about the behaviour of the UWEC in terms of efficiency and survivability.

CHAPTER 6

Conclusions

An extension of the capabilities of SPH-based DualSPHysics code has been presented in this doctoral dissertation to address more complex scenarios. The strategy of using coupling techniques to merge different computational codes enhance the potential of DualSPHysics. In fact, DualSPHysics takes a step towards its overall usability and versatility, greatly expanding the relevance of the code and its possible range of application. By means of the coupling between the SPH-based model and multiphysics libraries, it is possible to combine fluid dynamics and multiphysics problems within the same framework, encompassing a much wider range of applicability without having to develop new complex formulations. Specifically, the coupled libraries Project Chrono and MoorDyn+ provide multiple features to be exploited within the Lagrangian SPH environment. The core module of Project Chrono, called Chrono, can solve frictional contacts between rigid objects withing articulated multi-body systems using DEM, whereas it can reproduce flexible structures with the FEA formulation. On the other hand, MoorDyn+ implements a LM method to solve the dynamics of catenary and taut-mooring lines. Thus, in this work, the integration of the three two-way couplings SPH-DEM, SPH-FEA, and SPH-LM within a single co-operative framework of simulation has been presented.

The proposed coupling strategy follows a *master-slave* software architecture that facilitates the maintenance and the development tasks to include new functionalities or modules available in Project Chrono or in MoorDyn+. Furthermore, a general-purpose communication interface (the so-called DSPHChronoLib) has been implemented and presented to handle the data exchange between DualSPHysics and Chrono. The use of DSPHChronoLib increases the abstraction between both models and gives rise to a *low-coupling* concept strategy. This concept means that new changes or functionalities implemented in either side would not affect the operation of the other model. DSPHChronoLib has been

released as an open-source code under LGPL together with a program scientific article (see Section 4.1), including the description of the code, guidelines for use and compilation and benchmarks to test the code.

The first sub-objective, *extend the capabilities of the DualSPHysics code* (see Section 2), aims to boost the DualSPHysics code with new features to simulate more complex scenarios. A coupling of the SPH-based model with multiphysics libraries has been presented to achieve this goal. However, the initial version of the coupled code did not fulfil all the needs to address every feature of WECs currently under study. For that reason, new developments have been presented and validated in this work, such as the integration of SMC approach to solve soft contacts, a new formulation to solve frictional dampers, and the possibility of reproducing flexible structures within the SPH domain. All these new developments have been integrated from Chrono. On the other hand, MoorDyn+ has been benefiting from a new development to solve taut-mooring lines. Considering all these features, in addition to the ones previously available, the above-mentioned sub-objective is achieved. It should be noted that the implementations were also optimised to provide an SPH-based code highly parallelised that can simulate large domains at reasonable execution times.

The second sub-objective, *application in the design of WECs* (see Section 2), aims to apply the computational code to study the behaviour of WECs. This goal focuses on providing a reliable tool that can be used to solve real engineering applications, in general, and to support the design stage of WECs, in particular. Therefore, the UWEC has been selected as a real-life case to obtain useful information by studying the device under extreme waves. This test case made it possible to demonstrate the capabilities of the coupled code and to evaluate the accuracy of the new implementations resulting from the first sub-objective. In fact, the three models described in this work (DualSPHysics, Chrono and MoorDyn+) were required to address all the phenomena involved in simulating the UWEC and its properties. The setups performed showed an overall response of the computational code, capturing the most important aspects of the UWEC under extreme waves. The investigation suggested that the performance of the UWEC can be improved. In fact, the management of the internal damping of the PTO has proven to be essential to

enhance the capabilities of the device, for both short-term and long-term conditions. It can be assumed that including a control system with self-adjusting internal damping, variable on time and depending on prior knowledge of the sea state that affects the device, could increase the survivability. Therefore, and thanks to the capability computational code, it was possible to numerically reproduce a real-life case comprising a WEC that was experimentally tested before. Therefore, the second sub-objective is achieved as well.

The detailed procedure presented in this doctoral dissertation can be useful for developers, researchers, or industry, in general. The most relevant capabilities and new implementations have been evaluated and validated against analytical solutions, other numerical models, or experiment data. In fact, the selected benchmarks may be a reference point for the community to use the code for their target applications, but also the code itself may become a reference for other numerical models to be compared with. It is worth mentioning that the potential and reliability of this computational coupled code has already been tested for different areas of application. For example, in coastal protection, the SPH-DEM code was applied to study the behaviour of the Tetrapod armour units against solitary waves, in which frictional contacts take place (Mitsui et al., 2023), while the SPH-FEA was considered to analyse 3-D flexible vegetation interacting with waves (El Rahi et al., 2023). Within the renewable energy field, both the SPH-DEM and SPH-LM codes were employed to perform a state-of-the-art of CFD simulations for reproducing different types of WECs, their PTOs and the mooring systems (Crespo et al., 2023). The Floating Oscillating Wave Energy Converter (*FOSWEC*) device, which includes two flaps with rotational constraints to harvest the energy and taut-mooring lines, was investigated using the SPH-DEM and SPH-LM coupled methods (Tagliafierro et al., 2022b). Moreover, with the SPH-DEM code, the *DeepCwind* semi-submersible floating wind platform (FWT) was reproduced, for which the mooring system were modelled as linear springs that mimic tensioning cables (Tagliafierro et al., 2023a). On the other hand, the *DeepCwind* device was also investigated, but in this case, using the SPH-LM code to solve the taut-mooring lines (Pribadi et al., 2023). In addition, a tension-Leg Platform Wind Turbine (TLP) was simulated using the SPH-LM code (Tagliafierro et al., 2022a). Furthermore, as a coastal engineering application, the SPH-LM code simulated a moored wave-buoy in waves and currents

(Capasso et al., 2023a). Another interesting application of the SPH-DEM code, in the area of health sector, investigated heart valves for maintaining unidirectional blood flow, where the valves incorporated mechanical constraints to control blood flow (Laha et al., 2023). Finally, the SPH-FEA code was taken as reference to simulate a flexible baffle with elastic behaviour and compared with other modelling strategies (Tagliafierro et al., 2023b). Therefore, this manuscript shows the capabilities of a cooperative computation framework involving three different models to numerically reproduce the response of various concepts and characteristics of WECs and FWTs. However, this code proves its potential to address not only wave energy-related investigations, but also other problems belonging to different areas of knowledge. In this way, this computational code becomes a useful tool to address more challenging scenarios than those that could be represented previously.

Future work will lead to the investigation of flexible WECs (FlexWECs). These structures can dynamically deform under the action of waves and convert this deformation into electricity. More research will also focus on performing semi-submersible floating wind turbines (FWTs) and tension leg platforms (TLPs) for which the tower can be modelled as a semi-rigid structure that can experience some deformation accounting for bending stiffness. This type of configuration will make it possible to analyse the survivability of these platforms. In fact, the modelling of the tower with some flexibility could lead to a better absorption of energy reducing the fatigue in the whole structure. Going deeper on floating wind turbines, it would be interesting to reproduce the air effects on the structure and on the rotating blades to evaluate its efficiency and the survivability of the components. This work will therefore be extended not only to more complex wave energy scenarios, but also to the study of wind energy generated by floating wind turbines.

References

Ahamed, R., McKee, K., Howard, I., 2020. Advancements of wave energy converters based on power take off (PTO) systems: A review. Ocean Eng. 204, 107248. https://doi.org/10.1016/j.oceaneng.2020.107248

Altomare, C., Domínguez, J.M., Crespo, A.J.C., González-Cao, J., Suzuki, T., Gómez-Gesteira, M., Troch, P., 2017. Long-crested wave generation and absorption for SPH-based DualSPHysics model. Coast. Eng. 127, 37–54. https://doi.org/10.1016/j.coastaleng.2017.06.004

Altomare, C., Domínguez, J.M., Fourtakas, G., 2022. Latest developments and application of SPH using DualSPHysics. Comput. Part. Mech. 9, 863–866. https://doi.org/10.1007/s40571-022-00499-1

Altomare, C., Scandura, P., Cáceres, I., A, D.A. van der, Viccione, G., 2023. Large-scale wave breaking over a barred beach: SPH numerical simulation and comparison with experiments. Coast. Eng. 185, 104362. https://doi.org/10.1016/j.coastaleng.2023.104362

Altomare, C., Tafuni, A., Domínguez, J.M., Crespo, A.J.C., Gironella, X., Sospedra, J., 2020. SPH Simulations of Real Sea Waves Impacting a Large-Scale Structure. J. Mar. Sci. Eng. 8, 826. https://doi.org/10.3390/jmse8100826

Altomare, C., Tagliafierro, B., Dominguez, J.M., Suzuki, T., Viccione, G., 2018. Improved relaxation zone method in SPH-based model for coastal engineering applications. Appl. Ocean Res. 81, 15–33. https://doi.org/10.1016/j.apor.2018.09.013

Amicarelli, A., Manenti, S., Albano, R., Agate, G., Paggi, M., Longoni, L., Mirauda, D., Ziane, L., Viccione, G., Todeschini, S., Sole, A., Baldini, L.M., Brambilla, D., Papini, M., Khellaf, M.C., Tagliafierro, B., Sarno, L., Pirovano, G., 2020. SPHERA v.9.0.0: A Computational Fluid Dynamics research code, based on the Smoothed Particle Hydrodynamics mesh-less method. Comput. Phys. Commun. 250, 107157. https://doi.org/10.1016/j.cpc.2020.107157

Anitescu, M., Tasora, A., 2010. An iterative approach for cone complementarity problems for nonsmooth dynamics. Comput. Optim. Appl. 47, 207–235. https://doi.org/10.1007/s10589-008-9223-4

Antoci, C., 2006. Simulazione numerica dell'interazione fluido-struttura con la tecnica SPH (PhD Thesis). Ph. D. thesis, Universita di Pavia. 100.

Antoci, C., Gallati, M., Sibilla, S., 2007. Numerical simulation of fluid–structure interaction by SPH. Comput. Struct., Fourth MIT Conference on Computational Fluid and Solid Mechanics 85, 879–890. https://doi.org/10.1016/j.compstruc.2007.01.002

Antuono, M., Colagrossi, A., Marrone, S., 2012. Numerical diffusive terms in weakly-compressible SPH schemes. Comput. Phys. Commun. 183, 2570–2580. https://doi.org/10.1016/j.cpc.2012.07.006

Antuono, M., Colagrossi, A., Marrone, S., Molteni, D., 2010. Free-surface flows solved by means of SPH schemes with numerical diffusive terms. Comput. Phys. Commun. 181, 532–549. https://doi.org/10.1016/j.cpc.2009.11.002

Antuono, M., Sun, P.N., Marrone, S., Colagrossi, A., 2021. The δ-ALE-SPH model: An arbitrary Lagrangian-Eulerian framework for the δ-SPH model with particle shifting technique. Comput. Fluids 216, 104806. https://doi.org/10.1016/j.compfluid.2020.104806

Arnold, M., Kretschmer, M., Koch, J., Cheng, P.W., Biskup, F., 2015. A Validation Method for Fluid–Structure Interaction Simulations Based on Submerged Free Decay Experiments. J. Ocean Wind Energy 2. https://doi.org/10.17736/jowe.2015.mkr02

Asai, M., Li, Y., Chandra, B., Takase, S., 2021. Fluid–rigid-body interaction simulations and validations using a coupled stabilized ISPH–DEM incorporated with the energy-tracking impulse method for multiple-body contacts. Comput. Methods Appl. Mech. Eng. 377, 113681. https://doi.org/10.1016/j.cma.2021.113681

Bailoor, S., Annangi, A., Seo, J.H., Bhardwaj, R., 2017. Fluid–structure interaction solver for compressible flows with applications to blast loading on thin elastic structures. Appl. Math. Model. 52, 470–492. https://doi.org/10.1016/j.apm.2017.05.038

Barreiro, A., Crespo, A.J.C., Domínguez, J.M., García-Feal, O., Zabala, I., Gómez-Gesteira, M., 2016. Quasi-static mooring solver implemented in SPH. J. Ocean Eng. Mar. Energy 2, 381–396. https://doi.org/10.1007/s40722-016-0061-7

Batchelor, G.K., 2000. An Introduction to Fluid Dynamics, Cambridge Mathematical Library. Cambridge University Press. https://doi.org/10.1017/CBO9780511800955

Bauchau, O.A., Craig, J.I., 2009. Euler-Bernoulli beam theory, in: Bauchau, O.A., Craig, J.I. (Eds.), Structural Analysis, Solid Mechanics and Its Applications. Springer Netherlands, Dordrecht, pp. 173–221. https://doi.org/10.1007/978-90-481-2516-6_5

Beatty, S.J., Hall, M., Buckham, B.J., Wild, P., Bocking, B., 2015. Experimental and numerical comparisons of self-reacting point absorber wave energy converters in regular waves. Ocean Eng. 104, 370–386. https://doi.org/10.1016/j.oceaneng.2015.05.027

Belytschko, T., Glaum, L.W., 1979. Applications of higher order corotational stretch theories to nonlinear finite element analysis. Comput. Struct. 10, 175–182. https://doi.org/10.1016/0045-7949(79)90085-3

Benson, D.J., 1992. Computational methods in Lagrangian and Eulerian hydrocodes. Comput. Methods Appl. Mech. Eng. 99, 235–394. https://doi.org/10.1016/0045-7825(92)90042-I

Bićanić, N., 2007. Discrete Element Methods, in: Encyclopedia of Computational Mechanics. John Wiley & Sons, Ltd. https://doi.org/10.1002/0470091355.ecm006.pub2

Binh, P.C., Tri, N.M., Dung, D.T., Ahn, K.K., Kim, S.-J., Koo, W., 2016. Analysis, design and experiment investigation of a novel wave energy converter. IET Gener. Transm. Distrib. 10, 460–469. https://doi.org/10.1049/iet-gtd.2015.0821

Boccotti, P., 2004. Idraulica marittima. UTET univertità.

Brito, M., Canelas, R.B., García-Feal, O., Domínguez, J.M., Crespo, A.J.C., Ferreira, R.M.L., Neves, M.G., Teixeira, L., 2020. A numerical tool for modelling oscillating wave surge converter with nonlinear mechanical constraints. Renew. Energy 146, 2024–2043. https://doi.org/10.1016/j.renene.2019.08.034

Canelas, R.B., Brito, M., Feal, O.G., Domínguez, J.M., Crespo, A.J.C., 2018. Extending DualSPHysics with a Differential Variational Inequality: modeling fluid-mechanism interaction. Appl. Ocean Res. 76, 88–97. https://doi.org/10.1016/j.apor.2018.04.015

Canelas, R.B., Crespo, A.J.C., Domínguez, J.M., Ferreira, R.M.L., Gómez-Gesteira, M., 2016. SPH–DCDEM model for arbitrary geometries in free surface solid–fluid flows. Comput. Phys. Commun. 202, 131–140. https://doi.org/10.1016/j.cpc.2016.01.006

Canelas, R.B., Domínguez, J.M., Crespo, A.J.C., Gómez-Gesteira, M., Ferreira, R.M.L., 2017. Resolved Simulation of a Granular-Fluid Flow with a Coupled SPH-DCDEM Model. J. Hydraul. Eng. 143, 06017012. https://doi.org/10.1061/(ASCE)HY.1943-7900.0001331

Canelas, R.B., Domínguez, J.M., Crespo, A.J.C., Gómez-Gesteira, M., Ferreira, R.M.L., 2015. A Smooth Particle Hydrodynamics discretization for the modelling of free surface

flows and rigid body dynamics. Int. J. Numer. Methods Fluids 78, 581–593. https://doi.org/10.1002/fld.4031

Capasso, S., Tagliafierro, B., González-Ávalos, R., Martínez-Estévez, I., Domínguez, J.M., Altomare, C., Crespo, A.J.C., Viccione, G., 2023a. Numerical simulation of a moored wave-buoy in waves and current by smoothed particle hydrodynamics. Proc. Int. Conf. Offshore Mech. Arct. Eng. - OMAE. https://doi.org/10.1115/OMAE2023-105023

Capasso, S., Tagliafierro, B., Mancini, S., Martínez-Estévez, I., Altomare, C., Domínguez, J.M., Viccione, G., 2023b. Regular Wave Seakeeping Analysis of a Planing Hull by Smoothed Particle Hydrodynamics: A Comprehensive Validation. J. Mar. Sci. Eng. 11, 700. https://doi.org/10.3390/jmse11040700

Capasso, S., Tagliafierro, B., Martínez-Estévez, I., Domínguez, J.M., Crespo, A.J.C., Viccione, G., 2022. A DEM approach for simulating flexible beam elements with the Project Chrono core module in DualSPHysics. Comput. Part. Mech. 9, 969–985. https://doi.org/10.1007/s40571-021-00451-9

Carpintero Moreno, E., Fourtakas, G., Stansby, P.K., Crespo, A., 2020. Response of the multi-float WEC M4 in focussed waves using SPH, in: Proceedings of 4th International Conference on Renewable Energies Offshore, October 2020, Lisbon, Portugal.

Chen, C., Shi, W.-K., Shen, Y.-M., Chen, J.-Q., Zhang, A.-M., 2022. A multi-resolution SPH-FEM method for fluid–structure interactions. Comput. Methods Appl. Mech. Eng. 401, 115659. https://doi.org/10.1016/j.cma.2022.115659

Chen, W., Dolguntseva, I., Savin, A., Zhang, Y., Li, W., Svensson, O., Leijon, M., 2017. Numerical modelling of a point-absorbing wave energy converter in irregular and extreme waves. Appl. Ocean Res. 63, 90–105. https://doi.org/10.1016/j.apor.2017.01.004

Clemente, D., Rosa-Santos, P., Taveira-Pinto, F., 2021. On the potential synergies and applications of wave energy converters: A review. Renew. Sustain. Energy Rev. 135, 110162. https://doi.org/10.1016/j.rser.2020.110162

Coe, R., Bacelli, G., Wilson, D., Patterson, D., 2017. System identification of a heaving point absorber: Design of experiment and device modeling. Energies 10, 472. https://doi.org/10.3390/en10040472

Coe, R.G., Ahn, S., Neary, V.S., Kobos, P.H., Bacelli, G., 2021a. Maybe less is more: Considering capacity factor, saturation, variability, and filtering effects of wave energy devices. Appl. Energy 291, 116763. https://doi.org/10.1016/j.apenergy.2021.116763

Coe, R.G., Bacelli, G., Forbush, D., 2021b. A practical approach to wave energy modeling and control. Renew. Sustain. Energy Rev. 142, 110791. https://doi.org/10.1016/j.rser.2021.110791

Commission, E., Centre, J.R., Magagna, D., 2020. Ocean energy – Technology development report. https://dx.doi.org/10.2760/81693

Crespo, A., Tagliafierro, B., Martínez-Estévez, I., Domínguez, J.M., deCastro, M., Gómez-Gesteira, M., Altomare, C., Brito, M., Bernardo, F., Ferreira, R.M., Capasso, S., Viccione, G., Quartier, N., Stratigaki, V., Troch, P., Simonetti, I., Cappietti, L., Göteman, M., Engström, J., Clemente, D., Rosa-Santos, P., Taveira-Pinto, F., Bacelli, G., Coe, R., Fourtakas, G., Rogers, B., Stasnby, P., 2023. On the state-of-the-art of CFD simulations for wave energy converters within the open-source numerical framework of DualSPHysics. Proc. Eur. Wave Tidal Energy Conf. 15. https://doi.org/10.36688/ewtec-2023-145

Crespo, A.J., Gómez-Gesteira, M., Dalrymple, R.A., 2007. Boundary conditions generated by dynamic particles in SPH methods. Comput. Mater. Contin. 5, 173–184.

Crespo, A.J.C., Altomare, C., Domínguez, J.M., González-Cao, J., Gómez-Gesteira, M., 2017. Towards simulating floating offshore oscillating water column converters with Smoothed Particle Hydrodynamics. Coast. Eng. 126, 11–26. https://doi.org/10.1016/j.coastaleng.2017.05.001

Crespo, A.J.C., Domínguez, J.M., Rogers, B.D., Gómez-Gesteira, M., Longshaw, S., Canelas, R., Vacondio, R., Barreiro, A., García-Feal, O., 2015. DualSPHysics: Open-source parallel CFD solver based on Smoothed Particle Hydrodynamics (SPH). Comput. Phys. Commun. 187, 204–216. https://doi.org/10.1016/j.cpc.2014.10.004

Crisfield, M.A., Galvanetto, U., Jelenić, G., 1997. Dynamics of 3-D co-rotational beams. Comput. Mech. 20, 507–519. https://doi.org/10.1007/s004660050271

Cummins, S.J., Rudman, M., 1999. An SPH Projection Method. J. Comput. Phys. 152, 584–607. https://doi.org/10.1006/jcph.1999.6246

Cummins, W.E., 1962. The Impulse Response Function and Ship Motions. David Taylor Model Basin Reports; Department of the Navy: Hydromechanics Laboratories.

Cundall, P.A., Strack, O.D.L., 1979. A discrete numerical model for granular assemblies. Géotechnique 29, 47–65. https://doi.org/10.1680/geot.1979.29.1.47

Dalrymple, R.A., Knio, O., 2012. SPH Modelling of Water Waves 779–787. https://doi.org/10.1061/40566(260)80

Dalrymple, R.A., Rogers, B.D., 2006. Numerical modeling of water waves with the SPH method. Coast. Eng., Coastal Hydrodynamics and Morphodynamics 53, 141–147. https://doi.org/10.1016/j.coastaleng.2005.10.004

Dang, T.D., Phan, C.B., Ahn, K.K., 2019. Design and Investigation of a Novel Point Absorber on Performance Optimization Mechanism for Wave Energy Converter in Heave Mode. Int. J. Precis. Eng. Manuf.-Green Technol. 6, 477–488. https://doi.org/10.1007/s40684-019-00065-w

Davidson, J., Costello, R., 2020. Efficient Nonlinear Hydrodynamic Models for Wave Energy Converter Design—A Scoping Study. J. Mar. Sci. Eng. 8, 35. https://doi.org/10.3390/jmse8010035

Davidson, J., Giorgi, S., Ringwood, J.V., 2015. Linear parametric hydrodynamic models for ocean wave energy converters identified from numerical wave tank experiments. Ocean Eng. 103, 31–39. https://doi.org/10.1016/j.oceaneng.2015.04.056

Davidson, J., Ringwood, J.V., 2017. Mathematical Modelling of Mooring Systems for Wave Energy Converters—A Review. Energies 10, 666. https://doi.org/10.3390/en10050666

De Vuyst, T., Vignjevic, R., Campbell, J.C., 2005. Coupling between meshless and finite element methods. Int. J. Impact Eng. 31, 1054–1064. https://doi.org/10.1016/j.ijimpeng.2004.04.017

deCastro, M., Rusu, L., Arguilé-Pérez, B., Ribeiro, A., Costoya, X., Carvalho, D., Gómez-Gesteira, M., 2024. Different approaches to analyze the impact of future climate change on the exploitation of wave energy. Renew. Energy 220, 119569. https://doi.org/10.1016/j.renene.2023.119569

Det Norske Veritas, 2007. Recommended Practice: Environmental Conditions and Environmental Loads.

Domínguez, J.M., Crespo, A.J.C., Gómez-Gesteira, M., 2013a. Optimization strategies for CPU and GPU implementations of a smoothed particle hydrodynamics method. Comput. Phys. Commun. 184, 617–627. https://doi.org/10.1016/j.cpc.2012.10.015

Domínguez, J.M., Crespo, A.J.C., Gómez-Gesteira, M., Marongiu, J.C., 2011. Neighbour lists in smoothed particle hydrodynamics. Int. J. Numer. Methods Fluids 67, 2026–2042. https://doi.org/10.1002/fld.2481

Domínguez, J.M., Crespo, A.J.C., Hall, M., Altomare, C., Wu, M., Stratigaki, V., Troch, P., Cappietti, L., Gómez-Gesteira, M., 2019. SPH simulation of floating structures with moorings. Coast. Eng. 153, 103560. https://doi.org/10.1016/j.coastaleng.2019.103560

Domínguez, J.M., Crespo, A.J.C., Valdez-Balderas, D., Rogers, B.D., Gómez-Gesteira, M., 2013b. New multi-GPU implementation for smoothed particle hydrodynamics on heterogeneous clusters. Comput. Phys. Commun. 184, 1848–1860. https://doi.org/10.1016/j.cpc.2013.03.008

Domínguez, J.M., Fourtakas, G., Altomare, C., Canelas, R.B., Tafuni, A., García-Feal, O., Martínez-Estévez, I., Mokos, A., Vacondio, R., Crespo, A.J.C., Rogers, B.D., Stansby, P.K., Gómez-Gesteira, M., 2022. DualSPHysics: from fluid dynamics to multiphysics problems. Comput. Part. Mech. 9, 867–895. https://doi.org/10.1007/s40571-021-00404-2

Drew, B., Plummer, A.R., Sahinkaya, M.N., 2009. A review of wave energy converter technology. Proc. Inst. Mech. Eng. Part J. Power Energy 223, 887–902. https://doi.org/10.1243/09576509JPE782

Dunatunga, S., Kamrin, K., 2015. Continuum modelling and simulation of granular flows through their many phases. J. Fluid Mech. 779, 483–513. https://doi.org/10.1017/jfm.2015.383

El Rahi, J., Martínez-Estévez, I., Tagliafierro, B., Domínguez, J.M., Crespo, A.J.C., Stratigaki, V., Suzuki, T., Troch, P., 2023. Numerical investigation of wave-induced flexible vegetation dynamics in 3D using a coupling between DualSPHysics and the FEA module of Project Chrono. Ocean Eng. 285, 115227. https://doi.org/10.1016/j.oceaneng.2023.115227

Energy Institute, 2023. Statistical Review of World Energy (No. 72nd edition).

English, A., Domínguez, J.M., Vacondio, R., Crespo, A.J.C., Stansby, P.K., Lind, S.J., Chiapponi, L., Gómez-Gesteira, M., 2022. Modified dynamic boundary conditions (mDBC) for general-purpose smoothed particle hydrodynamics (SPH): application to tank sloshing, dam break and fish pass problems. Comput. Part. Mech. 9, 911–925. https://doi.org/10.1007/s40571-021-00403-3

Engström, J., Sjökvist, L., Göteman, M., Eriksson, M., Hann, M., Ransley, E., Greaves, M., D. andLeijon, 2017. Buoy geometry and its influence on survivability for a point absorbing wave energy converter: Scale experiment and CFD simulations. Sch. Eng. Comput. Math. 4.

Falcão, A.F. de O., 2010. Wave energy utilization: A review of the technologies. Renew. Sustain. Energy Rev. 14, 899–918. https://doi.org/10.1016/j.rser.2009.11.003

Falnes, J., 2002. Ocean Waves and Oscillating Systems: Linear Interactions Including Wave-Energy Extraction. Cambridge University Press. https://doi.org/10.1017/CBO9780511754630

Felippa, C.A., Haugen, B., 2005. A unified formulation of small-strain corotational finite elements: I. Theory. Comput. Methods Appl. Mech. Eng., Computational Methods for Shells 194, 2285–2335. https://doi.org/10.1016/j.cma.2004.07.035

Ferri, F., Palm, J., 2015. Implementation of a Dynamic Mooring Solver (MOODY) into a wave to wire model of a simple WEC. Dep. Civ. Eng.

Fleischmann, J., Serban, R., Negrut, D., Jayakumar, P., 2015. On the Importance of Displacement History in Soft-Body Contact Models. J. Comput. Nonlinear Dyn. 11. https://doi.org/10.1115/1.4031197

Fleissner, F., Gaugele, T., Eberhard, P., 2007. Applications of the discrete element method in mechanical engineering. Multibody Syst. Dyn. 18, 81. https://doi.org/10.1007/s11044-007-9066-2

Flores, P., Machado, M., Silva, M.T., Martins, J.M., 2011. On the continuous contact force models for soft materials in multibody dynamics. Multibody Syst. Dyn. 25, 357–375. https://doi.org/10.1007/s11044-010-9237-4

Folley, M., 2016. Numerical Modelling of Wave Energy Converters: State-of-the-Art Techniques for Single Devices and Arrays. Academic Press.

Fourey, G., 2012. Développement d'une méthode de couplage fluide structure SPH Eléments Finis en vue de son application à l'hydrodynamique navale (Ph.D.thesis). Ecole Centrale de Nantes.

Fourey, G., Hermange, C., Le Touzé, D., Oger, G., 2017. An efficient FSI coupling strategy between Smoothed Particle Hydrodynamics and Finite Element methods. Comput. Phys. Commun. 217, 66–81. https://doi.org/10.1016/j.cpc.2017.04.005

Fourtakas, G., Dominguez, J.M., Vacondio, R., Rogers, B.D., 2019. Local uniform stencil (LUST) boundary condition for arbitrary 3-D boundaries in parallel smoothed particle hydrodynamics (SPH) models. Comput. Fluids 190, 346–361. https://doi.org/10.1016/j.compfluid.2019.06.009

Fourtakas, G., Rogers, B.D., 2016. Modelling multi-phase liquid-sediment scour and resuspension induced by rapid flows using Smoothed Particle Hydrodynamics

(SPH) accelerated with a Graphics Processing Unit (GPU). Adv. Water Resour. 92, 186–199. https://doi.org/10.1016/j.advwatres.2016.04.009

Fourtakas, G., Vacondio, R., Domínguez, J.M., Rogers, B.D., 2020. Improved density diffusion term for long duration wave propagation, in: In: Proceedings of the International SPHERIC Workshop, Harbin, China.

García-Feal, O., Crespo, A.J.C., Gómez-Gesteira, M., 2022. VisualSPHysics: advanced fluid visualization for SPH models. Comput. Part. Mech. 9, 897–910. https://doi.org/10.1007/s40571-020-00386-7

Garcia-Teruel, A., DuPont, B., Forehand, D.I.M., 2021. Hull geometry optimisation of wave energy converters: On the choice of the objective functions and the optimisation formulation. Appl. Energy 298, 117153. https://doi.org/10.1016/j.apenergy.2021.117153

Gere, J.M., Goodno, B.J., 2012. Mechanics of materials. Cengage learning.

Gere, J.M., Timoshenko, S.P., 1991. Mechanics of Materials. Springer US, Boston, MA.

Giannini, G., Temiz, I., Rosa-Santos, P., Shahroozi, Z., Ramos, V., Göteman, M., Engström, J., Day, S., Taveira-Pinto, F., 2020. Wave Energy Converter Power Take-Off System Scaling and Physical Modelling. J. Mar. Sci. Eng. 8, 632. https://doi.org/10.3390/jmse8090632

Golbaz, D., Asadi, R., Amini, E., Mehdipour, H., Nasiri, M., Etaati, B., Naeeni, S.T.O., Neshat, M., Mirjalili, S., Gandomi, A.H., 2022. Layout and design optimization of ocean wave energy converters: A scoping review of state-of-the-art canonical, hybrid, cooperative, and combinatorial optimization methods. Energy Rep. 8, 15446–15479. https://doi.org/10.1016/j.egyr.2022.10.403

Gomes, R.P.F., Gato, L.M.C., Henriques, J.C.C., Portillo, J.C.C., Howey, B.D., Collins, K.M., Hann, M.R., Greaves, D.M., 2020. Compact floating wave energy converters arrays: Mooring loads and survivability through scale physical modelling. Appl. Energy 280, 115982. https://doi.org/10.1016/j.apenergy.2020.115982

Gómez-Gesteira, M., Crespo, A.J.C., Rogers, B.D., Dalrymple, R.A., Domínguez, J.M., Barreiro, A., 2012b. SPHysics – development of a free-surface fluid solver – Part 2: Efficiency and test cases. Comput. Geosci. 48, 300–307. https://doi.org/10.1016/j.cageo.2012.02.028

Gómez-Gesteira, M., Rogers, B.D., Crespo, A.J.C., Dalrymple, R.A., Narayanaswamy, M., Domínguez, J.M., 2012a. SPHysics – development of a free-surface fluid solver – Part

1: Theory and formulations. Comput. Geosci. 48, 289–299. https://doi.org/10.1016/j.cageo.2012.02.029

González-Cao, J., Altomare, C., Crespo, A.J.C., Domínguez, J.M., Gómez-Gesteira, M., Kisacik, D., 2019. On the accuracy of DualSPHysics to assess violent collisions with coastal structures. Comput. Fluids 179, 604–612. https://doi.org/10.1016/j.compfluid.2018.11.021

Göteman, M., Engström, J., Eriksson, M., Hann, M., Ransley, E., Greaves, D., Leijon, M., 2015. Wave loads on a point-absorbing wave energy device in extreme waves, in: ISOPE International Ocean and Polar Engineering Conference. ISOPE, p. ISOPE-I.

Göteman, M., Giassi, M., Engström, J., Isberg, J., 2020. Advances and Challenges in Wave Energy Park Optimization—A Review. Front. Energy Res. 8, 26. https://doi.org/10.3389/fenrg.2020.00026

Gotoh, H., Khayyer, A., 2018. On the state-of-the-art of particle methods for coastal and ocean engineering. Coast. Eng. J. 60, 79–103. https://doi.org/10.1080/21664250.2018.1436243

Gotoh, H., Khayyer, A., Shimizu, Y., 2021. Entirely Lagrangian meshfree computational methods for hydroelastic fluid-structure interactions in ocean engineering—Reliability, adaptivity and generality. Appl. Ocean Res. 115, 102822. https://doi.org/10.1016/j.apor.2021.102822

Gruwez, V., Altomare, C., Suzuki, T., Streicher, M., Cappietti, L., Kortenhaus, A., Troch, P., 2020. Validation of RANS Modelling for Wave Interactions with Sea Dikes on Shallow Foreshores Using a Large-Scale Experimental Dataset. J. Mar. Sci. Eng. 8, 650. https://doi.org/10.3390/jmse8090650

Gul, M.S., Chaudhry, H.N., 2022. Energy Efficiency, Low Carbon Resources and Renewable Technology. Energies 15, 4553. https://doi.org/10.3390/en15134553

Gulvanessian, H., Calgaro, J.-A., Holický, M., Gulvanessian, Haig, 2012. Designers' Guide to Eurocode: Basis of Structural Design, Second edition. ed. ICE Publishing. https://doi.org/10.1680/bsd.41714

Hagemeier, T., Thévenin, D., Richter, T., 2020. Settling of spherical particles in the transitional regime. https://doi.org/10.48550/arXiv.2009.02250

Hall, M., 2018. MoorDyn User's Guide [Online]:

Hall, M., 2017. Efficient modelling of seabed friction and multi-floater mooring systems in MoorDyn, in: Proceedings of the 12th European Wave and Tidal Energy Conference, Cork, Ireland.

Hall, M., 2015. MoorDyn user's guide. Dep. Mech. Eng. Univ. Maine Orono ME USA 15.

Hall, M., Goupee, A., 2015. Validation of a lumped-mass mooring line model with DeepCwind semisubmersible model test data. Ocean Eng. 104, 590–603. https://doi.org/10.1016/j.oceaneng.2015.05.035

Hann, M., Greaves, D., Raby, A., Howey, B., 2018. Use of constrained focused waves to measure extreme loading of a taut moored floating wave energy converter. Ocean Eng. 148, 33–42. https://doi.org/10.1016/j.oceaneng.2017.10.024

Hasselmann, K., Barnett, T., Bouws, E., Carlson, H., Cartwright, D., Enke, K., Ewing, J., Gienapp, H., Hasselmann, D., Kruseman, P., Meerburg, A., Muller, P., Olbers, D., Richter, K., Sell, W., Walden, H., 1973. Measurements of wind-wave growth and swell decay during the Joint North Sea Wave Project (JONSWAP). Deut Hydrogr Z 8, 1–95.

He, Y., Bayly, A.E., Hassanpour, A., Muller, F., Wu, K., Yang, D., 2018. A GPU-based coupled SPH-DEM method for particle-fluid flow with free surfaces. Powder Technol. 338, 548–562. https://doi.org/10.1016/j.powtec.2018.07.043

Hilber, H.M., Hughes, T.J.R., Taylor, R.L., 1977. Improved numerical dissipation for time integration algorithms in structural dynamics. Earthq. Eng. Struct. Dyn. 5, 283–292. https://doi.org/10.1002/eqe.4290050306

Holechek, J.L., Geli, H.M.E., Sawalhah, M.N., Valdez, R., 2022. A Global Assessment: Can Renewable Energy Replace Fossil Fuels by 2050? Sustainability 14, 4792. https://doi.org/10.3390/su14084792

Hsu, M.-C., Bazilevs, Y., 2012. Fluid–structure interaction modeling of wind turbines: simulating the full machine. Comput. Mech. 50, 821–833. https://doi.org/10.1007/s00466-012-0772-0

Hu, W., Rakhsha, M., Yang, L., Kamrin, K., Negrut, D., 2021. Modeling granular material dynamics and its two-way coupling with moving solid bodies using a continuum representation and the SPH method. Comput. Methods Appl. Mech. Eng. 385, 114022. https://doi.org/10.1016/j.cma.2021.114022

Hughes, S.A., 1993. Physical Models and Laboratory Techniques in Coastal Engineering. WORLD SCIENTIFIC. https://doi.org/10.1142/2154

Jing, L., Stephansson, O., 2007. 11 - Discrete Element Methods for Granular Materials, in: Jing, L., Stephansson, O. (Eds.), Developments in Geotechnical Engineering, Fundamentals of Discrete Element Methods for Rock Engineering. Elsevier, pp. 399–444. https://doi.org/10.1016/S0165-1250(07)85011-5

Jo, Y.B., Park, S.-H., Yoo, H.S., Kim, E.S., 2022. GPU-based SPH-DEM Method to Examine the Three-Phase Hydrodynamic Interactions between Multiphase Flow and Solid Particles. Int. J. Multiph. Flow 153, 104125. https://doi.org/10.1016/j.ijmultiphaseflow.2022.104125

Johanning, L., Smith, G.H., Wolfram, J., 2006. Mooring design approach for wave energy converters. Proc. Inst. Mech. Eng. Part M J. Eng. Marit. Environ. 220, 159–174. https://doi.org/10.1243/14750902JEME54

Kamranzad, B., Hadadpour, S., 2020. A multi-criteria approach for selection of wave energy converter/location. Energy 204. https://doi.org/10.1016/j.energy.2020.117924

Katsidoniotaki, E., Nilsson, E., Rutgersson, A., Engström, J., Göteman, M., 2021. Response of Point-Absorbing Wave Energy Conversion System in 50-Years Return Period Extreme Focused Waves. J. Mar. Sci. Eng. 9. https://doi.org/10.3390/jmse9030345

Khayyer, A., Gotoh, H., Falahaty, H., Shimizu, Y., 2018. An enhanced ISPH–SPH coupled method for simulation of incompressible fluid–elastic structure interactions. Comput. Phys. Commun. 232, 139–164. https://doi.org/10.1016/j.cpc.2018.05.012

Khayyer, A., Gotoh, H., Shimizu, Y., 2022a. On systematic development of FSI solvers in the context of particle methods. J. Hydrodyn. 34, 395–407. https://doi.org/10.1007/s42241-022-0042-3

Khayyer, A., Gotoh, H., Shimizu, Y., Gotoh, T., 2024. An improved Riemann SPH-Hamiltonian SPH coupled solver for hydroelastic fluid-structure interactions. Eng. Anal. Bound. Elem. 158, 332–355. https://doi.org/10.1016/j.enganabound.2023.10.018

Khayyer, A., Rogers, B.D., Zhang, A.-M., 2022b. Preface: Special Issue on Advances and Applications of SPH in Ocean Engineering. Appl. Ocean Res. 118, 103028. https://doi.org/10.1016/j.apor.2021.103028

Khayyer, A., Shimizu, Y., Gotoh, H., Nagashima, K., 2021. A coupled incompressible SPH-Hamiltonian SPH solver for hydroelastic FSI corresponding to composite structures. Appl. Math. Model. 94, 242–271. https://doi.org/10.1016/j.apm.2021.01.011

Khayyer, A., Shimizu, Y., Gotoh, T., Gotoh, H., 2023. Enhanced resolution of the continuity equation in explicit weakly compressible SPH simulations of incompressible free-

surface fluid flows. Appl. Math. Model. 116, 84–121. https://doi.org/10.1016/j.apm.2022.10.037

Khayyer, A., Tsuruta, N., Shimizu, Y., Gotoh, H., 2019. Multi-resolution MPS for incompressible fluid-elastic structure interactions in ocean engineering. Appl. Ocean Res. 82, 397–414. https://doi.org/10.1016/j.apor.2018.10.020

King, J.R.C., Lind, S.J., Nasar, A.M.A., 2020. High order difference schemes using the local anisotropic basis function method. J. Comput. Phys. 415, 109549. https://doi.org/10.1016/j.jcp.2020.109549

Laha, S., Fourtakas, G., Das, P.K., Keshmiri, A., 2023. Fluid–structure interaction modeling of bi-leaflet mechanical heart valves using smoothed particle hydrodynamics. Phys. Fluids 35, 121902. https://doi.org/10.1063/5.0172043

Landau, L.D., Lifshitz, E.M., 1970. Theory of Elasticity: Volume 7. Pergamon Press.

Lavidas, G., Blok, K., 2021. Shifting wave energy perceptions: The case for wave energy converter (WEC) feasibility at milder resources. Renew. Energy 170, 1143–1155. https://doi.org/10.1016/j.renene.2021.02.041

Lee, E.-S., Moulinec, C., Xu, R., Violeau, D., Laurence, D., Stansby, P., 2008. Comparisons of weakly compressible and truly incompressible algorithms for the SPH mesh free particle method. J. Comput. Phys. 227, 8417–8436. https://doi.org/10.1016/j.jcp.2008.06.005

Leimkuhler, B., Matthews, C., 2015. Introduction, in: Leimkuhler, B., Matthews, C. (Eds.), Molecular Dynamics: With Deterministic and Stochastic Numerical Methods, Interdisciplinary Applied Mathematics. Springer International Publishing, Cham, pp. 1–51. https://doi.org/10.1007/978-3-319-16375-8_1

Li, M.-J., Lian, Y., Zhang, X., 2022. An immersed finite element material point (IFEMP) method for free surface fluid–structure interaction problems. Comput. Methods Appl. Mech. Eng. 393, 114809. https://doi.org/10.1016/j.cma.2022.114809

Li, Y., Yu, Y.-H., 2012. A synthesis of numerical methods for modeling wave energy converter-point absorbers. Renew. Sustain. Energy Rev. 16, 4352–4364. https://doi.org/10.1016/j.rser.2011.11.008

Li, Z., Leduc, J., Nunez-Ramirez, J., Combescure, A., Marongiu, J.-C., 2015. A non-intrusive partitioned approach to couple smoothed particle hydrodynamics and finite element methods for transient fluid-structure interaction problems with large

interface motion. Comput. Mech. 55, 697–718. https://doi.org/10.1007/s00466-015-1131-8

Liao, K., Hu, C., Sueyoshi, M., 2015. Free surface flow impacting on an elastic structure: Experiment versus numerical simulation. Appl. Ocean Res. 50, 192–208. https://doi.org/10.1016/j.apor.2015.02.002

Lin, Z., Chen, H., Qian, L., Ma, Z., Causon, D., Mingham, C., 2021. Simulating focused wave impacts on point absorber wave energy converters. Proc. Inst. Civ. Eng. - Eng. Comput. Mech. 174, 19–31. https://doi.org/10.1680/jencm.19.00038

Liu, C., Yang, Q., Bao, G., 2017. Performance investigation of a two-raft-type wave energy converter with hydraulic power take-off unit. Appl. Ocean Res. 62, 139–155. https://doi.org/10.1016/j.apor.2016.12.002

Liu, M.B., Liu, G.R., 2006. Restoring particle consistency in smoothed particle hydrodynamics. Appl. Numer. Math. 56, 19–36. https://doi.org/10.1016/j.apnum.2005.02.012

Lo, E.Y.M., Shao, S., 2002. Simulation of near-shore solitary wave mechanics by an incompressible SPH method. Appl. Ocean Res. 24, 275–286. https://doi.org/10.1016/S0141-1187(03)00002-6

López, I., Andreu, J., Ceballos, S., Martínez de Alegría, I., Kortabarria, I., 2013. Review of wave energy technologies and the necessary power-equipment. Renew. Sustain. Energy Rev. 27, 413–434. https://doi.org/10.1016/j.rser.2013.07.009

Machado, M., Moreira, P., Flores, P., Lankarani, H.M., 2012. Compliant contact force models in multibody dynamics: Evolution of the Hertz contact theory. Mech. Mach. Theory 53, 99–121. https://doi.org/10.1016/j.mechmachtheory.2012.02.010

Madsen, O.S., 1971. On the generation of long waves. J. Geophys. Res. 1896-1977 76, 8672–8683. https://doi.org/10.1029/JC076i036p08672

Manenti, S., Wang, D., Domínguez, J.M., Li, S., Amicarelli, A., Albano, R., 2019. SPH Modeling of Water-Related Natural Hazards. Water 11, 1875. https://doi.org/10.3390/w11091875

Markauskas, D., Kruggel-Emden, H., 2019. Coupled DEM-SPH simulations of wet continuous screening. Adv. Powder Technol. 30, 2997–3009. https://doi.org/10.1016/j.apt.2019.09.007

Markauskas, D., Kruggel-Emden, H., Sivanesapillai, R., Steeb, H., 2017. Comparative study on mesh-based and mesh-less coupled CFD-DEM methods to model particle-laden flow. Powder Technol. 305, 78–88. https://doi.org/10.1016/j.powtec.2016.09.052

Marrone, S., Antuono, M., Colagrossi, A., Colicchio, G., Le Touzé, D., Graziani, G., 2011. δ-SPH model for simulating violent impact flows. Comput. Methods Appl. Mech. Eng. 200, 1526–1542. https://doi.org/10.1016/j.cma.2010.12.016

Martínez-Estévez, I., 2022. MoorDyn+ [Online]: https://github.com/imestevez/MoorDynPlus

Martínez-Estévez, I., Domínguez, J.M., Tagliafierro, B., Canelas, R.B., García-Feal, O., Crespo, A.J.C., Gómez-Gesteira, M., 2023a. Coupling of an SPH-based solver with a multiphysics library. Comput. Phys. Commun. 283, 108581. https://doi.org/10.1016/j.cpc.2022.108581

Martínez-Estévez, I., Tagliafierro, B., El Rahi, J., Domínguez, J.M., Crespo, A.J.C., Troch, P., Gómez-Gesteira, M., 2023b. Coupling an SPH-based solver with an FEA structural solver to simulate free surface flows interacting with flexible structures. Comput. Methods Appl. Mech. Eng. 410, 115989. https://doi.org/10.1016/j.cma.2023.115989

McLoone, M., Quinlan, N.J., 2022. Coupling of the meshless finite volume particle method and the finite element method for fluid–structure interaction with thin elastic structures. Eur. J. Mech. - BFluids 92, 117–131. https://doi.org/10.1016/j.euromechflu.2021.12.001

Meng, Z.-F., Zhang, A.-M., Yan, J.-L., Wang, P.-P., Khayyer, A., 2022. A hydroelastic fluid–structure interaction solver based on the Riemann-SPH method. Comput. Methods Appl. Mech. Eng. 390, 114522. https://doi.org/10.1016/j.cma.2021.114522

Meringolo, D.D., Colagrossi, A., Marrone, S., Aristodemo, F., 2017. On the filtering of acoustic components in weakly-compressible SPH simulations. J. Fluids Struct. 70, 1–23. https://doi.org/10.1016/j.jfluidstructs.2017.01.005

Mitsui, J., Altomare, C., Crespo, A.J.C., Domínguez, J.M., Martínez-Estévez, I., Suzuki, T., Kubota, S., Gómez-Gesteira, M., 2023. DualSPHysics modelling to analyse the response of Tetrapods against solitary wave. Coast. Eng. 183, 104315. https://doi.org/10.1016/j.coastaleng.2023.104315

Mokos, A., Rogers, B.D., Stansby, P.K., Domínguez, J.M., 2015. Multi-phase SPH modelling of violent hydrodynamics on GPUs. Comput. Phys. Commun. 196, 304–316. https://doi.org/10.1016/j.cpc.2015.06.020

Molteni, D., Colagrossi, A., 2009. A simple procedure to improve the pressure evaluation in hydrodynamic context using the SPH. Comput. Phys. Commun. 180, 861–872. https://doi.org/10.1016/j.cpc.2008.12.004

Monaghan, J.J., 2005. Smoothed particle hydrodynamics. Rep. Prog. Phys. 68, 1703–1759. https://doi.org/10.1088/0034-4885/68/8/R01

Monaghan, J.J., 1992. Smoothed Particle Hydrodynamics. Annu. Rev. Astron. Astrophys. 30, 543–574. https://doi.org/10.1146/annurev.aa.30.090192.002551

Monaghan, J.J., Cas, R. a. F., Kos, A.M., Hallworth, M., 1999. Gravity currents descending a ramp in a stratified tank. J. Fluid Mech. 379, 39–69. https://doi.org/10.1017/S0022112098003280

Monaghan, J.J., Gingold, R.A., 1983. Shock simulation by the particle method SPH. J. Comput. Phys. 52, 374–389. https://doi.org/10.1016/0021-9991(83)90036-0

Monaghan, J.J., Kos, A., 1999. Solitary Waves on a Cretan Beach. J. Waterw. Port Coast. Ocean Eng. 125, 145–155. https://doi.org/10.1061/(ASCE)0733-950X(1999)125:3(145)

Monaghan, J.J., Kos, A., Issa, N., 2003. Fluid Motion Generated by Impact. J. Waterw. Port Coast. Ocean Eng. 129, 250–259. https://doi.org/10.1061/(ASCE)0733-950X(2003)129:6(250)

Morikawa, D.S., Asai, M., 2021. Coupling total Lagrangian SPH–EISPH for fluid–structure interaction with large deformed hyperelastic solid bodies. Comput. Methods Appl. Mech. Eng. 381. https://doi.org/10.1016/j.cma.2021.113832

Morison, J.R., Johnson, J.W., Schaaf, S.A., 1950. The Force Exerted by Surface Waves on Piles. J. Pet. Technol. 2, 149–154. https://doi.org/10.2118/950149-G

Muliawan, M.J., Karimirad, M., Gao, Z., Moan, T., 2013. Extreme responses of a combined spar-type floating wind turbine and floating wave energy converter (STC) system with survival modes. Ocean Eng. 65, 71–82. https://doi.org/10.1016/j.oceaneng.2013.03.002

Myers, C., Palmer, T., Palmer, C., 2023. A hybrid Finite Volume-Smoothed Particle Hydrodynamics approach for shock capturing applications. Comput. Methods Appl. Mech. Eng. 417, 116412. https://doi.org/10.1016/j.cma.2023.116412

Nasar, A.M.A., Fourtakas, G., Lind, S.J., King, J.R.C., Rogers, B.D., Stansby, P.K., 2021. High-order consistent SPH with the pressure projection method in 2-D and 3-D. J. Comput. Phys. 444, 110563. https://doi.org/10.1016/j.jcp.2021.110563

Nasar, A.M.A., Rogers, B.D., Revell, A., Stansby, P.K., 2019. Flexible slender body fluid interaction: Vector-based discrete element method with Eulerian smoothed particle hydrodynamics. Comput. Fluids 179, 563–578. https://doi.org/10.1016/j.compfluid.2018.11.024

Negrut, D., Rampalli, R., Ottarsson, G., Sajdak, A., 2006. On an Implementation of the Hilber-Hughes-Taylor Method in the Context of Index 3 Differential-Algebraic Equations of Multibody Dynamics (DETC2005-85096). J. Comput. Nonlinear Dyn. 2, 73–85. https://doi.org/10.1115/1.2389231

Newmark, N.M., 1962. A Method of Computation for Structural Dynamics. Trans. Am. Soc. Civ. Eng. 127, 1406–1433. https://doi.org/10.1061/TACEAT.0008448

Ng, K.C., Alexiadis, A., Chen, H., Sheu, T.W.H., 2021. Numerical computation of fluid–solid mixture flow using the SPH–VCPM–DEM method. J. Fluids Struct. 106, 103369. https://doi.org/10.1016/j.jfluidstructs.2021.103369

O'Connor, J., Domínguez, J.M., Rogers, B.D., Lind, S.J., Stansby, P.K., 2022. Eulerian incompressible smoothed particle hydrodynamics on multiple GPUs. Comput. Phys. Commun. 273, 108263. https://doi.org/10.1016/j.cpc.2021.108263

O'Connor, J., Rogers, B.D., 2021. A fluid–structure interaction model for free-surface flows and flexible structures using smoothed particle hydrodynamics on a GPU. J. Fluids Struct. 104, 103312. https://doi.org/10.1016/j.jfluidstructs.2021.103312

Oger, G., Le Touzé, D., Ducrozet, G., Candelier, J., Guilcher, P.-M., 2014. A Coupled SPH-Spectral Method for the Simulation of Wave Train Impacts on a FPSO. Presented at the ASME 2014 33rd International Conference on Ocean, Offshore and Arctic Engineering, American Society of Mechanical Engineers Digital Collection. https://doi.org/10.1115/OMAE2014-24679

Olabi, A.G., Abdelkareem, M.A., 2022. Renewable energy and climate change. Renew. Sustain. Energy Rev. 158, 112111. https://doi.org/10.1016/j.rser.2022.112111

Orphin, J., Nader, J.-R., Penesis, I., 2021. Size matters: Scale effects of an OWC wave energy converter. Renew. Energy. https://doi.org/10.1016/j.renene.2021.11.121

Owusu, P.A., Asumadu-Sarkodie, S., 2016. A review of renewable energy sources, sustainability issues and climate change mitigation. Cogent Eng. 3, 1167990. https://doi.org/10.1080/23311916.2016.1167990

Park, S.-H., Jo, Y.B., Ahn, Y., Choi, H.Y., Choi, T.S., Park, S.-S., Yoo, H.S., Kim, J.W., Kim, E.S., 2020. Development of Multi-GPU–Based Smoothed Particle Hydrodynamics Code for Nuclear Thermal Hydraulics and Safety: Potential and Challenges. Front. Energy Res. 8.

Parshikov, A.N., Medin, S.A., Loukashenko, I.I., Milekhin, V.A., 2000. Improvements in SPH method by means of interparticle contact algorithm and analysis of perforation tests at moderate projectile velocities. Int. J. Impact Eng. 24, 779–796. https://doi.org/10.1016/S0734-743X(99)00168-2

Pazouki, A., Kwarta, M., Williams, K., Likos, W., Serban, R., Jayakumar, P., Negrut, D., 2017. Compliant contact versus rigid contact: A comparison in the context of granular dynamics. Phys. Rev. E 96, 042905. https://doi.org/10.1103/PhysRevE.96.042905

Pecher, A., Kofoed, J.P. (Eds.), 2017. Handbook of Ocean Wave Energy, Ocean Engineering & Oceanography. Springer International Publishing, Cham. https://doi.org/10.1007/978-3-319-39889-1

Penalba, M., Davidson, J., Windt, C., Ringwood, J.V., 2018. A high-fidelity wave-to-wire simulation platform for wave energy converters: Coupled numerical wave tank and power take-off models. Appl. Energy 226, 655–669. https://doi.org/10.1016/j.apenergy.2018.06.008

Penalba, M., Giorgi, G., Ringwood, J.V., 2017a. Mathematical modelling of wave energy converters: A review of nonlinear approaches. Renew. Sustain. Energy Rev. 78, 1188–1207. https://doi.org/10.1016/j.rser.2016.11.137

Penalba, M., Kelly, T., Ringwood, J., 2017b. Using NEMOH for Modelling Wave Energy Converters: A Comparative Study with WAMIT, in: 12th European Wave and Tidal Energy Conference (EWTEC).

Pribadi, A.B.K., Donatini, L., Lataire, E., Verao Fernandez, G., Martínez-Estévez, I., 2023. Validation of a computationally efficient time-domain numerical tool against DeepCwind experimental data. Trends Renew. Energ. Offshore - Proc. 5th Int. Conf. Renew. Energ. Offshore RENEW 2022. https://doi.org/10.1201/9781003360773-68

Quartier, N., Crespo, A.J.C., Domínguez, J.M., Stratigaki, V., Troch, P., 2021a. Efficient response of an onshore Oscillating Water Column Wave Energy Converter using a one-phase SPH model coupled with a multiphysics library. Appl. Ocean Res. 115, 102856. https://doi.org/10.1016/j.apor.2021.102856

Quartier, N., Ropero-Giralda, P., M. Domínguez, J., Stratigaki, V., Troch, P., 2021b. Influence of the Drag Force on the Average Absorbed Power of Heaving Wave Energy Converters Using Smoothed Particle Hydrodynamics. Water 13, 384. https://doi.org/10.3390/w13030384

Rahmati, M.T., Aggidis, G.A., 2016. Numerical and experimental analysis of the power output of a point absorber wave energy converter in irregular waves. Ocean Eng. 111, 483–492. https://doi.org/10.1016/j.oceaneng.2015.11.011

Rakhsha, Milad, Kees, C.E., Negrut, D., 2021. Lagrangian vs. Eulerian: An Analysis of Two Solution Methods for Free-Surface Flows and Fluid Solid Interaction Problems. Fluids 6, 460. https://doi.org/10.3390/fluids6120460

Rakhsha, M., Yang, L., Hu, W., Negrut, D., 2021. On the use of multibody dynamics techniques to simulate fluid dynamics and fluid–solid interaction problems. Multibody Syst. Dyn. 53, 29–57. https://doi.org/10.1007/s11044-021-09784-y

Randolph, M., Quiggin, P., 2010. Non-Linear Hysteretic Seabed Model for Catenary Pipeline Contact. Presented at the ASME 2009 28th International Conference on Ocean, Offshore and Arctic Engineering, American Society of Mechanical Engineers Digital Collection, pp. 145–154. https://doi.org/10.1115/OMAE2009-79259

Rankin, C.C., Nour-Omid, B., 1988. The use of projectors to improve finite element performance. Comput. Struct. 30, 257–267. https://doi.org/10.1016/0045-7949(88)90231-3

Ransley, E.J., Greaves, D., Raby, A., Simmonds, D., Hann, M., 2017. Survivability of wave energy converters using CFD. Renew. Energy 109, 235–247. https://doi.org/10.1016/j.renene.2017.03.003

Rastelli, P., Vacondio, R., Marongiu, J.C., Fourtakas, G., Rogers, B.D., 2022. Implicit iterative particle shifting for meshless numerical schemes using kernel basis functions. Comput. Methods Appl. Mech. Eng. 393, 114716. https://doi.org/10.1016/j.cma.2022.114716

Ren, Y., Khayyer, A., Lin, P., Hu, X., 2023. Numerical modeling of sloshing flow interaction with an elastic baffle using SPHinXsys. Ocean Eng. 267, 113110. https://doi.org/10.1016/j.oceaneng.2022.113110

Romano, A., Bellotti, G., Briganti, R., Franco, L., 2015. Uncertainties in the physical modelling of the wave overtopping over a rubble mound breakwater: The role of the seeding number and of the test duration. Coast. Eng. 103, 15–21. https://doi.org/10.1016/j.coastaleng.2015.05.005

Ropero-Giralda, P., Crespo, A.J.C., Coe, R.G., Tagliafierro, B., Domínguez, J.M., Bacelli, G., Gómez-Gesteira, M., 2021. Modelling a Heaving Point-Absorber with a Closed-Loop Control System Using the DualSPHysics Code. Energies 14, 760. https://doi.org/10.3390/en14030760

Ropero-Giralda, P., Crespo, A.J.C., Tagliafierro, B., Altomare, C., Domínguez, J.M., Gómez-Gesteira, M., Viccione, G., 2020. Efficiency and survivability analysis of a point-absorber wave energy converter using DualSPHysics. Renew. Energy 162, 1763–1776. https://doi.org/10.1016/j.renene.2020.10.012

Roul, R., Kumar, A., 2020. Fluid-Structure Interaction of Wind Turbine Blade Using Four Different Materials: Numerical Investigation. Symmetry 12, 1467. https://doi.org/10.3390/sym12091467

Shadloo, M.S., Oger, G., Le Touzé, D., 2016. Smoothed particle hydrodynamics method for fluid flows, towards industrial applications: Motivations, current state, and challenges. Comput. Fluids 136, 11–34. https://doi.org/10.1016/j.compfluid.2016.05.029

Shadmani, A., Nikoo, M.R., Gandomi, A.H., 2024. Adaptive systematic optimization of a multi-axis ocean wave energy converter. Renew. Sustain. Energy Rev. 189, 113920. https://doi.org/10.1016/j.rser.2023.113920

Sjökvist, L., Göteman, M., 2019. Peak forces on a point absorbing wave energy converter impacted by tsunami waves. Renew. Energy 133, 1024–1033. https://doi.org/10.1016/j.renene.2018.10.092

Sjökvist, L., Wu, J., Ransley, E., Engström, J., Eriksson, M., Göteman, M., 2017. Numerical models for the motion and forces of point-absorbing wave energy converters in extreme waves. Ocean Eng. 145, 1–14. https://doi.org/10.1016/j.oceaneng.2017.08.061

Skillen, A., Lind, S., Stansby, P.K., Rogers, B.D., 2013. Incompressible smoothed particle hydrodynamics (SPH) with reduced temporal noise and generalised Fickian smoothing applied to body–water slam and efficient wave–body interaction. Comput. Methods Appl. Mech. Eng. 265, 163–173. https://doi.org/10.1016/j.cma.2013.05.017

Su, Z., Xiang, Y., Li, D., Wang, S., Sheng, J., 2024. SPH-DEM modeling of cable-controlled ROVs: Underwater mobility and path planning. Ocean Eng. 292, 116623. https://doi.org/10.1016/j.oceaneng.2023.116623

Sun, J., Zou, L., Govender, N., Martínez-Estévez, I., Crespo, A.J.C., Sun, Z., Domínguez, J.M., 2023. A resolved SPH-DEM coupling method for analysing the interaction of polyhedral granular materials with fluid. Ocean Eng. 287, 115938. https://doi.org/10.1016/j.oceaneng.2023.115938

Sun, P.N., Le Touzé, D., Oger, G., Zhang, A.-M., 2021. An accurate FSI-SPH modeling of challenging fluid-structure interaction problems in two and three dimensions. Ocean Eng. 221, 108552. https://doi.org/10.1016/j.oceaneng.2020.108552

Sun, P.N., Le Touzé, D., Zhang, A.-M., 2019. Study of a complex fluid-structure dam-breaking benchmark problem using a multi-phase SPH method with APR. Eng. Anal. Bound. Elem. 104, 240–258. https://doi.org/10.1016/j.enganabound.2019.03.033

Sun, Y., Xi, G., Sun, Z., 2019. A fully Lagrangian method for fluid–structure interaction problems with deformable floating structure. J. Fluids Struct. 90, 379–395. https://doi.org/10.1016/j.jfluidstructs.2019.07.005

Sunday, C., Murdoch, N., Tardivel, S., Schwartz, S.R., Michel, P., 2020. Validating N-body code chrono for granular DEM simulations in reduced-gravity environments. Mon. Not. R. Astron. Soc. 498, 1062–1079. https://doi.org/10.1093/mnras/staa2454

Suzuki, T., García-Feal, O., Domínguez, J.M., Altomare, C., 2022. Simulation of 3D overtopping flow–object–structure interaction with a calibration-based wave generation method with DualSPHysics and SWASH. Comput. Part. Mech. https://doi.org/10.1007/s40571-022-00468-8

Tagliafierro, B., Karimirad, M., Altomare, C., Göteman, M., Martínez-Estévez, I., Capasso, S., Domínguez, J.M., Viccione, G., Gómez-Gesteira, M., Crespo, A.J.C., 2023a. Numerical validations and investigation of a semi-submersible floating offshore wind turbine platform interacting with ocean waves using an SPH framework. Appl. Ocean Res. 141, 103757. https://doi.org/10.1016/j.apor.2023.103757

Tagliafierro, B., Karimirad, M., Martínez-Estévez, I., Domínguez, J.M., Viccione, G., Crespo, A.J.C., 2022a. Numerical Assessment of a Tension-Leg Platform Wind Turbine in Intermediate Water Using the Smoothed Particle Hydrodynamics Method. Energies 15, 3993. https://doi.org/10.3390/en15113993

Tagliafierro, B., Martínez-Estévez, I., Capasso, S., Domínguez, J.M., O'Connor, J., Altomare, C., Viccione, G., Crespo, A.J.C., Rogers, B.D., Serban, R., Negruț, D., 2023b. Comparative Analysis of Smoothed Particle Hydrodynamics (SPH) for Fluid-Structure Interaction: Computational Performance of Lagrangian SPH and Structural Modeling Strategies. Presented at the ASME 2023 International Design Engineering Technical Conferences and Computers and Information in Engineering Conference, American Society of Mechanical Engineers Digital Collection. https://doi.org/10.1115/DETC2023-111406

Tagliafierro, B., Martínez-Estévez, I., Crego-Loureiro, C., Domínguez, J.M., Crespo, A.J.C., Coe, R.G., Bacelli, G., Gómez-Gesteira, M., Viccione, G., 2022b. Numerical Modeling of Moored Floating Platforms for Wave Energy Converters Using DualSPHysics. Presented at the ASME 2022 41st International Conference on Ocean, Offshore and Arctic Engineering, American Society of Mechanical Engineers Digital Collection. https://doi.org/10.1115/OMAE2022-78810

Tagliafierro, B., Martínez-Estévez, I., Domínguez, J.M., Crespo, A.J.C., Göteman, M., Engström, J., Gómez-Gesteira, M., 2022c. A numerical study of a taut-moored point-absorber wave energy converter with a linear power take-off system under extreme wave conditions. Appl. Energy 311, 118629. https://doi.org/10.1016/j.apenergy.2022.118629

Tagliafierro, B., Montuori, R., Vayas, I., Ropero, P., Crespo, A.J., Domínguez Alonso, J.M., Altomare, C., Viccione, G., Gómez Gesteira, M., 2020. A new open source solver for modelling fluid-structure interaction: case study of a point-absorberwave energy converter with power take-off unit, in: EURODYN 2020: Proceedings of the XI International Conference on Structural Dynamics, Streamed from Athens, Greece, 23-26 November 2020. National Technical University of Athens, pp. 657–668.

Tasora, A., Anitescu, M., 2011. A matrix-free cone complementarity approach for solving large-scale, nonsmooth, rigid body dynamics. Comput. Methods Appl. Mech. Eng. 200, 439–453. https://doi.org/10.1016/j.cma.2010.06.030

Tasora, A., Anitescu, M., 2010. A Convex Complementarity Approach for Simulating Large Granular Flows. J. Comput. Nonlinear Dyn. 5. https://doi.org/10.1115/1.4001371

Tasora, A., Masarati, P., 2015. Analysis of Rotating Systems Using General-Purpose Multibody Dynamics, in: Pennacchi, P. (Ed.), Proceedings of the 9th IFToMM International Conference on Rotor Dynamics, Mechanisms and Machine Science. Springer International Publishing, Cham, pp. 1689–1701. https://doi.org/10.1007/978-3-319-06590-8_139

Tasora, A., Serban, R., Mazhar, H., Pazouki, A., Melanz, D., Fleischmann, J., Taylor, M., Sugiyama, H., Negrut, D., 2016. Chrono: An Open Source Multi-physics Dynamics Engine, in: Kozubek, T., Blaheta, R., Šístek, J., Rozložník, M., Čermák, M. (Eds.), High Performance Computing in Science and Engineering, Lecture Notes in Computer Science. Springer International Publishing, Cham, pp. 19–49. https://doi.org/10.1007/978-3-319-40361-8_2

Tian, F.-B., Dai, H., Luo, H., Doyle, J.F., Rousseau, B., 2014. Fluid–structure interaction involving large deformations: 3D simulations and applications to biological systems. J. Comput. Phys. 258, 451–469. https://doi.org/10.1016/j.jcp.2013.10.047

Timoshenko, S., Woinowsky-Krieger, S., 1959. Theory of plates and shells. McGraw-hill New York.

Tromans, P.S., Anaturk, A.R., Hagemeijer, P., 1991. A New Model For The Kinematics Of Large Ocean Waves-Application As a Design Wave, in: International Ocean and Polar Engineering Conference.

Trueworthy, A., DuPont, B., 2020. The Wave Energy Converter Design Process: Methods Applied in Industry and Shortcomings of Current Practices. J. Mar. Sci. Eng. 8, 932. https://doi.org/10.3390/jmse8110932

Vacondio, R., Altomare, C., De Leffe, M., Hu, X., Le Touzé, D., Lind, S., Marongiu, J.-C., Marrone, S., Rogers, B.D., Souto-Iglesias, A., 2021. Grand challenges for Smoothed Particle Hydrodynamics numerical schemes. Comput. Part. Mech. 8, 575–588. https://doi.org/10.1007/s40571-020-00354-1

Valdez-Balderas, D., Domínguez, J.M., Rogers, B.D., Crespo, A.J.C., 2013. Towards accelerating smoothed particle hydrodynamics simulations for free-surface flows on multi-GPU clusters. J. Parallel Distrib. Comput., Novel architectures for high-performance computing 73, 1483–1493. https://doi.org/10.1016/j.jpdc.2012.07.010

van Rij, J., Yu, Y.-H., Guo, Y., Coe, R.G., 2019. A Wave Energy Converter Design Load Case Study. J. Mar. Sci. Eng. 7. https://doi.org/10.3390/jmse7080250

Verbrugghe, T., Stratigaki, V., Altomare, C., Domínguez, J.M., Troch, P., Kortenhaus, A., 2019. Implementation of Open Boundaries within a Two-Way Coupled SPH Model to Simulate Nonlinear Wave–Structure Interactions. Energies 12, 697. https://doi.org/10.3390/en12040697

Violeau, D., Rogers, B.D., 2016. Smoothed particle hydrodynamics (SPH) for free-surface flows: past, present and future. J. Hydraul. Res. 54, 1–26. https://doi.org/10.1080/00221686.2015.1119209

Wang, S., González-Cao, J., Islam, H., Gómez-Gesteira, M., Guedes Soares, C., 2022. Uncertainty estimation of mesh-free and mesh-based simulations of the dynamics of floaters. Ocean Eng. 256, 111386. https://doi.org/10.1016/j.oceaneng.2022.111386

Waters, R., Stålberg, M., Danielsson, O., Svensson, O., Gustafsson, S., Strömstedt, E., Eriksson, M., Sundberg, J., Leijon, M., 2007. Experimental results from sea trials of an offshore wave energy system. Appl. Phys. Lett. 90.

Wei, Z., Edge, B.L., Dalrymple, R.A., Hérault, A., 2019. Modeling of wave energy converters by GPUSPH and Project Chrono. Ocean Eng. 183, 332–349. https://doi.org/10.1016/j.oceaneng.2019.04.029

Wendland, H., 1995. Piecewise polynomial, positive definite and compactly supported radial functions of minimal degree. Adv. Comput. Math. 4, 389–396. https://doi.org/10.1007/BF02123482

Whittaker, C.N., Fitzgerald, C.J., Raby, A.C., Taylor, P.H., Orszaghova, J., Borthwick, A.G.L., 2017. Optimisation of focused wave group runup on a plane beach. Coast. Eng. 121, 44–55. https://doi.org/10.1016/j.coastaleng.2016.12.001

Willmott, C.J., Ackleson, S.G., Davis, R.E., Feddema, J.J., Klink, K.M., Legates, D.R., O'Donnell, J., Rowe, C.M., 1985. Statistics for the evaluation and comparison of models. J. Geophys. Res. Oceans 90, 8995–9005. https://doi.org/10.1029/JC090iC05p08995

Willmott, C.J., Robeson, S.M., Matsuura, K., 2012. A refined index of model performance. Int. J. Climatol. 32, 2088–2094. https://doi.org/10.1002/joc.2419

Windt, C., Davidson, J., Ringwood, J.V., 2018. High-fidelity numerical modelling of ocean wave energy systems: A review of computational fluid dynamics-based numerical wave tanks. Renew. Sustain. Energy Rev. 93, 610–630. https://doi.org/10.1016/j.rser.2018.05.020

Wu, K., Yang, D., Wright, N., 2016. A coupled SPH-DEM model for fluid-structure interaction problems with free-surface flow and structural failure. Comput. Struct. 177, 141–161. https://doi.org/10.1016/j.compstruc.2016.08.012

Xie, F., Zhao, W., Wan, D., 2021. MPS-DEM coupling method for interaction between fluid and thin elastic structures. Ocean Eng. 236, 109449. https://doi.org/10.1016/j.oceaneng.2021.109449

Xu, S., Wang, S., Guedes Soares, C., 2019. Review of mooring design for floating wave energy converters. Renew. Sustain. Energy Rev. 111, 595–621. https://doi.org/10.1016/j.rser.2019.05.027

Xu, W.-J., Dong, X.-Y., 2021. Simulation and verification of landslide tsunamis using a 3D SPH-DEM coupling method. Comput. Geotech. 129, 103803. https://doi.org/10.1016/j.compgeo.2020.103803

Yang, L., Rakhsha, M., Hu, W., Negrut, D., 2022. A consistent multiphase flow model with a generalized particle shifting scheme resolved via incompressible SPH. J. Comput. Phys. 458, 111079. https://doi.org/10.1016/j.jcp.2022.111079

You, Y., Khayyer, A., Zheng, X., Gotoh, H., Ma, Q., 2021. Enhancement of δ-SPH for ocean engineering applications through incorporation of a background mesh scheme. Appl. Ocean Res. 110, 102508. https://doi.org/10.1016/j.apor.2020.102508

Zhang, F., Crespo, A., Altomare, C., Domínguez, J., Marzeddu, A., Shang, S., Gómez-Gesteira, M., 2018. DualSPHysics: A numerical tool to simulate real breakwaters. J. Hydrodyn. 30, 95–105. https://doi.org/10.1007/s42241-018-0010-0

Zhang, G., Zhao, W., Wan, D., 2021. Partitioned MPS-FEM method for free-surface flows interacting with deformable structures. Appl. Ocean Res. 114, 102775. https://doi.org/10.1016/j.apor.2021.102775

Zhang, S., Kuwabara, S., Suzuki, T., Kawano, Y., Morita, K., Fukuda, K., 2009. Simulation of solid–fluid mixture flow using moving particle methods. J. Comput. Phys. 228, 2552–2565. https://doi.org/10.1016/j.jcp.2008.12.005

Zou, L., Sun, J.Z., Sun, Z., Yu, Z.B., Zhao, H.B., 2022. Study of two free-falling spheres interaction by coupled SPH–DEM method. Eur. J. Mech. - BFluids 92, 49–64. https://doi.org/10.1016/j.euromechflu.2021.09.006

Universidade Vigo